UNIVERSIDADE DE BRASÍLIA
INSTITUTO DE GEOCIÊNCIAS
PROGRAMA DE PÓS-GRADUAÇÃO EM GEOLOGIA

CAROLINE LESSIO CAZARIN

TECTÔNICA, CONTROLE ESTRATIGRÁFICO E CIRCULAÇÃO DE FLUIDOS NA FORMAÇÃO DO CARSTE HIPOGÊNICO - BACIA DE IRECÊ, CRÁTON SÃO FRANCISCO

Orientador: Roberto Ventura Santos

Coorientador: Francisco Hilário Rego Bezerra

TESE DE DOUTORADO Nº 175

Brasília-DF

2021

UNIVERSIDADE DE BRASÍLIA
INSTITUTO DE GEOCIÊNCIAS
PROGRAMA DE PÓS-GRADUAÇÃO EM GEOLOGIA

CAROLINE LESSIO CAZARIN

TECTÔNICA, CONTROLE ESTRATIGRÁFICO E CIRCULAÇÃO DE FLUIDOS NA FORMAÇÃO DO CARSTE HIPOGÊNICO - BACIA DE IRECÊ, CRÁTON SÃO FRANCISCO

Orientador: Prof. Dr. Roberto Ventura Santos

Coorientador: Prof. Dr. Francisco Hilário Rego Bezerra

Tese de Doutorado apresentada ao Instituto de Geociências da Universidade de Brasília, como parte dos requisitos para a obtenção de título de Doutor em Geologia.

Comissão Examinadora:

Prof. Dr. Roberto Ventura Santos (Presidente – UnB)

Prof. Dr. Francisco Pinheiro Lima Filho (UFRN)

Prof. Dr. Francisco Cézar Costa Nogueira (UFCG)

Prof. Dra. Lucieth Cruz Vieira (UnB)

Brasília-DF

2021

Ficha catalográfica elaborada automaticamente,
com os dados fornecidos pelo(a) autor(a)

Lessio Cazarin, Caroline
LC386t TECTÔNICA, CONTROLE ESTRATIGRÁFICO E CIRCULAÇÃO DE FLUIDOS NA FORMAÇÃO DO CARSTE HIPOGÊNICO - BACIA DE IRECÊ, CRÁTON SÃO FRANCISCO / Caroline Lessio Cazarin; orientador Roberto Ventura Santos; co-orientador Francisco Hilário Rego Bezerra. -- Brasília, 2021.
144 p.

Tese (Doutorado - Doutorado em Geologia) -- Universidade de Brasília, 2021.

1. carste hipogênico. 2. carbonatos. 3. fluido hidrotermal. 4. Formação Salitre. 5. Cráton São Francisco. I. Ventura Santos, Roberto , orient. II. Rego Bezerra, Francisco Hilário, co-orient. III. Título.

Dedico esta Tese de Doutorado aos meus pais.

(in memorian)

AGRADECIMENTOS

Agradeço, inicialmente, à Petróleo Brasileiro S.A. e ao Centro de Pesquisas (CENPES), juntamente com seu corpo gerencial pelo apoio e liberação no período do doutorado.

Agradeço às Universidades de Brasília e do Rio Grande do Norte, e aos projetos ProCarste e CristalDOM, suportados pela Agência Nacional de Petróleo, Gás e Biocombustíveis (ANP).

Agradeço aos colegas e professores que colaboraram e me incentivaram na conclusão da Tese, em especial: aos Professores Leonardo Borghi, José A. Brod, Narendra Srivastava, David Castro, Paola Barbosa, John Reijmer, Giovanni Bertotti; aos colegas Augusto Auler, Julia Favoretto, Vincenzo La Bruna, Danielle Caroline Silva e Robin van der Velde.

Em destaque, agradeço ao meu orientador Prof Roberto Ventura Santos e ao meu coorientador Prof Francisco Hilário Bezerra. Sem o apoio, orientação e a paciência deles teria sido uma trajetória com muito mais obstáculos.

O presente trabalho foi realizado com apoio da Coordenação de Aperfeiçoamento de Pessoal de Nível Superior - Brasil (CAPES) - Código de Financiamento 001.

RESUMO

O estudo dos sistemas cársticos e dos fluidos que geram porosidade nas rochas carbonáticas são de fundamental importância para reservatórios de petróleo e aquíferos. Os objetivos da presente tese são investigar (1) o papel da fácies sedimentares e da estratigrafia de zonas de alta permeabilidade e cavernas originadas por fluidos ascendentes; e (2) a distribuição, mineralogia e composição isotópica de depósitos hidrotermais ao longo de um sistema de falha *strike-slip* e suas rochas hospedeiras. Realizamos ambos os estudos na Formação Salitre, Neoproterozóico (700-560 Ma), Cráton São Francisco, Brasil. O primeiro estudo foi realizado nas cavernas Toca da Boa Vista (~ 107 km de extensão) e Toca da Barriguda (~ 34 km), sistema TBV-TBR, na Bacia de Irecê (Campo Formoso, BA) e formam o maior sistema de cavernas da América do Sul. O segundo estudo foi realizado no sistema de falhas Cafarnaum, que separa a Formação Salitre (bloco oeste na Bacia do Irecê) e o Grupo Chapada Diamantina (bloco leste, área do Morro do Chapéu). A presente tese usa uma combinação de análise de fácies sedimentares, análise estrutural, petrografia, microscopia eletrônica de varredura, petrofísica, isótopos e inclusões fluidas. Os principais resultados indicam que o sistema cárstico TBV-TBR é composto por cinco unidades estratigráficas principais, da base para o topo: (a) *grainstone* oolítico com estratificação cruzada, (b) *grainstone* fino com nódulos de *chert*, (c) carbonato microbial, (d) siliciclásticos finos e margas; e (e) *grainstone* cristalino intercalado com camadas de *chert*. Essas cavernas foram desenvolvidas pelo fluxo de fluido ascendente (hipogênese) ao longo de fraturas, que eram seladas pelas unidades (d) e (e). O fluido então se espalhou lateralmente ao longo das unidades (a), (b), (c), onde a carstificação ocorreu e onde os principais condutos da caverna foram formados. A falha de Cafarnaum é uma estrutura transcorrente, com direção N-S, vertical e extensão de ~ 170 km de comprimento. A zona de influência da falha de Cafarnaum tem aproximadamente 20 km de largura à partir da falha principal. Veios de calcita nas rochas carbonáticas apresentam fluidos meteóricos com δD próximo a -45 ‰ e $\delta^{18}O$ próximo a -6,5 ‰ e temperaturas de 40-70°C. Em contraste, brechas hidráulicas na zona de falha apresentam valores de $\delta^{18}O$ muito mais baixos, indicando temperaturas de cristalização mais altas e fontes mais profundas. Estes resultados são essenciais para a compreensão do comportamento da porosidade-permeabilidade em sistemas cársticos e da origem, mineralogia e composição isotópica de fluidos no sistema *strike-slip*. Esses resultados podem ser aplicados a reservatórios carbonáticos carstificados e fraturados.

Palavras-chave: carste hipogênico; carbonatos; fluido hidrotermal; Formação Salitre; Cráton São Francisco.

ABSTRACT

The study of karst systems and the fluids that generate porosity in carbonate rocks are of primary importance for oil reservoirs and aquifers. The goals of the present thesis are to investigate (1) the role of sedimentary facies and stratigraphy of high-permeability zones and caves originated by deep-seated fluids; and (2) the distribution, mineralogy, and isotope composition of hydrothermal deposits along a strike-slip fault system and its host rocks. We performed both studies in the Neoproterozoic Salitre Formation (700-560 Ma), São Francisco Craton, Brazil. The first study was carried in the Toca da Boa Vista (~107 km long) and Toca da Barriguda (~34 km) caves (TBV-TBR system) in the Irecê Basin (Campo Formoso, BA) and form the longest cave system in South America. The second study was accomplished in the Cafarnaum fault system, which marked the boundary between the Salitre Formation (west block in the Irecê Basin) and the Chapada Diamantina Group (east block, Morro do Chapéu area). The present thesis uses a combination of sedimentary facies analysis, structural analysis, petrography, scanning electron microscopy, petrophysics, isotopes, and fluid inclusions. The main results indicate that the TBV-TBR karst system is composed of five main stratigraphic units, from bottom to top: (a) cross-bedded oolitic grainstone, (b) fine grainstone with chert nodules, (c) microbial carbonate, (d) interbedded fine siliciclastics and marls, and (e) crystalline grainstone interfingered with chert layers. These caves were developed by ascending fluid flow (hypogenesis) along fractures, which were sealed by units (d) and (e). The fluid then spread laterally along units (a), (b), (c), where karstification took place and where the main cave conduits were formed. The strike-slip Cafarnaum fault is a N-S-striking vertical, ~170 km long fault zone. The zone of the influence of the Cafarnaum fault is ~20 km wide from the main fault. Calcite veins in carbonate rocks exhibit meteoric fluids with δD near -45‰ and $\delta^{18}O$ near -6.5‰ and temperatures at 40-70°C. In contrast, hydraulic breccias in the fault zone present much lower $\delta^{18}O$ values indicating higher crystallization temperatures and deeper sources. These results are essential for understanding porosity-permeability behavior in karst systems and the origin, mineralogy, and isotope composition of fluids in the strike-slip system. These results could be applied to carbonate karstified and fractured oil reservoirs.

Keywords: hypogene karst; carbonates; hydrothermal fluid; Salitre Formation; São Francisco Craton.

SUMÁRIO

LISTA DE FIGURAS

CAPÍTULOS I, II e III

CAPÍTULO IV

CAPÍTULO V

LISTA DE TABELAS

CAPÍTULO I – INTRODUÇÃO

I.1 Estrutura da Tese

A presente Tese é apresentada em seis capítulos da seguinte forma, apresentada abaixo.

O Capítulo I apresenta a contextualização e a justificativa da pesquisa desenvolvida, além dos objetivos principais e específicos.

O segundo capítulo traz a fundamentação teórica, com foco no processo de carstificação, e o contexto geológico regional da área estudada, incluindo o carste hipogênico de Irecê. E o Capítulo III foca nos materiais e métodos utilizados para alcançar os objetivos deste trabalho.

Os Capítulos IV e V trazem os resultados em forma de artigos científicos. O primeiro artigo, publicado no *Marine And Petroleum Geology Journal,* ***"The Conduit-seal System Of Hypogene Karst In Neoproterozoic Carbonates In Northeastern Brazil"*** apresenta o estudo realizado no Sistema Hipogênico Toca da Boa Vista-Toca da Barriguda (TBV-TBR) com a definição do sistema barreira-conduto de fácies para a circulação de fluidos que promovem o processo de carstificação. O segundo artigo, submetido ao *Precambrian Research Journal,* ***"Hydrothermal Activity Along A Strike-slip Fault Zone And Host Units In The São Francisco Craton, Brazil - Implications For Fluid Flow In Sedimentary Basins"***, discute, de forma multiescalar, como fluidos são canalizados por sistemas de falhas e causam brechação e precipitação de minerais hidrotermais, afetando também a rocha hospedeira.

Encerrando, o Capítulo VI apresenta as considerações finais e indicações de novos trabalhos a serem desenvolvidos sobre o tema.

I.2 Apresentação e Justificativas

A produção de hidrocarbonetos em reservatórios carbonáticos fraturados apresenta grandes desafios e incertezas, pois a qualidade do reservatório pode ser muito variável de acordo com a evolução tectono-sedimentar e diagenética (Cazarin et al, 2019). Redes e corredores de fraturas e falhas são elementos-chave na arquitetura do reservatório que podem impactar positivamente ou negativamente a produção. Além disso, fluidos bacinais (muitas vezes hidrotermais) circulam ao longo desses sistemas multiescalares de fraturas e podem resultar em processos como silicificação, dolomitização e/ou dissolução/lixiviação, desenvolvendo carstificação e gerando porosidade secundária. O conhecimento profundo desses múltiplos fatores que controlam a qualidade do reservatório é a chave para a predição efetiva, tanto na exploração (escala regional), quanto na produção.

Com o desenvolvimento dos reservatórios carbonáticos do pré-sal, cresceu a importância do reconhecimento e da adequada representação dos intervalos carstificados, de modo a adotar a estratégia correta de desenvolvimento do campo, bem como melhor prever o comportamento do fluxo de fluidos nestes reservatórios e as incertezas associadas a esta previsão. A presença de regiões macro/megaporosas com elevadas permeabilidades e continuidade espacial, formadas pela combinação de fraturas e feições de dissolução, resultam frequentemente em um sistema de dupla-permeabilidade. De uma maneira geral, os condutos de alta permeabilidade são determinantes do fluxo de fluidos no reservatório, enquanto a porosidade de matriz da rocha reservatório é responsável principalmente pela estocagem de fluidos e, portanto, pelo volume de hidrocarbonetos no sistema em subsuperfície.

Existem diversos exemplos no mundo de reservatórios com carstificação epigênica (Loucks, 1999). Porém, só recentemente, os fenômenos de dissolução hipogênica de rochas carbonáticas têm merecido destaque, sobretudo pelo reconhecimento de sua eficácia em gerar permo-porosidade tardia e no seu alto potencial de preservação no tempo geológico. A origem da dissolução possui implicação direta na estratégia exploratória de um reservatório carbonático, pois existem diferenças fundamentais na morfologia, no grau e na distribuição do

espaço poroso na rocha quando esta é submetida à dissolução epigênica ou hipogênica (Klimchouck et al., 2016).

A compreensão dos processos de carstificação é muitas vezes viabilizada por meio de estudo de área análogas, tais como bacias carbonáticas de diferentes idades. O Brasil possui cerca de 425.000 a 600.000 km2 de cobertura de rochas carbonáticas com diferentes características de carstificação (Karmann, 1994), conforme mostrado na Figura 1. O foco neste trabalho será o carste do Grupo Una no Cráton do São Francisco, mais especificamente na bacia Neoproterozóica de Irecê.

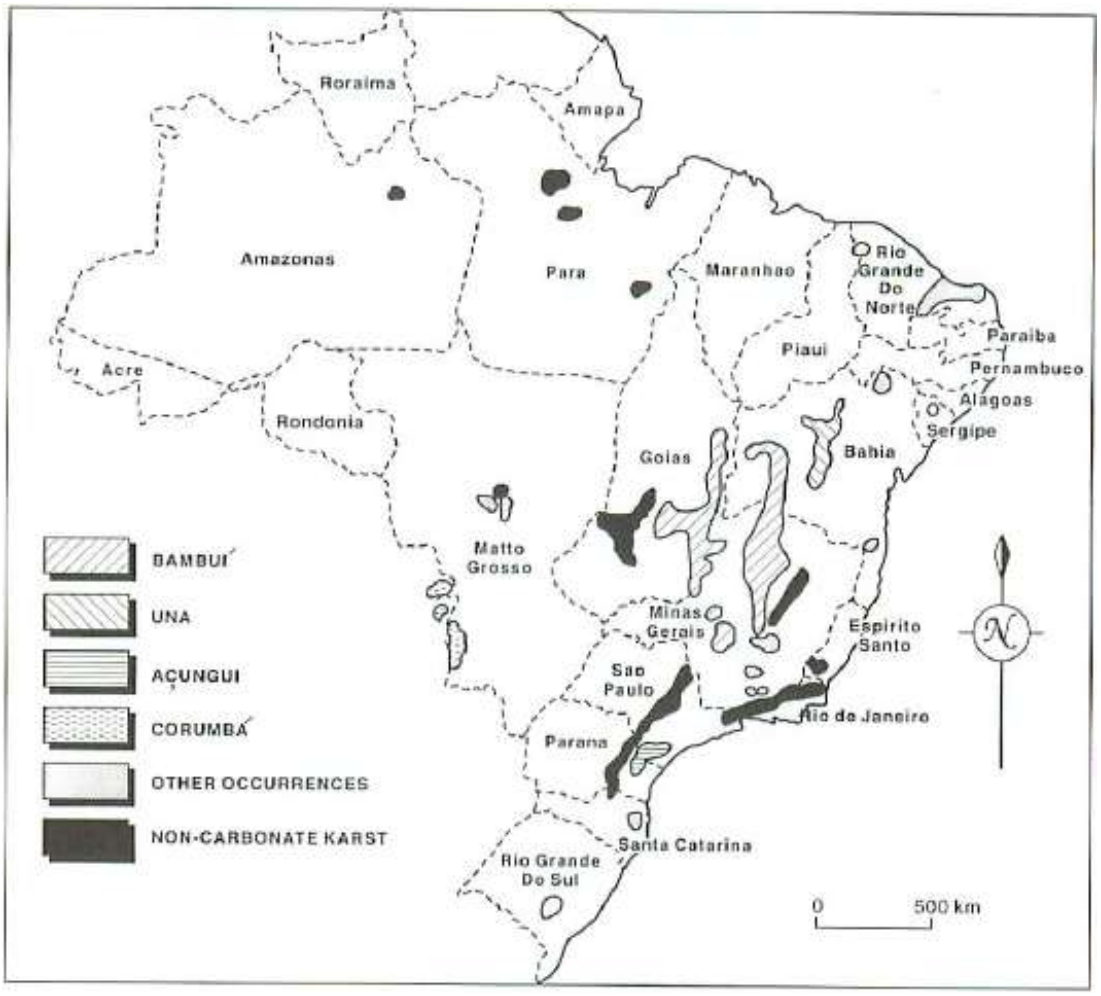

Figura 1. Carste carbonático no Brasil (Auler e Farrant, 1996).

I.3 Objetivos

O presente trabalho teve como objetivo principal analisar a relação da formação do carste hipogênico com a litoestratigrafia e a circulação de fluidos com o arcabouço tectônico, a partir de dados petrográficos, texturais, químicos, isotópicos e estruturais de rochas carbonáticas.

Como objetivos específicos pretende-se:

i. identificar o intervalo estratigráfico de ocorrência dos processos cársticos;

ii. determinar o papel das fácies sedimentares no desenvolvimento das zonas de alta permeabilidade (cavernas);

iii. investigar os depósitos hidrotermais e a rocha hospedeira (mineralogia e análise isotópica) na borda leste da Bacia de Irecê.

CAPÍTULO II – FUNDAMENTAÇÃO TEÓRICA E CONTEXTUALIZAÇÃO GEOLÓGICA REGIONAL

II.1 Conceituação sobre Carste

O estudo do carste é um ramo das geociências bastante específico, de domínio de raros especialistas espalhados pelo mundo. Ao mesmo tempo é um tema de interesse muito grande para controle de meio ambiente e, em especial, para estudos de aquíferos, atividade de extrema importância de onde vem grande parte do conhecimento científico aplicado de sistemas carbonáticos carstificados (Palmer, 2011; Klimchouk et al., 2016; Hosseini and Ataie-Ashtiani, 2017). A indústria do petróleo também apresenta forte interesse por este tema, já que boa parte das reservas de petróleo do mundo se associa a carbonatos com diferentes graus e tipos de carstificação (Hardage et al., 1996; Ehrenberg et al., 2012). Com relação aos estudos de reservatórios carstificados, um tema de particular interesse refere-se à modelagem de condutos e de zonas de altíssimas permeabilidades que controlam fortemente o fluxo de fluidos no interior do reservatório (Heubeck et al., 2004; Sullivan et al., 2006; Ehrenberg et al., 2012).

O carste epigênico é gerado a partir da exposição de rochas, geralmente carbonáticas, seja por soerguimento tectônico, seja por rebaixamento do nível de base em períodos de seca. Este processo se dá essencialmente por infiltração de água meteórica rica em CO2 que promove dissolução em ambiente vadoso e freático superior (Esteban and Wilson, 1993). A área de recarga alógena é constituída pelas redes fluviais situadas à montante, que invadem e infiltram o subsolo da região carstificada, enquanto a área autógena representa a recarga por água de chuva exclusivamente na região exposta.

A carstificação hipogênica se forma em geral sem contato com a superfície, sendo gerada a partir da dissolução por fluidos ascendentes ricos em CO2 ou H2S de origem diversa (Klimchouk, 2005; Palmer, 2011; Kempe et al., 2015; Auler and Smart, 2003). Esses autores discutem que a carstificação por fluidos ascendentes se dá abaixo do lençol freático, podendo ocorrer a grandes profundidades de soterramento. Ao contrário da epigênica, o limite de atuação destes fluidos

ascendentes em geral são barreiras ao fluxo vertical ou, no caso de carstificação hipogênica rasa, o próprio nível freático.

De acordo com Klimchouck (2005), a carstificação hipogênica pode ser dominantemente discordante (*cross–stratal*), dominantemente concordante (estratiforme) ou combinada (rede 3D de condutos).

A estrutura das cavernas hipogênicas depende principalmente dos seguinte fatores: (1) permeabilidade da rocha pré-carstificação; (2) presença de falhas e fraturas condutoras associadas; (3) agressividade e natureza dos fluidos; (4) tipo de recarga; (5) presença de barreiras estratigráficas, e, nos casos em que ela se desenvolve próxima à superfície; (6) posição do lençol freático.

A origem dos fluidos de carstificação é um fator diferencial entre os dois processos (Auler e Smart, 2003; Cazarin et al., 2019). Enquanto na carstificação epigênica as águas ácidas são de origem essencialmente meteórica e ricas em CO2, na carstificação hipogênica diferentes fatores (temperatura e composição do fluido) podem atuar para aumentar o poder de dissolução das rochas carbonáticas pelos fluidos ascendentes (Auler e Smart, 2003).

Outro processo de formação destes sistemas tem sido estudado nas últimas décadas. O carste hipogênico, formado em profundidade, pela ação de fluidos ascendentes, se distingue do processo epigênico, que se dá pela ação de águas meteóricas (Klimchouk, 2012). Ford e Williams (1989) e Worthington e Ford (1997) definiram que cavidades hipogênicas se formam por fluidos hidrotermais ou pela oxidação de H2S.

Outra definição, mais abrangente, é a de Palmer (1995) onde as cavernas hipogênicas se formam pela ação da água, com agressividade produzida em profundidade, e independente de relação com a superfície ou fontes de CO2. Essa “agressividade” da água é transitória e pode ocorrer pela profundidade ou por alguma formação solúvel. Ford (2006) define espeleogênese hipogênica como “a formação de cavernas por recarga de água de uma formação solúvel pela pressão hidrostática ou outras fontes de energia”

Um dos aspectos mais importantes do carste hipogênico é o desenvolvimento de rocha reservatório para hidrocarbonetos. Reservatórios em

rochas carbonáticas produzem, aproximadamente, 50% do óleo e gás mundial (Mazzulo e Harris, 1992). Desta forma, a compreensão das propriedades petrofísicas (porosidade e da permeabilidade) em um sistema cárstico, assim como dos atributos estruturais é fundamental para definir as condições da formação de rochas reservatório em carbonatos.

Montanhas Guadalupe (Novo México, Estados Unidos), Black Hills (Dakota do Sul, Estados Unidos), Bacia Big Horn (Wyoming, Estados Unidos), Grand Canyon (Arizona, Estados Unidos), Tabasco (México), Namíbia, centro e sul da Itália e Montanhas Buda (Hungria) são exemplos de áreas estudadas que apresentam processos hipogênicos (Auler e Smart, 2003).

II.2 Contexto Geológico da Bacia de Irecê

O Cráton do São Francisco é a parte ocidental de um cráton maior, que ocupava a porção central do Gondwana Ocidental, o Cráton do Congo (ou Zaire) – São Francisco, ele foi separado em dois quando com a abertura do Atlântico Sul (Trompette et al, 1992). Almeida (1977) definiu o Cráton do São Francisco como uma entidade geotectônica sinbrasiliana. Nele distinguem-se coberturas meso-cenozóicas não deformadas e depositadas sobre três conjuntos de rochas de idade Pré-cambriana: supergrupos São Francisco e Espinhaço (coberturas plataformais dobradas, do Proterozóico Superior e do Proterozóico Médio) e a Associação Pré-Espinhaço, embasamento arqueano-eoproterozóico, composto pelos blocos crustais Gavião e Jequié (Figura 2).

O Supergrupo São Francisco contém todas as sequências deposicionais do Neoproterozóico, compreendendo a Formação Jequitaí e os grupos Macaúbas e Bambuí (Minas Gerais) e o Grupo Una (Bahia). Essas unidades são as que recobrem o centro-sul do Cráton São Francisco, ocorrendo até a área da Chapada Diamantina. São coberturas sedimentares sobre o cráton (Formação Jequitaí, e parte do Grupo Bambuí, em Minas Gerais, Bahia e Goiás e Grupo Una, na Chapada Diamantina) ou metassedimentos na Faixa de Dobramentos Araçuaí (Grupo Macaúbas e parte do Grupo Bambuí em Minas Gerais).

Figura 2. Cráton do São Francisco, mapa simplificado. Limites segundo Alkmin et al.1993.

As formações Jequitaí e Bebedouro (Grupo Una) e o Grupo Macaúbas são (meta) diamictitos e arenitos, depositados sob a influência de processos glaciais. Os grupos Una e Bambuí são (meta) sedimentos carbonáticos e pelíticos, de plataforma marinha estável (Dardenne, 1978).

A Formação Salitre (Grupo Una), objeto de estudo deste trabalho, é uma sequência carbonática de ca. 530 m de espessura, com intercalações de depósitos siliciclásticos e ocupa grande extensão da Bacia de Irecê (BA).

Depositada em ambiente marinho raso de mar epicontinental (Medeiros e Pereira, 1994), a unidade apresenta depósitos de supra a infra-maré, que representam episódios deposicionais transgressivos e regressivos.

A Formação Salitre apresenta extensas exposições de rochas carbonáticas afetadas por processos de exposição, hidrotermalismo, e eventos de deformação dúctil e rúptil, além disso, abriga o maior sistema cárstico da América do Sul, que necessita de mais estudos sobre os processos de geração da permo-porosidade secundária.

Duas propostas estratigráficas são mais aceitas para a Formação Salitre (Figura 3): uma definida por Bonfim et al. 1985, e outra de Misi e Silva (1996). Bonfim et al. (1985) consideram 4 fácies distintas de acordo com os ciclos de sedimentação, descritas a seguir:

Unidade Nova América: Caracterizados como calcarenito róseo com forte recristalização e dolomitização, comumente com estratificação cruzada acanalada. Presença de tapetes algais, estromatólitos de pequeno porte (*Jurusania Krylov*), intraclastos, laminação cruzada e bird eyes.

Unidade Gabriel: Composta por estreitas intercalações de calcissiltitos, calcilutito e calcarenito fino, caracterizados por uma coloração rósea, creme e cinza, laminação plano- paralela e presença constante de cristais cúbicos de pirita e/ou limonita. O processo de dolomitização é intenso.

Unidade Jussara: Jussara inferior (i) é composta por calcarenito quartzoso de coloração cinza escura a preta, grã média, cuja feição característica é a presença de grãos de quartzo visíveis macroscopicamente. (ii) Litologicamente, na subunidade Jussara Médio, predominam calcarenito finos, calcissiltitos e calcilutitos de coloração cinza a preta. (iii) A subunidade Jussara Superior, litologicamente apresenta como tipo característico um calcarenito oncolítico intraclástico de coloração cinza escura a preta, interacamadado e interlaminado com calcilutitos e calcissiltitos de mesma coloração. A estratificação planoparalela é uma constante por toda a área de ocorrência dos calcarenitos. Apresentam por toda sua área de ocorrência nódulos de sílex com forma esferoidal acompanhando o aleitamento das camadas, de composição similar à da rocha encaixante.

Unidade Irecê: Constituem turbiditos distais e/ou proximais, predominam calcilutitos laminados com variação para calcarenitos de textura fina a média, coloração cinza escura a negra, com intercalações de margas, siltitos, arenitos imaturos e sílex.

Misi e Silva (1996) consideraram as unidades: C, B, B1, A e A1. A unidade C é caracterizada por dolomito avermelhado argiloso, à leste da Bacia de Irecê. A unidade B apresenta calcários laminados cinza com gradação para camadas dolomíticas, é uma sucessão rítmica de camadas centimétricas de calcários ou

dolomitos e folhelhos. A unidade B1 inclui dolomitos sílticos avermelhados cinzas, dolomitos com lentes plano-paralela e calcarenitos cinza escuro. A unidade A possui intercalações de marga, folhelhos e siltito, sendo a unidade A1 é composta por calcários ricos em matéria orgânica com oólitos, pisólitos e estratificação cruzada.

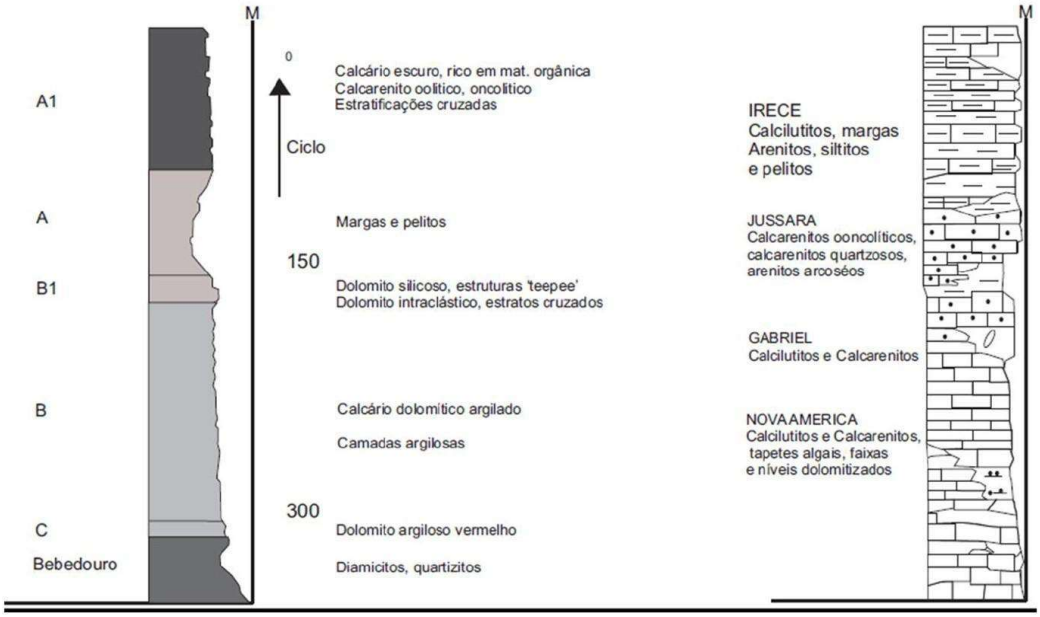

Figura 3. Colunas estratigráficas da Formação Salitre. À esquerda Misi and Silva (1996) e à direita Bonfim et al. (1985).

Essas rochas fazem parte de um sistema deposicional de mar raso epicontinental (Medeiros e Pereira,1994), composto por depósitos de supra a infra-maré, representando episódios deposicionais transgressivos e regressivos.

II.3 O Carste Hipogênico na Bacia de Irecê

O principal complexo de cavernas hipogênicas da América do Sul, e um dos principais do mundo, localizam-se no norte da Bahia, no município de Campo Formoso, representado pela Toca da Boa Vista e Toca da Barriguda (Figura 4). O início das pesquisas nessas cavernas se deu nos anos 80 com o Grupo Bambuí de Pesquisas Espeleológicas. Resultando nos mapas das cavernas, utilizados em nossas análises. Auler e Smart (2003) e Klimchouk et al (2016) concluíram a caverna tem origem hipogênica. A integração de estudos de litoestratigrafia e

geologia estrutural permitiram concluir que esse grande sistema de cavernas nos carbonatos da Formação Salitre é organizado e controlado pela geologia no desenvolvimento de cada salão da caverna. A localização das cavernas é determinada por condições estruturais específicas, que permitem o acesso de fluidos profundos até a porção basal da Fm Salitre, e o espraiamento desse fluido ocorre através de fraturamentos intensos com trend NE-SW associadas à litologia.

As cavernas se desenvolvem em duas fácies de dolomito: uma fácies com abundantes e espessas camadas de chert e uma fácies dolomítica mais pura. Apresentam carbonatos secundários (espeleotemas), passando por depósitos clásticos como abatimento, silte e argila, e incluindo extensas acumulações de guano e ossadas fósseis (Auler e Smart, 2003). Em um dos mapeamentos geológicos realizado pela CPRM (Bonfim et. al., 1985) foi identificado que os carbonatos que afloram acima da caverna como pertencentes à Unidade Gabriel (Auler e Smart, 1999).

Os carbonatos da Formação Salitre na área ocupam uma bacia arealmente restrita, limitada ao leste e ao norte por quartzitos do Supergrupo Espinhaço (Proterozóico Médio), e ao sul por filitos que provavelmente pertencem à Faixa Rio Salitre (Arqueano). Estes encontram-se expostos em fundos de vales e são recobertos por calcários lacustrinos da Formação Caatinga (Plio-Pleistoceno), que recobrem os carbonatos do Grupo Una ao sul das cavernas.

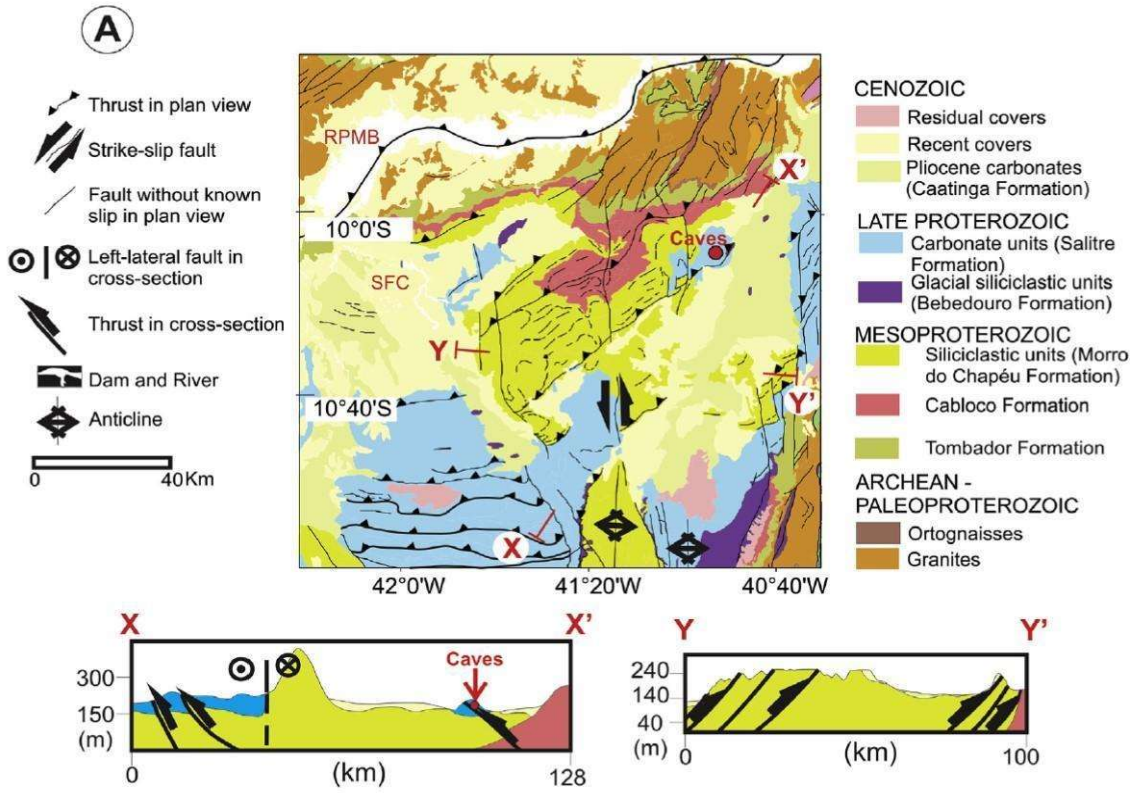

Figura 4. Mapa Geológico da área de estudo modificado de Ennes-Silva et al (2016).

Este sistema cárstico tem características hipogênicas, isto é, formada por ácidos gerados em subsuperfície. Evidências morfológicas, hidroquímicas e isotópicas indicam que as cavernas foram formadas pela dissolução provocada por ácido sulfúrico devido à oxidação de pirita (Auler, 1999).

Idades obtidas por paleomagnetismo em depósitos sedimentares na Toca da Boa Vista (TBV) indicam que o sistema cárstico foi drenado há, no mínimo, 778 ka. Dados de traço de fissão em apatita em área vizinha do Cráton São Francisco indicam que a denudação regional ocorreu em torno de 30 ± 10 m/Ma (Harman et al. 1998). Isto sugere que as galerias atualmente secas das cavernas foram formadas em um período anterior a 1,5 Ma. Desta forma, o sistema cárstico da Toca da Boa Vista foi descrito inicialmente como Paleógeno (Auler, 1999).

A caracterização litológica das rochas do complexo Toca da Boa Vista e Toca da Barriguda foi proposta inicialmente por Cazarin (2015), na qual cinco unidades foram reconhecidas, são elas, da base para o topo: unidade 1- grainstone com estratificações cruzadas, unidade 2 - grainstone fino com nódulos de chert, unidade 3 - carbonatos microbiais, unidade 4 - siliciclásticos finos

intercalados com marga, e unidade 5 - carbonato cristalino intercalado com camadas centimétricas de chert. A unidade tectônica é constituída por brechas em zonas de falhas e fraturas, localizadas. A Figura 5 ilustra o perfil ideal encontrado dentro do complexo TBV-TBR. Os contatos entre as fácies são, geralmente, abruptos, entretanto na passagem da unidade 3 para 4 foi descrito um contato erosional, com pseudomorfos de evaporitos. A unidade tectônica é encontrada em pontos específicos, e corta praticamente todas as litologias (brecha de falha e de colapso).

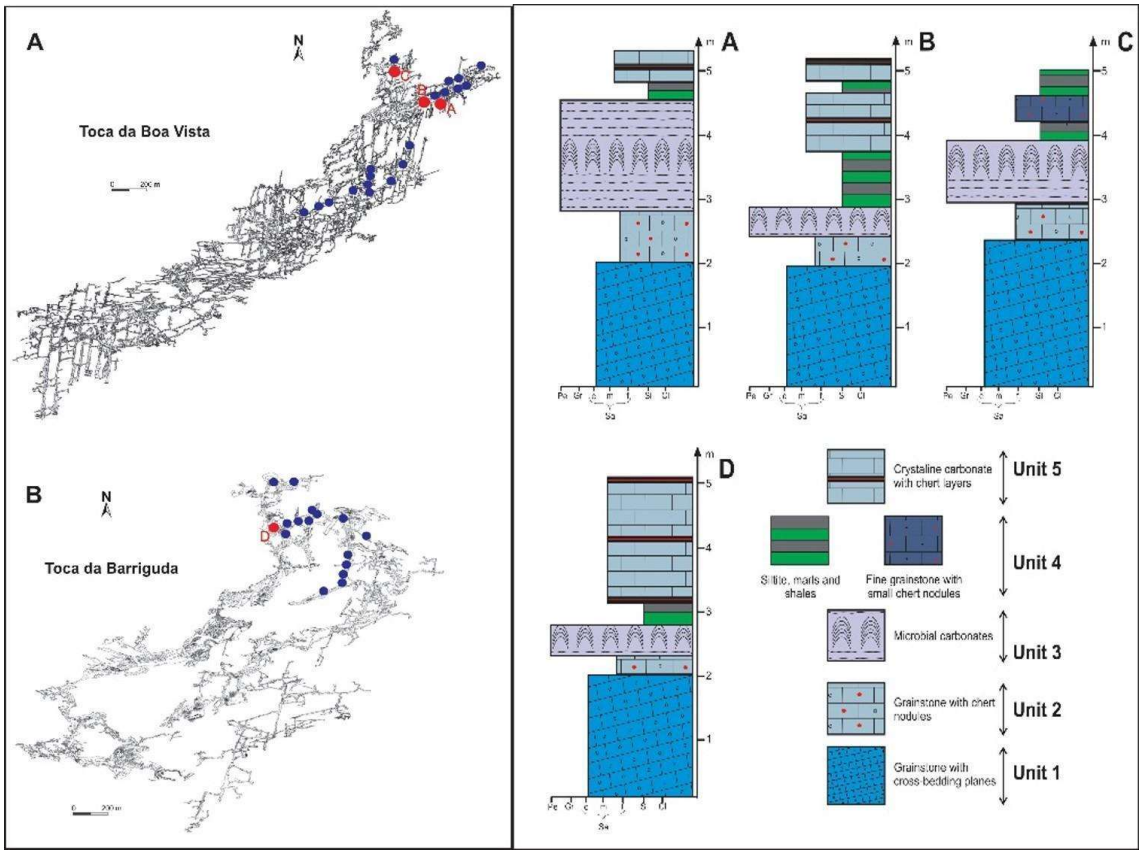

Figura 5. Mapa das Cavernas Toca da Boa Vista (A) e Toca da Barriguda (B) e Perfis Estratigráficos (Cazarin, 2015).

CAPÍTULO III - MATERIAIS E MÉTODOS

III.1 Reconhecimento e Delimitação da Área

A área de estudo está localizada na parte norte do Cráton de São Francisco, com foco na Formação Salitre. Esta área é caracterizada pela presença de grandes sistemas de cavernas que são principalmente influenciados pelo carste epigênico, mas também mostra evidências de carstificação hipogênica.

Para uma melhor compreensão da localização e desenvolvimento do Complexo Hipogênico TBV-TBR e dos eventos hidrotermais na bacia foi fundamental o reconhecimento de superfície do contexto estrutural e das principais litologias aflorantes e nas cavernas. Além disso também foi realizada pesquisa bibliográfica sobre processos cársticos e seu papel no desenvolvimento da porosidade secundária em reservatórios carbonáticos.

III.2 Mapeamento e Coleta de Amostras

No complexo Toca da Boa Vista e Toca da Barriguda as amostras foram coletadas com auxílio de plugadeira manual com foco nas principais fácies definidas por mapeamento estratigráfico (Figura 6). Nas zonas de falhas da borda da Bacia de Irecê foram coletadas amostras manualmente em afloramentos de brechas contendo barita e galena (Fazenda Mamonas e Melancias), Figura 7.

III.3 Análises Laboratoriais

III.3.1 Petrofísica Básica

Para análise de petrofísica básica os plugs coletados nas Tocas da Boa Vista e Barriguda foram selecionados e cortados em um tamanho de 5 cm com o objetivo de se obter dados de porosidade, densidade de grãos e permeabilidade (Figura 8).

Figura 6. Coleta de amostras (plugs) na Toca da Boa Vista.

Figura 7. Amostras coletadas contendo barita e galena das Fazendas Melancias (MEL) e Mamonas (MAM).

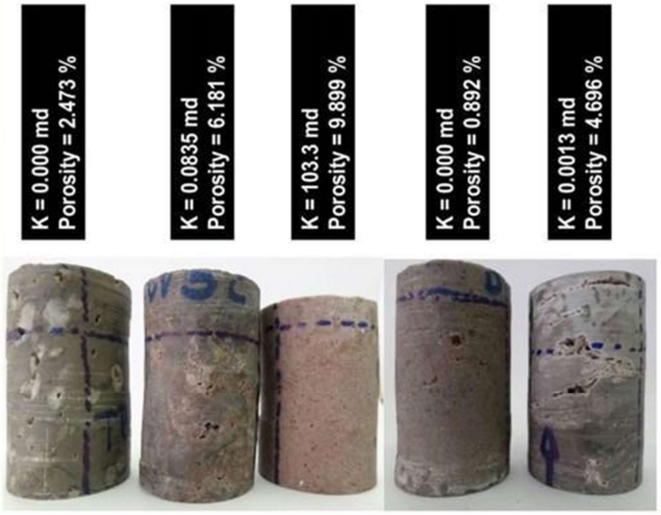

Figura 8. Plugs selecionados das fácies definidas na TBV-TBR e dados de porosidade e permeabilidade associados.

III.3.2 Microtomografia

Dez amostras (plugs) coletadas nas Toca da Boa Vista e Toca da Barriguda foram submetidas à µ-CT visando identificar a arquitetura dos poros (sistema Skyscan-Bruker, modelo 1173), Figura 9.

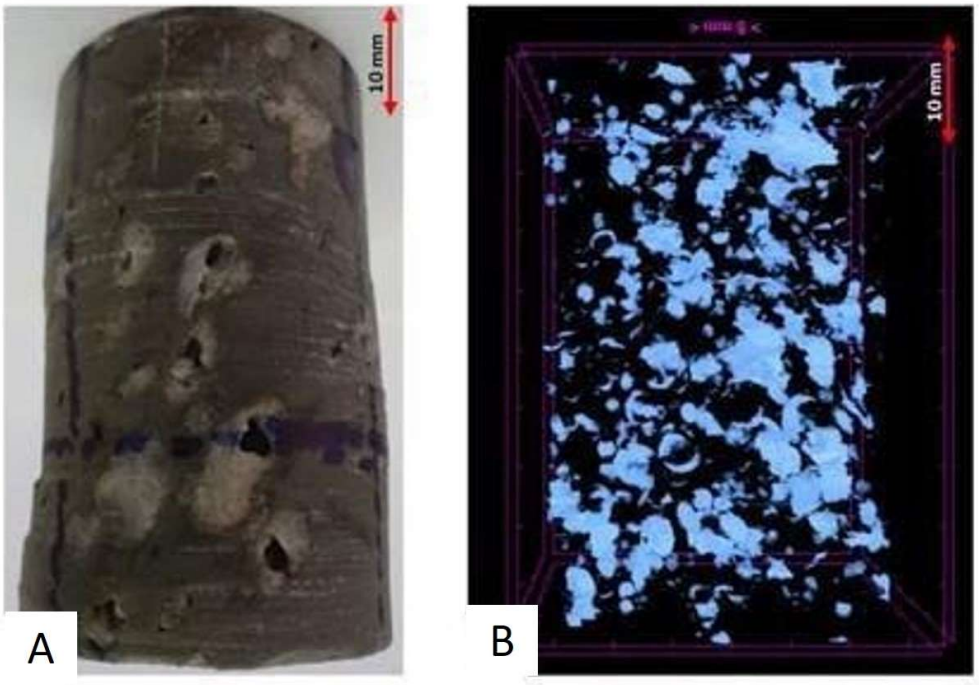

Figura 9. Plug (A) e imagem microtomográfica destacando os poros (B).

III.3.3 Petrografia

Plugs e amostras selecionadas foram encaminhados para a confecção de lâminas delgadas para descrição petrográfica em microscópio ótico de luz transmitida (Zeiss, Axio Imager A2).

As análises petrográficas seguiram a classificação de Dunham (1962) para rochas carbonáticas, e a descrição da porosidade seguiu a classificação de Choquette e Pray (1970). Foram utilizadas mais de 100 lâminas delgadas para estudar as microfácies (Figura 10).

III.3.4 MEV/EDS (Microscopia eletrônica de Varredura e Espectroscopia por Energia Dispersiva)

Amostras selecionadas foram estudadas por microscopia eletrônica de varredura (MEV) para investigar as características de dissolução e / ou mineralização e sua possível relação com os sistemas hidrotérmicos. As análises SEM foram conduzidas usando um JEOL JSM-IT300 equipado com um detector de espectrometria de dispersão de energia X-MaxN da Oxford Instruments (EDS). As amostras foram analisadas “in natura” (sem revestimento e sem polimento) sob uma condição de baixo vácuo a 15 kV. As imagens de elétrons retroespalhados (EEB) foram combinadas com mapas elementares e a identificação das fases foi baseada nos espectros de EDS.

Figura 10. Lâminas das amostras coletadas nas Fazendas Melancias e Mamonas.

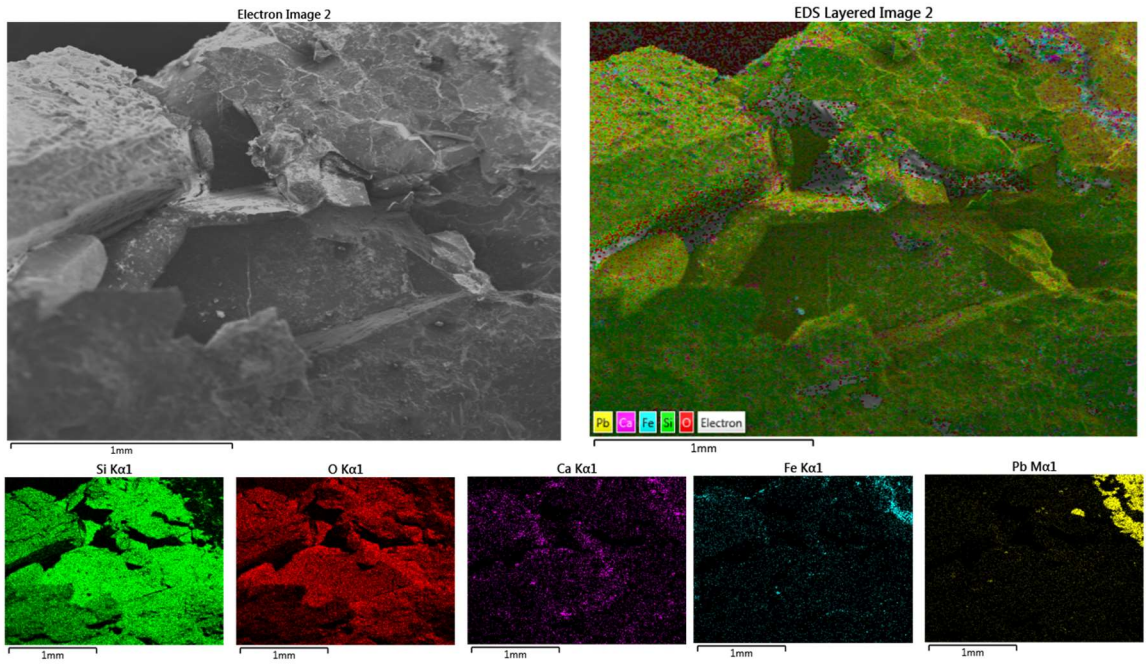

Figura 11. MEV e EDS em uma das amostras estudadas.

III.3.5 DRx/FRx (Difração e Fluorescência de Raio-X)

Amostras selecionadas foram analisadas no Laboratório de Difração do Departamento de Física Teórica e Experimental e no Laboratório de Caracterização Estrutural de Materiais do Departamento de Engenharia de Materiais, ambos da UFRN. As amostras foram analisadas pelo difratômetro Rigaku modelo Miniflex Dtex Ultra.

No Centro de Tecnologias do Gás e Energias Renováveis (CTGAS-ER), realizamos Análise Química Semiquantitativa por Fluorescência de Raios-X (FRX) com perda ao fogo.

III.3.6 QEMSCAN (Quantitative Evaluation of Minerals by Scanning electron microscopy)

O QEMSCAN® (Quantitative Evaluation of Minerals by Scanning Electron Microscopy) é um sistema de microanálise automatizado que permite a análise química quantitativa de materiais e a geração de mapas e imagens de minerais de alta resolução, bem como a estrutura de porosidade (Gottlieb et al., 2000) Utilizando plataforma de microscopia eletrônica de varredura (MEV) com fonte de feixe de elétrons combinados com quatro espectrômetros de raios X dispersivos

em energia (EDS) analisamos 15 amostras dos afloramentos de brechas contendo barita e galena (Mamonas - MAM e Melancias - MEL), Figura 12. Os espectros de emissão de elétrons secundários retroespalhados medidos e de raios-X induzidos por elétrons são usados para classificar a mineralogia da amostra. Uma variedade de informações quantitativas pode ser obtida, incluindo distribuição, composição e angularidade de minerais, bem como distribuição, textura e porosidade dos materiais.

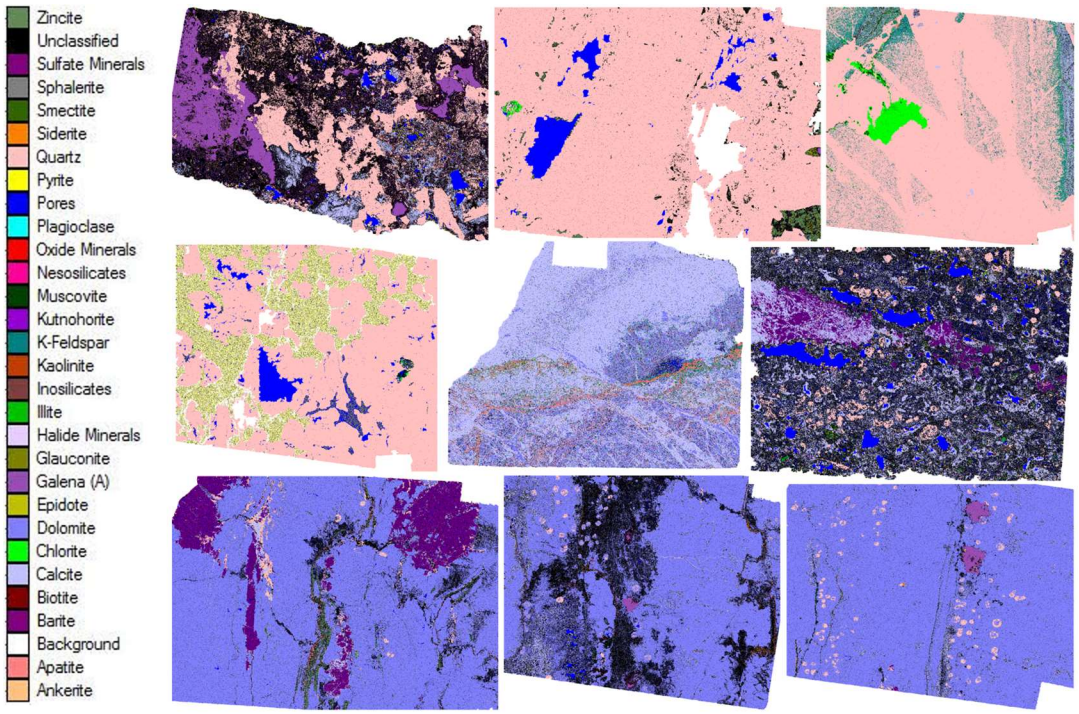

Figura 12. QUEMSCAN realizado em amostras selecionadas da Fazenda Melancias e Mamonas, contendo quartzo, galena e barita.

III.3.7 Determinações Isotópicas e Inclusões Fluidas

Foram selecionadas lâminas dos afloramentos Mamonas (MAM) e Melancias (MEL), brechas com galena e barita, para determinações isotópicas (Figura 13). Para extrair as amostras com alto controle espacial, preservando assim a relação entre as fases minerais, foi utilizado *microdrill* da marca Sherline.

As amostras coletadas foram então colocadas em tubos de vidro, que após fechados, foram aquecidos e purificados com gás He visando eliminar contaminação de gases atmosféricos. Em seguida, as amostras foram reagidas

com H_3PO_4 concentrado e o CO_2 liberado analisado para isótopos de C e O. Os resultados são apresentados na forma da notação $\delta^{13}C$ e $\delta^{18}O$.

Para as análises de inclusões fluidas, cristais de calcita pura de veios foram coletados, tratados e analisados na Universidade de Vrije, Amsterdam.

Figura 13. Brechas hidráulicas selecionadas para análise isotópica.

CAPÍTULO IV - **Artigo 1:** PUBLICADO NO MARINE AND PETROLEUM GEOLOGY JOURNAL: THE CONDUIT-SEAL SYSTEM OF HYPOGENE KARST IN NEOPROTEROZOIC CARBONATES IN NORTHEASTERN BRAZIL

https://www.sciencedirect.com/science/article/abs/pii/S0264817218305245?via%3Dihub

Contents lists available at ScienceDirect

Marine and Petroleum Geology

journal homepage: www.elsevier.com/locate/marpetgeo

Research paper

The conduit-seal system of hypogene karst in Neoproterozoic carbonates in northeastern Brazil

Caroline L. Cazarin[a], Francisco H.R. Bezerra[b,*], Leonardo Borghi[c], Roberto V. Santos[d], Julia Favoreto[c], José A. Brod[e], Augusto S. Auler[f], Narendra K. Srivastava[b]

[a] Petrobras, Research and Development Center (CENPES), 21.941-915, Rio de Janeiro, RJ, Brazil
[b] Department of Geology, Federal University of Rio Grande do Norte, Natal, RN, Brazil
[c] Institute of Geosciences, Federal University of Rio de Janeiro, Rio de Janeiro, RJ, Brazil
[d] Institute of Geosciences, University of Brasília, Brasília, DF, Brazil
[e] Faculty of Sciences and Technology, Federal University of Goiás, GO, Brazil
[f] Instituto do Carste, Belo Horizonte, MG, Brazil

ABSTRACT

Karst processes are of primary importance for the generation of secondary porosity and permeability in carbonate reservoirs and aquifers. The topic investigated in this study are the effects of the facies and stratigraphy of different layers on the vertical distribution of solution cavities formed by hypogenic fluids in a carbonate sequence. This work uses the Toca da Boa Vista (TBV) and Toca da Barriguda (TBR) caves as analogues of carbonate reservoirs that are affected by karst processes. These are two different caves that are 400m apart but exhibit the same geological characteristics and occur in the Neoproterozoic Salitre Formation (700-560 Ma), São Francisco Craton, Brazil. These caves form the longest cave system in South America, with conduits of lengths ~107 km (TBV) and ~34 km (TBR). Previous studies of these caves indicated their hypogene origins. These caves developed by an ascending fluid flow, mainly along fractures. The fluid then flowed laterally and was influenced by the following five stratigraphic units, from the bottom to the top: (1) cross-bedded oolitic grainstone, (2) fine grainstone with chert nodules, (3) microbial carbonate, (4) interbedded fine siliciclastics and marls, and (5) crystalline grainstone interfingered with chert layers. Units 4 and 5 formed a stratigraphic seal. Units 1, 2, and 3 below the seal supported the lateral

redistribution of flow and respective conduit development. Therefore, these units exhibit a high degree of karstification. Veins related to the first fluid phases that compose a hydrothermal mineral assemblage cut across these units. We conclude that stratigraphic control is important for determining the architecture of the hypogenic cave system at the local scale.

Keywords: Carbonates; Hypogene Karst; Carbonate reservoir; Seal

1. Introduction

The development of macroscopic dissolution porosity and related organized permeability systems is referred to as karstification or speleogenesis (Worthington and Ford, 1997; Klimchouk, 2012). Karst porosity has been increasingly recognized and investigated during the last several decades in many carbonate reservoirs. The occurrence of karst porosity in deep-seated settings was commonly thought to be related to past periods of subaerial exposure and epigenetic karstification, i.e., was attributed to paleokarst (e.g., Esteban and Wilson, 1993). However, deep-burial dissolution in the mesogenetic realm was also recognized more than two decades ago (e.g., Mazzullo and Harris, 1992; Al-Shaieb and Lynch, 1993; Machel, 1999). The formation of related dissolution porosity has been addressed in numerous subsequent publications regarding deep-seated carbonate reservoirs and ore deposits (e.g., Heward et al., 2000).

Additionally, it has become increasingly accepted that large-scale dissolutional voids that are observed in some of the largest cave systems in the world are unrelated to meteoric or other surface sources of acidity but rather due to deep fluids percolation processes termed hypogene karst (Ford and Williams, 1989; Palmer, 1991; Klimchouk et al., 2017). Palmer (2012) defined hypogene karst as the effect of rising groundwater or the production of deep-seated aggressive dissolution, which produces widespread hypogenic porosity that is not always represented in caves. One example of this aggressive dissolution generated at depth is the Buso della Rana-Pisatela karst system in northeastern Italy, where the oxidation of pyrite assists epigenetic erosion/corrosion of the cave passages via underground rivers (Tisato et al., 2012). This initial recognition of hypogene karst was followed by the increased awareness of its wide global occurrence (Klimchouk and Ford, 2000; Klimchouk et al., 2017) and status as one

of the fundamental categories of karst, which is at least of equal importance as epigene karst (Klimchouk, 2012, 2013). Following Klimchouk (2012), hypogene karstification (speleogenesis) is understood in this paper as the development of macroscopic dissolution porosity and organized solution-enlarged permeability structures in deep-seated conditions that are unrelated to the recharge from the overlying or immediately adjacent surface; it is, however, related to the recharge to the cave forming zone coming from depth, i.e., by ascending flow.

Despite progress in terms of how hypogenic karst influences carbonate reservoirs and proposed models of hypogene karst evolution, important gaps in scientific understanding remain. First, karst conduits are usually smaller than the required size to be detected in seismic images but are, however, much too large and complex to be analyzed properly at the borehole scale. As a consequence, karst systems have not often been incorporated in karst reservoir studies (Burchette, 2012). Therefore, the study of field analogues has become an important method to better understand the system and to enhance predictive models. Second, despite the architecture of cave porosity being of primary importance in reservoir models and simulations, studies that address the factors that control its spatial distribution are still rare. Furthermore, the influence of cave conduits on the formation of porosity surrounding the conduits (Klimchouk et al., 2012) has not been considered in karstified reservoir models. Third, the relationship between deep-burial diagenesis and hypogene karstification is still poorly understood and requires further research. Fourth, the existing 3D models of cave-stratigraphic stories (e.g., Klimchouk et al., 2016) describe the importance of fractures as channel paths for fluid ascending from deepseated conditions, but they do not consider the petrography and petrophysical parameters of the carbonate and siliciclastic units that comprise the karst system. These layers have an important impact on the origin of the master passages (fluid channel paths) and the development of most of the caves. The present study aims to develop a better understanding of oil carbonate reservoir controls by further detailing the evolution of the hypogene Toca da Boa Vista (TBV) and Toca da Barriguda (TBR) caves (Fig. 1) that were previously investigated by Auler and Smart (2003), Ennes-Silva et al. (2016), and Klimchouk et al. (2016). To use TBV-TBR as an analogue of karstified and fractured carbonate reservoirs, this study presents a detailed lithostratigraphic framework of the caves and addresses how carbonate

petrographic and petrophysical features may control the development of massive subhorizontal passages. Based on previous and new data, we discuss

how the structural framework (e.g., fractures and fault zones) led to the development of fluid zones (channel paths) along which the caves have evolved. This study includes detailed petrography and mineralogical analyses that indicate that fracture zones were filled by hydrothermal mineral assemblages. This study contributes towards the understanding of the development of hypogene caves and their role in the generation of porosity in carbonate reservoirs.

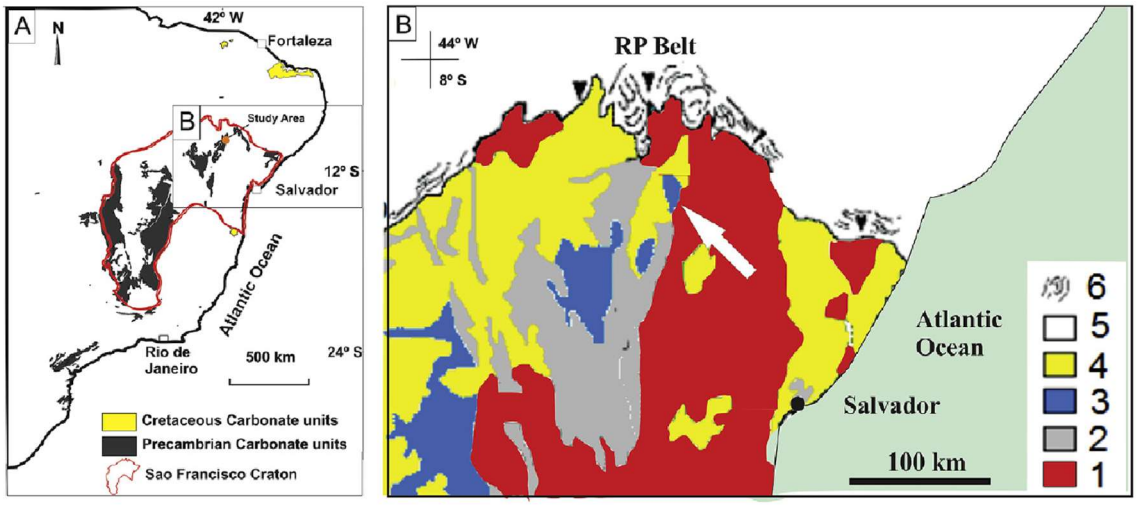

Figure 1. Tectonic and stratigraphic setting of study area: (A) Major carbonate units, location of South America's largest karst system in the São Francisco Craton, and location of the study area (modified from Auler et al., 2001); (B) Detail of the northern part of the São Francisco Craton Key: RP, Riacho do Pontal belt, 1—Archean–Proterozoic basement, 2—Mesoproterozoic sedimentary rocks of the Espinhaço Supergroup, 3—Neoproterozoic rocks of the São Francisco Supergroup, 4—Phanerozoic sedimentary covers, 5—Neoproterozoic Folding belts, 6—Structural lineaments (modified from Bizzi et al., 2003 and Ennes- Silva et al., 2016).

2. Geological and hypogene setting of the TBV-TBR caves

2.1 Stratigraphic and structural settings

The study area comprises the Salitre Formation (Una Group) of the Campo Formoso Basin, in the northern part of the São Francisco Craton (Fig. 1). This craton represents the western portion of a previous major cratonic mass, which also included the Congo craton (or Zaire craton). This major craton was split into two fragments during the Pangea breakup and opening of the South Atlantic Ocean

in the Late Jurassic and Early Cretaceous (Trompette et al., 1992). The São Francisco Craton contains Meso- and Neoproterozoic sedimentary units, which overlie older and deformed Paleoproterozoic and Archean basement units. Fold belts around the craton were deformed during the Brasiliano/Pan-African orogeny that affected both the eastern part of South America and Africa from 740 to 560 Ma (Brito Neves et al., 2014). Neoproterozoic carbonate units within the São Francisco Craton were preserved from pervasive ductile deformation and metamorphism, including fragile to fragile-ductile deformation, that affected the terrains near the mobile belts (Brito Neves et al., 2014). Carbonate units in the craton include the Salitre Formation, which belongs to the Una Group (Fig. 1) and comprises carbonate and pelitic rocks that are interpreted as marine platform units (e.g., Dardenne, 1978).

The Salitre Formation, which forms the main infill of the Campo Formoso Basin, is part of the Una Group. This formation occurs in separate basins that are limited by quartzite and younger freshwater carbonates and has been subjected to brittle deformation and intense karstification (Auler and Smart, 2003). The Salitre Formation is a carbonate unit of up to 530m thickness that has a few siliciclastic lenses and outcrops in the São Francisco Craton (Bonfim et al., 1985). In its northernmost basin, north of Campo Formoso, the Salitre Formation is limited to the east and north by the quartzites of the Espinhaço Supergroup (meso-Proterozoic), to the west by the schists of the Archaean Rio Salitre Belt and to the south by the freshwater carbonates of the Caatinga Formation (Auler, 1999). The basement of the Salitre Formation comprises either Archean schists of the Rio Salitre Belt or Precambrian diamictites of the Bebedouro Formation. The Salitre Formation is capped by freshwater/secondary limestones of the late Pliocene – early Pleistocene Caatinga Formation (Bonfim et al., 1985; Penha, 1994; Auler, 1999).

Carbonates of the Salitre Formation were deposited in a shallow epicontinental marine system (Medeiros and Pereira, 1994) and comprised supra- and infra-tidal deposits, which correspond to transgressive and regressive sea-level episodes. The most common sedimentary facies of the Salitre Formation are stromatolites/microbiolites (planar, domal, columnar, and oncolites). Other microfacies include mudstones, wackestones, packstones, grainstones, and

boundstones (Bonfim et al., 1985). All these facies were subjected to diagenetic processes, such as recrystallization, dolomitization, silicification, and dissolution. Among the several proposed subdivisions for the Salitre Formation (Souza et al., 1993; Pedreira da Silva, 1994; Misi and Veizer, 1998), we have used the classification from the study of Misi and Silva (1996) since it better fits our stratigraphic data (Fig. 2).

The Brasiliano orogeny affected the Riacho do Pontal fold belt and part of the São Francisco Craton (Fig. 1), which resulted in NNE–SSW and E–W thrusts and related folds (Caxito and Ulhein, 2013; Lagoeiro, 1990). The Riacho do Pontal and other marginal Neoproterozoic fold belts around the São Francisco craton consist of sedimentary basins subjected to tectonic inversion during the Brasiliano Orogeny (Caxito and Ulhein, 2013).

The TBV-TBR caves, which are the main focus of this study, developed along the same NE-SW-striking thrust belt with local E-W-striking sectors. These cave conduits, which formed via dissolutional enlargement of fracture corridors, are concentrated along these fold hinges due to the folding of competent grainstone layers (Fig. 2). The cave passages exhibit variable sizes. The conduits range from centimeter-scale dissolution features to passages more than 10m wide and high. However, they are normally 3–10m wide and approximately 2–4m high (Klimchouk et al., 2016). The caves occur along (a) NE–SW to E–W (045–090) and (b) NeS to NNE-oriented (000–030) hinges that are roughly parallel to the main thrust system. Fold limbs of anticlines exhibit dip angles between 10° and 30°. The folds form a superposed pattern formed by two folding events in a compressive collisional setting that was related to the collision between the Riacho do Pontal fold belt and the São Francisco Craton during the Brasiliano orogeny at 750–540 Ma. The F1 event is marked by a set of NE–SW-oriented gentle folds, coeval with NE–SW strata-bound stylolites, NNW–SSE veins, and NW–SE to NeS joints. The cave passages were still not developed, and bedding-parallel by stylolites developed due to overburden, most likely at depths of 1–2 km during this event. The F2 fold event is characterized by a mild E–W-oriented compression that resulted in a set of N-S fold hinges and E–W joint sets (Ennes-Silva et al., 2016).

2.2 Hypogene features and origin of the TBV-TBR caves

Hypogene karst has been identified in the Neoproterozoic Salitre Formation in the São Francisco Craton, Brazil (Figs. 1 and 2); this craton hosts the longest caves in South America, in which the Toca da Boa Vista (TBV) and Toca da Barriguda (TBR) are found. These giant hypogene caves exhibit no features that are typical of epigenic caves, such as a branchwork pattern, fluvial sediments or integration with the surface geomorphology; therefore, these caves are not compatible with a formation via climate-controlled epigenic processes (Auler and Smart, 2003).

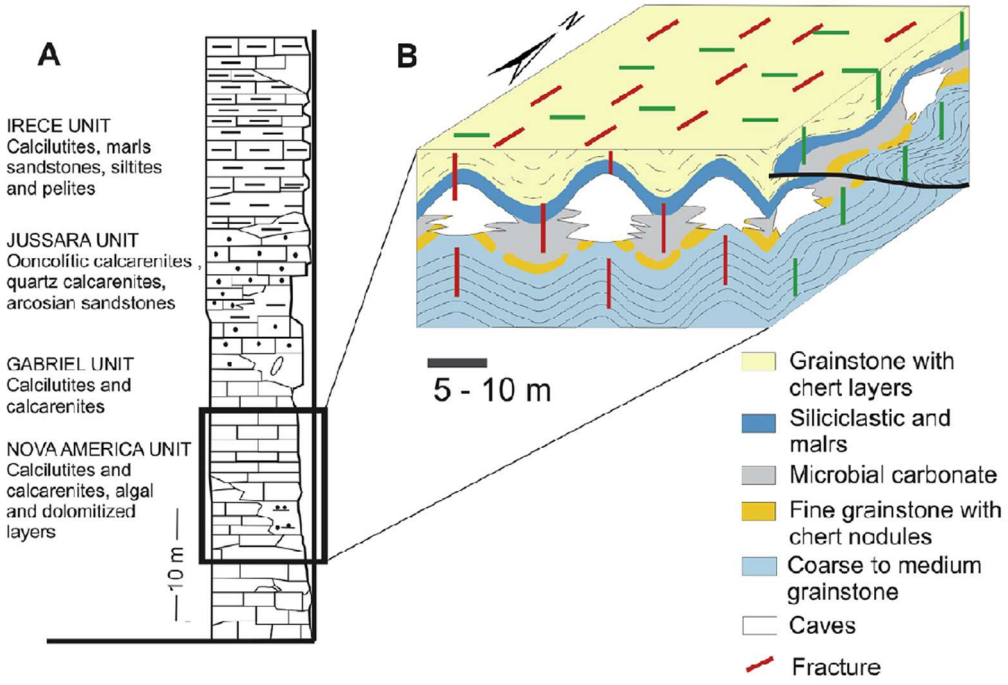

Figure 2. Stratigraphic and Structural scheme (A) Stratigraphic column after Misi and Silva (1996), with location of the stratigraphic level that corresponds to the TBV-TBR system; (B) Structural scheme of caves developed along anticline hinges (modified from Ennes-Silva et al., 2016).

Auler (1999) and Auler and Smart (2003) proposed a hypogene evolution for the TBV-TBR caves and described their morphological features, which include a mixed network/ramiform pattern (Fig. 3B and C), abrupt variations in cross section, widespread cupolas (with some over 10m high), rock pendants, irregular rock projections and vertical rifts, a lack of vadose speleogens and fluvial sediments, and features of condensation-corrosion processes (dolomitic sand, friable walls and redissolved speleothems). This hypogene evolution model suggested that the

caves had a shallow hypogenic origin and formed in a laterally flowing aquifer, in which the dissolution capacity of groundwater was enhanced by the oxidation of bedrock sulfides concentrated in specific stratigraphic units.

Klimchouk et al. (2016) presented new data that provide evidence for the major role played by ascending fluids and joint spacing and distribution along distinct stratigraphic horizons. These authors confirmed abundant evidence of hypogene features, such as cupolas, wall projections, pendants and partitions, and very irregular cave walls and ceilings on a meter scale. The presence of ascending conduits (feeders) would allow rising fluids to be distributed along three cave-stratigraphic stories, which reflect the hydrostratigraphy during speleogenesis (Fig. 2). The lower cave-stratigraphic story served as a recharge component of the system, which formed along fracture corridors and comprises chambers of different sizes that were enlarged by ascending flow. The middle cave stratigraphic story is mainly comprised of subhorizontal cave passages that developed along highly conductive carbonate layers, which are capped by a seal that prevented fluid flow from ascending directly to the upper part of the karst system. The upper cave-stratigraphic story comprises outlets that formed along fractures. This last story represents fracture zones, which allowed the outflow paths through the seal. This 3D architecture of conduits functioned to allow the rising flow from deep-seated confined conditions to reach shallow levels of the crust. The model envisaged by Klimchouk et al. (2016) contains most of the classical elements of a deep-seated source of acidic groundwater, with distinct morphological features and levels (stories) determined by the highly variable joint pattern.

The subhorizontal cave passages developed along anticline hinges (Ennes-Silva et al., 2016). A closely spaced set of joints guided the development of the cave system along these fold hinges and favored the coalescence of adjacent cave conduits, which resulted in larger volumes in the system (Klimchouk et al., 2016; Ennes-Silva et al., 2016). In the model by Klimchouk et al. (2016), episodes of rising acidic fluids may have occurred during the last major regional tectonic events: hydrothermal activity along faults late in the Brasiliano orogeny (c. 550 Ma) or Jurassic-Cretaceous rifting related to the breakup of Pangea. This study noted that either of these two possibilities would have established the TBV-TBR caves as among the oldest caves on Earth.

Auler et al. (2017) suggested that the chemistry of the cave-forming fluids could not be determined with certainty, and the lack of poorly soluble sulfur-derived minerals (halloysite or alunite, Hill, 1990; Polyak et al., 1998) indicates that H2S was not the main fluid conveyed by the many ancient faults.

3. Methods

We have performed a detailed stratigraphic and sedimentary facies description at several cave sites from both the TBV and TBR caves. This part of our study was strongly supported by the extensive cave maps that have been produced by the Bambuí Speleological Group (Grupo Bambuí de Pesquisas Espeleológicas) since 1987. We also applied the structural framework of the TBV-TBR caves established by Ennes-Silva et al. (2016) and the morphological hypogene features defined by Auler and Smart (2003), Klimchouk et al. (2016), and Auler et al. (2017). We sampled the most representative layers exposed in the caves using a manual drill to collect 10-cm-diameter mini-cores of rock samples for petrographic and petrophysical studies. Fig. 3 shows the locations of the 4 sampling sites and the other 34 sites at which there are detailed stratigraphic studies. The cores were cut in the field and reduced in the lab to yield plugs 3.8 cm in diameter with a minimum length of 5 cm.

The petrographic analysis followed the Dunham (1962) classification of carbonate rocks, and the porosity description followed the classification by Choquette and Pray (1970). Hydrochloric acid with alizarin red-S solution (Dickson, 1966) was used to identify the main carbonate minerals. In total, we used 89 thin sections to study the microfacies and analyzed 10 samples of the different stratigraphic units to measure and identify the architecture of the pores via X-ray microtomography (Skyscan-Bruker system, model 1173). The system operated at an energy level of 130 kV and 61 currents, using a 1.0-mm-thick aluminum and 0.5-mm-thick copper filters to reduce the contribution of low-energy photons. The pixel size used to scan was 17.81 μm. A plan screen detector (2240×2240) was used to register an X-ray transmission, and a 360° projection with a 0.50° of rotation was used. The reconstruction of porosity, which was based on the Feldkamp algorithm (Feldkamp et al., 1984), was performed using the InstaRecon® software. Selected samples were studied further via scanning electron microscopy (SEM) to investigate the

dissolution and/or mineralization features and their possible relation with hydrothermal systems. SEM analyses were conducted using a JEOL JSM-IT300 equipped with an Oxford Instruments X-MaxN Energy Dispersive Spectrometry (EDS) detector. Samples were analyzed “in natura” (uncoated and unpolished) under a low-vacuum condition at 15 kV. Back-scattered electron (BSE) images were combined with elemental maps, and the phase identification was based on EDS spectra.

4. Results

4.1. Stratigraphy-petrography of sedimentary units and corresponding morphology

The detailed analysis of the caves (Fig. 3) allowed the identification of five sedimentary units (Fig. 4), which were later confirmed in thin sections. The five cave-bearing stratigraphic units, previously outlined by Klimchouk et al. (2016), were analyzed in detail. From the bottom to the top, these units are (1) grainstone with cross-bedding stratification, (2) fine grainstone with chert nodules, (3) microbial carbonates, (4) fine siliciclastic layers and marls, and (5) crystalline carbonate interfingered with chert layers. This stratigraphic section has good lateral continuity within the TBV-TBR caves, despite the fact that the depth of the units may change due to gentle folding (Ennes-Silva et al., 2016). Fig. 3B and C depicts 38 points at which the cave stratigraphy was investigated.

Unit (1) mainly comprises fine-to-coarse oolitic grainstones with cross-bedded stratification (Figs. 4 and 5). The grainstones are white to gray on the cave wall due to condensation corrosion that caused the powderization of dolomite; the fresh samples, however, are pink in color. The lowermost passages in the caves are developed within this unit and are sometimes represented by large chambers that are created by the lateral coalescence of once individual cavities. The absence of chert and pellite layers and the homogeneous nature of the unit have precluded the breakdown, which results in the full expression of dissolution- sculptured morphological features. The visible thickness of this unit in the cave passages could reach 12–15 m.

The grainstones feature oolites that are surrounded by quartz-filling vugular porosity and intraclastic fragments (Fig. 6). The grain contacts are planar and less-frequently concave-convex. The grain size is homogeneous and presents some degree of mechanical compaction with tangential and punctual contacts and neomorphism. The grain size ranges from 200 to 350 μm, and the grains exhibit rounded-to-subrounded shapes (Fig. 6A, B, C, D). Despite intense micritization, it is possible to recognize a thin marine fringe around the grains and intergranular cementation. The lithologies of Unit (1) present vugular and interparticle porosity. Fracturing is commonly observed and is partially filled by silica (Fig. 6E and F). Late dolomitization, which occurred during mesodiagenesis, has obliterated most of the original features and resulted in anhedral crystals. A few euhedral crystals may occur in the interparticle pores that are generated by dissolution (Fig. 6G and H).

Unit (2) exhibits oolitic, peloidal grainstones and packstones with intraclasts. They are white to gray on the cave wall, but fresh samples are pink. The layers of carbonate are 0.5–1.0m thick and exhibit a planparallel stratification and concentric chert nodules that are 10–30 cm in diameter (Figs. 4, 5 and 7). This unit is locally exposed at the top of the lower-level passages, but mainly in areas that represent the middle cave level, which is the most laterally extensive.

The rock grain size of Unit (2) ranges from fine to very fine sand (0.50mm–0.25 mm), with smaller amounts of quartz and intraclasts than Unit (1) (Fig. 7A and B). The grain contacts are punctual to planar. The intense late dolomitization during mesodiagenesis resulted in euhedral crystals of dolomite in the intergranular porosity. Despite the strong dolomitization process, it was possible to identify zoned rhombohedra that indicates hydrothermal processes. We observed at least three generations of silicification: (1) precipitation of mega-quartz with biphase fluid inclusion, (2) precipitation of cryptocrystalline silica and chert, and (3) deformed quartz with undulose extinction filling fractures up to 1–2mm thick (Fig. 7C and D, E, F). Fractures are also filled by saddle dolomite. The lithologies of this unit exhibit vugular and interparticle porosity (Fig. 7G and H).

Unit (3) is exposed mainly at the middle cave level and consists of microbial carbonates such as laminites and purple-to-green stromatolites and columnar

thrombolites (Figs. 4, 5 and 8). This unit ranges from a few centimeters to 1m thick. The main difference observed between caves within this unit is the size of the columnar structures. The presence of evaporite pseudomorphs at the top of columnar structures and laminites indicates subaerial exposure.

In thin section, we observed fossil organic structures, laminations, and, in the case of thrombolites, micritic clots. This unit exhibits two microfacies with quite distinct textures. The first is a microcrystalline mudstone mainly comprising calcite and dolomite, with vugular porosity 2–4 mm in diameter (Fig. 8A, B, C, D). The mudstone exhibits bands that range from silt to clay diameter surrounding the vugs in which the mineralogy is either mainly dolomitic or mainly calcitic. The carbonate grain size varies from silt to clay. Intense silicification is marked by the presence of quartz infillings that are 177–88 μm in diameter (mostly silt size) (Fig. 8A). The vugs are connected by fractures filled with quartz that may exhibit undulose extinction. The second microfacies is microbial with clothed features (Fig. 8E, F, G, H) and completely dolomitized (Fig. 8F, G, H), exhibiting euhedral and anhedral dolomites in the pores. Rounded and subrounded skeletal grains and dissolved stylolites that exhibit channel porosity are also present (Fig. 8F).

Unit (4) is a siliciclastic unit that can be up to 1m thick and comprises siltstones interfingered with layers of fine-to very fine-grained sandstones, marls, and shales. Layers of peloidal grainstone featuring chert nodules a few centimeters thick also occur in this unit (Figs. 4, 5 and 9). Unit (4) is easily mapped and followed along cave passages due to its predominantly reddish color. Unit (4) is commonly exposed in the upper parts of the walls in passages and in the ceiling at the middle level of the caves. This unit acted as the first fluid barrier due to its siliciclastic petrographic characteristics.

Unit (5) is the topmost unit and comprises microcrystalline carbonates interfingered with a few centimeter-thick chert layers (Figs. 4, 5 and 9). Carbonates are gray to white on the cave wall, but fresh exposure exhibits a pink color, and the chert layers present a reddish color. In thin section, despite the intense dolomitization process, we recognized ooids and peloids, which characterize grainstones. Because the bottom part of this unit has low amounts of fracturing and is commonly massive, it forms the main fluid-flow barrier of the sequence,

causing the lateral redistribution of flow and respective conduit development along the units below it (Klimchouk et al., 2016). Units (4) and (5) acted as fluid barriers during fluid flow in the TBV-TBR caves. In thin sections, the crystalline carbonate features a few opaque minerals, a very low channel along fractures and interparticle porosity (Fig. 10). The main features include local oxidation, abundant stylolites, neomorphism and fracture filling with spathic calcite and with quartz exhibiting undulose extinction (Fig. 10). Up to three sets of fractures that were closed and filled by minerals are observed, and cryptocrystalline silica fills the voids (Fig. 10).

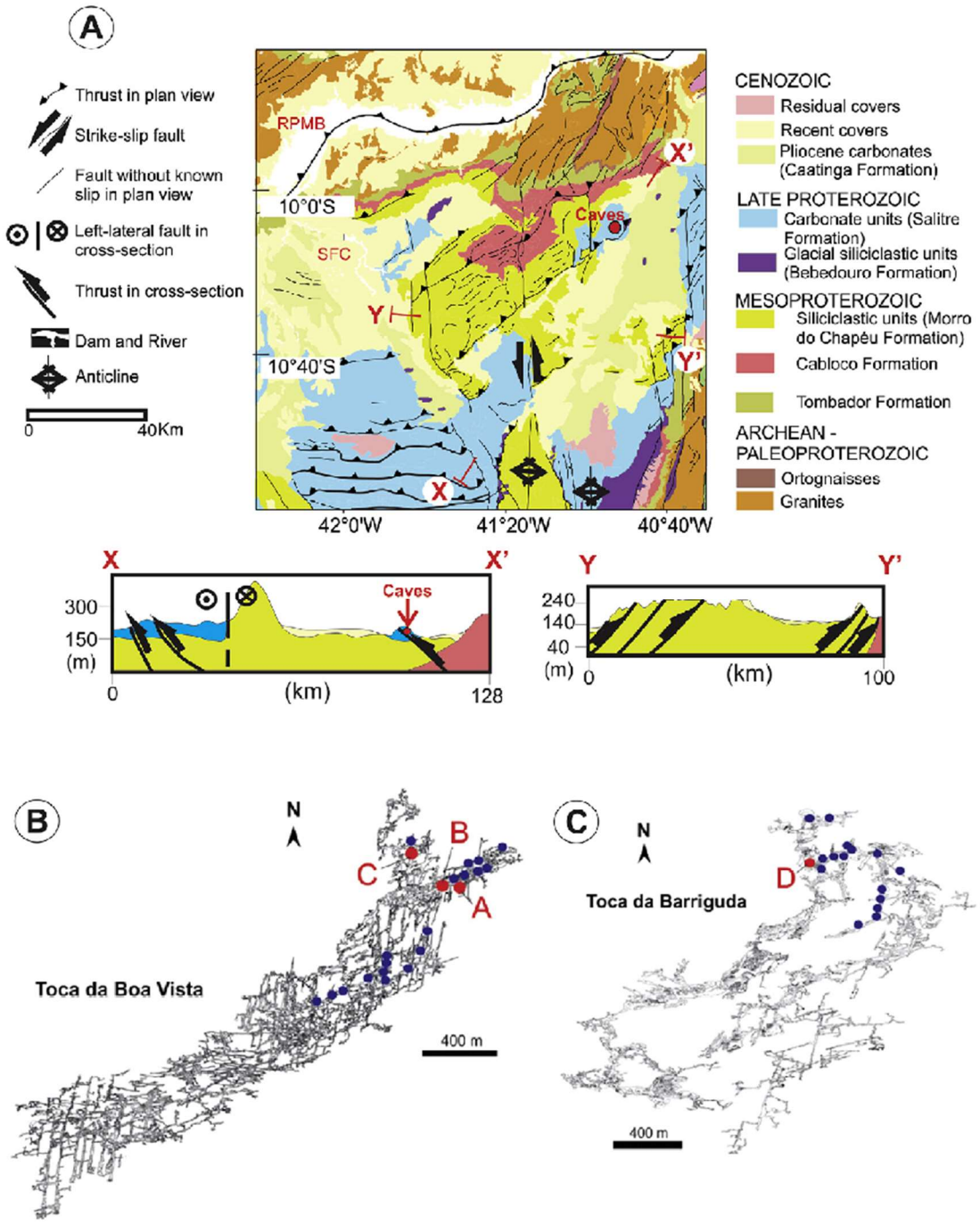

Figure 3. Map of cave system: (A) Geological map of study area modified from Ennes-Silva et al. (2016); (B) Toca da Boa Vista (TBV) and (C) Toca da Barrigura (TBR) caves with location of sample sites (blue dots) and stratigraphic columns (red dots) (Map of caves from the Bambuí Group of Speleology, Grupo Bambuí de Pesquisas Espeleológicas). (For interpretation of the references to color in this figure legend, the reader is referred to the Web version of this article).

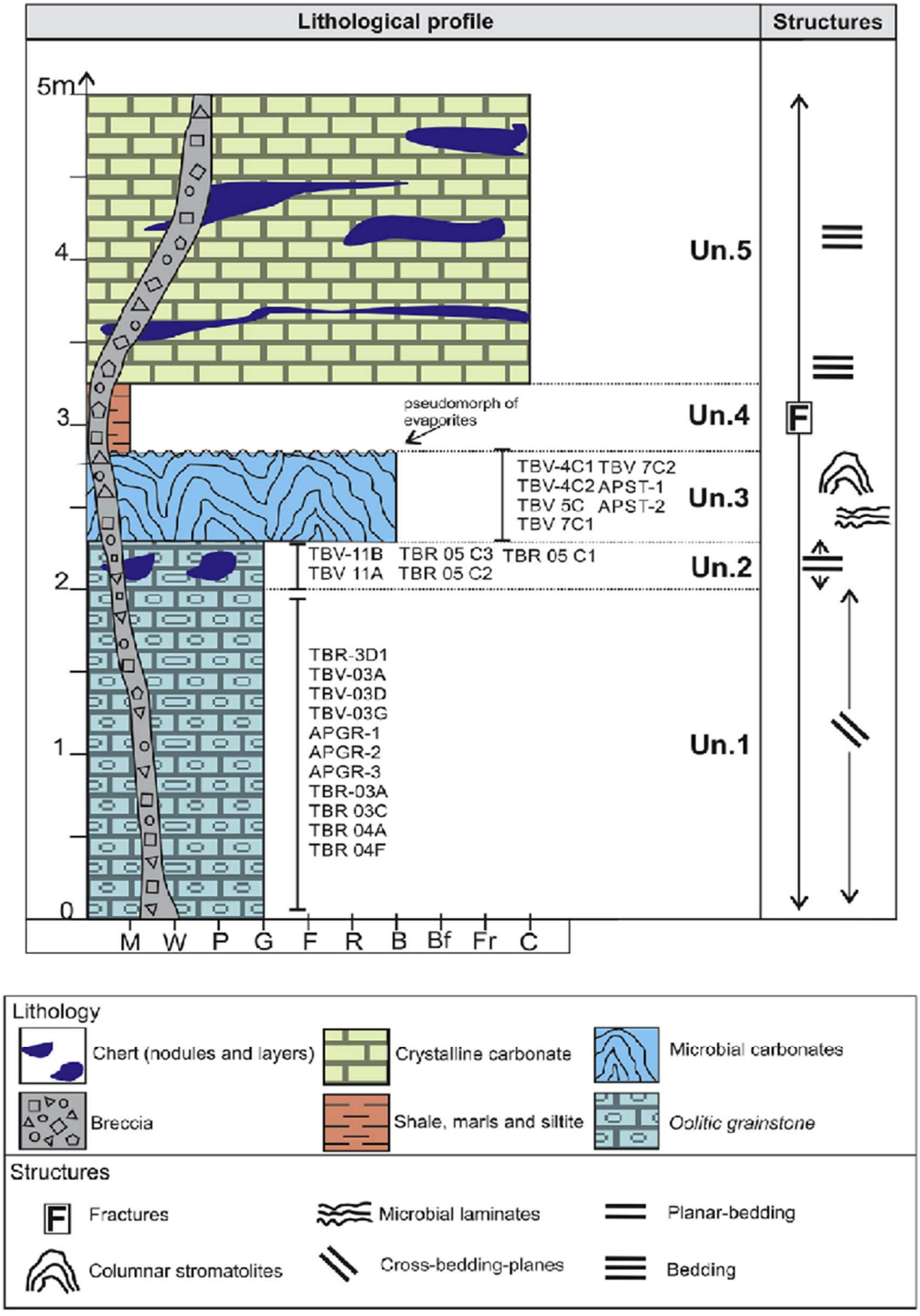

Figure 4. Main features of stratigraphic units as they occur in the caves. Schematic stratigraphic column of study area from locations A, B, C, and D provided in Fig. 3. The units below and above the columnar section are not seen in the caves. Key: Un., stratigraphic unit described in text, M, Mudstone, W, Wackestone, P, Packstone, G, Grainstone, F, Floatstone, R, Rudstone, B, Bindstone, Bf, Bafflestone, Fr, Framestone, C, Crystalline.

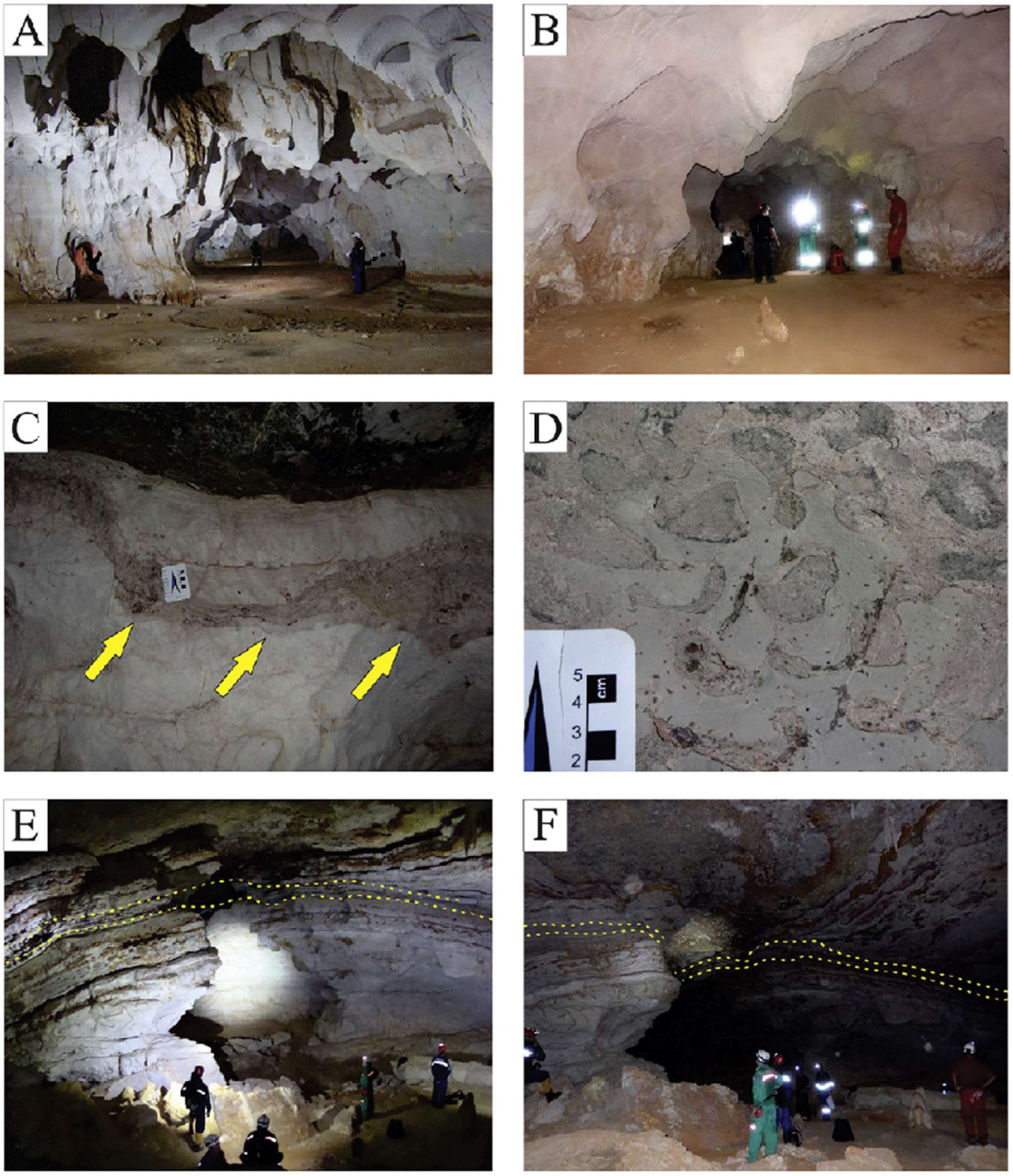

Figure 5. Main features of the conduit-seal system in the cave: (A) and (B) general aspects of Unit 1 with cupolas, which marks the conduit base; (C) Unit 3 composed of microbialites (base of unit marked by yellow arrows); (D) detail of stromatolites in Unit 3; (E) and (F) Unit 4 (marked by yellow bracket lines) and Unit 5 mark the cave ceiling, below which occur the dissolved units 1,2, and 3. (For interpretation of the references to color in this figure legend, the reader is referred to the Web version of this article.)

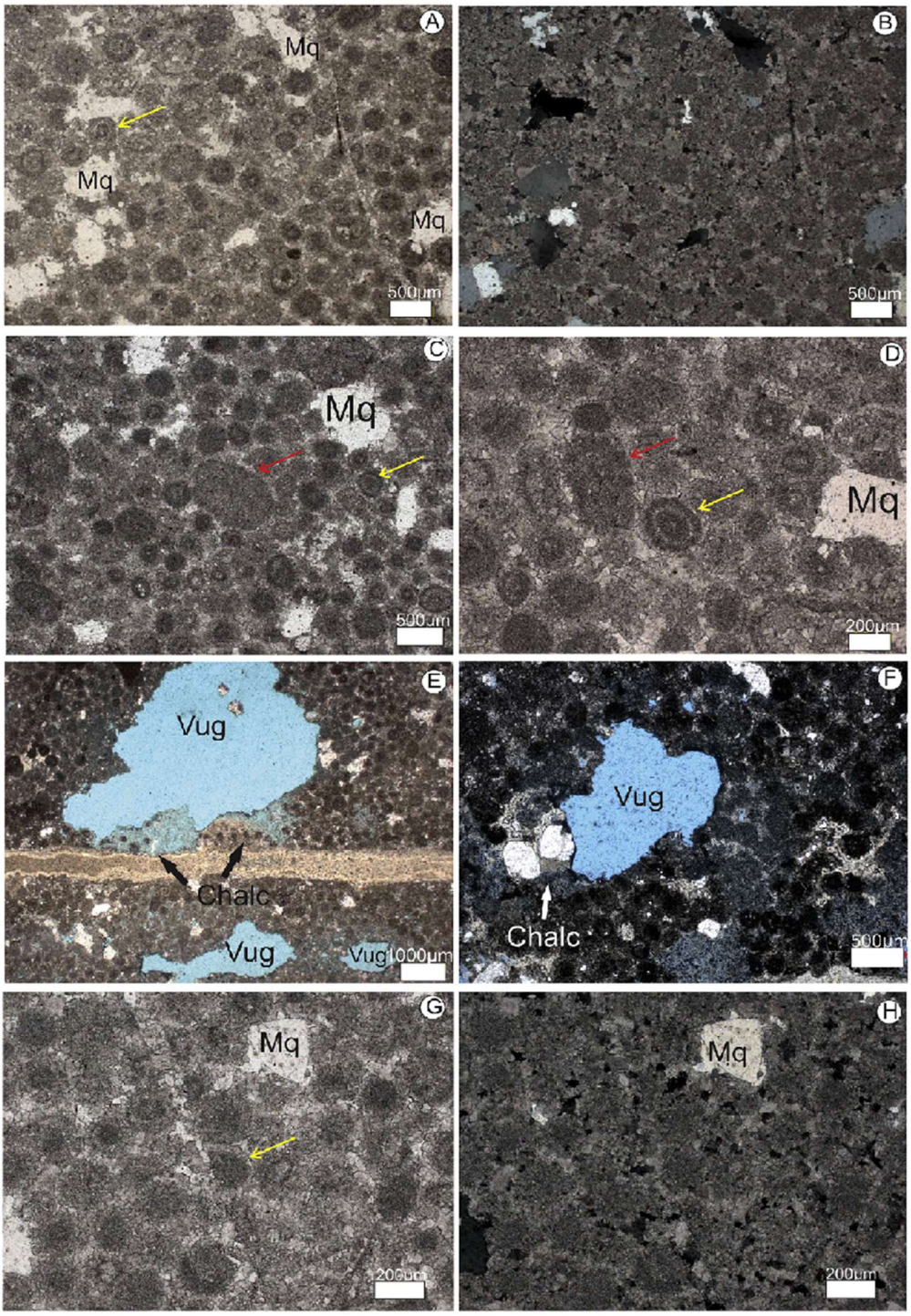

Figure 6. Main features of Unit 1 at the thin section scale: (A) uncrossed and (B) cross –polarized images of oolites with concentric laminations. Yellow arrows indicate concentric laminations in oolites; (C) and (D) oolite laminations and maga-crystals of quartz filling vugular porosity; (E) and (F) vugular pores and fractures filled by chalcedony (Chalc, yellow infilling); (G) and (H) micritisized oolites and mega-crystals of quartz filling vugular porosity. Yellow arrow indicates fracture filled by calcite. Key: Mq, mega-quartz crystals; yellow arrows indicate concentric laminations in oolites. (For interpretation of the references to color in this figure legend, the reader is referred to the Web version of this article.)

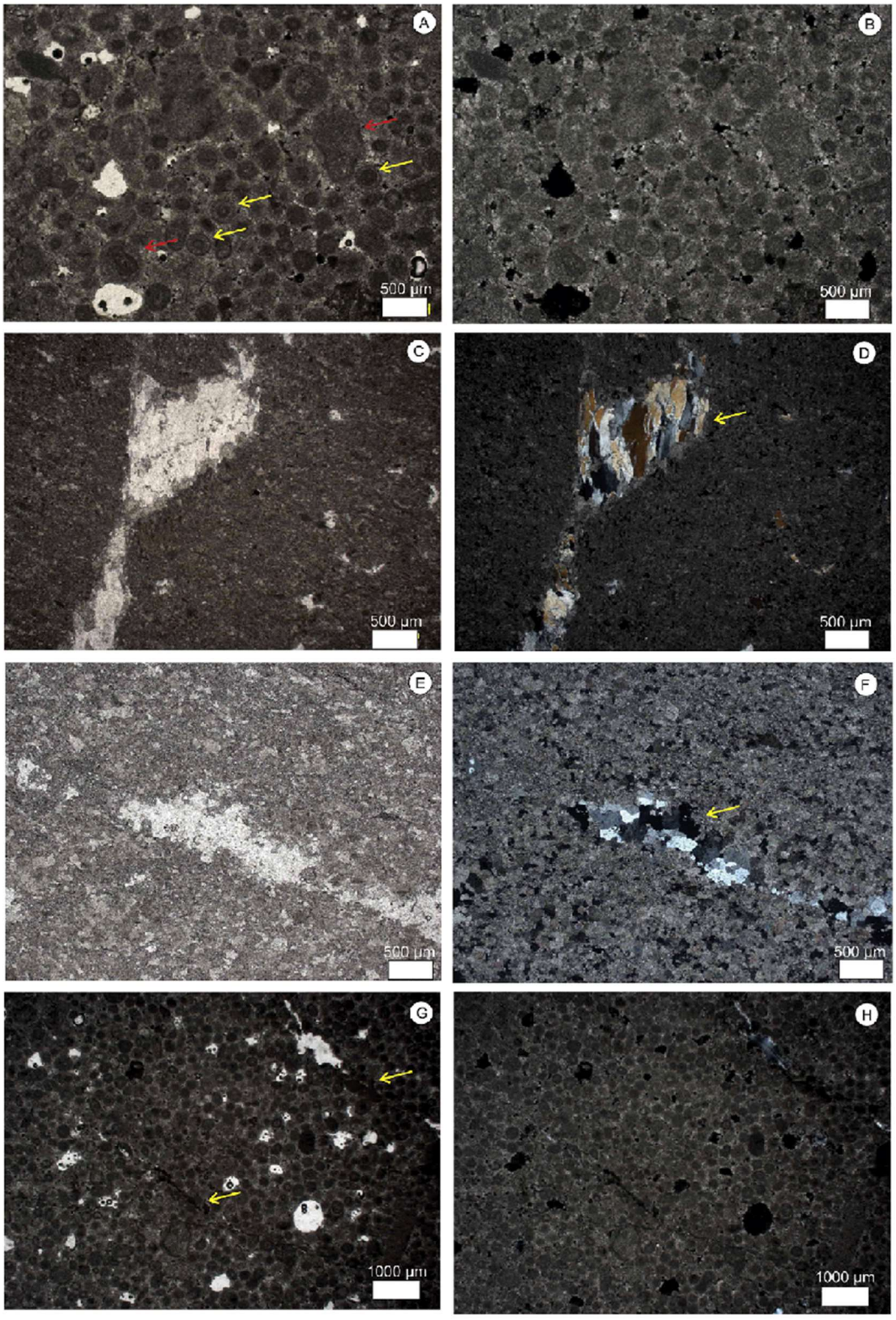

Figure 7. Main features of Unit (2) in thin section: (A) unpolarized and (B) polarized general aspect of oolitic grainstone; (C) unpolarized and (D) polarized vein filled with quartz with undulose extinction; (E) unpolarized and (F) polarized vugular porosity filled with mega-quartz crystals; (G) unpolarized and (H) polarized oolitic grainstone with vugular porosity. Yellow arrows point to features described in captions. (For interpretation of the references to color in this figure legend, the reader is referred to the Web version of this article).

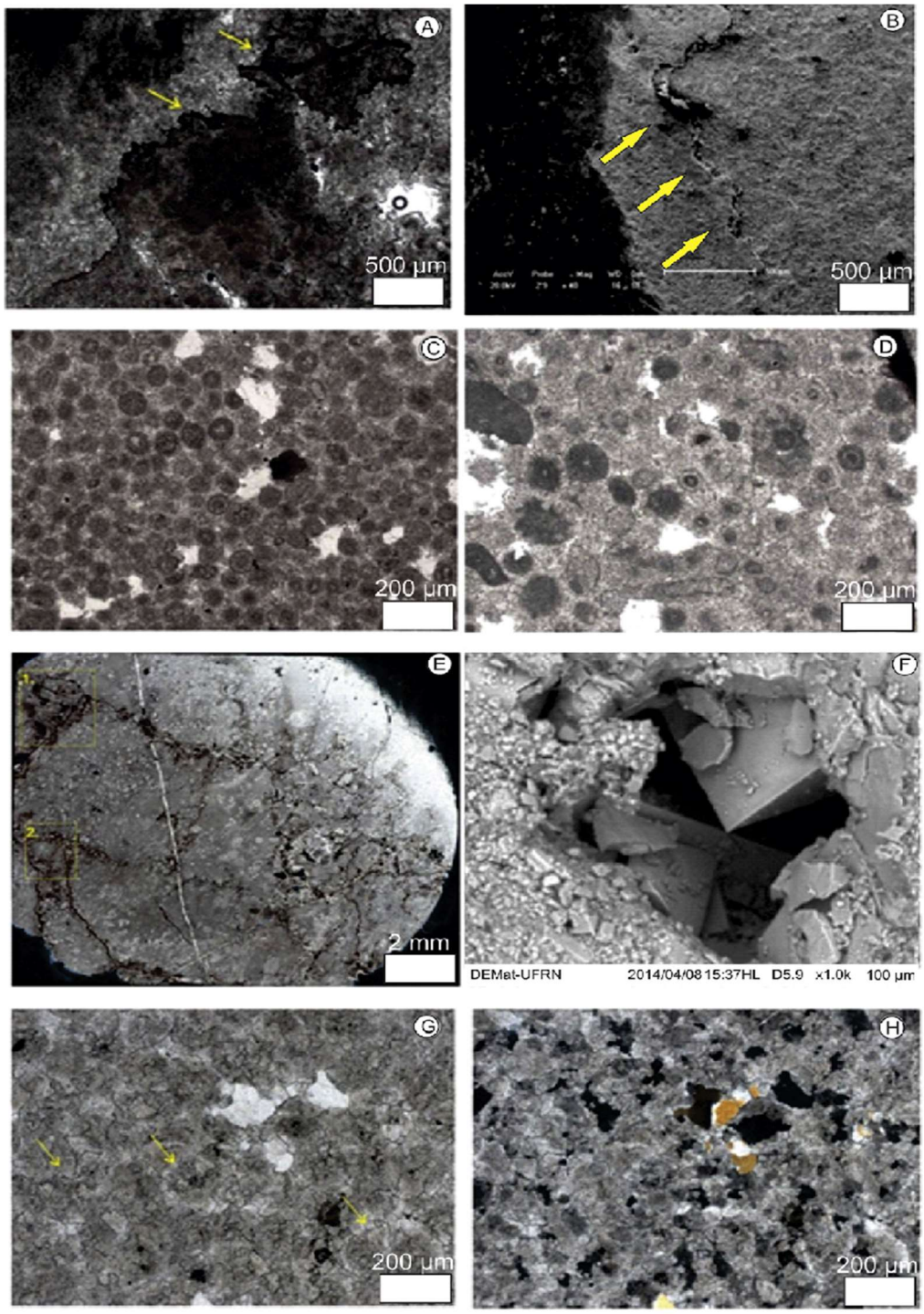

Figure 8. Main diagenetic features: (A) Dissolution associated with stylolites; (B) image from SEM showing surface of chemical compaction marked by yellow arrows; (C) oolite grainstone with punctual and tangential contacts between grains indicating early diagenesis; (D) oolitic grainstone with open framework and total recrystallization; (E) percolation of iron related to limonite during the telodiagenesis phase; (F) SEM image of fracture filled by dolomite crystals; (G) completely recrystallized sample (//Nicolls), where dissolution between crystals occurs; and (H) same sample (X Nicolls).

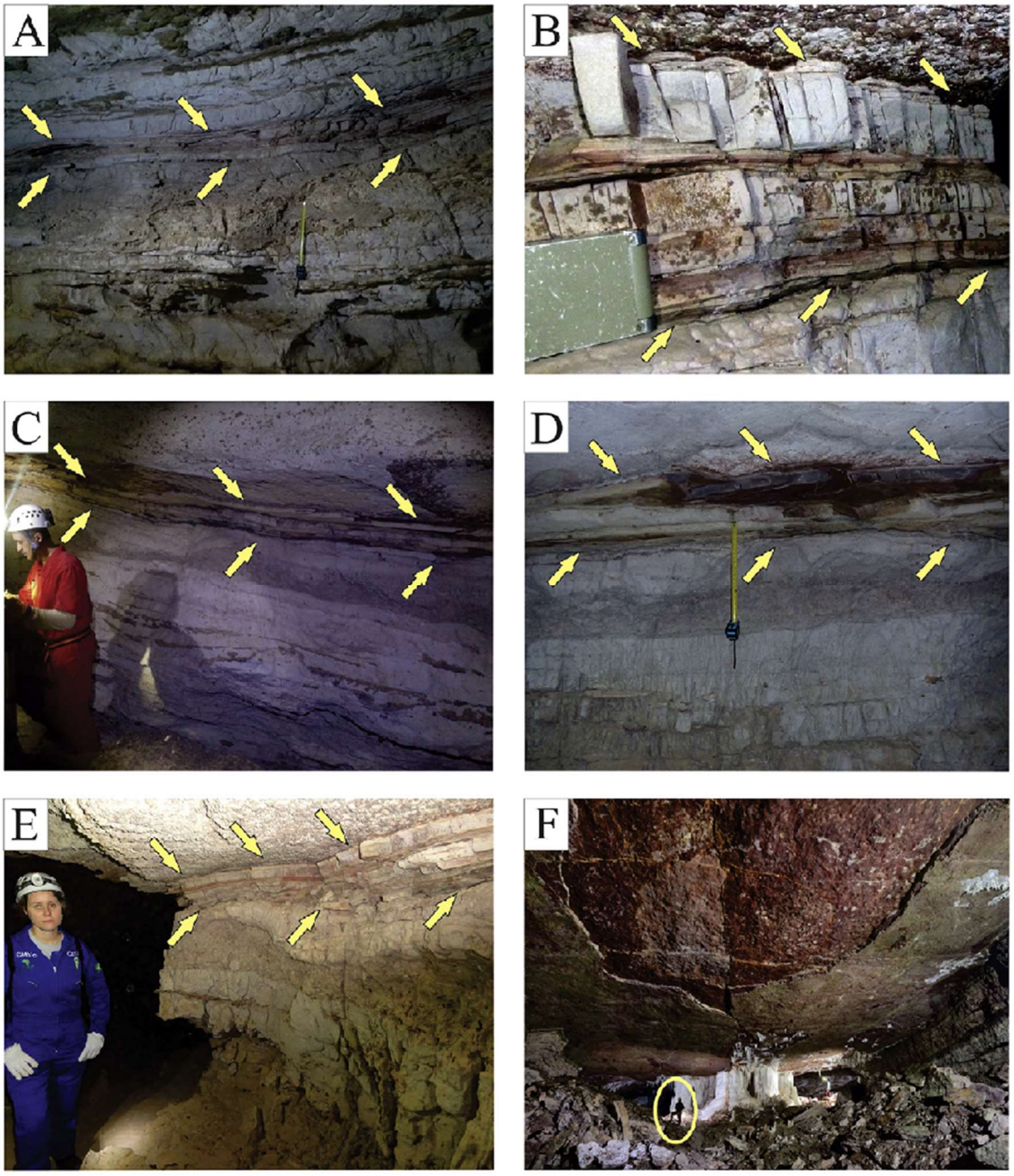

Figure 9. Main features of the conduit units capped by the sealing units: (A) Unit 4 composed of siltstone (marked by yellow arrows) caps Unit 3 and is capped by Unit 5; (B), (C), (D), and (E) Unit 4 composed of thin bedded siltstones marks the bottom of the sealing units; (F) Unit 4 (red color) marks the ceiling of the cave. (For interpretation of the references to color in this figure legend, the reader is referred to the Web version of this article.)

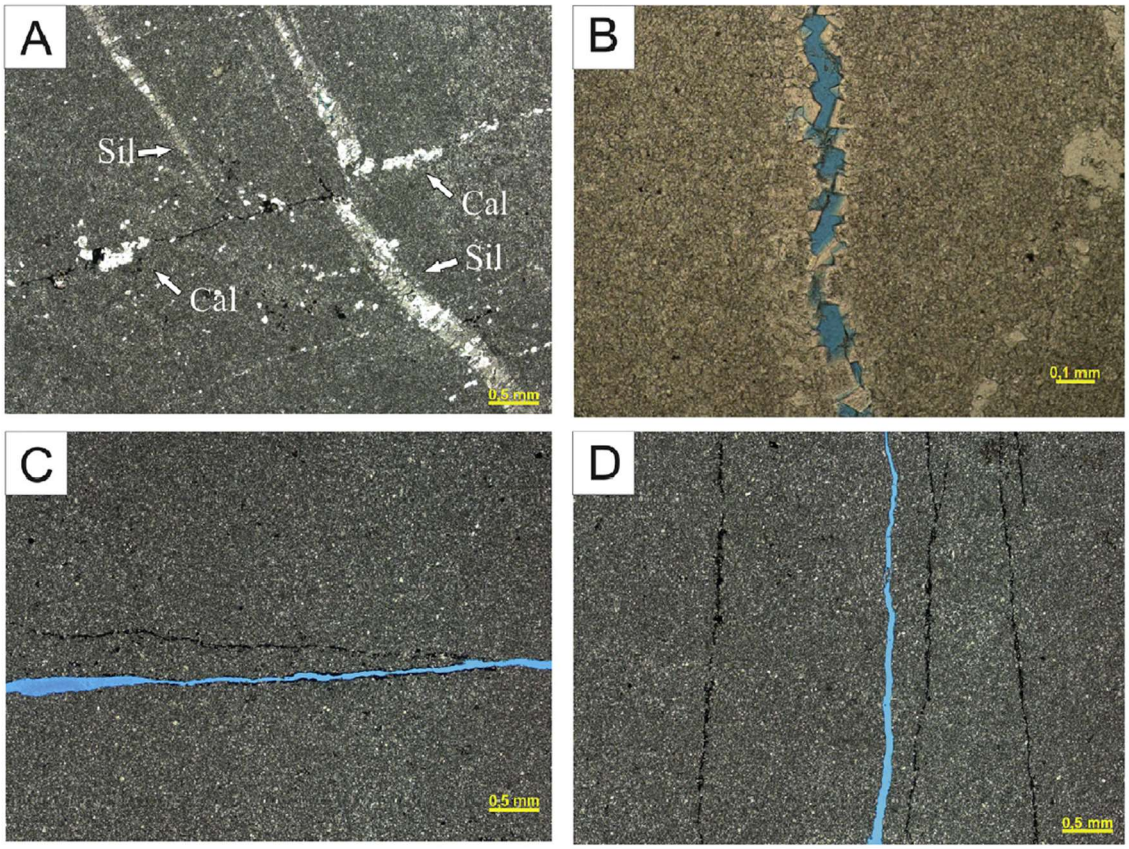

Figure 10. Main textural features of low porosity mudstones from Unit (5): (A) micrite with fractures filled with cryptocrystalline silica (Sil) and spatic calcite (Cal); (B) micrite with channel porosity along fracture; (C) and (D) micrite with closed fractures and a few fractures with canal porosity.

4.2 Mineralogy of vein infilling

Veins and veinlets in the TBV and TBR mainly occur in units (1), (2), (3) and are usually a few millimeters thick. They often have a planar form, but curved surfaces may also occur (Fig. 11A, B, C). The mineralogy of the vein infill indicates a hydrothermal assemblage, as determined by the EDS/SEM analyses of veins from TBV, which reveal a complex and distinct mineralogy compared to the host rock. For instance, veins from sample TBV3G exhibit an assemblage of quartz, barite, iron hydroxides, apatite, calcite, and dolomite (Fig. 11A–D). In other portions of the same sample, the vein evolves to a recrystallized area in which the crystals are well developed and associated with calcite, clay minerals, and apatite. Fig. 11C shows a fracture in a dolomitized rock from TBV that is filled with a zoned assemblage of hydrothermal minerals that include feldspar, apatite, iron oxide, calcite and quartz. Quartz and calcite are irregularly distributed within the original dolomite rock. The fracture filling minerals appear to have been crystallized during

two different stages: one is characterized by apatite + K-feldspar + quartz + calcite + iron oxide/hydroxide, and the other, which most likely formed at a later stage, is characterized by calcite + barite.

Apatite is a mineral commonly observed in many samples and is usually associated with different hydrothermal assemblages (Fig. 11A, B, D, E). Fig. 11E and F shows a fracture in dolomitized rock where apatite occurs associated with quartz and Fe-hydroxides. In other parts of this sample, these minerals occur as well-formed crystals disseminated in the dolostone.

As another example, sample TBR 3 displays the concentration of apatite along a vein that partially replaces the dolomite wall-rock (Fig. 11G). Other minerals in this hydrothermal assemblage include quartz, monticellite, and diopside. A hydrothermal mineral assemblage featuring K-bearing minerals, such as K-feldspar, was also observed. This mineral occurs along the main fracture zones and is also disseminated in the dolomite host rock. In addition to K-feldspar, the sample features quartz, iron hydroxides, and apatite.

Silicification was observed under different conditions (Fig. 12): (1) as cement and prismatic fringes around the vugular pore, and sometimes as discrete euhedral crystals; (2) as a microcrystalline texture with 62–125 μm grain size (silt to clay), filling the central cavities of the vugular pores; (3) as crystals resulting from chemical precipitation in cavities (mega-quartz) and presenting biphasic fluid inclusions (gas and liquid); and as (4) infilling of wide fractures with altered (stretched) crystal lattice, as demonstrated by the crystals with undulose extinction. The different forms of silica indicate that at least two main stages of silicification may have prevailed in the TBV-TBR caves. An earlier stage was most likely associated with sedimentary burial in which chert nodules were formed following sedimentary bedding (Fig. 12A and B). A second and later stage of silica formation exhibits megaquartz and the silica infill of fractures (Fig. 12C and D). This second silica stage is associated with the complex mineralogy described at the beginning of this paragraph (Figs. E–H).

4.3. Porosity and permeability of the conduit units

Carbonate rocks from Units (1), (2) and (3) exhibit decreases in primary porosity and secondary porosity that vary in type and percentage. Whereas the primary porosity was reduced mostly by mesodiagensis cementation, the secondary porosity is characterized by features similar to those reported by Choquette and Pray (1970), such as vugular, fracture, interparticle, moldic, intraparticle, intercrystalline, and intracrystalline features (Figs. 13 and 14). The secondary porosity affected oids/oncoids resulted in the formation of vugs and enlarged fractures. Based on the architecture of the pores determined by X-ray microtomography, we have identified three types of porosity-permeability patterns (Fig. 15): (A) very low porosity values in the range of 0.0–3.0% and low permeability values of 0.00–0.01 mD. This pattern is usually observed in the grainstones of Units (1) and (2), which were recrystallized and cemented by spathic calcite and megaquartz. (B) Intermediate porosity of 3.0–7.0% and permeability of 0.01–1.00 mD; this pattern is observed in the vugular porosity in the microbial grainstones of Unit (3) and the partially closed fractures in the grainstones of Unit (1). (C) High porosity of 3.0–13.0% and high permeability of 1.00–200.00 mD; this pattern is observed in units (1), (2), and (3), which are associated with fractures and channel porosity that interconnects vugular porosity with vugs as large as 2mm in diameter. In general, there is a positive correlation between porosity and permeability for porosity values greater than 1.00%. This good correlation indicates that secondary porosity and permeability are more important in the rock matrix and are mainly related to microscale dissolution along fractures.

4.4. Diagenesis of sedimentary units

The main diagenetic processes that affected the carbonates of the Salitre Formation at the TBV-TBR caves were mechanical and chemical compaction, micritization, cementation, dissolution, recrystallization, dolomitization and silicification (Fig. 16). In the studied rocks, physical compaction is observed mainly in samples with granular textures, as indicated by the punctual contacts of the grains that evolved soon after deposition. Pressure dissolution characteristics are primarily in grainstones, which correspond to high-amplitude stylolites, dissolution

seams, and tangential contacts between grains. The stylolites rarely generated secondary porosity.

Changes in the carbonate fabric included micritization and circumngranular eogenetic cementation, followed by the mosaic cementation of spatic calcite. Micritization is commonly observed in all five lithostratigraphic units, causing total or partial modification of the internal structure of oncoids, ooids and intraclasts. It is often difficult to recognize the primary sedimentary features after micritization. In addition, it is observed that cementation occurred in the isopac fringe and equigranular mosaic of spastic (fine) calcite.

Circumgranular eogenetic cementation has occurred in a manner that supports the framework comprising grains. This framework is observed in oolites, intraclasts, oncolites and microstriped grains with occasional and tangential rare contacts (due to the slight mechanical compaction). These rocks were cemented in an isopic way by fringes, which secured their components almost without contact. The fringe itself was completely obliterated by recrystallization, and effective recognition is not possible.

Later, mosaic cementation of spatic calcite occurred in almost all granular samples. The cementation completely filled the intergranular space, obliterating the primary porosity of the rock. Generally, they correspond to small crystals with equigranular features and recrystallized character. The samples also exhibit evidence of telodiagenesis, in which rocks from the TBV-TBR caves were uplifted and again exposed to meteoric conditions, being influenced by deep-water infiltration of water through fractures and faults. The main features related to telodiagenesis are iron-rich cement comprising limonite, calcite cement in porosities and in fractures and the presence of organic matter.

Dissolution processes related to karstification occurred in three stages: (1) early generation of porosities in vugs and interparticle (eodiagenesis), (2) intermediate fracture widening (mesodiagenesis), and (3) late subaerial exposure promoting a third dissolution process (telodiagenesis). In this last phase, cements that filled the fractures were dissolved, causing them to widen and to develop new vugs (telodiagenesis). In contrast, the samples may also exhibit intense recrystallization processes. The most common case is the replacement of the

micritic matrix by equigranular spiral microcrystalline calcite that preserved the relics of ooids and oncoids.

The five described units exhibit two main types of dolomitization. Type 1 is a fine microcrystalline-to-cryptocrystalline dolomite with a grain size of 0.125–0.088 mm. Type 1 dolomite is either of the following: (a) nonhomogeneous and replaces the primary rock matrix. Type 1 dolomite is characterized by microcrystalline dolomite that partially replaces the original texture (oolite grains have concentric internal structures). (b) Total dolomitization of the original rock leading to total obliteration of the primary rock texture. This late-onset type of crystalline dolomite comprises xenotopic to fine hipidiotopic crystal mosaic fabric. Type 2 dolomitization presents aggregates of eucalyptus and subhedal crystals of dolomites, generally filling vugular pores.

5. Discussion

5.1. The interplay between fractures and stratigraphy in controlling hypogene karst from the local to the regional scale

The data presented here provides a lithostratigraphic framework for further understanding the origin, evolution, and functioning of caves. The data also allow a discussion of the petrographic and petrophysical properties of carbonate and siliciclastic units and their role in karstification. Below, we present a conceptual model (Fig. 17) supported by our field and laboratory studies. The model departs from the local features described in the present study and from the works by Ennes-Silva et al. (2016), Klimchouk et al. (2016), and Auler et al. (2017) and makes regional assumptions based on the maps by Bizzi et al. (2003).

The fluid flow is strongly controlled by conductive carbonate layers from the intermediate story, which are the main focus of the present work. These layers were separated into five distinct lithostratigraphic units, from the bottom to the top: (1) grainstone with cross-bedding stratification, (2) fine grainstone with chert nodules, (3) microbial carbonate, (4) interbedded fine siliciclastics and marls, (5) crystalline carbonate that interfinger with chert layers. The fluid flow is also controlled by the petrophysical properties and fracturing of these intermediate units, which become the main pathways for the lateral dissolution of fluids that later evolved into conduits and passages. Units (4) and (5) acted as a stratigraphic seal

to upward fluid migration, which preserved overpressures and below which hydrothermal fluids migrated laterally and promoted dissolution (Fig. 17A). The carbonate units were hydrologically isolated above and below the seal. Elsewhere, it has already been observed that a low concentration of fractures across seals causes a hydrological system to be compartmentalized, whereas a high concentration of fractures tends to homogenize the system above and below the seal (Evans and Fischer, 2012). Fluid overpressure below the seal could eventually fracture it and could allow aggressive fluids to migrate into overlying units (Roberts and Nunn, 1995). In the TBV-TBR caves, units (4) and (5) were locally breached, which allowed the formation of conduit outlets (Klimchouk et al., 2016). The seal bypass enabled a new phase of dissolution.

The TBV-TBR caves are located at the top of the same regional NESW-striking thrust, which trends roughly in the same direction for both caves (Fig. 17B, C, D). The thrust system developed along quartzites and carbonates on a regional scale (Ennes-Silva et al., 2016; Klimchouk et al., 2016). This last unit hosts the karst system (Fig. 17A). Thrusts systems are usually observed as flats and not efficient conduits for upward flow. However, fluid flow has been recorded along thrust systems in several basins in different tectonic settings, such as in the southern Pyrenees, Spain (e.g., Travé et al., 2007; Beaudoin et al., 2015), in the Appalachian Valley and Ridge, USA (Evans and Fischer, 2012), and offshore Brunei (Morley et al., 2014).

The caves were developed along anticline axis of a dome and basin system (NeS and E-W trends), parallel to which a fractures system also evolved (Fig. 17B). This system of fractures is associated with the Brasiliano event, which occurred on the north bank of the São Francisco craton in the period from 750 to 540 Ma (Ennes-Silva et al., 2016). The age of the hypogene karstification, however, is still a matter of debate, as already noted by Klimchouk et al. (2016). Fluid flow along faults is likely to have occurred when these structures were active. These faults and folds were active during the Brasiliano orogeny and inactive ever since. In the TBV-TBR cave area, fault reactivation could have occurred in the Pangea breakup in the Jurassic-Cretaceous. These are likely to be the most important period for hypogene speleogenesis. However, teasing apart the features of the karst system

necessitates higher sampling density and better time constraints, which requires further studies.

The stratigraphic horizon related to the conductive layers of the intermediate story of the TBV-TBR caves are mapped on a regional scale, thus suggesting that the stratigraphic control of the hypogene karst system may be extended to the whole basin. These stratigraphic units correspond to the Nova América unit, as described by Misi and Silva (1996). These types of lithostratigraphic units, therefore, may have broad implications for carbonate units affected by karst processes; this favors the creation of highly permeable horizons that will be prime for dissolution and porosity generation.

The conceptual model presented above (Fig. 17) is consistent with observations of current fluid flow and sea-conduit systems that create overpressure zones in sedimentary basins (Tingay et al., 2009). Similar systems occur at the top of anticlines developed at shallow depths, such as in the central basin in Iran and offshore Brunei (Morley et al., 2014) and in the Late Ordovician Trenton-Black River hydrothermal dolomite reservoirs in New York, USA (Smith and Davies, 2006).

5.2 Diagenesis and hydrothermal processes in hypogene karst

Secondary porosity such as that generated by karst processes crosscuts unconformities and is mainly related to faults and fractures (Barnett et al., 2015). In our study, these features concentrate along fold hinges (Ennes-Silva et al., 2016) and below local-scale stratigraphic seals. The variations in porosity in carbonate reservoirs occur at a high frequency cycle scale (Ehrenberg, 2004), hence justifying the need to map local-scale seal-conduit systems, such as in the present study, in detail.

The characterization of properties in carbonates must consider both the stratigraphic and diagenetic model as a result (Lucia, 1995; 1999). Dissolution in deep-burial, mesogenetic settings can also result in the development of macro- and mega- (meter-scale) porosity and conduit permeability (Hill, 1995; Klimchouk, 2012), which is still rarely considered in studies of carbonate reservoirs despite the

growing body of evidence reported from deep-seated hydrocarbon fields (e.g., Heward et al., 2000).

The mineralogical assembly associated with veins and fractures along which the cave galleries evolved suggests that hypogene processes played an important role in speleogenesis. The complexity of the vein infilling-mineral assemblage, which includes quartz, barite, pyrite, K-feldspar, calcite, Fe hydroxides, and, more rarely, diopside and monticellite, indicates both the hydrothermal origin and the hypogene multistage character of the TBV-TBR caves. Similarly, complex assemblages have been recognized in other studies and are equally attributed to hydrothermalism (e.g., Dristas et al., 2017; Środoń et al., 2018; Schoenherr et al., 2018), which is consistent with the secondary porosity observed in carbonates that are believed to be dissolved by hydrothermal fluids that become increasingly more aggressive at depth (Wright and Harris, 2013). Our study has important implications for carbonate reservoirs that are intensively cemented and have a low matrix porosity-permeability. In these cases, reservoir porosity-permeability is mainly concentrated in vugs and fractures (e.g., Zhiqian et al., 2016).

The hydrothermal mineral assemblage described in this study could be the result of an initial phase of speleogenesis in the area that was most likely associated with one of the events of ascending fluid flow suggested by Klimchouk et al. (2016). These early mineral phases, which are preserved as relicts in fractures and veins, have been largely obliterated by the more recent pervasive dissolutional phase that resulted in the massive volumes of cave passages observed in the TBVTBR caves. Although these caves accounts for a small part when compared with the vast volume of cave passages, the tectonic framework and the mineralogical suite suggest that solutionally aggressive fluids ascended from deep-seated zones, yielding a byproduct of a characteristic set of minerals.

It follows that the mineralogy assemblage observed in the veins from TBR and TBV caves does not indicate specific thermal conditions but strongly suggests that the fluid composition was completely distinct from that in equilibrium with the host carbonate units. The observed mineralogy is commonly associated with structurally controlled hydrothermal fluids related to dolomitization of carbonates rocks (Davies and Smith, 2006; Ronchi et al., 2012; Yardley and Bodnar, 2014).

Barite and apatite, together with variable amounts of Fe-oxide, sphalerite and galena, are commonly associated with breccia and saddle dolomites in carbonate-bearing hydrocarbon reservoir (Davies and Smith, 2006) and Mississippi Valley Type (MTV) of ore deposits (Davies and Smith, 2006l; Yardley and Bodnar, 2014). Mineral transformations associated with these fluids have also been related to important changes in porosity and permeability of carbonates, thus strongly affecting fluid circulation (Zhang et al., 2009; Gomez-Rivas et al., 2014; Mahboubi et al., 2016). The origin of the fluids responsible for the vein mineralogical assemblage observed in the TBR and TBV caves is unclear, as already noted by Klimchouk et al. (2016). Based on available geological data, there may have been contributions from both external sources (i.e., deep fluid circulation along faults) and basinal sources, as revealed by the phosphate and sulfides mineralized horizons reported in the Salitre basin (Misi and Silva, 1996; Kyle and Misi, 1997; Caird et al., 2017).

A limited number of studies have addressed the effects of fluid-rock interaction in these rocks from a geochemical perspective (e.g., Kyle and Misi, 1997; Klimchouk et al., 2016). For instance, carbon and oxygen isotope data of carbonates from the walls of the TBV cave were previously presented by Klimchouk et al. (2016). The data, based on 9-to-20-cm-long cores, exhibit a narrow variation range for both δ13C (average −4.9 ± 0.4‰) and δ18O (average −1.7 ± 0.2‰). A detailed profile along one of the cores shows that the isotope variations fall within the same narrow range, thus indicating that the fluid-rock interaction in the cave wall did not imprint significant isotopic variations in the carbonate host rock. Similarly, to the findings of Klimchouk et al. (2016), available regional isotope data from the Salitre Formation carbonates also indicate that these rocks were not strongly affected by pervasive high-temperature hydrothermal fluids (Misi and Veizer, 1998). The exceptions are structural controlled fluid zones that concentrate Fe-Pb-Zr-Ag sulfides and in which sphalerite fluid inclusions point to temperatures ranging from 140° to 200 °C and water salinity between 3 and 12 wt% equivalent NaCl (Kyle and Misi, 1997). According to the authors, these sulfide-rich zones are related to deep fluid circulation controlled by reactivation of basement faults. The hydrothermal mineralogy observed in veins from TBR and TBV caves suggests a possible connection with these sulfide-rich zones, at least in terms of the mineral

composition. To better detail this relationship, however, further specific studies are needed.

5.3. Diagenetic evolution of the TBV-TBR caves

The diagenetic features observed at the TBV-TBR caves indicate that a succession of eo-, meso- and telodiagenesis processes played a major role in the caves' evolution (Fig. 16). During eodiagenesis, newly deposited grains (units 1 and 2) were subjected to intense micritization and light grain packing (mechanical compaction). Physical compaction started shortly after deposition, as commonly observed in other sedimentary basins (Tucker and Wright, 1990). This diagenetic stage caused a decrease in primary porosity and most likely occurred while the carbonate succession was still at the marine water table.

Oscillations of the relative sea level led to a major change in the environmental setting, which allowed the input of meteoric fluids. In this phase, eogenetic cementation occurred, resulting in isopic fringe cement, which kept the rock structure open. Eogenetic fine mosaic cementation occurred, and the recrystallization of oolite, oncolite and intraclast grains occurred. Silica formed in this stage was possibly derived from organic matter and silica minerals of the sediment itself. The intensity of cementation and recrystallization eventually closed the pores and obliterated almost all the depositional structures of the rock. At the same time, sea level oscillations also provided meteoric environmental conditions (eogenetic) and exposed the rocks, which favored dissolution, and thus generated interparticle and vugular porosities in the grainstones. In this evolutionary stage, the stratigraphic units were subjected to intense fracturing at the shallow crustal level that acted as a preferred route for fluid percolation. In the context of mixing of meteoric and marine waters, the TBV-TBR caves were subjected to the second process of dolomitization, which was less intense than the former process and had a longer crystallization time. During the second dolomitization, the vugular porosity was partially filled, and the infiling crystals were engulfed by the subsequent silicification.

During the mesogenetic phase, units (1) and (2) were affected by interparticle dissolution, fracture widening and cementation, and finally dissolution by rock pressure. Two hydrothermal processes reduced porosity during this phase. First,

fractures were filled by chalcedony and by quartz with undulating extinction (high temperatures), and second, the porosities were filled by megaquartz crystals. In addition, there was a gradual increase of burial-generated stylolites and dissolution seams. This late silicification and may have been derived from a source outside the basin.

The uplift and exposure of these rocks during the telogenetic phase is marked by the precipitation of limonite and a higher concentration of organic matter, mainly in the fractures. This process was coeval with cementation of spatic calcite as a fine mosaic that closed the newly created porosity in the fractures.

6. Conclusion

We investigated the largest caves in South America, Toca da Boa Vista and Toca da Barriguda, which developed in the Neoproterozoic carbonates of the Salitre Formation. The study area is a well-known example of hypogene speleogenesis in an ancient cratonic setting. Our multidisciplinary study resulted in the following conclusions.

(1) Karst porosity is considered to be mainly controlled by fracture systems. This study, however, indicates that major hypogene karstification follows a stratigraphic-controlled conduit-seal system. In the TBV-TBR caves, the cross-stratified grainstone (Unit 1) is the guiding layer for the dissolution and formation of cave passages and the main conduit for hydrothermal flow. The thin siliciclast intercalated with marl (Unit 4) and the crystalline carbonate (Unit 5) acted together as a "sealing" rock for kart processes. Considering this, the hydrothermal fluid ascended through the thrust fault, and, when it reached the sealing rocks (Units 4 and 5), it was laterally sprayed, which caused major dissolution in units (1), (2) and (3).

(2) The complex mineral assemblage of vein infilling indicates that hydrothermal fluids were involved in hypogenesis.

(3) The dissolution promoted by hydrothermal fluids occurred mainly during mesodiagenesis in a deep-seated environment. This process promoted fracture widening and the generation of megaporosity (the cave conduits).

(4) The conduit-seal system occurs at the top of a thrust, where sealing units prevented upward fluid migration, induced hydrothermal fluids to flow laterally and promoted karstification.

(5) Field analogue studies in representative caves are crucial to better understanding the complex interplay among fractures, stratigraphic horizons and karstification processes in carbonate sequences. The study results provide critical information for the understanding and modeling of carbonate reservoirs.

Acknowledgments

We thank two anonymous reviewers for their detailed and constructive reviews, which significantly improved our work. We thank the Brazilian Agency of Oil, Gas, and Biofuels (Agência Nacional do Petróleo, Gás e Biocombustíveis, ANP). We thank Rubson Maia for helping with the drawings. This work was partially sponsored by a Petrobras/Federal University of Rio Grande do Norte project (Advanced project for acquisition and interpretation of parameters to characterize and model karst reservoirs) and a Petrobras/Federal University of Rio de Janeiro project (Qualitative and quantitative parameters for geological modeling of karst reservoirs). We also thank the Bambuí Group of Speleology (Grupo Bambuí de Pesquisas Espeleológicas) for the cave maps.

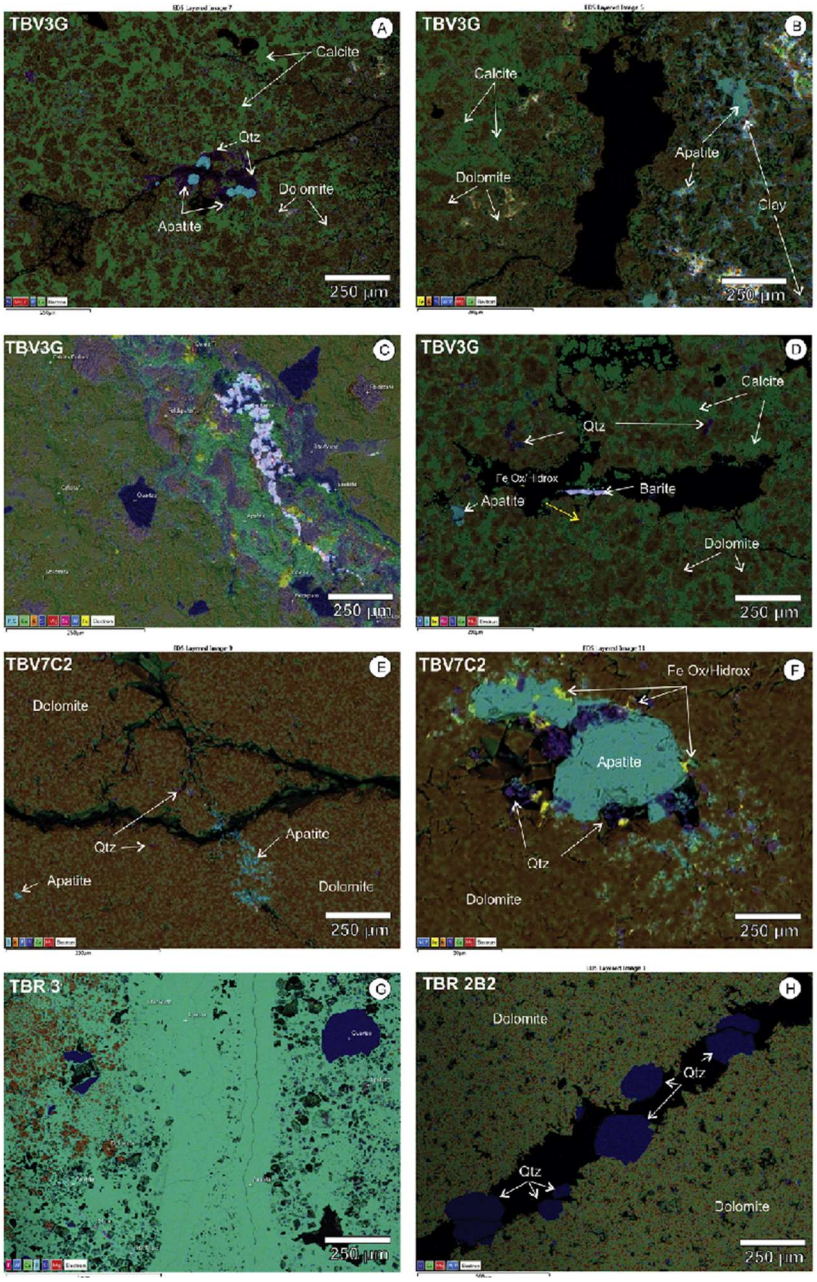

Figure 11. Mineralogy of veins from TBV cave showing hydrothermally-generated mineral associations. A. Fractures along which precipitates apatite and quartz; B. Hydrothermal alteration zone near a fracture in which the host carbonate has been recrystallized and impregnated by disseminated apatite; C. Detail of a vein mineral assemblage with apatite, potassium feldspar, quartz and Fe-Hydroxides; D. Vein filled with quartz, barite, and apatite crosscutting dolomite host rock; E. Fracture in dolomite with quartz and apatite; F. Aggregate of hydrothermal minerals (apatite, quartz, Fehydroxides) near a fracture that crosscut dolomites; G. Massive apatite concentrated along a fracture zone that presents inclusions of pyroxene, montcellite, and quartz. The vein wall-rock dolomite has been replaced by apatite; H. Quartz vein cutting across dolomite. Key: qz, quartz; ap, apatite; cal, calcite; dol, dolomite; ba, barite; Fe-hyd, iron hydroxides; py, pyroxene; mont, montcellite; ox=iron oxide/hydroxide; kf=K-feldspar; H. coarse quartz crystals filling a fracture in fine-grained dolomite.

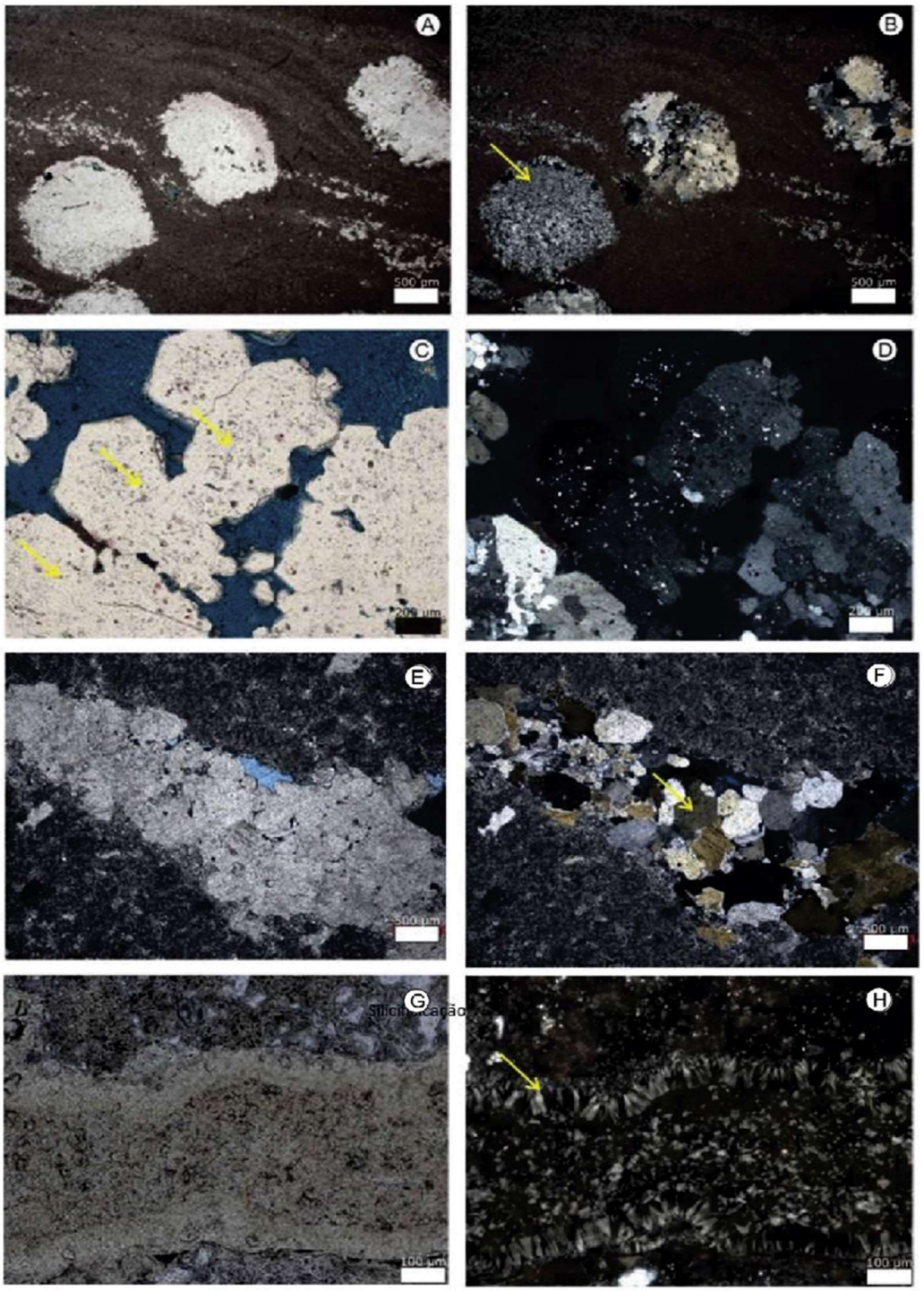

Figure 12. Processes of silicification observed in the studied rocks: (A) chert nodules (cryptocrystalline silica) accompanying the lodging (intercalation of dolomite and calcite); (B) the same photo with crossed cicois; (C) megaquarzt precipitation in the vugular porosities, arrows indicate fluid inclusions; (D) the same photo with crossed Nicolls; (E) fracturing extended by dissolution with subsequent filling of silica. (F) Same photo with crossed Nicolls, arrow indicating quartz crystals; (G) fracture widened by dissolution with posterior filling of chalcedony. (H) Same photo with crossed Nicolls, arrow indicating the botryoidal habit of crystals.

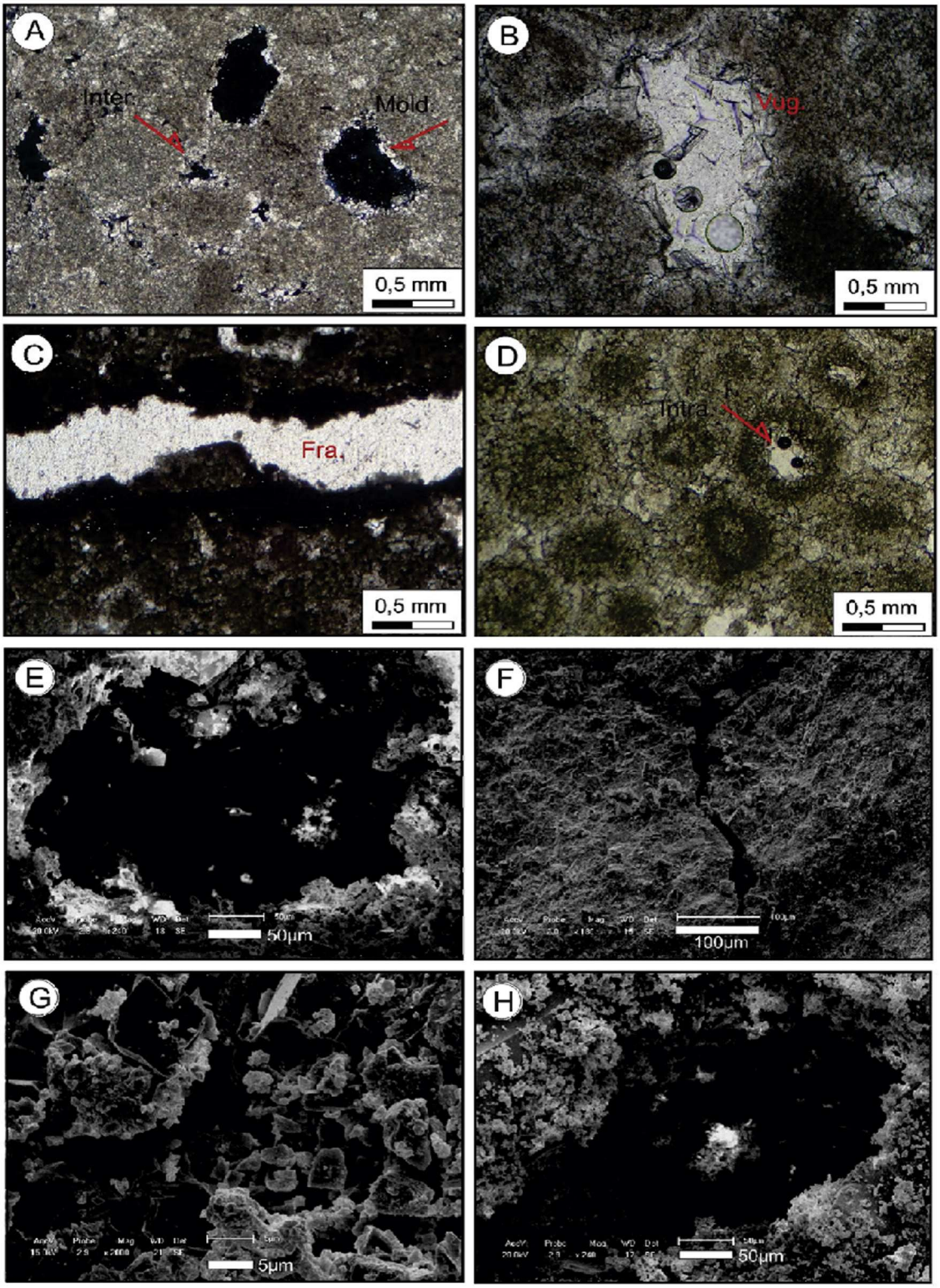

Figure 13. Types of pores in the conduit units: (A) moldic and interparticle porosity; (B) vugular porosity; (C) enlarged fracture that is filled by calcite; (D) interparticle porosity; (E) vugular porosity, (F) dissolution of fracture; (G) interparticle porosity; (H) vugs. (A), (B), (C), (D) are thin section photos; (E), (F), (G), (F) are SEM images.

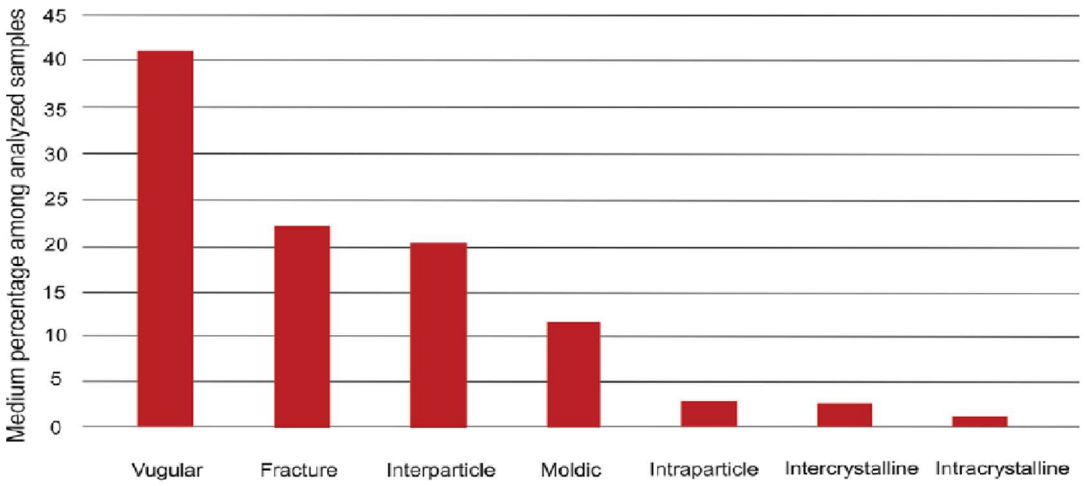

Figure 14. Percentage of porosity, mostly secondary, in samples from units 1, 2, and 3. These porosity values were calculated on thin section using visual inspection.

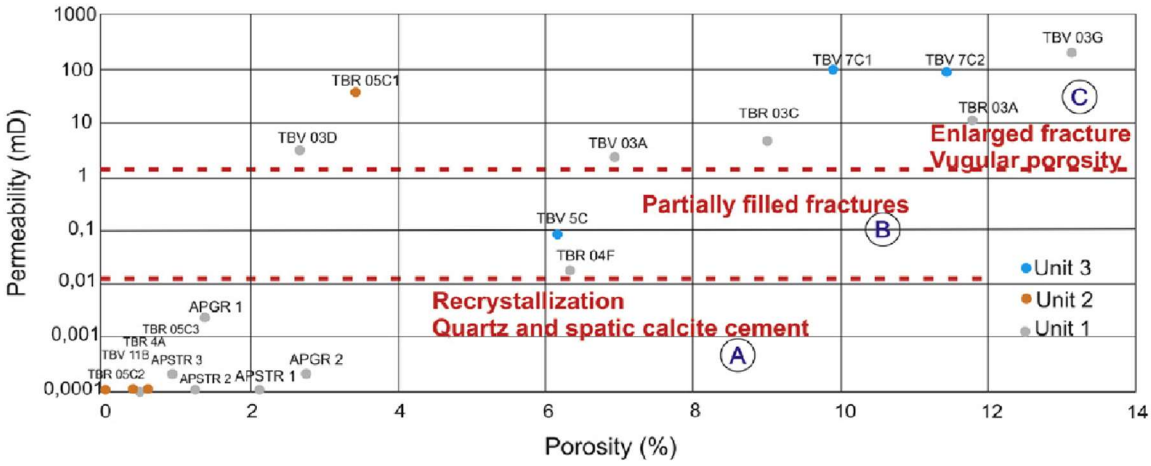

Figure 15. Porosity-permeability of units 1, 2, and 3 and separation of three patterns by dotted lines.

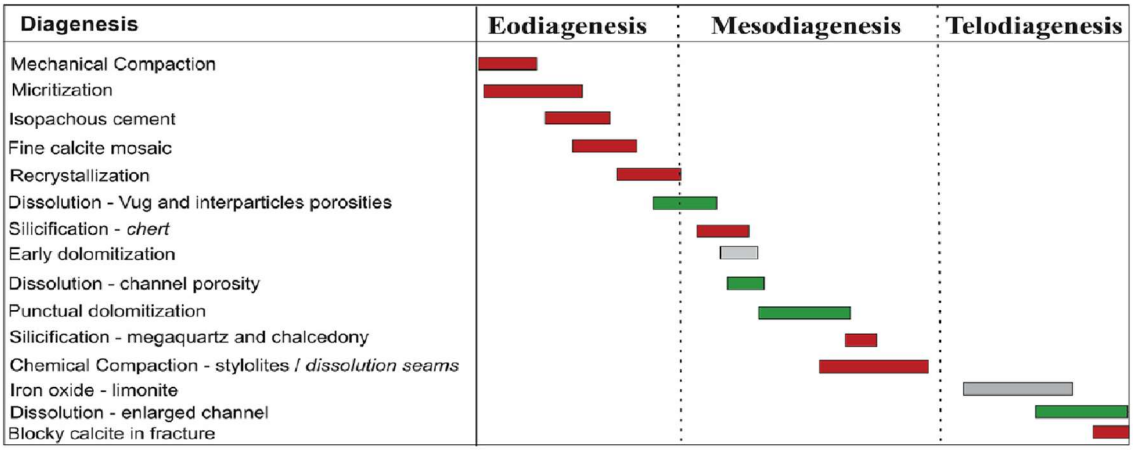

Figure 16. Simplified paragenetic sequence in diagenetic phases of the TBV-TBR caves based on petrographic studies. Green represents creation of porosity with generation of karst, red represents porosity reduction, and gray represents unknown effect. The bar length indicates relative time during diagenesis. (For interpretation of the references to color in this figure legend, the reader is referred to the Web version of this article).

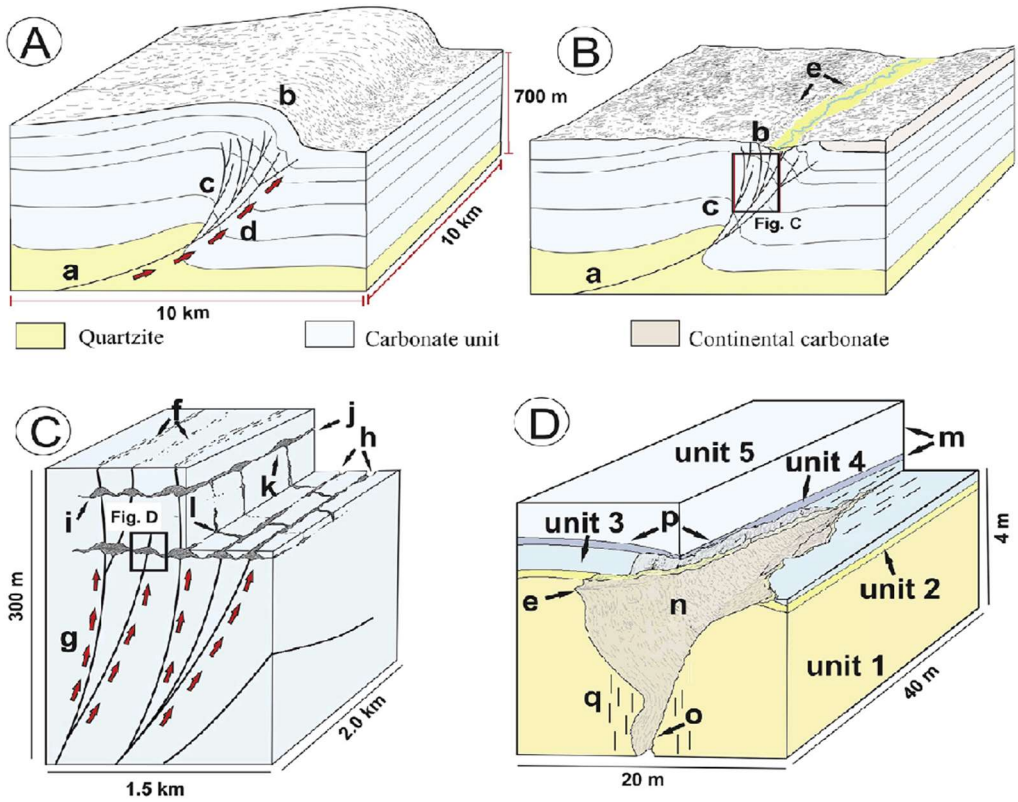

Figure 17. Conceptual model of lithostratigraphic and structural setting of the TBV-TBR caves depicts where fluid-rock interaction took place and where karstification concentrated. Letters in circle show components of the hypogene system. (A) Original thrust system in the TBV-TBR cave area. (B) Present-day setting of the TBV-TBR cave area after a period of subsidence and subsequent erosion. Thrust structure is based on the study from Bizzi et al. (2003). Anticline structure was modified from Ennes-Silva et al. (2016). (C) Karst concentration along fracture corridor and at seal levels. (D) Cave formation along units (1), (2), and (3) at anticlinal hinge and below sealing units (4) and (5). Hypogenic system is modified from the studies from Klimchouk et al. (2016) and Auler et al. (2017). The local stratigraphy is based on the present study. Key: (A) (B) (a) basal detachment, (b) crest of thrust zone, (c) thrust-related fold, (d) arrows show fluid migration pathways, (e) river incision along fracture corridors. (C) (f) fracture corridor and fault termination, (g) arrows mark fluid migration along fractures, (h) karst zone in anticlinal hinge, (i) dissolution (gray) below stratigraphic seals (j) karstification due to lateral fluid migration, (k) hypogenic fluid accumulation below seal, (l) local seal breaches give rise to ascending fluids. (D) (m)

lithostratigraphic seal, (n) large cave passage, (o) feeder of hypogenic fluids, (p) anticline hinge, (q) fracture corridor.

Appendix A. Supplementary data

Supplementary data to this article can be found online at https://doi.org/10.1016/j.marpetgeo.2018.11.046.

References

Al-Shaieb, Z., Lynch, M., 1993. Paleokarst features and thermal overprints observed in some of the Arbuckle cores in Oklahoma. In: In: Fritza, R.D., Wilson, J.L., Yurewicz, D.A. (Eds.), Paleokarst Related Hydrocarbon Reservoirs, vol. 18. SEMP Core workshop, pp. 11–59.

Auler, A.S., 1999. Karst Evolution and Palaeoclimate in Eastern Brazil. Ph.D. Thesis. University of Bristol.

Auler, A.S., Rubbioli, E., Brandi, R., 2001. As grandes cavernas do Brasil. Grupo Bambuí de Pesquisas Espeleológicas, Belo Horizonte.

Auler, A.S., Smart, P.L., 2003. The influence of bedrock derived acidity in the development of surface and underground karst: evidence for the Precambrian carbonates of semi-arid northeastern Brazil. Earth Surf. Process. Landforms 28, 157–168.

Auler, A.S., Klimchouk, A., Bezerra, H.R., Cazarin, C.L., Ennes-Silva, R., Balsamo, F., 2017. In: Klimchouk, A., Palmer, A., De Waele, J., Auler, A., Audra, P. (Eds.), Hypogene Karst Regions and Caves of the World. Cave and Karst Systems of the World. Springer International Publishing, pp. 827–840.

Barnett, A.J., Wright, V.P., Chandra, V.S., Jain, V., 2015. Distinguishing between eogenetic, unconformity-related and mesogenetic dissolution: a case study from the Panna and Mukta fields, offshore Mumbai, India. From. In: In: Armitage, P.J., Butcher, A.R., Churchill, J.M., Csoma, A.E., Hollis, C., Lander, R.H., Omma, J.E., Worden, R.H. (Eds.), Reservoir Quality of Clastic and Carbonate Rocks: Analysis, Modelling and Prediction, vol. 435 Geological Society, London, Special Publications. http://doi.org/10.1144/SP435.12.

Beaudoin, N., Huyghe, D., Bellahsen, N., Lacombe, O., Emmanuel, L., Mouthereau, F., Ouanhnon, L., 2015. Fluid systems and fracture development during syn-depositional fold growth: an example from the Pico del Aguila anticline, Sierras Exteriores, southern Pyrenees, Spain. J. Struct. Geol. 70, 3–38. Bizzi, L.A., Schobbenhaus, C., Vidotti, R.M., Gonçalves, J.H. (Eds.), 2003. Geologia, Tectônica e Recursos Minerais do Brasil, Texto, Mapa e SIG. CPRM, Serviço Geológico do Brasil, Brasília, pp. 692.

Bonfim, L.F.C., Rocha, A.J.D., Pedreira, A.J., Morais, J.C., Guimarães, J.T., Tesch, N.A., 1985. Projeto Bacia de Irecê. Salvador. CPRM (Relatório Final).

Brito Neves, B.B., Fuck, R.A., Pimentel, M.M., 2014. The Brasiliano collage in South America: a review. Braz. J. Genet. 44, 493–518.

Burchette, T.P., 2012. Carbonate rocks and petroleum reservoirs: a geological perspective from the industry. In: In: Garland, J., Neilson, J., Laubach, S.E., Whidden, K. (Eds.), Advances in Carbonate Exploration and Reservoir Analysis, vol. 370. Geological Society, London, Special Publications, pp. 17–37.

Caird, R.A., Pufahl, P.K., Hiatt, E.E., Abram, M.B., Dourado, A.R., Kyser, T.K., 2017. Ediacaran stromatolites and intertidal phosphorite of the Salitre formation, Brazil: phosphogenesis during the Neoproterozoic oxygenation event. Sediment. Geol. 350, 55–71.

Caxito, F.A., Ulhein, A., 2013. Arcabouço tectônico e estratigráfico da Faixa Riacho do Ponta, divisa Pernambuco-Piaui-Bahia. Geonomos 21, 19–37.

Choquette, P.W., Pray, L.C., 1970. Geologic nomenclature and classification of porosity in sedimentary carbonates. AAPG (Am. Assoc. Pet. Geol.) Bull. 54, 207–244.

Dardenne, M., 1978. Síntese sobre a estratigrafia do Grupo Bambuí no Brasil Central. Congresso Bras. Geologia, vol. 31. SBG, Recife, pp. 597–610 Anais 2.

Davies, G.R., Smith Jr., L.B., 2006. Structurally controlled hydrothermal dolomite reservoir facies: an overview. Am. Assoc. Petrol. Geol. Bull. 90, 1641–1690.

Dickson, J.A.D., 1966. Carbonate identification and diagenesis as revealed by Staining. J. Sediment. Petrol. 36, 491–505.

Dristas, J.A., Martinez, J.C., vanden Kerkhof, A.M., Massonne, H.J., Theye, T., Frisicale, M.C., Gregori, D.A., 2017. Hydrothermal karst and associated breccias in Neoproterozoic limestone from the Barker-Villa Cacique area (Tandilia belt), Argentina. J. S. Am. Earth Sci. 76, 182–197.

Dunham, R.J., 1962. Classification of carbonate rocks according to depositional texture. In: In: HAM, W.E. (Ed.), Classification of Carbonates Rocks Amer, Assoc. Petrol. Geol., pp. 108–121 (Memoir I).

Ennes-Silva, R.A., Bezerra, F.H.R., Nogueira, F.C.C., Balsamo, F., Klimchouk, A., Cazarin, C.L., Auler, A.S., 2016. Superposed folding and associated fracturing influence hypogene karst development in Neoproterozoic carbonates, São Francisco Craton, Brazil. Tectonophysics 666, 244–259.

Esteban, M., Kappla, C. F., 1983. Subaerial exposure environment. In: Carbonate Depositional Environments (Eds P.A. Scholle, D.G. Bebout and C.H. Moore), AAPG Mem., 33: 1-54.

P.A.Scholle, D.G.Bebout and C.H.Moore), AAPG Mem., 33: 1-54

Esteban, M., Wilson, J.L., 1993. Introduction to karst system and Paleokarst reservoirs. In: In: Fritza, R.D., Wilson, J.L., Yurewicz, D.A. (Eds.), Paleokarst Related Hydrocarbon Reservoirs, vol. 18. SEMP Core workshop, pp. 1–9.

Ehrenberg, S.N., 2004. Factors controlling porosity in upper carboniferous–lower Permian carbonate strata of the barents sea. AAPG (Am. Assoc. Pet. Geol.) Bull. 88, 1653–1676.

Evans, M.A., Fischer, M.P., 2012. On the distribution of fluids in folds: a review of the controlling factors and processes. J. Struct. Geol. 4, 2–24.

Feldkamp, L., Davis, L., Kress, J., 1984. Practical cone-beam algorithm. J. Opt. Soc. Am. 1, 612–619.

Ford, D.C., Williams, P.W., 1989. Karst Geomorphology and Hydrology. Unwin and Hyman, London, pp. 601.

Gomez-Rivas, E., Corbella, M., Martín-Martín, J.D., Stafford, S.L., Teixell, A., Bons, P.D., Griera, A., Cardellach, E., 2014. Reactivity of dolomitizing fluids and Mg source evaluation of fault-controlled dolomitization at the BenicAssim outcrop analogue (Maestrat basin, E Spain). Mar. Petrol. Geol. 55, 26–42.

Heward, A.P., Chuenbunchom, S., Mäke, I.G., Marsland, D., Spring, L., 2000. Nang Nuan oil field, B6/27, Gulf of Thailand: karst reservoirs of meteoric or deep-burial origin? Petrol. Geosci. 6, 15–27.

Hill, C.A., 1990. Sulfuric acid speleogenesis of Carlsbad Cavern and its relationship to hydrocarbons, Delaware Basin, New Mexico and Texas. AAPG (Am. Assoc. Pet. Geol.) Bull. 74, 1685–1694.

Hill, C.A., 1995. H2S-related porosity and sulfuric acid oil-field karst. In: In: Budd, D.A., Saller, A.H., Harris, P.M. (Eds.), Unconformities and Porosity in Carbonate Strata, vol. 63. AAPG Memoir, pp. 301–306.

Klimchouk, A.B., 2012. Speleogenesis, hypogenic. In: Culver, D.C., White, B.W. (Eds.), Encyclopedia of Caves, second ed. Elsevier, Chennai, pp. 748–765.

Klimchouk, A.B., 2013. Hypogene speleogenesis. In: Frumkin, A. (Ed.), Karst Geomorphology. Treatise on Geomorphology, vol. 6. Academic Press, San Diego, California, pp. 220–240.

Klimchouk, A., Auler, A.S., Bezerra, F.H.R., Cazarin, C.L., Balsamo, F., Dublyansky, Y., 2016. Hypogenic origin, geologic controls and functional organization of a giant cave system in Precambrian carbonates, Brazil. Geomorphology 253, 385–405.

Klimchouk, A., Palmer, A., De Waele, J., Auler, A., Audra, P. (Eds.), 2017. Hypogene Karst Regions and Caves of the World. Cave and Karst Systems of the World. Springer International Publishing.

Klimchouk, A.B., Ford, D.C., 2000. Types of karst and evolution of hydrogeologic settings. In: Klimchouk, A., Ford, D.C., Palmer, A.N., Dreybrodt, W. (Eds.),

Speleogenesis: Evolution of Karst Aquifers. National Speleological Society, Huntsville, pp. 45–53.

Klimchouk, A.B., Tymokhina, E.I., Amelichev, G.N., 2012. Speleogenetic effects of interaction between deeply derived fracture-conduit flow and intrastratal matrix flow in hypogene karst settings. Int. J. Speleol. 41, 37–55.

Kyle, J.R., Misi, A., 1997. Origin of Zn-Pb-Ag sulfide mineralization within upper Proterozoic phosphate-rich carbonate strata, Irecê Basin, Bahia, Brazil. Int. Geol. Rev. 39, 383–399.

Lagoeiro, L.E., 1990. Estudo da Deformação nas Sequências Carbonáticas do Grupo Una na Região de Irecê, BA Tese Mestrado. Universidade Federal de Ouro Preto, Ouro Preto, MG, Brazil, pp. 102 1990.

Lucia, F.J., 1995. Rock-fabric/petrophysical classification of carbonate pore space for reservoir characterization. AAPG (Am. Assoc. Pet. Geol.) Bull. 79, 1275–1300.

Lucia, F.J., 1999. Characterization of petrophysical flow units in carbon ate reservoirs: discussion. AAPG (Am. Assoc. Pet. Geol.) Bull. 83, 1161–1163.

Machel, H.G., 1999. Effects of groundwater flow on mineral diagenesis, with emphasis on carbonate aquifers. Hydrogeol. J. 7, 94–107.

Mahboubi, A., Nowrouzi, Z., Al-Aasm, I.S., Moussavi-Harami, R., Mahmudy-Gharaei, M.H., 2016. Dolomitization of the silurian niur formation, tabas block, east central Iran: fluid flow and dolomite evolution. Mar. Petrol. Geol. 77, 791–805.

Mazzullo, S.J., Harris, P.M., 1992. Mesogenetic dissolution: its role in porosity development in carbonate reservoirs. AAPG (Am. Assoc. Pet. Geol.) Bull. 76, 607–620.

Medeiros, R.A., Pereira, C.P., 1994. Chapada diamantina (São Francisco basin). In: 14th. International Sediment. Congress, Recife, Field Trip Guide Book, 5p.

Misi, A., Silva, M.G., 1996. Chapada Diamantina Oriental, Bahia. Geologia e Depósitos Minerais. Superintendência de Geologia e Recursos Minerais. Universidade Federal da Bahia, Salvador, pp. 194.

Misi, A., Veizer, J., 1998. Neoproterozoic carbonate sequences of the Una Group, Irecê basin, Brazil: chemostratigraphy, age and correlations. Precambrian Res. 89, 87–100.

Morley, C.K., Warren, J., Tingay, M., Boonyasaknanon, P., Julapour, A., 2014. Comparison of modern 660 fluid distribution, pressure and flow in sediments associated with anticlines growing in deepwater 661 (Brunei) and continental environments (Iran). Mar. Petrol. Geol. 663 (55), 230–249.

Palmer, A.N., 1991. Origin and morphology of limestone caves. Geol. Soc. Am. Bull. 103, 1–21.

Palmer, A.N., 2012. Passage growth and development. In: Culver, D.C., White, W.B. (Eds.), Encyclopedia of Caves. Elsevier, Amsterdam, pp. 440–444.

Penha, A.E.P.P., 1994. O calcário Caatinga de Ourolândia, Bahia: Feições diagnósticas, gênese e evolução de um perfil calcrete. MSc Dissertation) Universidade Federal da Bahia 1994.

Pedreira da Silva, A.J.C.L., 1994. O Supergrupo Espinhaço na Chapada Diamantina Centro Oriental, Bahia, Estratigrafia e Tectônica. PhD thesis. University of São Paulo.

Polyak, V.J., McInstosh, W.C., Guven, N., Provencio, P., 1998. Age and origin of Carlsbad Cavern and related caves from 40Ar/39Ar of alunite. Science 279, 1919–1922.

Roberts, S.J., Nunn, J.A., 1995. Episodic fluid expulsion from geopressured sediments. 688. Mar. Petrol. Geol. 12, 195–202.

Ronchi, P., Masetti, D., Tassan, S., Camocino, D., 2012. Hydrothermal dolomitization in platform and basin carbonate successions during thrusting: a hydrocarbon reservoir analogue (Mesozoic of Venetian Southern Alps, Italy). Mar. Petrol. Geol. 29, 68–89.

Smith Jr., L.B., Davies, G.R., 2006. Structurally controlled hydrothermal alteration of carbonate reservoirs: Introduction. AAPG (Am. Assoc. Pet. Geol.) Bull. 90, 1635–1640.

Souza, S.L., Brito, P.C.R., Silva, R.W.S., 1993. Estratigrafia, Sedimentologia e Recursos Minerais da Formação Salitre na Bacia de Irecê, Bahia. Salvador, CBPM. Série Arquivos Abertos 2, 36p.

Środoń, J., Anczkiewicz, A.A., Dunkl, I., Vlahović, I., Velić, I., Tomljenović, B., Kawiak, T., Banaś, M., von Eynatten, H., 2018. Thermal history of the central parto f the Karst Dinarides, Croatia: combined application of clay mineralogy and low-T thermochronology. Tectonophysics 744, 155–176.

Schoenherr, J., Reuning, L., Hallenberger, M., Lüders, V., Lemmens, L., Biehl, B.C., Lewin, A., Leupold, M., Wimmers, K., Strohmenger, C.J., 2018. Dedolomitization: review and case study of uncommon mesogenetic formation conditions. Earrth-Science Reviews 185, 780–805 October 2018.

Tisato, N., Sauro, C., Bernasconi, S.M., Bruijn, R.H.C., De Waele, J., 2012. Hypogene contribution to speleogenesis in a predominant epigenic karst system: a case study from the Venetian Alps. Italy. Geomorphology 151–152, 156–163.

Travé, A., Labaume, P., Vergés, J., 2007. Fluid systems in foreland fold-and-thrust belts: an overview from the Southern Pyréneés. In: Lacombe, O., Lavé, J., Roure, F., Vergés, J. (Eds.), Thrust Belts and Foreland Basins. Frontiersin Earth Sciences. Springer, pp. 93–116.

Tingay, M.R.P., Hillis, R.R., Swarbrick, R.E., Morley, C.K., Damit, A.R., 2009. Origin of overpressure and porepressure prediction in the Baram province, Brunei. AAPG (Am. Assoc. Pet. Geol.) Bull. 93, 51–74.

Trompette, R., Uhlein, A., Egydio-Silva, M., Karmann, I., 1992. The Brasiliano São Francisco cráton revisited (Central Brazil). J. S. Am. Earth Sci. 6 (1/2), 49–57.

Tucker, M.E., Wright, V.P., 1990. Carbonate Sedimentology. Blackwell Scientific Publication, Oxford, pp. 482.

Wright, V.P., Harris, P.M., 2013. Carbonate dissolution and porosity development in the burial (mesogenetic) environment. In: American Association of Petroleum Geology Annual Convention and Exhibition.

Worthington, S.R.H., Ford, D.C., 1997. Borehole tests for megascale channeling in carbonate aquifers. In: Proceedings of the 12th International Congress of Speleology, vol. 11. La Chaux-de-Fonds, Switzerland, pp. 195–198.

Yardley, B.W.D., Bodnar, R.J., 2014. Fluids in the continental crust. Geochem. Persp. 3, 1–127.

Zhang, J., Hu, W., Qian, Y., Wang, X., Cao, J., Zhu, J., Li, Q., Xie, X., 2009. Formation of saddle dolomites in Upper Cambrian carbonates, western Tarim Basin (northwest China): implications for fault-related fluid flow. Mar. Petrol. Geol. 26, 1428–1440.

Zhiqian, G., Zhongbao, L., Shanlin, G., Qunan, D., Shiqiang, W., Shilin, L., 2016. Characteristics and genetic models of Lower Ordovician carbonate reservoirs in southwest Tarim Basin, NW China. J. Petrol. Sci. Eng. 144, 99–112.

CAPÍTULO V - Artigo 2: SUBMETIDO AO PRECAMBRIAN RESEARCH JOURNAL: HYDROTHERMAL ACTIVITY ALONG A STRIKE-SLIP FAULT ZONE AND HOST UNITS IN THE SÃO FRANCISCO CRATON, BRAZIL - IMPLICATIONS FOR FLUID FLOW IN SEDIMENTARY BASINS

ABSTRACT

This study combines multiscale analyses of geological, fault, fracture, and stable isotope data to investigate strike-slip deformation and channeling of hydrothermal fluids along the Cafarnaum fault and calcite veins at different distances from the fault, which is a structure in the São Francisco Craton, northeastern Brazil. Meteoric fluids with δD values near -45‰ and $\delta^{18}O$ values near -6.5‰ and temperatures at 40-70°C precipitated as calcite veins in the host carbonate units. The Cafarnaum fault, a N-S-striking vertical, ~170 km long fault zone, juxtaposes Neoproterozoic carbonate rocks in the western block and Mesoproterozoic siliciclastic rocks in the eastern block. A zone of restraining bends occurs at the central part of the fault, whereas termination zones of horsetail geometry occur at both ends of the Cafarnaum fault. These zones are marked by NW-SE-striking extensional faults that are oblique to the main N-S-striking fault zone, where hydrothermal deposits occur. The zone of influence of the Cafarnaum fault is ~20 km wide around the main fault. The fault formed during the Brasiliano orogeny (740-560 Ma) after Neoproterozoic carbonate platform deposition. In contrast with the host units, fluids along the fault zone originated in deeper levels of the crust and show much lower $\delta^{18}O$ values, indicating higher crystallization temperatures. These fluids caused brecciation in the Neoproterozoic carbonate host rocks, whereas a subsequent decrease in fluid pressure and cooling near the surface

resulted in the precipitation of a hydrothermal paragenesis in veins, also affecting the host rock.

Keywords: carbonate veins, hydrothermal fluid, strike-slip fault, Salitre Formation, São Francisco Craton

1. Introduction

Sedimentary basins display different fluid migration regimes depending on the host rock, particularly in areas subjected to extensional tectonics. Sedimentary stratified layers may allow basinal fluids to migrate laterally parallel to bedding for hundreds of kilometers (Qing and Mountjoy, 1992). In most instances, sedimentary basins display limited vertical fluid flow due to impermeable layers; hence, fluid conduits cannot connect deep and shallow parts of a basin. Pore water usually has a low-velocity flow regime, and its primary geochemical values are therefore easily altered by reactions with host rock minerals and mixing with other fluids (Bjorlykke, 1993).

Vertical fluid flow pathways in sedimentary basins are associated with fault zones (Haneberg et al., 1999; Hardebeck and Hauksson, 1999). Depending on the structures and/or permeability properties, fault zones can either act as hydraulic barriers or as preferential conduits for geofluid migration (Gudmundsson, 2001; Rawling et al., 2001; Smeraglia et al., 2021). Moreover, the diagenetic phases of structural evolution, which start in the pristine rock portions in the earliest diagenetic stages and also affect the faulted domains (e.g., La Bruna et al., 2020). In fact, selective cementation and structural diagenetic processes are key factors in fault permeability control (Hausegger et al., 2010; Ngwenya et al., 2000).

Strike-slip faults create complex and heterogeneous permeability anisotropy and strongly influence fluid migration in crustal fault zones (Caine et al., 2010; Bense et al., 2013; Arancibia et al., 2014). A wide variety of processes at various scales can occur during fault growth and lead to a large range of fault architectures and properties that influence fluid flow behavior (Wibberley and Shipton, 2010). The activity of major and weak strike-slip fault systems is influenced by fluid flow (e.g., Byerlee, 1990; Rice, 1992; Sleep and Blanpied, 1992; Evans and Chester, 1995; Zhang et al., 2001). The internal structure of strike-slip faults is dominated by extensional zones where fault-fill veins, extensional vein arrays, and hydraulic breccias are common features. These features result from intense, deep-seated, and localized hydrothermal fluid flow (Cox and Munroe, 2016). Fluid flow history can be investigated in exhumed faults and fractures, which provide information about deformation mechanisms, fluid-rock interactions, and bulk chemical redistributions (Arancibia et al., 2014; Steyrer and Sturm, 2002). Among other features, synthetic faults, antithetic faults, deformation bands, joints, stylolites, veins, and breccia have been recognized in strike-slip fault zones affected by hydrothermal fluids (e.g., Fossen and Rotevatn, 2016; Choi et al., 2016; Liao et al., 2017; Peacock et al., 2017a, 2017b; Alsop et al., 2020; Ostermeijer et al., 2020). However, there is a debate about which of these structures, if any, exerts a primary influence on fluid flow and the role and origin of fluids in strike-slip fault zones (e.g., Gudmundsson et al., 2002; Gudmundsson, 2007). Several studies show that hydrothermal deposits occur in the São Francisco Craton region, including those around fault zones, while the region remained tectonically stable during the Brasiliano/Panafrican orogenic cycle at 740-540 Ma (e.g., Almeida et al., 2000; Brito Neves et al., 2014). This study focuses on the Cafarnaum fault, which occurs as a lateral ramp (Fig. 1A, B, C). However, the relationship between

the location and timing of hydrothermal deposit formation and fault geometry and evolution remains elusive.

This study is a multiscale and multidisciplinary approach that uses remote sensing, aeromagnetic data, field observations, petrography, and stable isotope geochemistry to compare the structural evolution of the hydrothermal system in the siliciclastic and carbonate host rocks along the Cafarnaum fault zone and the inner basin. We present stable isotope analyses on carbonate host rocks, veins, pockets, and fluid inclusions of the inner basin to reconstruct fluid-rock interactions and build a model to predict the development of hydrothermal activity on a regional scale, which can be used as a proxy for other basins elsewhere. New stable isotope data of fluid inclusions and veins and previously published data of sulfur in sulfides show that carbonate veins associated with fractures at the edge of the basin record much higher temperatures than those crystallized in the central part of the basin. This study also describes and discusses the kinematics, morphology, and magnetic characteristics of the fault zone and the formation of various types of hydrothermal dilation breccias in the damage zone. Finally, a comparison of the Precambrian Cafarnaum fault system and its host rocks with other faults that affect other carbonate and siliciclastic units helps understand regional predictability. This study concludes that fluid flow occurs mainly along extensional subsidiary faults and investigates the way they deform the host rocks. The isotope data indicate that fluids are meteoric in origin and, compared to the sedimentary basins, fluids that percolated the crystalline terrain may have circulated into much deeper zones.

2. Geological setting

The study area is mainly composed of Mesoproterozoic rocks of the Chapada Diamantina Group and Neoproterozoic units of the Una Group, primarily

the Salitre Formation (Fig. 1C). The groups contain distinct formations and contrasting structural styles. Both major terrains are bounded by a strike-slip fault that we name the Cafarnaum fault in this study.

The Chapada Diamantina Group is 1,000 m thick and includes the Morro do Chapéu Formation, which was deposited at ~1400-900 Ma (Pedreira et al., 1975; D'Angelo et al., 2020). This unit was affected by a first contractional inversion event that is mainly marked by symmetrical, N-S-trending, open folds (Danderfer et al., 2015; D'Angelo et al., 2020). High-angle fractures strike mostly N-S, NE-SW and NW-SE, and have a high degree of symmetry with the N-S regional folds (Danderfer et al., 2015).

The Salitre Formation is ~750 m thick in the central part of the Irecê Basin (D'Angelo et al., 2020), which was deposited in a carbonate pelitic marine basin (Misi et al. 2005, 2011) at ~750 Ma (D'Angelo et al., 2020). This sequence was deposited in the Irecê Basin, an asymmetric graben with an approximately

N-S-oriented axis that plunges toward the north (Lagoeiro, 1990; Kuchenbecker et al., 2011; Brito Neves et al., 2012; D'Angelo et al., 2020). The Irecê Basin was inverted in the Brasiliano orogeny, with a peak at ~600 Ma, which resulted in anomalous deformation concerning adjacent domains, with a series of south-verging fold and thrust systems (Lagoeiro, 1990; Teixeira et al., 2019; D'Angelo et al., 2020). The carbonate units of the Irecê Basin have similar Pb-Pb isochron ages and paleomagnetic poles, which fall close to ~520 Ma. This age is consistent with the Gondwana supercontinent's apparent polar wander path and indicates that isotopic and magnetic systems reset those of the Cambrian (Trindade et al., 2004).

This event was related to regional-scale fluid migration and subsequent mineralization at the end of the Brasiliano orogenic cycle (Trindade et al., 2004).

An E-W-oriented magnetic telluric section across the Irecê and Morro do Chapéu Basins reveals lithospheric resistive blocks bounded by major conductive deep zones, which are interpreted as faults. It shows that a lithospheric conductor, interpreted as a suture zone, occurs between the Neoproterozoic Irecê Basin and the Chapada Diamantina Group (Fig. 1C). The high conductance zone is a combination of high porosity and high fluid salinity (Padilha et al., 2019).

Detailed geological mapping on both sides of the fault indicates a great number of occurrences of hydrothermal minerals associated with faults. These occurrences encompass metals such as Au, Pb-Zn, and Ba. These metals occur in sulfides associated with quartz veins in dolomite units close to the main faults. In a few cases, minerals such as barite also occur in the host carbonate rocks (Sampaio et al., 2001).

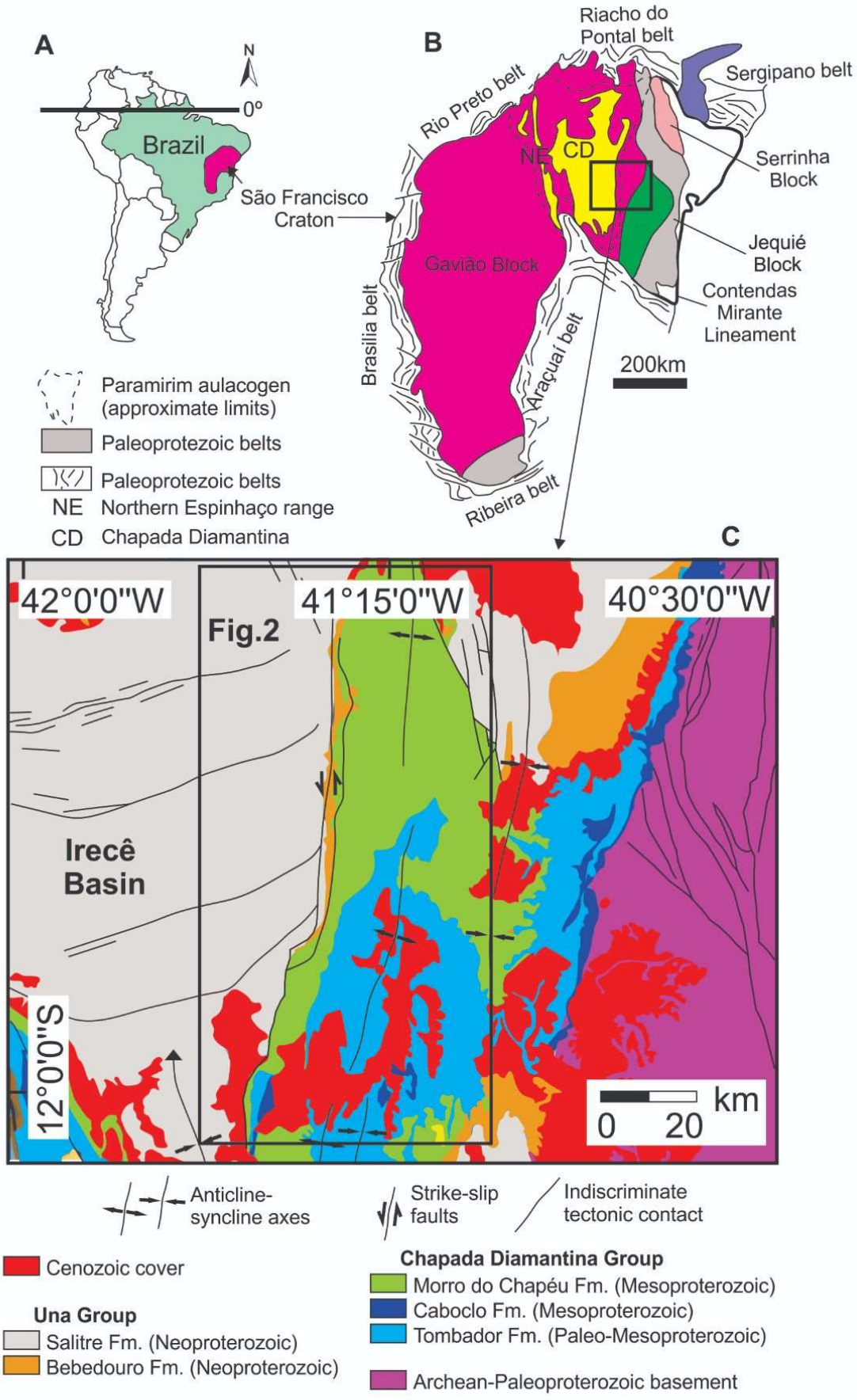

Fig. 1 (A) Continent of South America. (B) Saõ Francisco Craton showing the Archean blocks (modified after Cruz et al., 2007; D'Angelo et al., 2019). (C) Simplified geological map of Chapada Diamantina (modified after Danderfer et al., 2015; D'Angelo et al., 2019).

More detailed studies have also investigated hydrothermal silicification and dolomitization in a few karst systems. Several works have already investigated the cave geometry, stratigraphy, geochemistry, and mineralogy to indicate that fault and fracture systems were used as conduits for deep-seated fluid flow (Klimchouk et al., 2016; Cazarin et al., 2019) approximately 150 km to the north of the study area. In another case approximately 100 km to the south of the study area, a N-S-striking, strike-slip fault in the southern part of the Irecê Basin was the pathway for fluid flow confined to the Salitre Formation during the Brasiliano orogeny. A first stage of Mg-rich fluids caused extensive dolomitization in the Salitre Formation, which was subsequently followed by Si-rich fluids that caused pervasive silicification in the host units (Bertotti et al., 2020).

3. Methods

3.1 – Remote sensing and structural characterization

We combined previous geologic maps, interpretation of Shuttle Radar Topographic Mission (SRTM) and ALOS-PALSAR (Advanced Land Observing Satellite/Phased Array type L-band Synthetic Aperture Radar) imagery, and unmanned aerial vehicle (UAV) imagery in QGIS software for structural interpretation. The main faults are highlighted by geomorphological features (drainage and topographic lineaments). Fault patterns at the site scale (meter scale) were identified in fieldwork with the aid of a UAV survey. We compiled hydrothermal occurrences from the previous research and identified the primary areas of hydrothermal deposit occurrence.

Regional seismic-scale studies have been based on several geological maps (e.g., Cruz et al., 2007; Danderfer Filho et al., 2015). We complemented the structural data with high-resolution ALOS-PALSAR imagery. The study covered

an area 75 km wide and 210 km long using the digital elevation model extrapolated from ALOS-PALSAR images. The satellite images were processed to enhance and visualize several parameters on a regional scale, such as faults, fracture trends and folds. Topographic profiles were drawn in the N-S, E-W, NE-SW, and NW-SW directions to identify geomorphological and structural elements using a vertical color chart characterized by an interval of 10 m. A total of 50 fault lineaments and four fold hinges were measured, and their attitudes are presented in stereographic plots using Stereonet (Allmendinger et al., 2011).

Mesoscale fracture analysis was carried out at all sites. We completed the investigation with a qualitative structural analysis to decipher the nature, kinematics, relative timing, infilling material, and attitude of individual fractures crosscutting the sedimentary units at each study site. We measured fractures, veins, and bedding planes, which are presented in stereographic plots using Stereonet (Allmendinger et al., 2011).

3.2 - Geophysical data and processing

The Centro Norte Bahia Project is an airborne magnetic survey carried out by Companhia Baiana de Pesquisa Mineral (CBPM) that covers the study area with N-S-oriented flight lines spaced at intervals of 0.5 km and E-W-oriented control lines spaced at intervals of 10 km. The nominal flight height was 0.1 km, and the sampling rate was 10 Hz. The magnetic data were corrected for the transient geomagnetic variations and International Geomagnetic Reference Field (IGRF) and were then leveled, or micro-leveled. The dataset was interpolated onto a 250-m cell size grid using the bidirectional method. The grid was reduced to the magnetic north pole (RTP) to center the magnetic anomalies over their causative sources using a magnetic inclination and declination of −25.3° and -22.7°,

respectively. In addition, a matched filter was applied to the RTP anomalies to emphasize magnetic lineaments related to shallow causative sources, such as surface geological units, shear zones, faults.

These data allowed us to highlight and analyze different parameters. Based on magnetic patterns (wavelength, direction, polarity, and spatial distribution), a total of 2,818 magnetic lineaments were measured, which were subdivided into first-order, second-order, and third-order lineaments. These lineaments were extracted from the magnetic maps and are presented in stereographic plots using Stereonet (Allmendinger et al., 2011).

3.3 – Sampling and sample preparation

Samples for this study were collected at six sites in the Irecê Basil, where veins and breccias crosscutting carbonates of this unit were observed (Fig. 2A, B, C). The first four sites (ACH, SOR, IRE, and FAR) are carbonate sites in the central part of the basin. They occur as large pavements with exhumed bedding, fractures, veins, stylolites, and kinematic indicators. These features are used to reconstruct the stress field orientation at the time of deformation and determine the principal modes in which stress has been accommodated. The other two sites (MEL and MAM) are located at the Salitre Basin border and host two of the most important Pb occurrences in the region. Samples were collected in holes dug by an artisanal mining operation.

Once in the laboratory, hand samples and drill cores were cut to make thin sections with thicknesses of 30 μm and 200 μm and polished slabs. Both thin sections and slabs were scanned and described to map the mineralogy and geological features and identify the best sites for geochemical sampling. Samples

from the MAM and MEL sites were also examined with QUEMSCAN to map the main mineralogical phases.

3.4 - Mineralogy and petrography

Mineralogical and petrographic observations were performed using petrographic microscopy, X-ray diffraction (XRD), X-ray fluorescence (XRF), and scanning electron microscopy (SEM) at the Federal University of Rio Grande Norte (UFRN); QUEMSCAN data from the University of Brasília (UnB) was also used. XRD mineralogical data were obtained from twenty samples using a Rigaku Ultra Dtex Miniflex diffractometer. We used the *Match!* ® phase identification software from the power Diffraction 2.0 program (demo version) for mineralogical identification and SigmaPlot 14.0 to make diffractograms. XRF semiquantitative chemical analyses were performed on 3 samples using a Shimadzu EDX-720. Pressed beads were prepared using the residue from loss on ignition, in which sample aliquots were heated to 1000°C for one hour. SEM mineralogical and textural analyses were performed on fresh broken surfaces measuring approximately 1 cm. Samples were gold-coated and analyzed with an Oxford SEM Thin sections were carbon-coated and studied qualitatively and quantitatively using a QEMSCAN analyzer, model Quanta FEI 650F, with a two-coupled energy X-ray dispersion spectometers (EDS, model XFlash 6.30) from Bruker. The SEM conditions for analysis were high vacuum, current beam of 10 nA, and an acceleration voltage of 15 kV. The mineralogical images were generated with 15 µm of lateral resolution. QEMSCAN mapped the mineralogical distribution based on the proportion of chemical elements and a pre-existing mineralogical database.

3.5 - Stable isotope analysis of veins and host rock

For stable isotope analyses of calcite veins and host rocks, samples from the ACH, SOR, IRE, and FAR sites were sampled from 200 µm thick sections using a Merchantek Leica GZ6 Micromill at the Vrije Universiteit Amsterdam. The micromill was programmed to drill approximately 500 µm long and 60 µm deep lines parallel to the vein orientation along a transect perpendicular to the veins. The width of the drill allowed a minimal spacing of 300 µm. The spacing of lines was based on the morphology of the crystals. An aliquot of 300 µg of carbonate was extracted during each drilling procedure and stored in a labeled exetainer vial. Calcite from the MAM and MEL sites was sampled from polished thin sections and slabs using a Sherline micro drill. The sampling site was selected based on textural and petrographic observations. After drilling, an aliquot of approximately 300 µg of carbonate was placed in glass vials for isotope analyses.

Carbon and oxygen isotope analysis of carbonate aliquots was performed on a Thermo-Fisher GasBench II apparatus connected to a Thermo-Fisher Delta+ mass spectrometer from the Vrije Universiteit Amsterdam and the University of Brasília. After flushing the vials with a He flux, the carbonate samples reacted with concentrated phosphoric acid at 45°C (Vrije Universiteit Amsterdam) and 72°C (University of Brasília). The released CO_2 was later transferred to the mass spectrometer to determine the carbon and oxygen isotope ratios.

Both laboratories used international carbonate reference materials (IAEA-CO1, NBS-18, and NBS-19) to evaluate sample size fractionation and the analytical procedure's accuracy. The average standard deviation of the standard was 0.09‰ for $\delta^{18}O$ and 0.06‰ for ^{13}C for samples analyzed at the Vrije

Universiteit Amsterdam and 0.05 ‰ for ^{13}C and 0.10 ‰ for $\delta^{18}O$ for samples analyzed at the University of Brasília.

3.6 - Isotope geochemistry of fluid inclusions

Fluid inclusions are leftover fluid bubbles (<0.5 mm) from the actual fluid from which the calcite crystals crystallized (provided no exchange with the host calcite has occurred since that time). The $\delta^{18}O$ and δD of the fluid inclusions provide valuable information about the origin and characteristics of the fluid. Approximately 0.5 to 1 gram of pure vein calcite crystals were crushed to release enough fluid entrapped in the inclusions. The samples were crushed in a device at the Vrije Universiteit Amsterdam for analysis in which the released volatiles were heated to 1100 °C and guided into a coil by a constant helium flow. The reference materials included liquid water that was injected into the coil via a septum. The coil was cooled by a nitrogen-cooled ethanol sludge with a maximum temperature of -90°C. The water molecules were allowed to settle down in the cold coil for four minutes, after which a flash heater heated it. The released pulse of water vapor was guided into the carbon tube of a FlashEA 1112 Elemental Analyzer, thereby forming H_2 and CO. After passing through a gas chromatograph, these gases were transferred to a mass spectrometer for δD and $\delta^{18}O$ determination.

Each sample measurement was preceded by four measures of 2 µl of the standard DNS3. This procedure was necessary to stabilize the analyzer before sample introduction. After sample analysis, aliquots of the standard DNS3 were analyzed again until stable values were obtained. Details about analytical linearity and memory effect corrections are provided in the supplemented material.

4. Results

4.1 Macroscale geometry and kinematics of the Cafarnaum fault

The compiled structural map presents the primary structural alignments in an area of 38,000 km^2 (Figs. 2A, B, C, 3A, B). The tectonic structures were sorted into strike-slip faults, normal faults, reverse faults, and fold hinges based upon new original data interpretation and previous geological mapping (Cazarin et al., 2019; D'Angelo et al., 2019; Ennes-Silva et al., 2015; Souza et al., 2003). The satellite alignments were divided into the following three fault sets: NNE-SSW, NE-SW, and NW-SE. The NNE-SSW set is generally associated with strike-slip left-lateral faults, as already presented by D'Angelo et al. (2019) and Danderfer Filho et al. (2015). A zone of restraining bends coincides with an uplifted area (Fig. 2A). Additionally, drag folds occur on the west side of the Cafarnaum fault. The folded structures are E-W-striking thrusts of the Irecê Basin that bend where they reach the Cafarnaum fault. These mainly N-S trends, which are localized within the central portion of the study area, correspond to the main tectonic lineament associated with the Cafarnaum fault. In contrast, the NE-SW- and E-W-oriented sets are composed of reverse faults, as shown by D'Angelo et al. (2019) and Reis et al. (2013).

The NW-SE fault set has been interpreted as composed of normal faults (D'Angelo et al., 2019). Termination zones of horsetail geometry occur at both ends of the Cafarnaum fault (Fig. 2C). A few minor faults associated with veins and breccia bodies also occur at the central part of the fault zone, as at the MAM site (Fig. 4). These zones are marked by NW-SE-striking extensional faults oblique to the main N-S-striking fault zone that could possibly form R-shears, where

hydrothermal deposits concentrate on a 20 km wide zone on both sides of the central fault (Fig. 2A, C).

Both the NE-SW- and NW-SE-striking fault sets terminate against the NNE-SSW- to N-S-striking fault set. Eastward from the Cafarnaum fault, a larger folded zone was documented (Fig. 2B, C). Previous works have described how this sector is affected by several anticlines and synclines (Cazarin et al., 2019; D'Angelo et al., 2019; Danderfer Filho et al., 2015; Ennes-Silva et al., 2015; Souza et al., 2003). The fold hinges mainly trend along the NNE-SSW to N-S directions (Fig. 2B, C).

An area of ca. 14,000 km^2 was analyzed for structural magnetic lineament map characterization (Fig. 3A, B). The 2,818 documented lineaments were sorted into, I- order, II-order, and III order lineaments. The I-order lineaments are related to regional-scale magnetic features and are composed of a major NE-SW set and minor sets striking N-S and E-W, respectively. The II-order lineaments are characterized by a major NE-SW lineament and a minor NW-SE to WNW-ESE set associated with secondary magnetic anomalies. Both I- and II-order lineaments are crosscut by the III order lineaments.

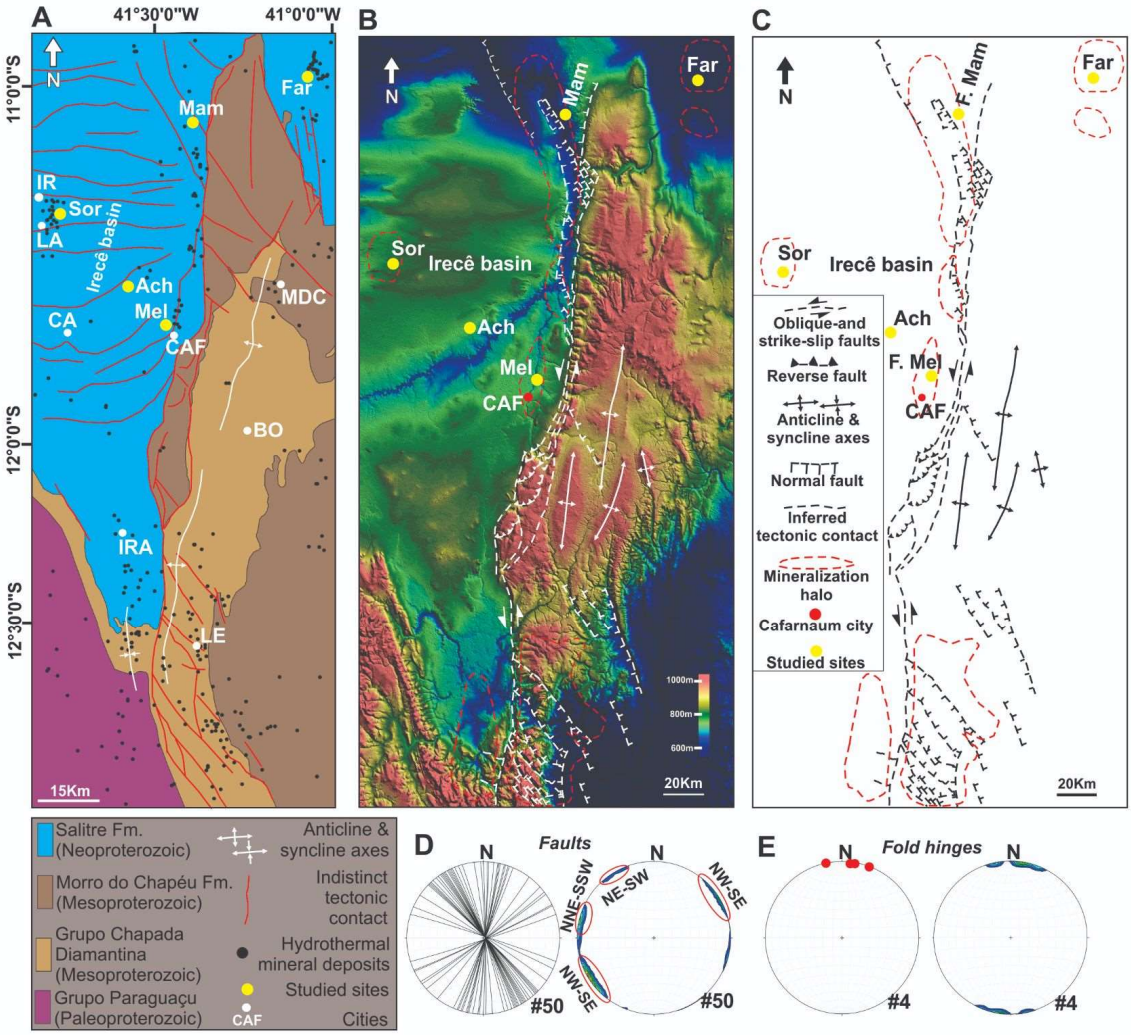

Fig. 2 (A) Simplified geological map modified after *Levantamento Aerogeofísico da Área de Centro Norte Bahia - CBPM, 2011/12 Geologia - Mapa Geológico do Estado da Bahia - CBPM/CPRM, 2003.* (B) Structural framework of the study area superposed on ALOS PALSAR imagery. Dashed lines represent the inferred faults. Continuous white lines represent both anticline and syncline axes. (C) Line drawing of the structural framework presented in B. (D) Lower hemisphere equal-area projections of great circles representing the attitude of the documented faults and equal-area projection/density contour plots of the poles of the measured faults. (E) Lower hemisphere equal-area projections of fold hinges and relative density contour plots. (the map location can be found in Fig. Geological map).

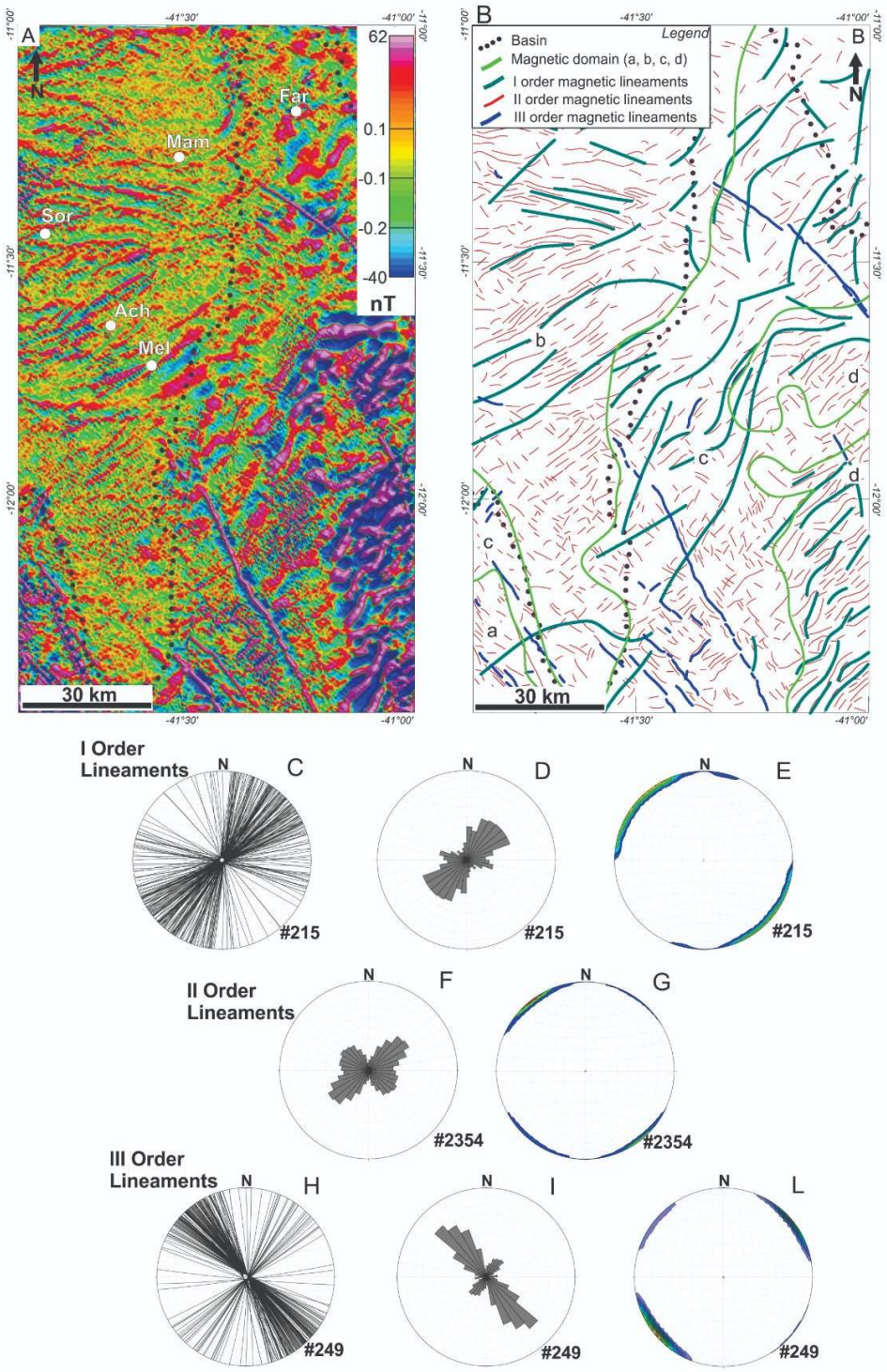

Fig. 3 Behavior of magnetic lineaments in the study area: (A) Map of first derivate. (B) Lineaments Line drawing of the map presented in A. (C-D) Lower hemisphere equal-area projections of great circles and Rose diagram representing the attitude of the documented first order lineaments. (E) Lower hemisphere equal-area projection/density contour plots of the poles of the measured first order lineaments. (F) Rose diagram representing the attitude of the documented second order lineaments. (G) Lower hemisphere equal-area projection/density contour plots of the poles of the measured second order lineaments. (H-I) Lower hemisphere equal-area projections of great circles and Rose diagram representing the attitude of the documented dikes. (L) Lower hemisphere equal-area projection/density contour plots of the poles of the measured dikes.

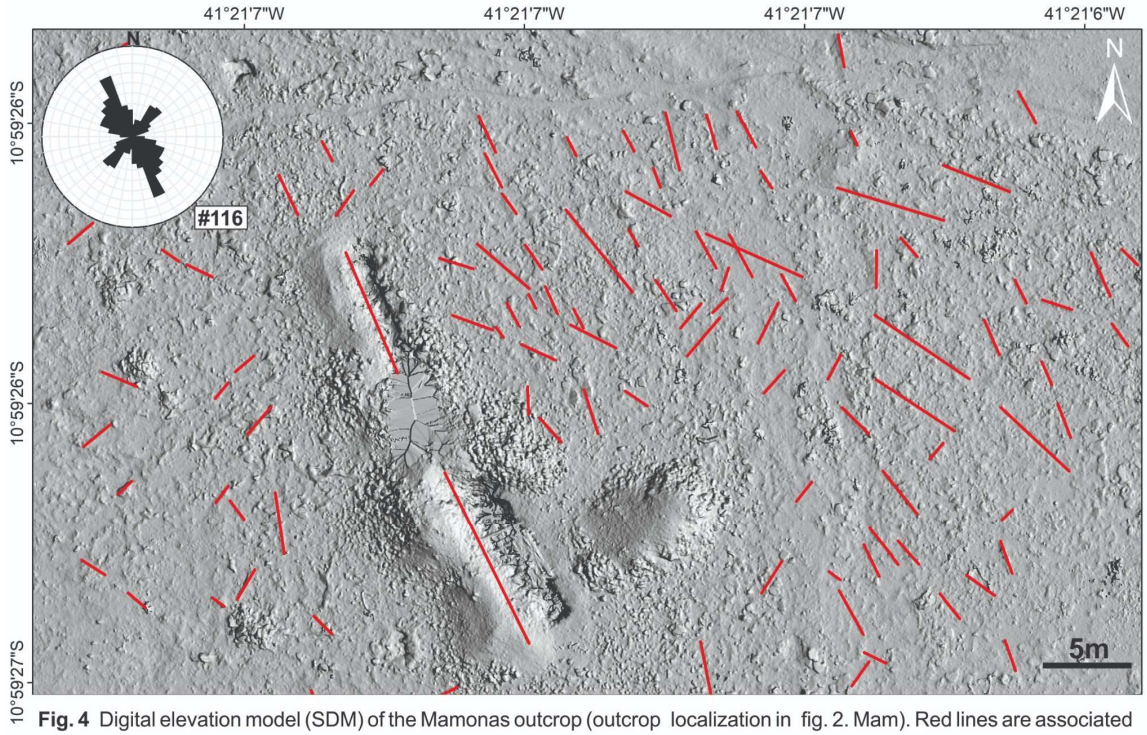

Fig. 4 Digital elevation model (SDM) of the Mamonas outcrop (outcrop localization in fig. 2. Mam). Red lines are associated to the identified structural lineaments reported also in the rose diagramm.

The III order lineaments exhibit a singular magnetic pattern, distinguished by striking high-amplitude magnetic lineaments with the extension of dozens of kilometers (Figs. 3A, B). They occur isolated or comprising sets with main NW-SE and minor NE-SW orientations. Sometimes, they are stepwise segmented (en echelon) and shifted by hundreds of meters. They truncate other magnetic lineaments in high to moderate angles, indicating a more recent geological event. Due to high magnetization contrast with bedrocks, linear and extensive waveform, and sparse spatial distribution, we associate these magnetic lineaments with mafic dikes as many authors elsewhere (e.g., Schwarz et al., 1987; Demarco et al., 2020). In fact, the NNW-SSE trending Chapada Diamantina mafic dike swarm is intrusive into the Mesoproterozoic sedimentary sequences of the Espinhaço Supergroup within the Paramirim Aulacogen (Brito, 2008; Silveira et al., 2013). The magnetite-bearing dikes are fine to medium-grained diabases. Recently Pessano

et al. (2021) associated NW-SE oriented magnetic anomalies in the central portion of the São Francisco Craton with Mesoproterozoic dikes of the Chapada Diamantina swarm.

4.2 - Hydrothermal vein and breccia characterization

Two main types of structures related to hydrothermal activity occur in the Cafarnaum fault zone and its surroundings. The first type is hydrothermal breccias, which mainly occur in dilational jogs. The second is calcite veins, which are widespread in the fault zone and the host rocks away from the fault. Two sites of hydrothermal breccias occur along N-W-striking extensional faults, which we describe below. In addition, we describe four sites with calcite veins at varying distances from the Cafarnaum fault.

Hydrothermal breccias are characterized by the interaction between rocks and hydrothermal solutions and are geometrically characterized by several parameters, such as morphology, particle size distribution, fabric, and expansion radius (Jébrak, 1997). Chemical and physical mechanisms can form these breccia bodies: the first by selective dissolution and the second by the excess tension exerted, which exceeds the tensile resistance of the material, or in some combination. The analyzed bodies are classified as mosaic breccias that are formed by fluid-assisted breach (hydraulic fracturing) using the classification given by Jebrák (1984b). Carbonate clasts are present, and clasts that are larger than 2 mm range between 60-75% of clasts and 75-100% of clasts.

Hydraulic breccias are rocks composed of angular to subangular fragments of dimensions ranging from 0.4 cm to 5 cm that are cut by several generations of fractures and veins. The fragments are present throughout the breccia bodies and

are derived from adjacent rocks. Generally, they are monolithologic and represented by carbonate rocks corresponding to the Salitre Formation.

Carbonates also contain calcite and quartz geodes surrounded by intense oxidation (limonitization). The interfragmentary filling is composed of iron oxide or quartz and calcite cement. The oxidized matrix is probably formed to replace rich materials in iron from the cementing fluid. Quartz is associated with calcite, galena, and malachite. There is intense veining by a network of veins with a branched structure that range from millimeters to centimeters thick and reach 30% of the total volume, and calcite veins of lesser thickness are related to quartz veins.

The description of carbonates can be compared to descriptions made by Souza et al. (1993), such as the association of intensely closed algal laminites corresponding to the Nova América inferior subunit (transgressive cycle III) at the MEL site, as well as area descriptions by Misi (1975) of fine dolomites with ankerite, barite and galena and light dolomites with millimeter bands, calcite impregnations and microcrystals of pyrite and galena. Nevertheless, occurrences only include sedimentary gaps along the Irecê Basin (Bonfim et al., 1985, and Souza et al., 1993).

The descriptions were made under transmitted light optical microscopy of the samples corresponding to MAM and MEL sites (Fig. 2A, C); the samples were divided into laminated carbonates with veins, laminated carbonates with a brittle aspect, and only the veins. The composition in these three divisions presents the same mineralogy in carbonates and the same mineralogy in the veins, differentiated by laminar and massive textural aspects in the case of carbonate alteration and fragmented textural aspects.

4.3 Mineralogy, texture, and isotope geochemistry

Sites from the central part of the basin (SOR, IRE, and ACH) and the eastern block (FAR) (Fig. 2C) are large carbonate pavements in which primary sedimentary features are observed. Except for the FAR site, these carbonates display vertical bedding and are crosscut by centimetric calcitic veins.

The limestones from the SOR site consist of microbial mats. The beds are oriented subvertically within tight N-S-trending folds (Fig. 2C). Two types of veins are observed at the SOR site. The first type of veins formed on transverse fault planes, which originate in E-W-striking low-angle thrust faults, predating folding to the present-day subvertical position (T16 and T19). The second type forms N-S-trending veins. These veins are associated with younger N-S shortening (T24). Isotope profiles across the veins reveal no significant difference in $\delta^{13}C$ and $\delta\ ^{18}O$ concentration between the carbonate host rock and the transverse fault carbonate filling (Fig. 5).

The FAR site (Fig. 6) consists of stromatolite bioherm colonies. Two veins were analyzed. The first vein (T9) occurs in inter-stromatolite silt crosscut by a sharp-edged 2.2 mm thick vein without signs of shear. It is filled with mosaic, organized, equidimensional transparent calcite varying from 0.05 mm to 0.2 mm. The other vein (T10) crosscuts a stromatolite unit. It has two different calcite fabrics: an equidimensional mosaic with oriented sparry calcite crystals varying in size from 0.1 to 1 mm and a milky white area with no calcite crystals. Most calcite

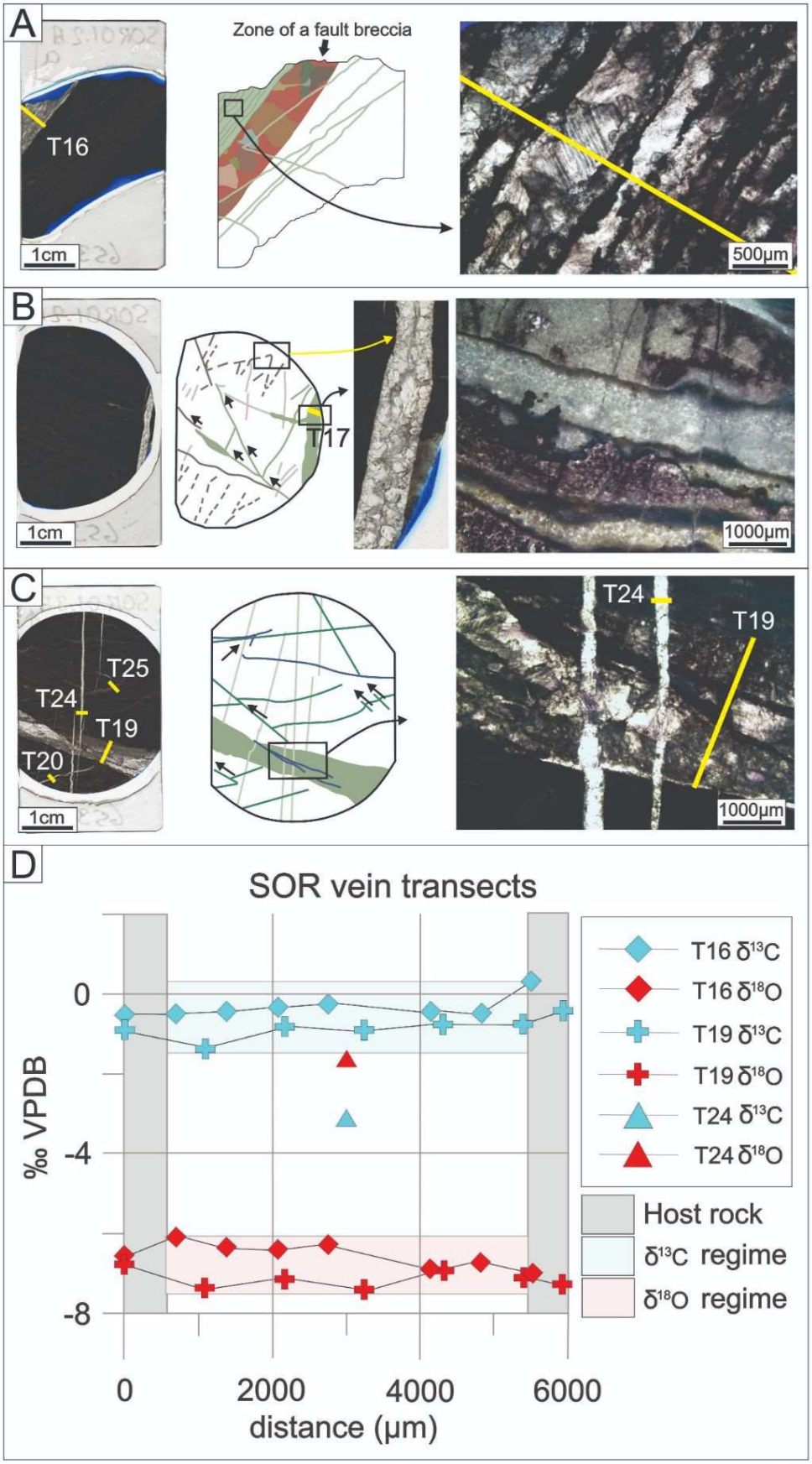

Figure 5. A) On the left, thick section SOR01.2Aa. On the center graphical representation of SOR01.2Aa with veins in green and fault breccia in multicolor. On the right, zoom in on sheeted character of vein T16. B) On the left, thick sections SOR01.2Ab. On the center graphical representation of SOR01.2Ab. On the right zoom in on bedding parallel stylolites and NNE-SSW fractures. C) On the left, thick section SOR01.3Aa. On the center Micro map of all present features. On the right, crosscutting of transverse fault T19 and N-S vein T24. D) Stable isotope transects of T16,T19 and T24.

veins from the FAR site display lower $\delta^{13}C$ and $\delta^{18}O$ values than the stromatolite host rock. Exceptions are a few carbonate samples from the vein that crosscut the inter-stromatolite silt (Fig. 6).

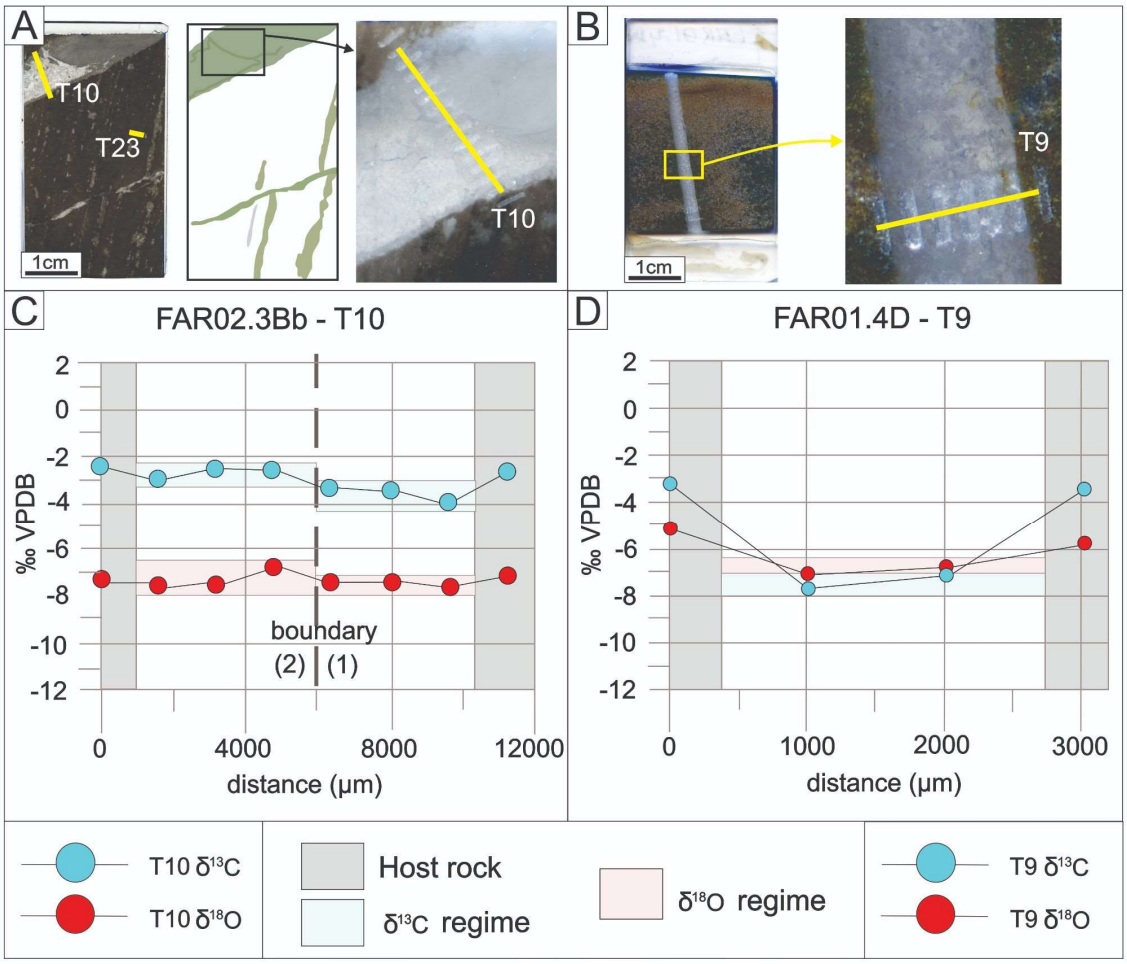

Fig. 6 A) On the left, thick section FAR02.3Bb. On the center, graphic representation of thick section. On the left, zoom in on transect T10 across two calcite phases including crystallization. B) Thick section FAR014D, and zoom in on vein T9 with sampling location including crystallization. C) Transect T10. D) Transect T9.

The ACH site consists of subvertical to NNW-dipping (average bedding plunge ranging from 76 to 358) dolostones. The present-day NNE-SSW burial fault carries most veins and is more prominent than its conjugate NW-SE counterpart (Fig. 7). Veins at the ACH site lack signs of shear and are syntaxially filled with blocky crystals. In addition to veins, the ACH site contains a pocket filled with crystal precipitates (T4) in which borders are vein wall remnants and dissolved host rock peloids (Fig. 7). Since these pockets dissolve burial-related fractures and

faults, they formed later than the burial fault set. In general, ACH samples show a higher porosity than other sites. Isotope data across these veins reveal much lower $\delta^{13}C$ and $\delta^{18}O$ values than the isotope values of the host rock (Fig. 7).

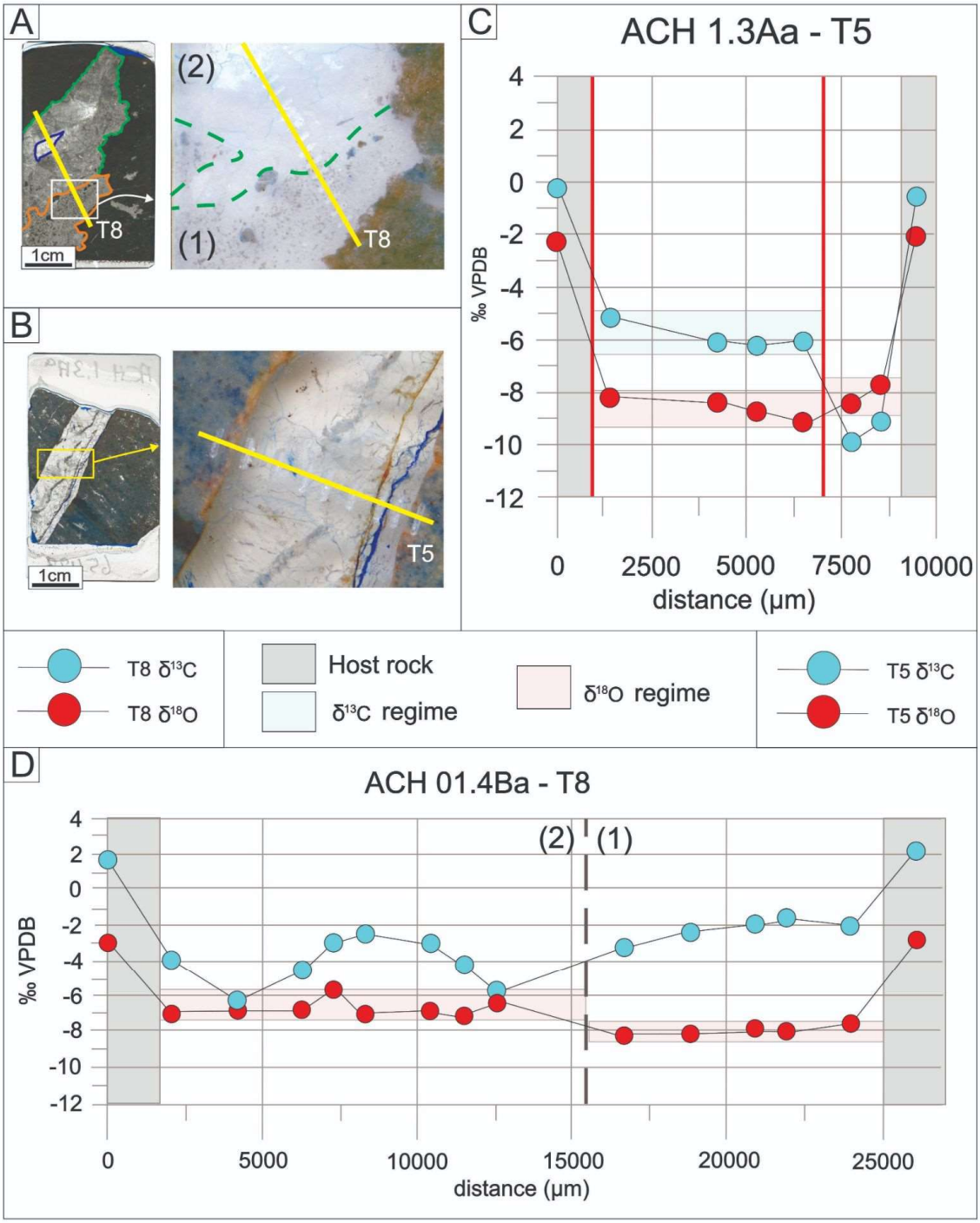

Fig. 7 A) Thick section ACH01.4Ba with T8 location and two zones and, zoom in on zone boundary between (1) no host rock remnants and (2) with host rock remnants B) Thick section ACH01.3Aa and, zoom in on transect T5. C) Transect T5. The red lines mark a change in $\delta^{13}C_{VPDB}$ and a new growth plane. D) Stable isotope transect of T8. Note the difference in $\delta^{18}O$.

Carbonate rocks of the IRE site consist of thinly layered (0.2-20 cm) black limestones with local slumps. The beds are tilted vertically and folded around an axial plane with an orientation of 355/86. Two types of veins are present (Fig. 8): thinner (<1 cm) bedding-perpendicular and bedding-parallel pre- or synfolding veins and thick veins (20 cm) filled with a mixture of calcite and barite that irregularly crosscut folded bedding. They are syn- or post-folding veins. Similar to the SOR site veins, IRE veins have isotope values similar to the host rock (Fig. 8).

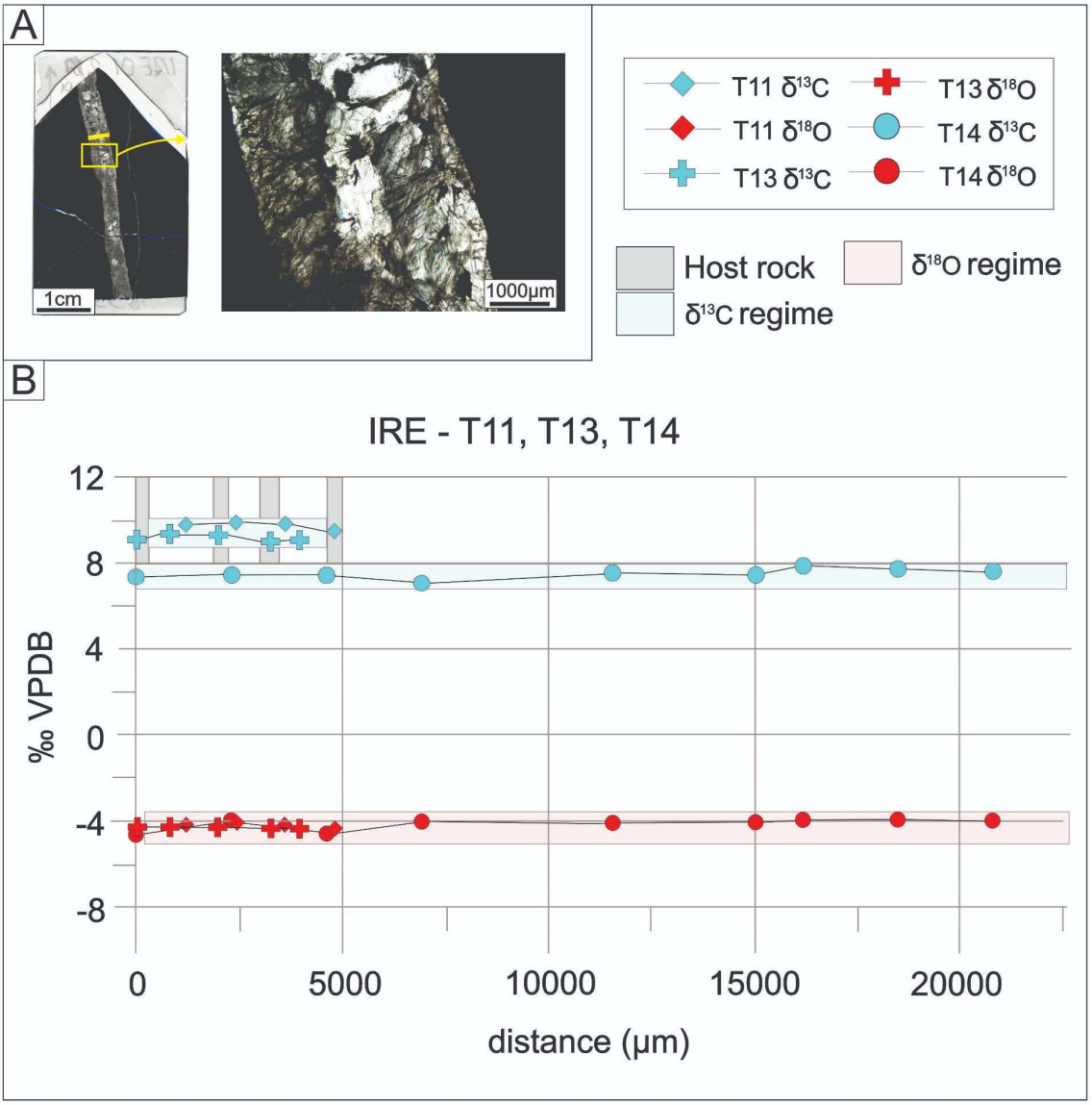

Fig. 8 A) Thick section IRE01.2Aa. and, zoom in on vein infill with needle shaped aragonite remnants. B) Stable isotope transects of vein T11, T13 and T14 from IRE. Host rock and vein infill have an almost identical isotope composition.

In contrast to sites in the central part of the basin, sites at the basin edges (i.e., MEL and MAM) are strongly deformed and exhibit pervasive hydrothermal features and hydraulic hydrothermal breccias (Fig. 9A-C). Samples from the MEL site are mostly breccias with white calcite cement. Previous studies by Misi et al. (2005) argue that the Salitre Formation stratigraphy controls the Pb-Zn concentrations. According to these authors, the Pb-Zn ore is associated with silicified stromatolites that overlie a shallowing-upward sequence (Unit B1). The MEL site is located in a flat area where sites are restricted by trenches dug by mining operations. Samples may exhibit primary lamination similar to rocks of the Salitre Formation. These features are obliterated by tectonic and hydrothermal processes toward the center of the brecciated zone at the outcrop scale (Fig. 9A). Clasts of primary carbonate rocks may also occur in the hydrothermal breccia cemented by white calcite devoid of laminations (Fig. 9B). Secondary vugular-type porosity that is less than 1% in the area is also observed under the microscope. The limestones and breccias are crosscut by two generations of veins: one measuring 4 mm thick and made of calcite and quartz microcrystals and a second measuring approximately 0.3 mm thick and made of quartz. The host carbonate and the cement display quite distinct mineralogy. The primary Salitre carbonates consist mainly of calcite, dolomite, ankerite, siderite, iron oxide, and limonite. SEM, XRD, and QUEMSCAN data indicate that the veins and hydrothermal breccias display complex mineralogy, where the main minerals are calcite, dolomite, galena, barite, quartz, sphalerite, illite, chlorite, zincite, cerussite, malachite, magnesite, apatite, and chalcedony. Barite, apatite, chlorite, and quartz are concentrated along fracture zones (Fig. 10A-D) and, in some instances, may form larger aggregates. Thin section observations indicate that tectonic and hydrothermal processes were accompanied by the formation of stylolites,

dolomitization, silicification, limonitization, microfractures, folding, and minerals with wavy extinction.

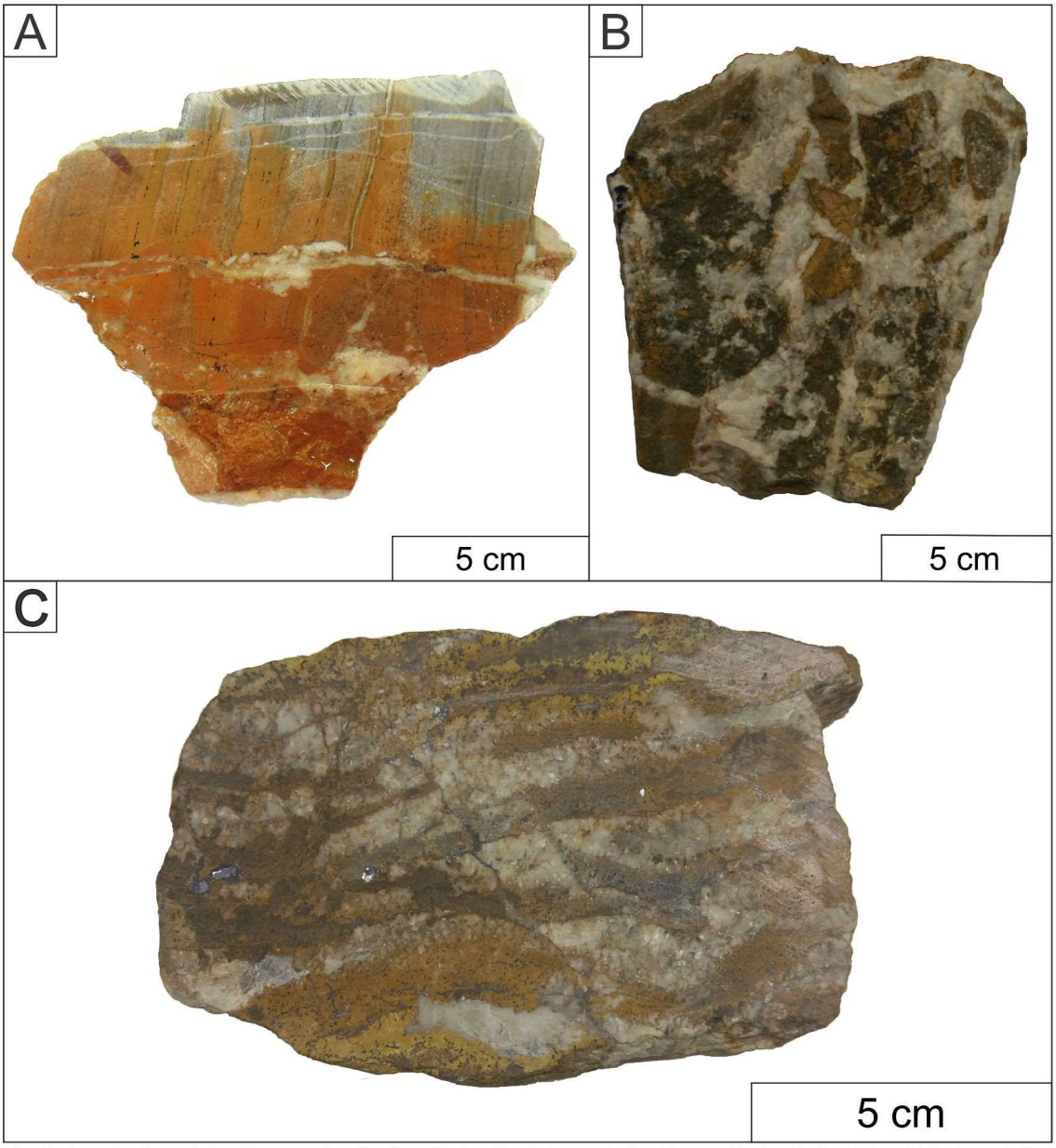

Fig. 9 Samples from Melancias area showing the effects of hydrothermal alteration and hydraulic fracturing. A) Carbonate that shows partially preserved primary features grading to a brecciated zone. In the lower part of the sample, the primary features were obliterated by the hydrothermal alteration. B)Vein of carbonate by sucessive precipitation of carbonate and Fe-rich zones. C) Hydralic breccia with clasts of the primary carbonate.

Figs. 10A and B at the MEL site display different facies of carbonate breccia and isotope $\delta^{13}C$ and $\delta^{18}O$ analyses performed at specific points in the samples. While the $\delta^{13}C$ values range between 0.22‰ and -2.24‰, the $\delta^{18}O$ values vary from -6.16‰ to -12.67‰. In most instances, the primary limestone fabric was

replaced by milky carbonate with large anhedral crystals. The sample in Fig. 9C displays a cyclic succession of milky calcite and iron-rich dolomite crosscut by veins containing galena. High-resolution $\delta^{13}C$ and $\delta^{18}O$ data indicate that these samples may have an area with homogenous isotope values (Fig. 10A-B), as well as areas with variable isotope values.

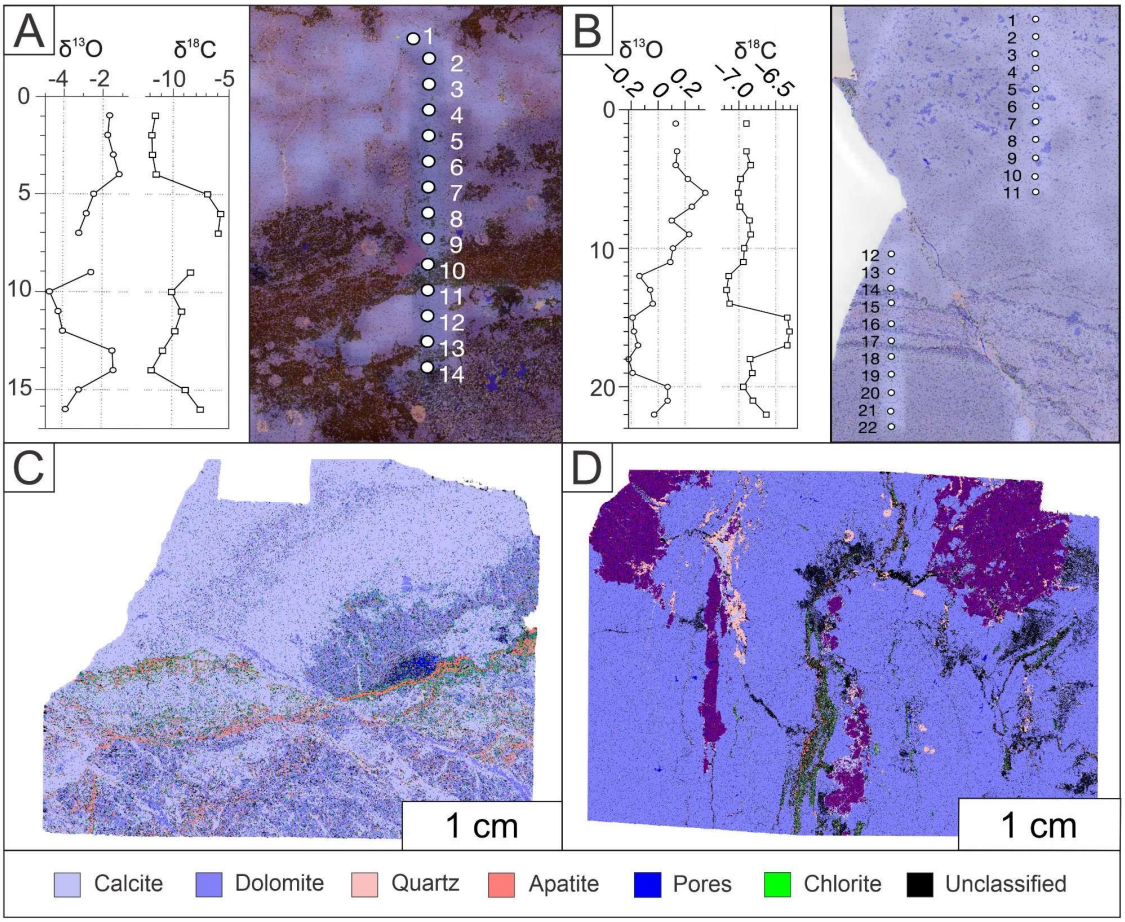

Fig.10 QemScan and isotope data on sellected samples from Melancias. A) and B) Thin section from Melancias in which calcite is the main mineral. The diagram also presents $\delta^{13}C$ and $\delta^{18}O$ across profiles. C) and D) QemScan image of samples from Melancias showing the hydrothermal mineralogy made of barite, quartz, illite, and chlorite. Note that these mineras concentrate along fractures.

The MAM site is also located in a flat area in which sites are restricted to trenches of the mining operation. Centimetric veins of milky quartz occur in the carbonate host unit. As at the MEL site, XRD and SEM data at the MAM site indicate galena, zincite, ankerite, dolomite, cerussite, apatite, magnesite, anglesite, chlorite, and illite. However, in contrast to the MEL site, the MAM site

exhibits strong silicification that may completely obliterate the primary carbonate texture. For instance, the QUEMSCAN images shown in Fig. 11 exhibit carbonate breccias replaced by silica in which ghost clasts can still be identified. Pores and laminated illite and chlorite areas indicate that silica-rich fluids replaced mostly carbonate minerals.

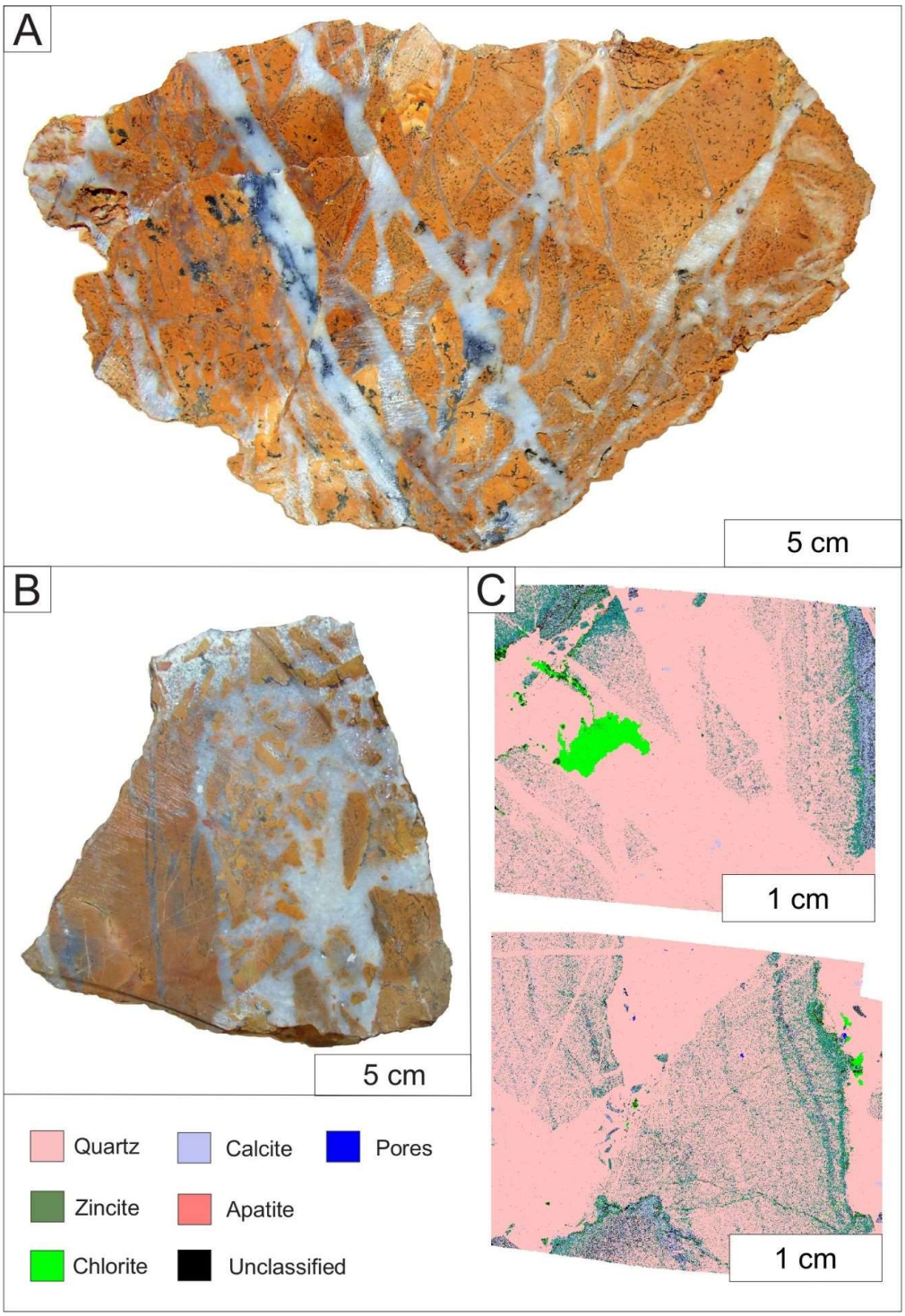

Fig.11 Samples from the Manonas site. A-B: silicified hydrothermal from the Mamonas sites. The primary carbonate was replaced by a yellowish silica that is crosscut by white quartz. C-D: QemScam image of Mamonas samples showing ghosts of the primary carbonates replaced by quartz, illite and chlorite. Same color chart as in Figure 10.

4.4 - Fluid inclusions

Table 01 presents the H and O isotopic compositions of fluid inclusions for 10 samples from the ACH, IRE, and SOR sites in the Irecê Basin and at the FAR site in the eastern block of the Cafarnaum fault. The supplemented materials detail

linearity and memory effect corrections applied to the H and O fluid isotope data. Table 01 also shows the average $\delta^{18}O$ isotopic composition of the carbonate associated with the fluid inclusions and the calculated temperature based on the isotope fractionation between calcite and water. The calculated temperature range is 40-74°C, with the highest values obtained in samples from the ACH and FAR sites.

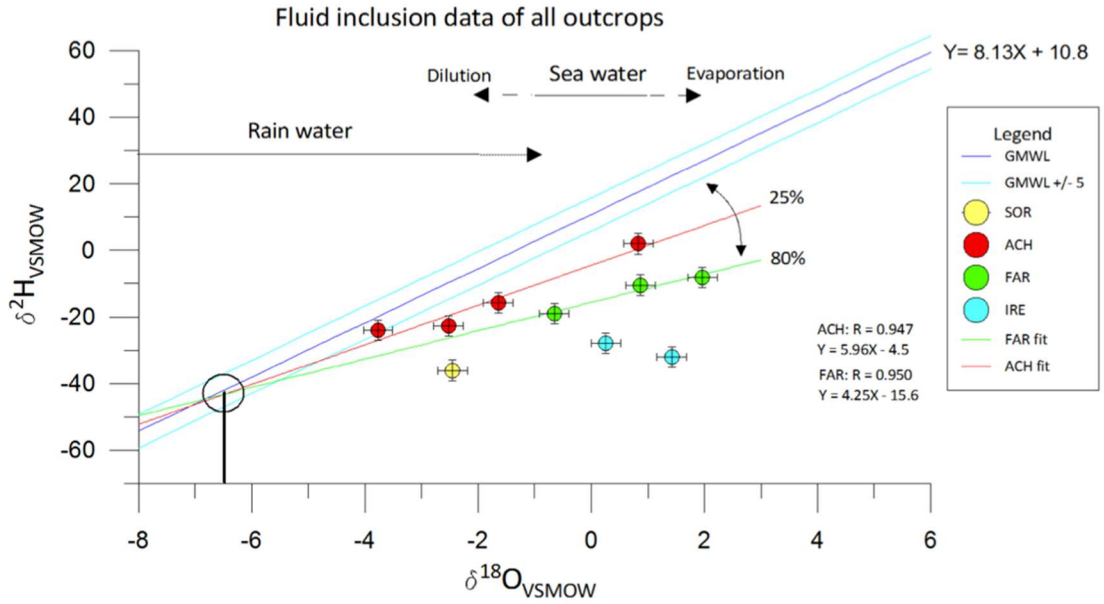

Fig. 12 Fluid inclusion data GMWL based on Rozanski et al. (1993). Regions of marine and meteoric waters based on Moore (1989). Sample plot in both meteoric and marine domain. Trend lines of ACH and FAR cross the GMWL on the same point (~-6.5‰ for $\delta^{18}O_{VSMOW}$;-45‰ for δD_{VSMOW}).

Except for one sample from the ACH site (ACH01.3Aa T5-1, left), all samples display negative δD_{SMOW} values. Fig. 12 plots the H and O isotope values with the global meteoric water line (GMWL) by Rozanski et al. (1993) and shows that the trending lines of samples from the ACH and FAR sites converge to a δD value of approximately -45‰ and a $\delta^{18}O$ value of -6.5‰.

Table 1: Isotopic composition of carbonates from central part of the basin. IRE; ACH; SOR; FAR. V refers to vein, HR to host-rock, and BREC to breccia.

Achado - ACH				Fazenda Arrecife - FAR				Irecê - IRE				Soares - SOR			
Sample	$\delta^{13}C$	$\delta^{18}O$	V/HR	Sample	$\delta^{13}C$	$\delta^{18}O$	V/HR	Sample	$\delta^{13}C$	$\delta^{18}O$	V/HR	Sample	$\delta^{13}C$	$\delta^{18}O$	V/HR
T3	0.1	-5.6	HR	T9.1	-3.2	-5.2	HR	T11.3	9.8	-4.2	V	T16.1	-0.9	-6.8	HR
T3.2	-4.5	-8.2	V	T9.3	-7.7	-7.1	V	T11.5	9.9	-4.1	V	T16.3	-1.4	-7.4	V
T3.3	-5.2	-7.5	V	T9.5	-7.2	-6.8	V	T11.7	9.8	-4.2	V	T16.5	-0.8	-7.1	V
T3.4	-5.6	-8.7	V	T9.7	-3.4	-5.8	HR	T11.9	9.5	-4.4	HR	T16.7	-0.9	-7.4	V
T3.5	-4.6	-8.6	V	T10.1	-2.5	-7.4	HR	T13.1	9.2	-4.3	HR	T16.9	-0.7	-6.9	V
T3.6	0.1	-5.8	V	T10.3	-3.0	-7.6	V	T13.2	9.4	-4.3	V	T16.11	-0.8	-7.1	V
T4.1	-0.3	-5.2	HR	T10.5	-2.6	-7.6	V	T13.3	9.3	-4.3	HR	T16.12	-0.4	-7.3	HR
T4.2	-0.3	-6.4	HR	T10.7	-2.6	-6.9	V	T13.4	9.0	-4.3	HR	T17.1	0.4	-7.1	V
T4.3	-3.9	-7.2	HR	T10.9	-3.4	-7.5	V	T13.5	9.1	-4.4	V	T17.3	-2.4	-8.2	V
T4.4	-3.4	-7.5	HR	T10.11	-3.5	-7.5	V	T14.1	7.3	-4.6	V	T17.5	-0.1	-6.2	V
T4.5	-0.3	-10.9	V	T10.13	-4.0	-7.7	V	T14.3	7.5	-4.0	V	T19.1	-0.5	-6.6	HR
T4.6	0.4	-10.0	V	T10.15	-2.7	-7.2	HR	T14.5	7.5	-4.6	V	T19.2	-0.5	-6.1	V
T4.7	-0.8	-9.0	V					T14.7	7.1	-4.0	V	T19.3	-0.4	-6.4	V
T4.8	-0.4	-11.7	V					T14.9	6.1	-4.7	V	T19.4	-0.3	-6.4	V
T4.9	0.5	-10.4	V					T14.11	7.6	-4.1	V	T19.5	-0.3	-6.3	V
T4.10	0.3	-10.3	V					T14.13	5.2	-5.0	V	T19.7	-0.5	-6.9	V
T4.12	0.3	-10.0	V					T14.14	7.5	-4.1	V	T19.8	-0.5	-6.7	V
T4.13	0.6	-8.2	V					T14.15	7.9	-4.0	V	T19.9	0.3	-7.0	HR
T5.1	-0.3	-2.3	HR					T14.17	7.7	-3.9	V	T24.1	-3.1	-1.6	V
T5.2	-5.1	-8.2	V					T14.19	7.7	-4.0	V				
T5.4	-6.1	-8.4	V					T12.1	8.7	-4.5					
T5.5	-6.2	-8.7	V												
T5.6	-6.1	-9.1	V												
T5.7	-9.9	-8.4	V												
T5.8	-9.1	-7.7	V												
T5.9	-0.6	-2.1	HR												
T6.1	2.2	-2.6	HR												
T6.2	-4.7	-8.4	V												
T6.3	-5.1	-8.6	V												
T6.5	-2.7	-7.0	BREC												
T6.6	1.2	-3.0	BREC												
T6.7	-2.4	-7.1	BREC												
T6.8	2.2	-2.4	BREC												
T8.1	1.6	-3.0	HR												
T8.3	-4.0	-7.0	V												
T8.5	-6.3	-6.8	V												
T8.7	-4.6	-6.8	V												
T8.8	-3.0	-5.7	V												
T8.9	-2.5	-7.1	V												
T8.11	-3.0	-6.9	V												
T8.12	-4.2	-7.1	V												
T8.13	-5.7	-6.4	V												
T8.17	-3.2	-8.3	V												
T8.19	-2.4	-8.2	V												
T8.21	-1.9	-7.9	V												
T8.22	-1.5	-8.0	V												
T8.24	-2.0	-7.6	V												
T8.26	2.1	-2.8	HR												

5. Discussion

5.1 – Fault evolution and hydrothermal fluids

Cratons are composed of thick and cool lithospheric keels with high resistivities and low porosities (e.g., Ferguson et al., 2012; Selway, 2014). However, several studies have increasingly indicated that cratons present low-resistivity zones in the lithosphere that behave as weakness zones prone to deformation, such as ductile shear zones and faults (e.g., Pinto et al., 2010; Thiel and Heinson, 2013; Dong et al., 2015). These shear zones/faults provide a high permeability and are pathways

for deep-seated fluids to ascend through the whole lithosphere (Caine et al., 2010; Bense et al., 2013). The study of hydrothermal fluids in fault zones in cratons may explain the permeability of fault zones and host units and deep geothermal exploration constraints (Taillefer et al., 2017). In the São Francisco Craton, Brazil, several faults and shear zones form vertical lithospheric conductors, some of which serve as suture zones in the Proterozoic. They are related to suture zones in collisional tectonic settings and lithospheric extension processes and form boundaries between crustal blocks (e.g., Teixeira et al., 2017; Padilha et al., 2017). The boundary between the Irecê Basin and the Chapada Diamantina Group is marked by the Cafarnaum fault (Figs. 1, 2), which coincides with a high conductor mapped by a magnetotelluric survey (Fig. 13). This zone was prone to hydrothermal activity and is consistent with high porosity-permeability, high-fluid salinity, and sulfide emplacement. In a few cases, it served as a conduit for mafic volcanism (Teixeira et al., 2017; Padilha et al. 2019).

Fluid dynamics along fault zones increase and decrease crustal permeability. Faults behave as high permeability conduits that facilitate fluid flow in the Earth's crust (Cox and Munroe, 2016). Deep-seated hydrothermal fluids precipitate minerals that form veins and breccias and decrease the permeability of the lithospheric fault zones (Sibson et al., 1988). The precipitation of hydrothermal minerals in fault zones and host rocks is caused by decompression and cooler conditions (Calvin et al., 2015). Therefore, based on the characteristics presented here, the Cafarnaum fault was a structure prone to hydrothermal activity. It controlled the upward hot fluid flow, indicated by the relationship between fault geometry and hydrothermal deposits (Fig. 13).

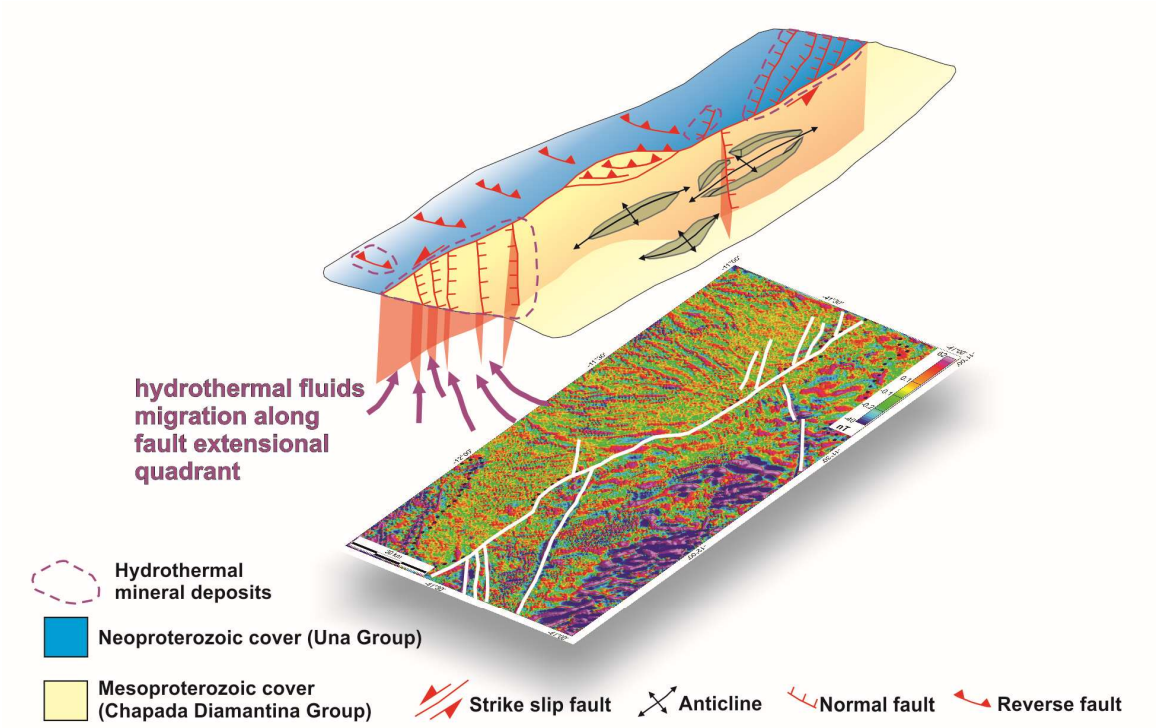

Fig. 13 Conceptual model proposed for the study area. Cartoon displaying the current regional scale configuration and the connection with the deep magnetic lineaments.

Hydrothermal activity occurs in faults in all kinds of settings with suprahydrostatic pressure gradients, where hydrothermal fluids are accommodated along seismically active faults (Sibson, 1990). Hydrothermal fluids channelized along faults can affect thousands of square kilometers, even in non magmatic settings (Nabavi et al., 2020). The hydrothermal activity in faults with shallow crustal levels under fluid overpressure is controlled by the geometry of the crustal-scale fault zone (Bellot, 2008). Dilational jogs flanking continental-scale strike-slip faults, for example, are locations prone to hydrothermal boiling and implosive brecciation (Sibson, 1987). Active examples of hydrothermal activity in dilational jogs occur in compressional settings such as New Zealand (Brathwaite et al., 1986 in 24) and the French Pyrenees (Taillefer et al., 2017).

We interpret the N-W-striking faults that arrest against the main N-S-trending Cafarnaum fault as dilational jogs that facilitate hydrothermal fluid ascension and flow (Fig. 13). Hydrothermal minerals are concentrated in dilational jogs that occur on both sides flanking the Cafarnaum fault, either on carbonate units in the western block or mainly on siliciclastic units in the eastern block (Fig. 2). This indicates that the structure, rather than the lithology, controls the fluid flow along the fault.

Hydrothermal breccias occur in dilational jogs on both sides of the main Cafarnaum fault (Fig. 2A, C). These breccias form when fluid migration becomes explosive (e.g., Jébrak, 1997). Subsequent precipitation of hydrothermal minerals forms breccias and heals the fault, decreasing their permeability (Katz et al., 2006; Taillefer et al., 2017). Fluid flow and subsequent precipitation have been interpreted with the seismic cycle and fault-valve behavior, influencing breccia occurrence (Taillefer et al., 2017).

Hydrothermal fluid flow should have been recurrent in the Proterozoic in the São Francisco Craton (Trindade et al., 2004); the main stage of hydrothermal flow is closely linked to the timing of fault movement. Several studies (Trindade et al., 2004) in the São Francisco Craton have described the relationships between hydrothermal and fault geometries. Previous studies and this new data indicate that a phase of normal-sense dip-parallel slip related to rifting that generated the Irecê Basin was succeeded by a phase of strike-parallel slip reactivation (D'Angelo et al., 2019). The same type of vein occurs in the basement (Mapa Geológico do Estado da Bahia-CBPM/CPRM, 2003), suggesting that these fluid pathways migrated through fractures and faults in the Paleoproterozoic crystalline basement and overlying sedimentary units.

5.2 – Geochemistry of hydrothermal fluids, fluid pathways and tectonics

Fluid flow in the crust is a powerful mechanism to remobilize chemical elements and concentrate metals of economic interest (Heinrich and Candela, 2014, Yardley and Bodnar, 2014). It may also be an essential mechanism to transfer heat between, for instance, deep and shallow crustal levels. Both chemical and thermal transfers depend on how efficient conduits allow fluid to migrate from deep to shallow crustal levels. The efficiency of heat transfer and chemical remobilization also depends on heat and chemical gradients, fluid-rock interactions, and tectonic settings. Many studies have addressed the question of how deep fluid penetrates the crust (e.g., Nesbitt and Muehlenbachs, 1989; Fricke, Wickham et al., 1992; Haines, Lynch et al., 2016). Most authors agree that fluid may penetrate as deep as 10 to 15 km into the crust, mainly in crystalline terrains submitted to an extensional tectonic regime. The isotope data presented here show that fluid sources in the central part and at the Irecê Basin edges had the same origin but underwent distinct pathways. The new data presented in this study allow a discussion of the source of these fluids, their primary isotopic composition, their interaction with the sedimentary rocks on both sides of the Cafarnaum fault, and how deep they may have penetrated each kind of terrain.

Different generations of carbonate veins and breccias crosscut the sedimentary rocks of the Irecê Basin. Figs. 5 to 8 show that carbonate veins from the central part of the basin do not display significant carbon and oxygen isotope differences relative to the carbonate host rock. More significant isotopic differences occur in samples from the ACH and FAR sites, where the veins present more negative isotopic values than the host rock (Fig. 6). Data in this study suggest that

the $\delta^{18}O$ value of the carbonate veins may be explained by a meteoric fluid source (Fig. 14), by a higher temperature of crystallization (Table 02) of these carbonates, or by the combination of both processes. The oxygen isotope fractionation between calcite and water varies from 28‰ to 7‰ in the temperature range of 25-250°C (Chacko et al. 1991; Kim, O'Neil et al., 2007; Chacko and Deines, 2008). In contrast, the low $\delta^{13}C$ values observed in the carbonate may only be explained by an external source of carbon, since the carbon isotope fractionation values between calcite and HCO_3^- and calcite and CO_2 are much less than 4‰ at temperatures below 200°C (Deines et al., 1974; Chacko et al., 1991; Chacko and Deines 2008). Samples from the MEL site, which are located at the edge of the basin, display even more negative oxygen isotope values. As shown in Fig. 14A, isotope data from this site display a narrow range of $\delta^{13}C$ values and a wide range of $\delta^{18}O$ values. Compared to the veins from the central part of the Irecê Basin, the lower $\delta^{18}O$ values of their carbonates indicate interactions with more ^{18}O-depleted fluids or higher crystallization temperatures.

Fig. 14B compares the isotopic composition of the carbonates studied here with previous isotope data reported for the same area. The diagram shows that the data in this study have a wide range of $\delta^{18}O$ (-13.0‰ to 1.8‰) and $\delta^{13}C$ (-10‰ to 10‰) values. However, most of our samples have a narrower range of $\delta^{13}C$ (-5‰ to 1‰). The exceptions are samples from the IRE site that exhibit higher $\delta^{13}C$ values and a few samples from the ACH, FAR, and SOR sites that present $\delta^{13}C$ values below -5‰. Samples from the IRE site are associated with ^{13}C-enriched carbonates from the upper section of the Irecê Basin and plotted as squares in Fig. 14. These primary high $\delta^{13}C$ carbonates have been reported in both the Irecê Basin (Misi 1988, Misi and Kyle 1994, Borges, Balsamo et al. 2016, Caird, Pufahl et al.

2017) and other Neoproterozoic basins (Santos, Alvarenga et al. 2000). Carbonate veins with $\delta^{13}C$ values below -5‰ are probably related to the same fluid that is responsible for the carbonates that formed the calcretes previously described in the basin (Borges, Balsamo et al. 2016, Caird, Pufahl et al. 2017). Published isotope data of these carbonates, plotted as "stars" in Fig. 14B, also presents low $\delta^{13}C$ values.

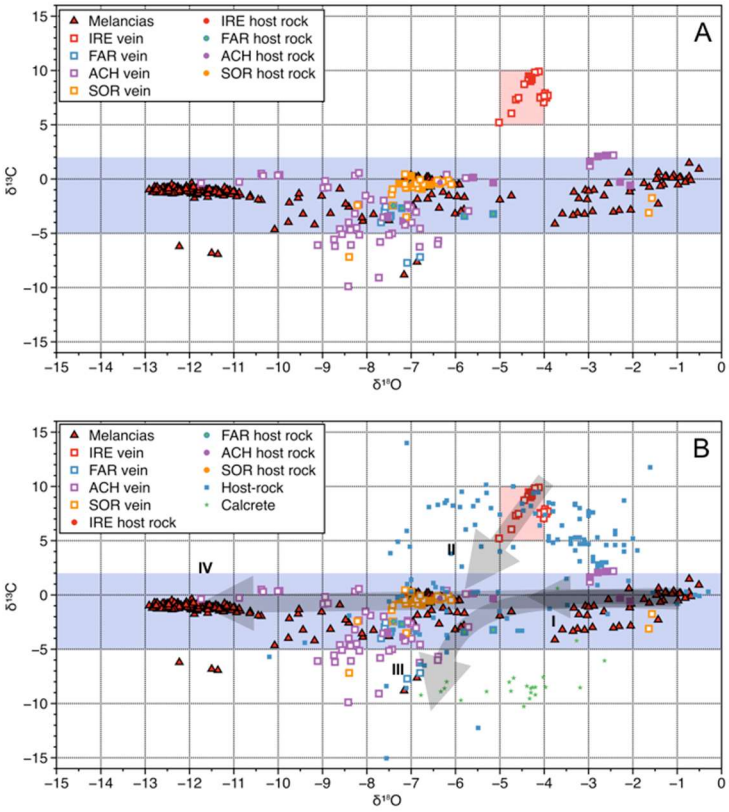

Fig. 14A. Carbon and oxygen isotopes of samples from the central part of the basin (IRE, FAR, ACH, and SOR) and samples from the Melancias outcrop; **B.** Our data compared to other published isotope data from the basin. Figure B also shows different scenarios of isotope evolution: I. Interaction between meteoric fluid and carbonates of the lower stratigraphic section; II. Interaction between meteoric fluid and carbonates of the upper stratigraphic section; III. Low d13C carbonates related to the same fluids responsible for calcrete formation in the area; IV. Carbonates formed by high-temperature fluids that interacted with deep-crustal levels. Host-rock data (Misi and Kyle, 1994; Misi and Veizer, 1998; Borges et al., 2016; Caird et al., 2017); Calcrete data (Borges et al., 2016; Caird et al., 2017)

The source of fluids related to the carbonate veins from the central part of the Irecê Basin may be further constrained by the isotopic composition of fluid inclusions trapped in the carbonate veins. Based on the oxygen isotopic

composition of these fluid inclusions and the associated carbonate, we estimate the temperature of carbonate crystallization to be between 39 and 67°C (Table 02). These temperature estimates were based on Kim and O'Neil (1997) oxygen isotope fractionation equation between calcite and water. Since calcite and fluid-inclusions may be affected by post-entrapment isotope exchange during exhumation (Nooitgedacht et al., 2021), these results should indicate minimum temperature conditions. Assuming an average thermal gradient of 30 C/km, these fluids circulated at depths reaching 1000 m within the crust. Fig. 11 displays the mean global meteoric water line by Rozanski et al. (1993) and the hydrogen and oxygen isotope values of these fluid inclusions. It also shows trending lines for fluid inclusions from the ACH and FAR sites, indicating that they converge to a δD value near -45‰ and a $\delta^{18}O$ value near -6.5‰ along the mean meteoric water line (Fig. 12). We argue that these isotopic values represent the local meteoric water, which upon interaction with the host rock changed its isotopic composition along the mixing lines. A similar process has been described in active hydrothermal systems (Criss and Taylor Jr, 1986), in which there is also a more extensive range of $\delta^{18}O$ values compared to δD values. This happens because water-rich fluids interact with oxygen-rich and hydrogen-poor rocks, promoting a more significant effect on the oxygen values.

Assuming the above values for the meteoric water that percolated rocks of the Irecê Basin, the isotopic variation observed in Fig. 14B may be explained by different geological scenarios. Arrows I and II represent veins formed by mixing meteoric fluids and carbonate host rocks of the inner part of the basin at low-temperature conditions (between 30 and 40°C). Arrow I indicates mixing between these fluids and carbonates from the lower section. In contrast, arrow II represents

the mixing between these fluids and the ^{13}C-enriched carbonates from the upper section. Arrow III represents carbonates formed by the same fluids as those of the calcretes, which have more negative $\delta^{13}C$ values. Samples from the MEL site, represented by arrow IV, fall within the same range of $\delta^{13}C$ values for most samples from the central part of the basin. However, they also have more negative $\delta^{18}O$ values, indicating that isotope exchange between the meteoric fluids and carbonates alone may not be reconciled with the observed data. We argue that carbonate from the MEL site crystallized from the same meteoric fluid but at higher temperatures. These fluids percolated through conduits that allowed them to reach deeper parts of the crust and return to shallow crustal levels without losing much heat. The emplacement of these carbonates along regional extensional fracture zones supports this interpretation. Compared to thrust systems alone, thrust followed by strike-slip and extensional faulting may provide deep fluid conduits. Based on hydrogen isotopes, Nesbitt and Muehlenbachs (1989) concluded that the tectonic regime might drastically control the depth of fluid interaction in the crust. This interpretation also agrees with previous studies based on fluid inclusions and sulfur isotope geothermometry performed in the MEL site area (Misi and Kyle 1994, Misi, Iyer et al. 1999, Misi, Iyer et al. 2005), which indicates that these rocks were formed at temperatures as high as 250°C. Fluid-rock interactions may also explain the presence of base metals in these high-temperature veins, suggesting that these chemical elements were scavenged from deeper crustal levels. Among the sites from the central part of the basin, only the ACH site exhibits isotope values comparable to those observed at the MEL site. They indicate that higher-temperature fluid percolation in the central part of the basin was very limited and restricted to conduits associated with hydrothermal breccias.

Table 2: Isotope data from fluid inclusions of carbonates from the central part of the basin. The temperature was calculated based on the oxygen isotopic composition of calcite and fluid, according to Kim & O'Neil (1997).

Sample	Location	Fluid δD_{SMOW}	Fluid $\delta^{18}O_{SMOW}$	Calcite $\delta^{18}O_{PDB}$	Calcite $\delta^{18}O_{SMOW}$	T in C
ACH01.2Bb T4-1	ACH	-22.7	-2.5	-7.4	23.3	39
ACH01.2Bb T4-2	ACH	-24.0	-3.8	-10.1	20.5	47
ACH01.3Aa T5-1 (left)	ACH	1.9	0.8	-8.6	22.1	66
ACH01.4BaT8-1 (grey)	ACH	-15.7	-1.6	-8.0	22.7	48
IRE01.2Aa T11	IRE	-32.0	1.4	-4.2	26.6	43
IRE01.3Ba T14	IRE	-27.9	0.3	-4.1	26.6	37
SOR01.3Aa T19	SOR	-36.0	-2.5	-6.5	24.3	35
FAR01.4D T9	FAR	-10.5	0.9	-7.0	23.7	56
FAR02.3Bb T10-1 (milky, right)	FAR	-8.2	2.0	-7.6	23.1	67
FAR02.3Bb T10-2 (transparant, left)	FAR	-19.0	-0.7	-7.5	23.1	51

The role of deep crustal fluids at the MEL and MAM sites is further suggested by the petrographic and mineralogical features observed at these sites (Figs. 9 and 10). In addition to the high concentration of base metals (e.g., Pb, Zn, Fe), these sites display a pervasive replacement of the primary carbonates by silica. Silicification events are recognized as a diagenetic process in which Si-rich fluids affect a host rock, modifying its texture and mineralogy (Menezes et al., 2019). For example, Haldar and Tisljer (2014) documented a silicification process where opal/chalcedony/low-temperature quartz replaces calcite/aragonite/dolomite. Quartz minerals and cement could be ascribed to different sources; for instance, they may be derived from more soluble silica phases (amorphous silica and opal), quartz dissolution by pressure solution, and reactions involving silica release from silicate minerals under low- and high-temperature conditions (Bjorlykke and Egeberg, 1993). The percolation of meteoric fluids at the deep crustal level provided the required conditions to mobilize silica at the MEL and MAM sites.

6. Conclusion

This study in the São Francisco Craton focuses on the hydrothermal activity in the Cafarnaum fault and its host rock and yields the following conclusions. The

São Francisco Craton is a cold and thick block preserved from deformation in the Brasiliano orogeny (740-580 Ma). However, a few tectono-thermal events affected the Craton along its boundary in Neoproterozoic times. One of these events was repeated hydrothermal activity along the Cafarnaum fault, a N-S-striking, 170 km long, strike-slip fault that juxtaposes Neoproterozoic carbonate units and Mesoproterozoic siliciclastic-carbonate units in the northern part of the Craton.

Hydrothermal boiling and implosive brecciation occurred along the fault. Decompression and cooler conditions induced precipitation of hydrothermal minerals in N-W-striking dilational jogs, mainly flanking the northern and southern fault terminations. The hydrothermal fluid structures are composed of hydrothermal breccias close to the main fault zones and along dilational jogs. In addition, calcite veins in the host units away from the fault are also part of the hydrothermal system. Therefore, the geometry of faults at shallow crustal levels influences the location of hydrothermal deposits.

Based on isotopic geochemistry, we show that meteoric water was the main fluid source that percolated the sedimentary rocks of the Irecê Basin and the Cafarnaum fault zone. Fluid inclusions in carbonate veins from the central part of the basin indicate a meteoric fluid with a δD value near -45‰ and a $\delta^{18}O$ value near -6.5‰. Temperature estimates based on the oxygen isotopic fractionation between the carbonate veins from the central part of the basin and the trapped fluid inclusions indicate temperatures ranging between 40 and 70°C. These temperature conditions agree with the lower $\delta^{18}O$ values of veins compared to the carbonate host rock. A similar $\delta^{18}O$ fluid value (-6.5‰) is obtained based on the interaction between these fluids and carbonates from the lower and upper parts of the succession.

In contrast, carbonates at the front edges of the basin associated with the Cafarnaum fault exhibit much lower $\delta^{18}O$ values, indicating higher crystallization temperatures. These carbonates are also associated with base metals and silica-rich fluids, suggesting that the fault behaved as a conduit for deeper fluid circulation in the basement. The mineral paragenesis (e.g., galena, sphalerite, barite, chlorite, illite, and quartz) and brecciated features associated with the veins and fault support this interpretation.

Acknowledgements

This work is part of the first author PhD research work. This work was partially sponsored by Petrobras/UnB/UFRN (CristalDOM Project, coordinated by FHB – UFRN and CLC – Petrobras). We thank the Brazilian Agency of Oil, Gas, and Biofuels (Agência Nacional do Petróleo, Gas e Biocombustíveis, ANP).

References

Alsop, G.I., Weinberger, R., Marco, S., Levi, T., 2020. Bed-parallel slip: Identifying missing displacement in mass transport deposits. J. Struct. Geol. 131. https://doi.org/10.1016/j.jsg.2019.103952

Arancibia, G., Fujita, K., Hoshino, K., Mitchell, T.M., Cembrano, J., Gomila, R., Morata, D., Faulkner, D.R., Rempe, M., 2014. Hydrothermal alteration in an exhumed crustal fault zone: Testing geochemical mobility in the Caleta Coloso Fault, Atacama Fault System, Northern Chile. Tectonophysics 623, 147–168. https://doi.org/10.1016/j.tecto.2014.03.024

Bellot, J.P., 2008. Hydrothermal fluids assisted crustal-scale strike-slip on the Argentat fault zone. Tectonophysics 450, 21–33. https://doi.org/10.1016/j.tecto.2007.12.009

Bense, V.F., Gleeson, T., Loveless, S.E., Bour, O., Scibek, J., 2013. Fault zone hydrogeology. Earth-Science Rev. 127, 171–192. https://doi.org/10.1016/j.earscirev.2013.09.008

BjØrlykke, K., Egeberg, P.K., 1993. Quartz cementation in sedimentary basins. Am. Assoc. Pet. Geol. Bull. 77, 1538–1548. https://doi.org/10.1306/bdff8ee8-1718-11d7-8645000102c1865d

Brito, D.C., 2008. Geologia, Petrografia e Litogeoquímica dos Diques Máficos que ocorrem na porção sudeste da Chapada Diamantina, Bahia, Brasil. Master Degree thesis, Instituto de Geociências, Universidade Federal da Bahia, Brazil, 107p.

Brito Neves, B.B., Fuck, R.A., Pimentel, M.M., 2014. The Brasiliano collage in South America: A review. Brazilian J. Geol. https://doi.org/10.5327/Z2317-4889201400030010

Brito Neves, B.B., Dos Santos, R.A., Da Cruz Campanha, G.A., 2012. A discordância angular e erosiva entre os grupos Chapada Diamantina e Bambuí (Una) na folha Mirangaba-Bahia. Geol. USP - Ser. Cient. 12, 99–114. https://doi.org/10.5327/Z1519-874X2012000200007

Byerlee, J., 1990. Friction, overpressure and fault normal compression. Geophys. Res. Lett. 17, 2109–2112. https://doi.org/10.1029/GL017i012p0210Caine, J.S., Bruhn, R.L., Forster, C.B., 2010. Internal structure, fault rocks, and inferences regarding deformation, fluid flow, and mineralization in the seismogenic Stillwater normal fault, Dixie Valley, Nevada. J. Struct. Geol. 32, 1576–1589. https://doi.org/10.1016/j.jsg.2010.03.004

Calvin, W.M., Littlefield, E.F., Kratt, C., 2015. Remote sensing of geothermal-related minerals for resource exploration in Nevada. Geothermics 53, 517–526. https://doi.org/10.1016/j.geothermics.2014.09.002

Choi, J.H., Edwards, P., Ko, K., Kim, Y.S., 2016. Definition and classification of fault damage zones: A review and a new methodological approach. Earth-Science Rev. https://doi.org/10.1016/j.earscirev.2015.11.006

Choi, J.H., Edwards, P., Ko, K., Kim, Y.S., 2016. Definition and classification of fault damage zones: A review and a new methodological approach. Earth-Science Rev. https://doi.org/10.1016/j.earscirev.2015.11.006

Danderfer Filho, A., Lana, C.C., Nalini Júnior, H.A., Costa, A.F.O., 2015. Constraints on the Statherian evolution of the intraplate rifting in a Paleo-Mesoproterozoic paleocontinent: New stratigraphic and geochronology record from the eastern São Francisco craton. Gondwana Res. 28, 668–688. https://doi.org/10.1016/j.gr.2014.06.012

D'Angelo, T., Barbosa, M.S.C., Danderfer Filho, A., 2019. Basement controls on cover deformation in eastern Chapada Diamantina, northern São Francisco Craton, Brazil: Insights from potential field data. Tectonophysics 772. https://doi.org/10.1016/j.tecto.2019.228231

Demarco, P.N., Masquelin, H., Prezzi, C., Aïfa, T., Muzio, R., Loureiro, J., Peel, E., Campal, N., Sánchez Bettucci, L., 2020. Aeromagnetic patterns in Southern Uruguay: Precambrian-Mesozoic dyke swarms and Mesozoic rifting structural and tectonic evolution. Tectonophysics 789. https://doi.org/10.1016/j.tecto.2020.228373

Dong, Z., Tang, J., Unsworth, M., Chen, X., 2015. Electrical resistivity structure of the upper mantle beneath Northeastern China: Implications for rheology and the mechanism of craton destruction. J. Asian Earth Sci. 100, 115–131. https://doi.org/10.1016/j.jseaes.2015.01.008

Evans, J.P., Chester, F.M., 1995. Fluid–rock interaction and weakening of faults of the San Andreas system: inferences from San Gabriel fault-rock geochemistry and microstructures. Journal of Geophysical Research. 100,13007–13020.

Ferguson, I.J., Jones, A.G., Chave, A.D., 2012. Case histories and geological applications, in: Chave, A.D., Jones, A.G. (Eds.), The Magnetotelluric Method: Theory and Practice. Cambridge University Press, New York, pp. 480–544. https://doi.org/10.1017/CBO9781139020138.012.

Fossen, H., Rotevatn, A., 2016. Fault linkage and relay structures in extensional settings-A review. Earth-Science Rev. https://doi.org/10.1016/j.earscirev.2015.11.014

Gudmundsson, A., Fjeldskaar, I., Brenner, S.L., 2002. Propagation pathways and fluid transport of hydrofractures in jointed and layered rocks in geothermal fields. J. Volcanol. Geotherm. Res. 116, 257–278. https://doi.org/10.1016/S0377-0273(02)00225-1

Gudmundsson, A., 2007. Infrastructure and evolution of ocean-ridge discontinuities in Iceland. J. Geodyn. 43, 6–29. https://doi.org/10.1016/j.jog.2006.09.002

Gudmundsson, A., 2001. Fluid overpressure and flow in fault zones: Field measurements and models. Tectonophysics 336. https://doi.org/10.1016/S0040-1951(01)00101-9

Haldar, S.K., Tišljar, J., 2014. Introduction to Mineralogy and Petrology, Introduction to Mineralogy and Petrology. Elsevier Inc. https://doi.org/10.1016/C2012-0-03337-6

Haneberg, W.C., Mozley, P.S., Moore, J.C., Goodwin, L.B., 1999. Faults and Subsurface Fluid Flow in the Shallow Crust. Geophys. Monogr. Ser. 113, 222.

Hardebeck, J.L., Hauksson, E., 1999. Role of Fluids in Faulting Inferred from Stress Field Signatures. Science. 285, 236–239. https://doi.org/10.1126/science.285.5425.236.

Hausegger, S., Kurz, W., Rabitsch, R., Kiechl, E., Brosch, F.J., 2010. Analysis of the internal structure of a carbonate damage zone: Implications for the mechanisms of fault breccia formation and fluid flow. J. Struct. Geol. 32, 1349–1362. https://doi.org/10.1016/j.jsg.2009.04.014

Jébrak, M., 1997. Hydrothermal breccias in vein-type ore deposits: A review of mechanisms, morphology and size distribution. Ore Geol. Rev. 12, 111–134. https://doi.org/10.1016/S0169-1368(97)00009-7

Katz, D.A., Eberli, G.P., Swart, P.K., Smith, L.B., 2006. Tectonic-hydrothermal brecciation associated with calcite precipitation and permeability destruction in Mississippian carbonate reservoirs, Montana and Wyoming. Am. Assoc. Pet. Geol. Bull. 90, 1803–1841. https://doi.org/10.1306/03200605072

Kuchenbecker, M., Reis, H.L.S., Fragoso, D.G.C., 2011. Caracterização Estrutural e Considerações sobre a evolução tectônica da Formação Salitre na porção central da Bacia de Irecê, norte do Cráton do São Francisco (BA). Geonomos. 19, 42–49. https://doi.org/10.18285/geonomos.v19i2.40.

La Bruna, V., Lamarche, J., Agosta, F., Rustichelli, A., Giuffrida, A., Salardon, R., Marié, L., 2020. Structural diagenesis of shallow platform carbonates: Role of early embrittlement on fracture setting and distribution, case study of Monte Alpi (Southern Apennines, Italy). J. Struct. Geol. 131. https://doi.org/10.1016/j.jsg.2019.103940

Lagoeiro, L.E., 1990. Estudo Da Deformação Nas Sequências Carbonáticas Do Grupo Una Na Região De Irecê, BA. Departamento de Geologia, Universidade Federal de Ouro Preto, Ouro Preto, MSc, thesis 105 p.

Liao, Z., Liu, H., Jiang, Z., Marfurt, K.J., Reches, Z., 2017. Fault damage zone at subsurface: A case study using 3D seismic attributes and a clay model analog for the Anadarko Basin, Oklahoma. Interpretation 5, T143–T150. https://doi.org/10.1190/INT-2016-0033.1

Mapa Geológico do Estado da Bahia-CBPM/CPRM, 2003. Levantamento Aerogeofísico da Área do Centro Norte Bahia-CBPM, 2011/12.

Misi, A., Iyer, S.S.S., Coelho, C.E.S., Tassinari, C.C.G., Franca-Rocha, W.J.S., de Abreu Cunha, I., Rocha Gomes, A.S., de Oliveira, T.F., Teixeira, J.B.G., Filho, V.M.C., 2005. Sediment hosted lead-zinc deposits of the Neoproterozoic Bambuí Group and correlative sequences, São Francisco Craton, Brazil: A review and a possible metallogenic evolution model. Ore Geol. Rev. 26, 263–304. https://doi.org/10.1016/j.oregeorev.2004.12.004

Misi, A., Kaufman, A.J., Azmy, K., Dardenne, M.A., Sial, A.N., de Oliveira, T.F., 2011. Neoproterozoic successions of the São Francisco Craton, Brazil: The Bambuí, Una, Vazante and Vaza Barris/Miaba groups and their glaciogenic deposits. Geol. Soc. Mem. 36, 509–522. https://doi.org/10.1144/M36.48

Nabavi, S.T., Alavi, S.A., Wibberley, C.A.J., Jahangiri, M., 2020. Normal fault networks and their spatial relationships in Plio-Quaternary sedimentary series: A case study in the Zanjan Depression, NW Iran. J. Struct. Geol. 136. https://doi.org/10.1016/j.jsg.2020.104072

Ngwenya, B.T., Elphick, S.C., Main, I.G., Shimmield, G.B., 2000. Experimental constraints on the diagenetic self-sealing capacity of faults in high porosity rocks. Earth Planet. Sci. Lett. 183, 187–199. https://doi.org/10.1016/S0012-821X(00)00261-2

Nooitgedacht, C.W., H.J.L. van der Lubbe, S. de Graaf, M. Ziegler, P.T. Staudigel, and J.J.G. Reijmer., 2021.Restricted Internal Oxygen Isotope Exchange in Calcite Veins: Constraints from Fluid Inclusion and Clumped Isotope-Derived Temperatures. Geochimica et Cosmochimica Acta. 297, 24–39. https://doi.org/10.1016/j.gca.2020.12.008.Ostermeijer, G.A., Mitchell, T.M., Aben, F.M., Dorsey, M.T., Browning, J., Rockwell, T.K., Fletcher, J.M., Ostermeijer, F., 2020. Damage zone heterogeneity on seismogenic faults in crystalline rock; a field study of the Borrego Fault, Baja California. J. Struct. Geol. 137. https://doi.org/10.1016/j.jsg.2020.104016.

Padilha, A.L., Vitorello, Í., de Pádua, M.B., Fuck, R.A., 2019. Magnetotelluric images of Paleoproterozoic accretion and Mesoproterozoic to Neoproterozoic reworking processes in the northern São Francisco Craton, central-eastern Brazil. Precambrian Res. 333. https://doi.org/10.1016/j.precamres.2019.105416

Peacock, D.C.P., Nixon, C.W., Rotevatn, A., Sanderson, D.J., Zuluaga, L.F., 2017a. Interacting faults. J. Struct. Geol. 97, 1–22. https://doi.org/10.1016/j.jsg.2017.02.008

Peacock, D.C.P., Dimmen, V., Rotevatn, A., Sanderson, D.J., 2017a. A broader classification of damage zones. J. Struct. Geol. 102, 179–192. https://doi.org/10.1016/j.jsg.2017.08.004

Peacock, D.C.P., Dimmen, V., Rotevatn, A., Sanderson, D.J., 2017b. A broader classification of damage zones. J. Struct. Geol. 102, 179–192. https://doi.org/10.1016/j.jsg.2017.08.004

Pedreira, A.J., Arcanjo, J.B., Oliveira, J.E., Silva, B.C.E., 1975. Projeto Bahia: Geologia Da Chapada Diamantina (Relatório Final). DNPM/CPRM, Salvador, Texto e Mapas. 182p.

Pessano, P.C., Ganade, C.E., Tupinambá, M., Teixeira, W., 2020. Updated map of the mafic dike swarms of Brazil based on airborne geophysical data. J. South Am. Earth Sci. 66. https://doi.org/10.1016/j.jsames.2020.103076

Pinto, L.G.R., de Pádua, M.B., Ussami, N., Vitorello, I., Padilha, A.L., Braitenberg, C., 2010. Magnetotelluric deep soundings, gravity and geoid in the south São Francisco craton: Geophysical indicators of cratonic lithosphere rejuvenation and crustal underplating. Earth Planet. Sci. Lett. 297, 423–434. https://doi.org/10.1016/j.epsl.2010.06.044

Rawling, G.C., Goodwin, L.B., Wilson, J.L., 2001. Internal architecture, permeability structure, and hydrologic significance of contrasting fault-zone types. Geology 29, 43–46. https://doi.org/10.1130/0091-7613(2001)029<0043:IAPSAH>2.0.CO;2

Rice, J.R., 1992. Fault Stress States, Pore Pressure Distributions, and the Weakness of the San Andreas Fault. Int. Geophys. 51, 475–503. https://doi.org/10.1016/S0074-6142(08)62835-1

Rozanski, K., Araguás-Araguás, L., & Gonfiantini, R., 1993. Isotopic patterns in modern global precipitation. Reference to a chapter in an edited book: P. K. Swart, K. C. Lohmann, J. McKenzie, & S. Savin, Climate change in continental climate records, American physical union,78, pp. 1-36.

Sampaio A.R., Santos R.A., Rocha A.J.D., Guimarães J.T., 2001. Programa Levantamentos Geológicos Básicos do Brasil - PLGB. Jacobina, Folha SC.24-Y-C, estado da Bahia. Escala 1:250.000. Brasília, CPRM/DIEDIG/DEPAT., p. 31.

Schwarz, E.J., Hood, P.J. and Teskey, D.J., 1987. Magnetic expression of Canadian diabase dykes and downward modelling. Reference to a chapter in an edited book: Halls, H.C. and Fahrig, W.F. (Eds.), Mafic Dyke Swarms. Geological Association of Canada, Special Paper,34, pp. 153–162.

Selway, K., 2014. On the Causes of Electrical Conductivity Anomalies in Tectonically Stable Lithosphere. Surv. Geophys. 35, 219–257. https://doi.org/10.1007/s10712-013-9235-1

Sibson, R. H., 1990. Faulting and fluid flow, in B. E. Nesbitt, ed., Short course on fluids in tectonically active regimes of the continental crust: Mineralogical Association of Canada Short Course Handbook, 18, pp. 93–131.

Sibson, R.H., 1987. Earthquake rupturing as a mineralizing agent in hydrothermal systems. Geology 15, 701–704. https://doi.org/10.1130/0091-7613(1987)15<701:ERAAMA>2.0.CO;2

Sibson, R.H., Robert, F., Poulsen, K.H., 1988. High-angle reverse faults, fluid-pressure cycling, and mesothermal gold-quartz deposits. Geology 16, 551–555. https://doi.org/10.1130/0091-7613(1988)016<0551:HARFFP>2.3.CO;2

Silveira, E.M., Söderlund, U., Oliveira, E.P., Ernst, R.E., Leal, A.B.M., 2013. First precise U-Pb baddeleyite ages of 1500Ma mafic dykes from the São Francisco Craton, Brazil, and tectonic implications. Lithos 174, 144–156. https://doi.org/10.1016/j.lithos.2012.06.004

Sleep, N.H., Blanpied, M.L., 1992. Creep, compaction and the weak rheology of major faults. Nature 359, 687–692. https://doi.org/10.1038/359687a0

Smeraglia, L., Giuffrida, A., Grimaldi, S., Pullen, A., La Bruna, V., Billi, A., Agosta, F., 2021. Fault-controlled upwelling of low-T hydrothermal fluids tracked by travertines in a fold-and-thrust belt, Monte Alpi, southern apennines, Italy. J. Struct. Geol. 144. https://doi.org/10.1016/j.jsg.2020.104276

Steyrer, H.P., Sturm, R., 2002. Stability of zircon in a low-grade ultramylonite and its utility for chemical mass balancing: The shear zone at Miéville, Switzerland. Chem. Geol. 187, 1–19. https://doi.org/10.1016/S0009-2541(02)00010-4

Souza, J. D. D., Melo, R. C. D., & Kozin, M., 2003. Mapa geológico do Estado da Bahia. Escala 1 : 1.000.000. CPRM/CBPM.

Taillefer, A., Soliva, R., Guillou-Frottier, L., Goff, E. Le, Martin, G., Seranne, M., 2017. Fault-related controls on upward hydrothermal flow: An integrated geological study of the têt fault system, Eastern Pyrénées (France). Geofluids 2017. https://doi.org/10.1155/2017/8190109

Teixeira, J.B.G., Misi, A., Da Silva, M.D.G., De Brito, R.S.C., 2019. Reconstruction of precambrian terranes of northeastern Brazil along cambrian strike-slip faults: A new model of geodynamic evolution and gold metallogeny in the State of Bahia. Brazilian J. Geol. 49. https://doi.org/10.1590/2317-4889201920190009

Teixeira, W., Oliveira, E.P., Marques, L.S., 2017. Nature and Evolution of the Archean Crust of the São Francisco Craton, in: Heilbron, M., Cordani, U.G., Alkmim, F.F. (Eds.), São Francisco Craton, Eastern Brazil: Tectonic Genealogy of a Miniature Continent. Springer, Cham, pp. 29–56.doi: 10.1007/978-3-319-01715-0_3.

Thiel, S., Heinson, G., 2013. Electrical conductors in Archean mantle-Result of plume interaction? Geophys. Res. Lett. 40, 2947–2952. https://doi.org/10.1002/grl.50486

Wibberley, C.A.J., Shipton, Z.K., 2010. Fault zones: A complex issue. J. Struct. Geol. https://doi.org/10.1016/j.jsg.2010.10.006

Yilmaz, T.I., Prosser, G., Liotta, D., Kruhl, J.H., Gilg, H.A., 2014. Repeated hydrothermal quartz crystallization and cataclasis in the Bavarian Pfahl shear zone (Germany). J. Struct. Geol. 68, 158–174. https://doi.org/10.1016/j.jsg.2014.09.004

Zhang, S., Tullis, T.E., Scruggs, V.J., 2001. Implications of permeability and its anisotropy in a mica gouge for pore pressures in fault zones. Tectonophysics 335, 37–50. https://doi.org/10.1016/S0040-1951(01)00044-0.

CAPÍTULO VI – CONSIDERAÇÕES FINAIS

A questão inicial desta pesquisa é o papel dos fluidos hidrotermais na diagênese de rochas carbonáticas e na formação do carste. O papel dos fluidos na geração do carste é um conceito associado à carstificação hipogênica, um conceito solidificado apenas nas últimas três décadas (Klimchouk, 2012). Por outro lado, o papel dos fluidos hidrotermais na diagênese de rochas carbonáticas tem sido objeto de estudo há muito tempo (Palmer 1991; Ford e Willians, 1989), embora pouca atenção tenha sido dada a geração de porosidade durante a diagênese.

Até a década de 1980, a literatura mundial era dominada pelo conceito de carste epigênico (e.g., Esteban e Klappa, 1983). Dentro desta lógica, a formação do carste ocorria apenas em ambiente superficial, onde os fluidos meteóricos exerceriam um papel único na dissolução de rochas carbonáticas e formação de cavidades em várias escalas (Esteban e Klappa, 1983). Na indústria do petróleo, esse conceito foi aplicado extensivamente nos trabalhos de reservatórios nas bacias de Santos e Campos (offshore Brasil). Apesar de vários trabalhos pioneiros apontarem a existência de dissolução e carstificação de rochas carbonáticas em ambientes profundos e causadas por fluidos hidrotermais (Palmer, 1991), apenas a partir de 1990 trabalhos sistemáticos levaram ao entendimento de processos hipogênicos na carstificação de rochas carbonáticas em larga escala (Dublyanski, 2000; Auler e Smart, 1999). Este conhecimento culminou mais recentemente com uma compilação de vários trabalhos em escala mundial sobre o carste hipogênico (Klimchouk et al., 2019). Igualmente, apenas mais recentemente, estes conceitos começaram a ser aplicados à indústria do petróleo em campos das bacias de Tarim (e.g., Cai et al., 2020) e Ordos (e.g. Wang e Al-Aasm, 2002) na China, Campos, Santos no Brasil (e.g., Lima et al., 2019 e 2020).

Neste sentido, o estudo de análogos de reservatórios de rochas carbonáticas tem sido considerado de grande importância para o entendimento de processos de diagênese e dissolução de rochas carbonáticas em várias escalas e diversos ambientes tectônicos e sedimentares (e.g., Cazarin et al., 2019; Klimchouk et al., 2016). Nesta tese, pretendeu-se mostrar como a

diagênese e o sistema cárstico são influenciados por fluidos hidrotermais na Formação Salitre, uma unidade neoproterozóica do Cráton São Francisco, Bahia.

Inicialmente, investigamos a Formação de carste hipogênico na Formação Salitre, mais especificamente na Toca da Boa Vista e Toca da Barriguda, porção norte do Cráton São Francisco, Bacia de Campo Formoso. Estas duas cavernas constituem o maior conjunto cárstico da América do Sul (Auler et al., 2001). No trabalho de Cazarin et al. (2019), mostramos o papel das falhas e zonas de fraturas na ascensão dos fluidos hidrotermais. Além disso, mostramos como algumas camadas, mesmo que finas, compostas de rochas siliciclásticas finas e margas, formam selos estratigráficos e influenciam na concentração de fluidos em determinados níveis de rochas carbonáticas (principalmente *grainstones*) que são, subsequentemente carstificados.

A formação do carste em ambiente hipogênico é determinada inicialmente por condutos de natureza tectônica ao longo dos quais ocorreu a ascensão de fluidos. Estes condutos podem ser corredores de fraturas em eixos de dobras, como apontaram Ennes-Silva et al. (2016) e La Bruna et al. (2021) no sistema de cavernas da Toca da Boa Vista e Toca da Barriguda e na Formação Caboclo (Mesoproterozóico), respectivamente. Neste caso, dobras abertas com caimento máximo de 10º são capazes de promover a geração de fraturamento paralelo ao eixo da dobra, onde a percolação de fluidos se concentra. Estes eixos de dobras, por sua vez, estão relacionados a grandes empurrões de escala regional (Formação Salitre) e eixos de dobras regionais (Formação Caboclo), o que torna a previsão da direção de dobramento e fraturamento subsequente uma tarefa possível (Ennes-Silva et al., 2016). Os condutos gerados pela carstificação subsequente ao longo das fraturas em eixos de dobras pode concentrar condutos com mais de 100 km de extensão em áreas de 3,5 km de comprimento e 2,5 km de largura, como no caso das cavernas acima citadas.

O mesmo processo pode também ocorrer em ambiente epigênico. Na Bacia Potiguar, anticlinais com 10 km de amplitude, relacionados à propagação de falhas da fase rifte, concentram corredores de fraturas de dezenas de metros de extensão e de profundidade (Bagni et al., 2020). Num processo semelhante ao ocorrido em ambiente hipogênico, este fraturamento em ambiente superficial

promove a circulação de fluidos meteóricos, que se infiltram em camadas porosas de arenitos (Formação Açu) da Bacia Potiguar e ascendem por fraturas em carbonatos da Formação Jandaíra, numa temperatura de até 63ºC (Bertotti et al., 2017; De Graaf et al., 2017). Esses fluidos, juntamente com aqueles existentes na superfície, promovem a carstificação na Formação Jandaíra ao longo de eixos de dobras facilitando a formação de cavernas e relevo cárstico nestes locais (Bagni et al., 2020).

As fraturas relacionadas aos dobramentos com eixos sub-horizontais com direção N-S e E-W são essenciais para promover a carstificação e promover a formação de porosidade secundária em rochas onde a porosidade primária é baixa. O estudo de GPR e *drone* em uma pedreira próximo às Tocas da Boa Vista e da Barriguda mostrou que uma porosidade com arquitetura de labirinto controlado pelo fraturamento com as duas direções acima citadas é responsável pela porosidade do bloco rochoso (Conti et al., 2018). Da mesma forma, a alteração dessas rochas nas zonas adjacentes às fraturas promove a formação de uma porosidade secundária relacionada à telodiagênese.

As fraturas e sua relação com as camadas também têm forte influência nos formação do carste. Um estudo de estratigrafia de fraturas foi feito no sistema cárstico da Toca de Boa Vista e Toca da Barriguda (Balsamo et al., 2020). Camadas finas tendem a ter grande fraturamento, com fraturas pouco espaçadas, estas camadas tendem a favorecer o fluxo de fluidos horizontais. Às vezes, tais camadas podem funcionar com selos ao fluxo vertical. Por outro lado, camadas mais espessas tendem a ter fraturas mais extensas, que facilitam o fluxo vertical. Fraturas não stratabound, ou seja, que cortam todas as camadas, são essenciais para o fluxo vertical (Balsamo et al., 2020). Estas promovem o fluxo de fluidos hidrotermais, que se concentram abaixo de camadas selantes (Cazarin et al., 2019) ou camadas finas com intenso fraturamento contido na camada (stratabound) (Balsamo et al., 2020).

O controle estratigráfico é igualmente essencial na concentração de fluídos em determinados horizontes. O trabalho de Souza et al. (2021) indicou que camadas de carbonatos oolíticos de alta porosidade primária concentraram fluídos hidrotermais. Estes fluidos foram responsáveis pela silicificação hidrotermal

destas camadas que se localizam abaixo de um selo estratigráfico composto de rochas pelíticas (Souza et al., 2021). A origem destes fluidos é provavelmente de fonte profunda, dado a mineralogia hidrotermal composta de barita, galena, quatzo, calcedônia, hialofana, talco e clorita (Souza et al., 2021). Da mesma forma que nas Tocas da Boa Vista e da Barriguda, os condutos de cavernas concentram-se em eixos de dobra, com orientação e geometria similar às dobras regionais na Formação Caboclo de idade mesoproterozóica (La Bruna et al., 2021) e na Formação Salitre (Pontes et al., 2021).

O estudo da Falha de Cafarnaum indica que dois sistemas hidrotermais ocorrem neste ambiente. O primeiro é um sistema hidrotermal raso cujo processo de convecção é fundamental na ascensão de fluidos. Este sistema é encontrado em rochas encaixantes da Formação Salitre, afetadas pela Falha de Cafarnaum (Cazarin et al., submetido). As características isotópicas deste sistema meteórico têm valores de δD values ~ -45‰ e $\delta^{18}O$ ~ -6.5‰, com temperatures de 40-70°C em veios de calcita nas rochas encaixantes. Outro sistema mais profundo ocorre ao longo da zona central da falha. Atentado pelas paragêneses minerais composta de clorita, barita, hialofana, calcedônia, quartzo e galena (Souza et al., 2021) e depósitos *Mississippi Valley Type (MVT)* (Misi, 2004, 2012; Cazarin et al., submetido). Neste caso, a concentração de depósitos minerais hidrotermais ocorre nas porções extensionais da zona de falha transcorrente (Cazarin et al., submetido).

A presente tese indica a necessidade de investigação mais profunda nos temas abordados e na presente área de estudo. O primeiro tema de interesse de investigação é a origem do processo de carstificação na Bacia em várias unidades, como na Formação Caboclo (Mesoproterozóico), Salitre (Neoproterozóico) e Caatinga (Paleógeno-Neógeno). Estes processos podem ser melhor avaliados com a continuidade de estudos isotópicos e inclusões fluídas. Um segundo ponto de estudo é a determinação da idade dos eventos de carstificação através de datações geocronológicas de carbonatos. Uma das técnicas mais usadas no momento, e com maior potencial de sucesso, é a geocronologia por U-Pb em veios de calcita.

Um terceiro ponto a ser enfocado é o estudo tectônico. As geometrias e dimensões do sistema cárstico em escala sísmica e subsísmicas precisam de melhor detalhamento. Desta forma, não é inteiramente conhecido a relação de origem e espacial entre as duas escalas. Há, portanto, necessidade de mapeamento de estruturas em detalhe e upscaling para escalas de bacia a serem detectadas pela sísmica. Técnicas de campo envolvendo imageamento 3D (LiDAR e fotogrametria) devem ser combinadas com geofísica rasa (GPR, resistividade e poços), para posterior upscaling e comparação com dados sísmicos com carste em bacias sedimentares.

REFERÊNCIAS

Almeida, F.F.M. 1977. O Cráton do São Francisco. Revista Brasileira de Geociências, 7 (4), 349-364.

Auler, A.S.; Farrant, A.R. 1996. A brief introduction to karst and caves in Brazil. Proc. Univ. Bristol Spelaeol. Soc., 20 (3), 187-200.

Auler, A.S., 1999. Karst Evolution and Palaeoclimate in Eastern Brazil. Ph.D. Thesis. University of Bristol.

Auler, A. S.; Smart, P. L. 1999. Toca da Boa Vista, Bahia state the longest known cave in the Southern Hemisphere. In: Schobbenhaus, C.; Campos, D.A; Queiroz, E.T.; Winge, M.; Berbert-Born, M. Sítios Geológicos e Paleontológicos do Brasil.

Auler, A.S.; Smart, P.L. 2001. Late Quaternary paleoclimate in semiarid northeastern Brazil from U Series dating of travertine and water-table speleothems. Quaternary Research, 55, 159-167.

Auler, A.S.; Rubbioli, E.; Brandi, R. 2001. As grandes cavernas do Brasil. Grupo Bambuí de Pesquisas Espeleológicas, Belo Horizonte.

Auler, A.S.; Smart, P.L. 2003. The influence of bedrock derived acidity in the development of surface and underground karst: Evidence for the Precambrian carbonates of semi-arid northeastern Brazil. Earth Surface Processes and Landforms, 28, 157-168.

Auler, A.S.; Klimchouk, A.; Bezerra, H.R.; Cazarin, C.L.; Ennes-Silva, R.; Balsamo, F. 2017. In: Klimchouk, A., Palmer, A., De Waele, J., Auler, A., Audra, P. (Eds.), Hypogene Karst Regions and Caves of the World. Cave and Karst Systems of the World. Springer International Publishing, 827–840.

Bagni, F.L.; Bezerra, F.H.; Balsamo, F.; Maia, R.P.; Dall'Aglio, M. 2020. Karst dissolution along fracture corridors in an anticline hinge, Jandaíra Formation, Brazil: implications for reservoir quality. Mar. Petrol. Geol., 115, 104249.

Balsamo, F.; Bezerra, F.H.R.; Klimchouk, A.B.; Cazarin, C.L.; Auler, A.S.; Nogueira, F.C.; Pontes, C. 2020. Influence of fracture stratigraphy on hypogene

cave development and fluid flow anisotropy in layered carbonates, NE Brazil. Mar. Petrol. Geol., 114, 104207.

Bertotti, G.; de Graaf, S.; Bisdom, K.; Oskam, B.; Vonhof, H. B.; Bezerra, F. H.; Reijmer, J.J.G.; Cazarin, C. L. 2017. Fracturing and fluid-flow during post-rift subsidence in carbonates of the Jandaíra Formation, Potiguar Basin, NE Brazil. *Basin Research*, *29* (6), 836-853.

Bonfim, L.F.C.; Rocha, A.J.D.; Pedreira, A.J.; Morais, J.C.; Guimarães, J.T.; Tesch, N.A. 1985. Projeto Bacia de Irecê. Salvador, CPRM. (Relatório Final).

Cai, Z.; Zhang, H.; Qi, L.; Yun, L.; Cao, Z.; Sha, Xuang. 2020. Types and characteristics of karst hydrogeomorphologic architectures in the Middle-Lower Ordovician, Tarim Basin. Acta Petrolei Sinica, 41 (1), 43-58.

Cazarin, C. L. Controle Faciológico do Sistema Cárstico Hipogênico de Campo Formoso, BA: Sistema conduto-barreira. (Dissertação de Mestrado) - Rio de Janeiro: UFRJ / IGeo, 2015. 34f.

Cazarin C. L.; Bezerra F. H. R.; Borghi L.; Santos R. V.; Favoreto J.; Brod J. A.; Auler A. S. and Srivastava N. K. 2019 The conduit-seal system of hypogene karst in Neoproterozoic carbonates in northeastern Brazil. *Marine and Petroleum Geology,* 101, 90–107.

Choquette, P.W.; Pray, L.C. 1970. Geological nomenclature and classification of porosity in sedimentary carbonates. American Association of Petroleum Geologists Bulletin, 54 (2), 207-250.

Conti, I.M.M.; de Castro, D.L.; Bezerra, F.H.R.; Cazarin, C.L. 2019. Porosity Estimation and Geometric Characterization of Fractured and Karstified Carbonate Rocks Using GPR Data in the Salitre Formation, Brazil. *Pure Appl. Geophys.* 176, 1673–1689.

CPRM/CBPM. 2003. Mapa Geológico Digital da Bahia ao Milionésimo. Disponível em http://geobank.cprm.gov.br/ acessado em 15/04/2015.

Dardenne, M. 1978. Síntese sobre a estratigrafia do Grupo Bambuí no Brasil Central. Congresso Bras. Geologia, vol. 31. SBG, Recife, 597–610. Anais 2

de Graaf, S.; Reijmer, J. J.; Bertotti, G. V.; Bezerra, F. H.; Cazarin, C. L.; Bisdom, K.; Vonhof, H. B. 2017. Fracturing and calcite cementation controlling fluid flow in the shallow-water carbonates of the Jandaíra Formation, Brazil. *Marine and Petroleum Geology*, *80*, 382-393.

Dublyansky, Y.V. 2000. Hydrothermal speleogenesis: its settings and peculiar features. In: Klimchouk AB, Ford DC, Palmer AN, Dreybrodt W (eds) Speleogenesis evolution of karst aquifers. National Speleological Society, Huntsville, Alabama, 298–303

Dunham, R. J. 1962. Classification of carbonate rocks according to depositional texture. In: Ham, W.E.(Ed.). Classification of carbonate rocks. Tulsa. *American Association of Petroleum Geologists, Memoir*, 1, 108-122.

Ehrenberg S. N.; Walderhaug O.; Bjørlykke K. 2012. Carbonate porosity creation by mesogenetic dissolution: Reality or illusion? *AAPG Bulletin,* 96, 217–233.

Ennes-Silva, RA.; Bezerra; F. H. R.; Nogueira, F.C.C.; Balsamo, F; Klimchouk, A.; Cazarin. C.L.; Auler, A. 2016. Superposed folding and associated fracturing influence hypogene karst development in Neoproterozoic carbonates, São Francisco Craton, Brazil. *Tectonophysics*, 666 (15), 244-259.

Esteban, M.; Wilson, J.L. 1993. Introduction to karst system and Paleokarst reservoirs. In: In: Fritza, R.D., Wilson, J.L., Yurewicz, D.A. (Eds.), Paleokarst Related Hydrocarbon Reservoirs, vol. 18. SEMP Core workshop, pp. 1–9.

Ford, D.C.; Williams, P.W. 1989. Karst Geomorphology and Hydrology. Unwin and Hyman, London, pp. 601.

Ford, D. C. 2006. Karst geomorphology, caves and cave deposits: A review of North American contributions during the past half century. In R. S. Harmon & C. W. Wicks (Eds.), Perspectives on karst geomorphology, hydrology and geochemistry, pp. 114. *Geological Society of America* (Special Paper 404).

Gottlieb, P.; Wilkie, G.; Sutherland, D.; Ho-Tun, E.; Suthers, S.; Perera, K.; Jenkins, B.; Spencer, S.; Butcher, A.; Rayner, J. 2000. Using quantitative electron microscopy for process mineralogy applications. *Journal of the Minerals, Metals and Materials Society*, 52 (4), 24-25.

Hardage B. A.; Carr D. L.; Lancaster D. E.; Simmons J. L. Jr. 1996. 3-D seismic evidence of the effects of carbonate karst collapse on overlying clastic stratigraphy and reservoir compartmentalization. *Geophysics*, 61 (5), 1245-1569.

Harman, R.; Gallagher, K.; Brown, R.; Raza, A.; Bizzi, L. 1998. Accelerated denudation and tectonic/geomorphic reactivation of the cratons of northeastern Brazil during the Late Cretaceous. *Journal of Geophysical Research,* 103 (B11), 27091-27105.

Heubeck, C.; Story K.; Peng P.; Sullivan C.; Duff S. 2004. An integrated reservoir study of the Liuhua 11-1 field using a high-resolution three-dimensional seismic data set, *AAPG*, 81, 49-168.

Hosseini S. M.; Ataie-Ashtiani B. 2017. Conceptualization of Karstic Aquifer with Multiple Outlets Using a Dual Porosity Model. *Groundwater,* 55, 558–564.

Karmann, L.1994. Evolução e dinâmica atual do sistema cárstico do Alto Vale do Rio Ribeira, sudeste do Estado de São Paulo. Tese de Doutoramento, IGc-USP. 228 p.

Kempe S.; Dirks H.; Bauer I. 2015. Hypogene karstification in Saudi Arabia (Layla limestone sinkholes, Ain Heeth Cave). *Hypogene Speleogenesis and Karst Hydrogeology of Artesian Basins*, 1, 247 - 251

Klimchouk, A. 2005. Conceptualisation of speleogenesis in multi-storey artesian systems: a model of transverse speleogenesis, *IJS,* 34, 45–64.

Klimchouk, A., 2007. Hypogene Speleogenesis: Hydrogeological and Morphogenetic Perspective. 106 pp.

Klimchouk, A., 2009. Morphogenesis of hypogenic caves. Geomorphology, 106, 1-2, 100–117.

Klimchouk, A.B. 2012. Speleogenesis, hypogenic. In: Culver, D.C., White, B.W. (Eds.), Encyclopedia of Caves, second ed. Elsevier, Chennai, pp. 748–765.

Klimchouk A.; Auler A. S.; Bezerra F. H. R.; Cazarin C. L.; Balsamo F.; Dublyansky Y. 2016. Hypogenic origin, geologic control and functional organization of a giant cave system in Precambrian carbonates, Brazil. *Geomorphology,* 253, 385–405.

La Bruna, V.; Bezerra, F.H.; Souza, V.H.P.; Maia, R.P.; Auler, A.S.; Araujo, R.E.B.; Cazarin, C.L.; Rodrigues, M.A.F.; Vieira, L.C.; Sousa, M.O.L. 2021. High-permeability zones in folded and faulted silicified carbonate rocks - Implications for karstified carbonate reservoirs. *Mar. Petrol. Geol.*, 128, 1-18.

Lima, B.E.M., De Ros, L.F., 2019. Deposition, diagenetic and hydrothermal processes in the Aptian Pre-Salt lacustrine carbonate reservoirs of the northern Campos Basin, offshore Brazil. Sediment. Geol. 383, 55–81.

Lima, B.E.M.; Tedeschi, L.R.; Pestilho, A.L.S.; Santos, R.V.; Vazquez, J.C.; Guzzo, J.V.P.; De Ros, L.F. 2020. Deep-burial hydrothermal alteration of the Pre-Salt carbonate reservoirs from northern Campos Basin, offshore Brazil: evidence from petrography, fluid inclusions, Sr, C and O isotopes. *Mar. Petrol. Geol.*, 113, 104143.

Loucks, R.G. 1999. Paleocave Carbonate reservoirs: Origins, Burial-Depth Modifications, Spatial Complexity, and Reservoirs Implications. *AAPG Bulletin*, 83 (11), 1795-1834.

Loucks, R. G.; Mescher, P.; McMechan, G. A. (2004). Three-dimensional architecture of a coalesced, collapsed-paleocave system in the Lower Ordovician Ellenburger Group, Central Texas. *American Association of Petroleum Geologists Bulletin*, 88, 545–564.

Mazzulo, S.J.; Harris, P.M. 1992. Mesogenetic dissolution: its role in porosity development in carbonate reservoir. AAPG (Am. Assoc. Pet. Geol.) Bull., 76, 607-620.

Medeiros, R.A.; Pereira, C.P. 1994. Chapada Diamantina (São Francisco Basin). In: 14th. International Sediment. Congress, Recife, Field Trip Guide Book, 5p.

Misi, A.; Souto, P. 1975. Controle estratigráfico das mineralizações de chumbo, zinco, flúor e bário no Grupo Bambuí, parte leste da Chapada de Irecê (Bahia). *Rev. Bras. Geoc*., 5(1), 30-45.

Misi, A., 1976. As Sequências Bambuí no Estado da Bahia e as Mineralizações de Chumbo e Zinco Associadas. 80 f. il. Tese (Livre Docência). Universidade Federal da Bahia, Instituto de Geociências, Salvador.

Misi, A., 1979. O Grupo Bambuí no Estado da Bahia. Salvador, SME/BA., 1, 119-154.

Misi, A.; Silva, M.G. 1996. Chapada Diamantina Oriental, Bahia. Geologia e Depósitos Minerais. Superintendência de Geologia e Recursos Minerais. Universidade Federal da Bahia, Salvador, 194 p.

Misi, A.; Veizer, J. 1996. Chemostratigraphy of Neoproterozoic Carbonate Sequences of the Una Group, Irecê Basin, Brazil. In: *Anais Congresso Brasileiro de Geologia. Sociedade Brasileira de Geologia*, 5, 487–489.

Misi, A.; Iyer, S.S.S.; Tassinari, C.C.G.; Franca-Rocha, W.J.S.; Coelho, C.E.S.; Cunha, I. de A.; Gomes, A.S.R. 2004. Dados isotópicos de chumbo em sulfetos e a evolução metalogenética dos depósitos de zinco e chumbo das coberturas neoproterozóicas do Cráton do São Francisco. *Rev. Bras. Geociências*, 34, 263–274.

Palmer, A.N., 1991. Origin and morphology of limestone caves. *Geological Society of America Bulletin*, 103, 1-21.

Palmer, A.N.,1995. Geochemical models for the origin of macroscopic solution porosity in carbonate rocks. - In Budd, D.A., P.M. Harris, & A. Saller (eds.): Unconformities in carbonate strata: Their recognition and the significance of associated porosity. *American Association of Petroleum Geologists*, Memoir 63, 77–101.

Palmer, A.N., 2007. Cave Geology. Cave Books, Ohio (Dayton).

Palmer A. N. 2011. Distinction between epigenic and hypogenic maze caves. *Geomorphology,* 134, 9–22.

Pontes, C.C.C; Bezerra, F.H.R; Bertotti, G.; La Bruna, V.; Audra, P.; De Waele, J.; Auler, A.S.; Balsamo, F.; De Hoop, S.; Pisani, L. 2021. Flow pathways in multiple-

direction fold hinges: Implications for fractured and karstified carbonate reservoirs, *Journal of Structural Geology*, 146, 104324.

Souza, S. L.; Brito, P.C.R.; Silva, R.W.S. 1993. Estratigrafia, Sedimentologia e Recursos Minerais da Formação Salitre na Bacia de Irecê, Bahia. Salvador, Companhia Baiana de Pesquisa Mineral (CBPM), 1993. 36 p. (Série Arquivos Abertos 2).

Souza, V.H.P.; Bezerra, F.H.R.; Vieira, L.C.; Cazarin, C.L.; Brod, J.A. 2021. Hydrothermal silicification confined to stratigraphic layers: implications for carbonate reservoirs. *Mar. Petrol. Geol.*, 124, 104818.

Trompette, R.; Uhlein, A.; Egydio-Silva, M.; Karmann, I. 1992. The brasiliano São Francisco Cráton revisited (Central Brazil). *J. South Am. Earth Sciences*, 6 (1/2), 49-57.

Sullivan E. C.; Marfurt K. J.; Lacazette A.; Ammerman M. 2006. Application of new seismic attributes to collapse chimneys in the Fort Worth Basin, *Geophysics*, 71, 111–B119.

Wang, B.; Al-Aasm, I.S. 2002. Karst-Controlled Diagenesis and Reservoir Development: Example from the Ordovician Main-Reservoir Carbonate Rocks on the Eastern Margin of the Ordos Basin, China. *AAPG Bulletin*, 86 (9), 1639–1658.

Worthington, S.R.H.; Ford, D.C. 1997. Borehole tests for megascale channeling in carbonate aquifers. In: Proceedings of the 12th International Congress of Speleology, vol. 11. La Chaux-de-Fonds, Switzerland, pp. 195–198.

ANEXOS

Em anexo, estão dois trabalhos publicados dos quais sou co-autora e que foram desenvolvidos durante minha tese. Tais trabalhos têm estreita relação com a tese e são colocados aqui para ilustrar e aprofundar a discussão.

Anexo A Artigo publicado no Marine and Petroleum Journal: Balsamo et al., 2020. Influence of fracture stratigraphy on hypogene cave development and fluid flow anisotropy in layered carbonates, NE Brazil

Anexo B Artigo publicado no Marine and Petroleum Journal: La Bruna et al., 2021. High-permeability zones in folded and faulted silicified carbonate rocks - Implications for karstified carbonate reservoirs

Marine and Petroleum Geology 114 (2020) 104207

Contents lists available at ScienceDirect

Marine and Petroleum Geology

journal homepage: www.elsevier.com/locate/marpetgeo

Research paper

Influence of fracture stratigraphy on hypogene cave development and fluid flow anisotropy in layered carbonates, NE Brazil

F. Balsamo[a,*], F.H.R. Bezerra[b], A.B. Klimchouk[c], C.L. Cazarin[d], A.S. Auler[e], F.C. Nogueira[f], C. Pontes[b]

[a] Next, Natural and Experimental Tectonic Research Group, Department of Chemistry, Life Sciences and Environmental Sustainability, University of Parma, Italy
[b] Department of Geology, Federal University of Rio Grande do Norte, Brazil
[c] Institute of Geological Sciences, National Academy of Science, Ukraine
[d] Petrobras, Centro de Pesquisa e Desenvolvimento Leopoldo A. Miguez de Mello, Brazil
[e] Instituto do Carste, Carste Ciência e Meio Ambiente, Brazil
[f] Federal University of Campina Grande, Brazil

ARTICLE INFO

Keywords:
Hypogene cave
Fracture stratigraphy
Karst porosity
Speleogenesis

ABSTRACT

Fractured and karstified carbonates are often major aquifers and hydrocarbon reservoirs. The Toca da Boa Vista (TBV) and Toca da Barriguda (TBR) caves in NE Brazil, which form the longest cave system in South America, developed in a gently folded, layered and fractured Neoproterozoic carbonate sequence made of different lithological units (limestones versus siliciclastic rocks and marls) with variable bed properties (bed thickness, surface roughness of bed-to-bed interlayers) and fracture attributes (spacing, height). The functional organization of the hypogenic cave system has been recently revealed, with subdivision in three speleo-stratigraphic storeys which, from bottom to top, acted as recharge, lateral redistribution and outflow components of the rising fluid flow system, respectively. Structural analysis and new fracture data from TBV and TBR indicate that the stratigraphic setting controlled the fracture pattern development during two tectonic phases, which determined the fluid flow anisotropy during speleogenesis. We found that mechanical and fracture stratigraphy, in conjunction with bed thickness and bed-to-bed interlayer characteristics, controlled the spacing and height of fractures and, as a result, strongly influenced the fluid flow pattern and functional organization of the cave system. In particular, bed-normal rising fluids localized along m-to tens of m-spaced throughgoing fractures developed in the lower and upper storeys, whereas horizontal and bed-parallel fluid flow was focused in a package of thin carbonates, siliciclastics and marls with cm-spaced, strata-bound fractures. This fluid flow anisotropy is attained also due to the presence of rough-walled, bedding-parallel interlayers (i.e., burial stylolites) in the lower massive grainstone which hampered bed-parallel flow, and smooth, planar bedding-parallel interlayers which enhanced lateral fluid movements in the well-layered and fractured middle storey units. Therefore, we conclude that in heterolithic layered carbonate packages, the intricate hypogenic karst pattern is related to heterogeneous fluid flow behaviour associated with the structural complexity imparted by the mechanical versus fracture stratigraphy.

1. Introduction

Understanding factors that control development of karst systems in carbonate rocks is a principal concern of speleogenetic studies (e.g., Palmer, 2007; Klimchouk et al., 2000), bedrock stability assessment in anthropic areas (Waltham et al., 2005), and groundwater management and exploitation of deep-seated hydrocarbon reservoirs (Heward et al., 2000). Stratigraphic and hydrologic setting play a primary role in determining the size, shape and spatial distribution of karst systems in carbonate rocks (Lowe, 2000; Klimchouk and Ford, 2000; Palmer, 2000, 2007; Cazarin et al., 2019). Another important factor that determines the occurrence, shape and main trends of cave systems is the presence and preferential orientation of major tectonic discontinuities and their networks (Palmer, 1989, 1991; Wang et al., 2017; Antonellini et al., 2019; Pisani et al., 2019). In sedimentary rocks, the attributes of fracture network (i.e., spacing, density, length, persistence), which may control the generation and evolution of karst features, depend on time-space evolution of both regional-scale processes (e.g., the evolution of

* Corresponding author.
E-mail address: fabrizio.balsamo@unipr.it (F. Balsamo).

https://doi.org/10.1016/j.marpetgeo.2019.104207
Received 23 September 2019; Received in revised form 15 December 2019; Accepted 24 December 2019
Available online 27 December 2019
0264-8172/

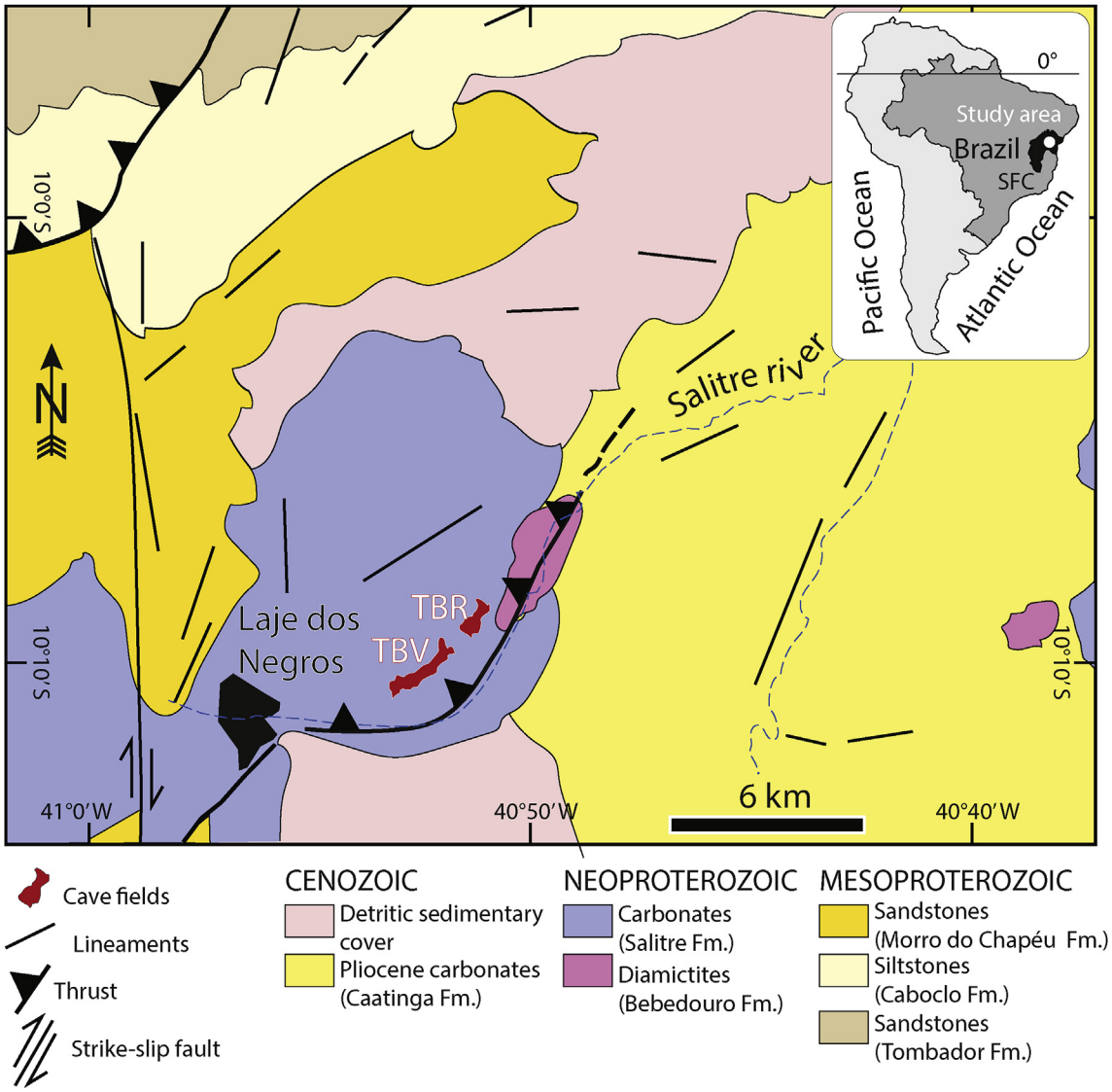

Fig. 1. Geological map showing the Campo Formoso region and TBV-TBR cave position, with major tectonic features (modified from Bizzi et al., 2003 and Ennes-Silva et al., 2016). SFC: São Francisco craton.

tectonic stress field) and local-scale factors (e.g., lithology, bed thickness, bed-to-bed interfaces, diagenesis, and faulting) (Laubach et al., 2009; Barbier et al., 2012; Lamarch et al., 2012; Rustichelli et al., 2016; Ogata et al., 2017; Balsamo et al., 2019). The mechanical and fracture stratigraphy concepts (Laubach et al., 2009 and references therein), which subdivide stratified sedimentary rocks either into discrete mechanical units with similar properties (e.g., tensile strength) or into intervals with similar fracture pattern (e.g., vertical extent, density), respectively, can be effectively used to describe the stratigraphic control on development of fracture patterns in many geological settings and rock types. Mechanical and fracture stratigraphy do not necessarily coincides due to the evolving mechanical properties with burial and diagenesis (Laubach et al., 2009 and references therein).

Cave and karst systems can develop at different burial depths and in response to both epigenic process (direct meteoric recharge) and hypogenic process (deep-seated ascending fluids). Hypogenic caves are widely recognized in many geological settings worldwide (Ford and Williams, 1989; Palmer, 1991; Galdenzi and Menichetti, 1995; Ford and Williams, 2007; Klimchouk, 2007; Klimchouk et al., 2017a,b; D'Angeli et al., 2019) and develop in response to dissolution associated with ascending flow (Klimchouk, 2007). Hypogene speleogenesis is generally connected to the presence and arrangement of faults and fracture systems, which may have focused rising fluid flow, thus determining the functional organization (shape and spatial distribution) of cave systems (e.g.,Klimchouk, 2019; Klimchouk et al., 2016).

Recent works on a major hypogenic cave system developed in Precambrian carbonate sequences in NE Brazil have highlighted the first-order role of tectonic structure in controlling the trend of cave passages (Ennes-Silva et al., 2016), as well as the role of stratigraphy in controlling the functional organization of cave system in three distinct speleo-stratigraphic storeys (Klimchouk et al., 2016; Auler, 2017; Cazarin et al., 2019). Despite such extensive work in the Precambian carbonates in NE Brazil, and the large amount of worldwide case studies on the link between tectonics and karst (e.g., Shanov and Kostov, 2015), a detailed understanding on the influence of mechanical and fracture stratigraphy in controlling pattern of cave passages and speleogenesis is still not fully established.

In this contribution we present a new multidisciplinary dataset collected in the Toca da Boa Vista (TBV) and Toca da Barriguda (TBR) cave system in northeaster Brazil, which provides insights on the role of stratigraphy and resulting fracture pattern in determining the observed cave morphology. In particular, by integrating structural data with stratigraphic and petrophysical data, we found that, in the different lithological units, bed properties (thickness) determined different

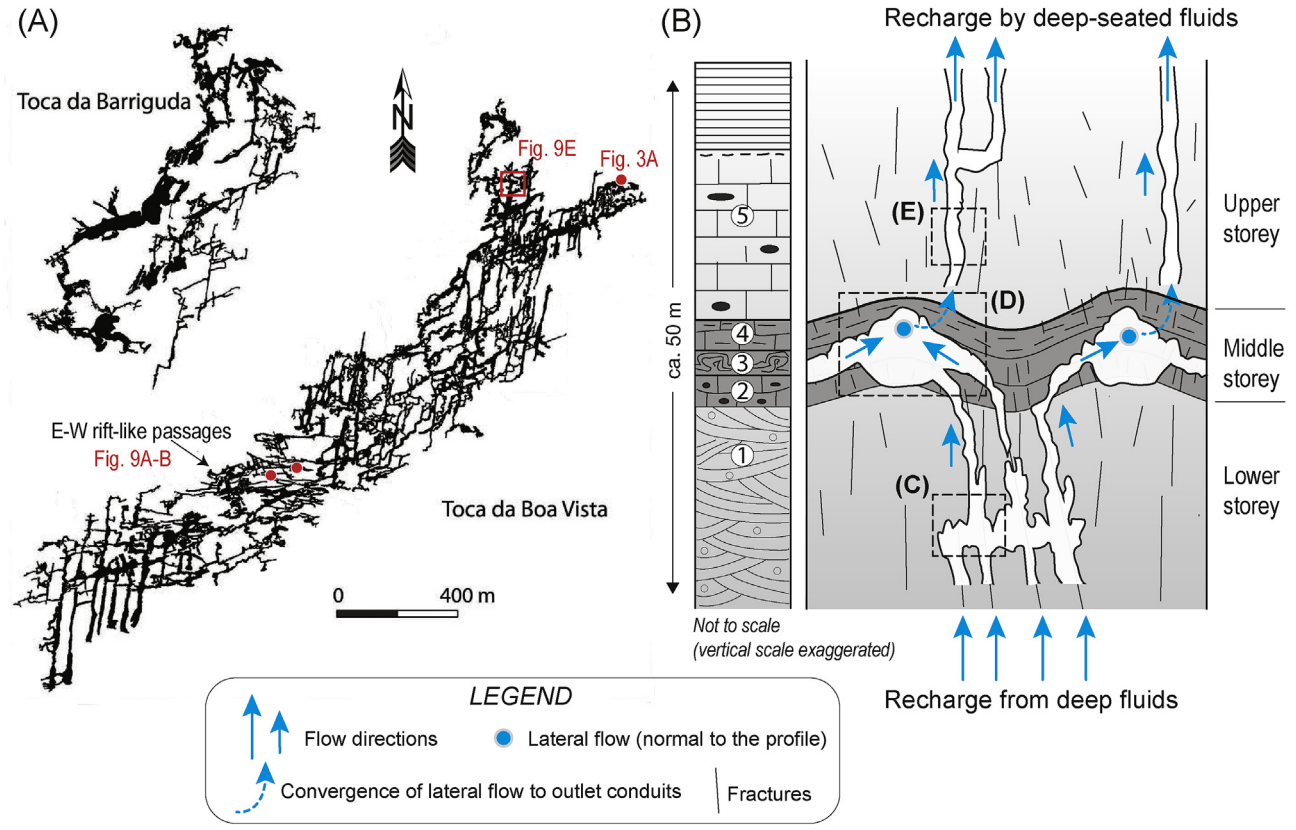

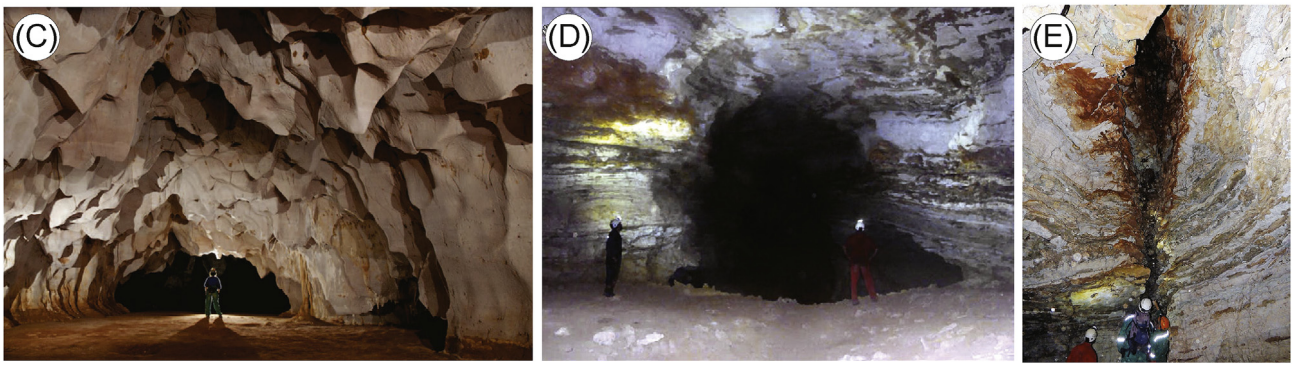

Fig. 2. Composite figure showing the planimetry in map view of the TBV-TBR cave system (A) and the functional organization of the cave system in a schematic profile (B) according to Klimchouk et al. (2016). (C-E) Morphological features in the lower massive grainstones (cupolas, pendants) (C), in well layered units (horizontal conduits, mostly fold controlled) (D), and in the upper micritic limestones (discharge, rift-like conduits). See text for detailed description of units 1–5 in (B). Photograph in (C) courtesy of Luciana Alt and Vitor Moura.

fracture densities (number of fractures per meter). Such difference in fracture density, combined with the nature of bed-to-bed interfaces, determined the large-scale permeability anisotropy that controlled the position and distributions, from bottom to top, of vertical feeders in the lower storey, horizontal passages in the middle storey and vertical outflows in the upper storey. The main outcome of this work is that cave patterns in hypogenic environments depend on a combination of factors such as (i) the evolution of the regional tectonic stress field, (ii) the thickness of mechanical units (single beds or bed packages) and bed-to-bed interlayer characteristics, and (iii) related fracture density. Results presented in this study are in agreement with numerical fluid flow simulations performed by different authors in other layered and fractured rocks (e.g. Doolin and Mauldon, 1996; Wang et al., 2017, and references therein), and indicate that the mechanical stratigraphy combined with the "speleo-stratigraphy" concept can be useful to predict large-scale karst porosity and cave morphology in carbonate reservoirs from tectonic evolution and stratigraphic setting.

2. Geological setting and the cave system

2.1. Tectonic and stratigraphic setting

The TBV and TBR cave system is developed in the Salitre Formation (Una Group) of the Campo Formoso Basin, in the northern part of the Sao Francisco Craton (Fig. 1). This cratonic area separated from its African counterparts during the opening of the South Atlantic Ocean in the Late Jurassic and Early Cretaceous (Trompette et al., 1992), and contains Meso- and Neoproterozoic sedimentary units overlying Paleoproterozoic and Archean basement units. Fold-related deformation affected the Neoproterozoic Salitre Formation carbonates during the Brasiliano Orogeny between 760 and 560 Ma (Brito Neves et al., 2014). In the study area, the Salitre Formation consists of a ~500 m thick unit made of shallow marine platform carbonate rocks intercalated with thin siliciclastic rocks (Dardenne, 1978; Bonfim et al., 1985). The Salitre Formation is capped by freshwater limestone probably of the Late

Pliocene-early Pleistocene Caatinga Formation (Penha, 1994; Auler, 1999). After deposition, the carbonates of Salitre Formation were subjected to diagenetic processes (mostly dolomitization), brittle deformation and intense karstification (Auler and Smart, 2003; Cazarin et al., 2019 and references therein).

Brittle deformation in the Salitre carbonates acquired during the Brasiliano Orogeny resulted in an E-W- to NNE-SSW-trending fold-and-thrust belt (Lagoeiro, 1990; Caxito and Ulhein, 2013). In the studied TBV-TBR caves, ~NE-trending fold hinges are associated with ~NE-striking joints and stylolites, i.e. parallel to the thrust system (Ennes-Silva et al., 2016). A second folding event, overprinting the NE-trending folds, is characterized by a mild E-W-oriented compression that resulted in a set of N-S fold hinges and E-W joint sets (Ennes-Silva et al., 2016). The TBV-TBR caves are maze systems stretching near and sub-parallel to the NE-trending fault. In the maze pattern, major lateral passages are controlled by NE-SW-striking fold anticlinal hinges characterized by intense fracturing (Ennes-Silva et al., 2016) which favoured the coalescence of adjacent cave conduits (Klimchouk et al., 2016).

From a stratigraphic point of view, the TBV-TBR cave system developed in a 50–60 m thick heterolithic carbonate-dominated sequence which encompasses five main stratigraphic units (Klimchouk et al., 2016), studied in detail by Cazarin et al. (2019). The lowermost unit 1 consists of massive cross-bedded oolitic grainstone about 15 m thick; its base has not been observed. Unit 2 is 1.5–2 m thick and consists of peloidal fine grainstone with chert nodules and plane-parallel stratification. Unit 3 is up to 1 m thick and contains microbial carbonates with laminites and stromatolites. Unit 4 is $<$ 1 m thick and consists of fine-grained siliciclastic rocks (siltstone, fine grained sandstones and clay) and marls. The uppermost cave-bearing unit 5 is $>$ 10–15 m thick and represented mostly by grainstone with abundant chert layers (lower unit 5A). At surface outcrops, a unit consisting of thin laminated carbonate limestone with chert lenses is interpreted as belonging to upper unit 5, here named Unit 5C. Between the upper and lower Unit 5, a discontinuous m-thick sequence made of 10–30 cm thick carbonate and shale layers has also been observed (unit 5B).

2.2. Hypogenic cave pattern

In plan view, the TBV-TBR cave system consists of a network of cave passages oriented NNE-SSW and E-W; the whole system forms an elongated “corridor” that follows the N65°E-strike of the thrust system at this site (Fig. 2A). These passages form the longest cave system in South America with total conduit lengths of 114 and 35 km long, respectively (Rubbioli et al., 2019). The hypogenic origin of TBV-TBR cave system was firstly proposed by Auler (1999) and Auler and Smart (2003) based on morphological features such as mixed network/ramiform pattern, widespread cupolas, vertical rifts, condensation-corrosion features, and the lack of features typical of epigenic processes (i.e., absence of sediments, absence of vadose speleogens, no link to surface geomorphology). These earlier studies assumed the formation of the caves in a shallow, lateral-flowing aquifer, due to the aggressiveness derived from oxidation of pyrite disseminated in the host rock. Klimchouk et al. (2016) further constrained the hypogenic origin of the cave system, provided speleo-morphogenetic evidence for the formation by ascending acidic paleo-fluids along fractures, and unravelled the functional organization of the cave system in the overall upwelling flow system, in which the presence of a leaky seal caused pronounced local lateral component of flow and speleogenesis. Concerning the source of dissolving fluids, Auler (2017) suggested that the absence of poorly soluble sulfur-derived minerals in the caves indicate that H_2S was not the main component of fluids ascending along fracture systems; more recently, Cazarin et al. (2019) also suggest that fluids were hydrothermal.

In vertical section, the functional organization of TBV-TBR caves, as described by Klimchouk et al. (2016), consists mainly of three cave-stratigraphic storeys (Fig. 2B): a lower, a middle and an upper storey. The lower storey is composed of recharge components (feeder cavities) through which ascending fluids entered the lateral maze cave interval from below; the middle storey is the main component which laterally integrates the whole cave system; and the upper storey is represented by outlets (dissolved vertical fractures) through which the fluids bypassed the seal and moved further upward (Klimchouk et al., 2016).

The lower storey is developed in the massive grainstone of unit 1 and consists of both sub-horizontal passages, chambers of different sizes and vertical conduits (Fig. 2C). Vertical rifts and inclined conduits and ramps connect the lower storey to the middle storey. The middle storey consists mostly of subhorizontal cave passages developed in 10–40 cm-thick carbonate layers of units 2 and 3 and partially capped by units 4 (siliciclastics) and 5A (cherty grainstone) (Fig. 2D). Such passages are associated mostly with anticline hinges oriented ~ NE-SW, and provide laterally extensive conduits with rectangular cross-sections. The upper storey comprises outlets formed along major fractures that cut across the seal units, and served as outflow discharge (Fig. 2E). In this model, vertical migration of fluids was hampered by differences in fracture density, limiting the growth of the cave system above unit 5. Overall, the three-dimensional pattern of the cave system is effectively organized to conduct rising flow in deep-seated confined conditions under stratigraphic constraints.

Recently, Cazarin et al. (2019) point to two main issues in the karstification process. First, they identified the hydrothermal assemblage in microscopic veins, which confirm previous interpretations that hydrothermal processes were responsible for the early karstification. Second, they indicated that dissolution enlarged fractures at the end of the eodiagenesis and mesodiagenesis and that dissolution processes mainly affected the carbonate units. In particular, this study recognized the importance of fractures but indicated the need of considering the role of the low-porosity siliciclastic unit (unit 4) in the sealing process.

The depth of cave formation was not established with exactness (Auler, 2017), but the host rocks were probably buried at least at several hundred meters ($>$ 600–900 m) as suggested by the presence of well-developed bedding-parallel stylolites in the carbonate beds (van Golf-Racht, 1982). Furthermore, deposition of younger sequences above Salitre carbonates (Japsen et al., 2012) could have been responsible for additional burial episodes. Finally, the age of cave formation is still unconstrained and two main possibilities were proposed (Klimchouk et al., 2016): one suggesting that speleogenesis occurred during the late-stage of Brasiliano orogeny (550 Ma), the other during the rifting event associated with break-up of Pangea in the Triassic-Cretaceous.

3. Methods

Classical structural analysis was performed in 34 sites distributed in several passages distributed through TBR and the most of the TBV (except its southwestern part) to reconstruct the structural evolution of the Salitre carbonates in the study area. Different deformation elements (i.e., joints, veins, tectonic stylolites, and fold limbs) were measured (n = 433 data) and statistically analysed using Daisy software (Salvini et al., 1999). Structural data were integrated with fracture attribute quantification (mostly spacing) in all the speleo-stratigraphic units (Fig. 2B) identified by Klimchouk et al. (2016). Fracture data acquisition was performed along 23 bed-parallel linear scan lines (e.g., Zeeb et al., 2013 and references therein) oriented orthogonal to the fracture sets in order to avoid further corrections. Measured fracture attributes are spacing (S), height (H, vertical persistence), and thickness of fractured beds (for strata-bound fractures, i.e., confined within beds). A total of 637 data of fracture spacing were collected and analysed. In the middle storey, most of fractures measured in scan lines are bed-confined (i.e., strata bound) in agreement with the mechanical stratigraphy concept. In the lower and upper storeys, more persistent throughgoing fractures (i.e., multilayer structures whose spacing exceed the size of the cave passages) are common but difficult to measure systematically

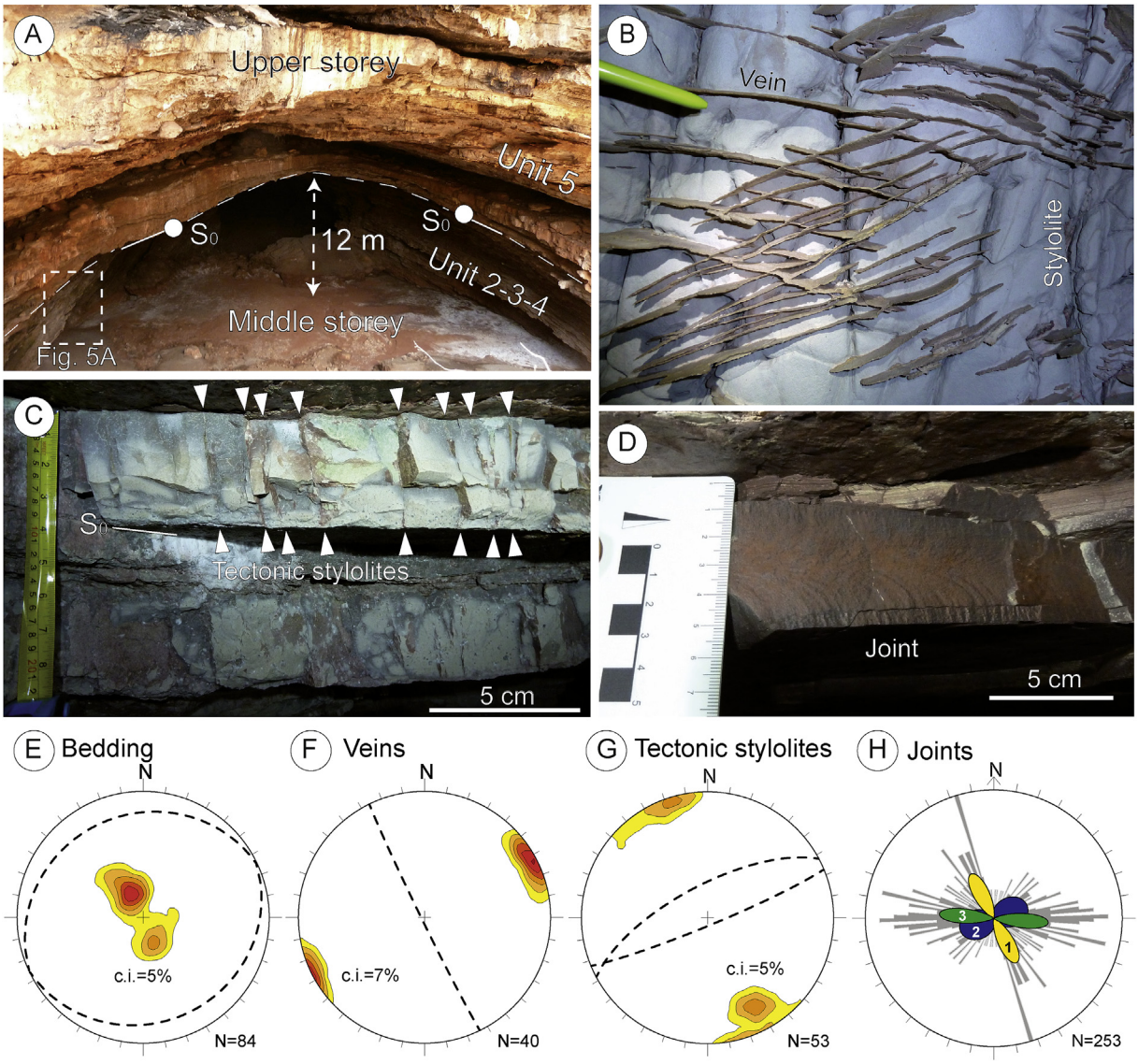

Fig. 3. Deformation elements measured in the TBV-TBR cave system. (A) NE-SW-oriented fold developed in the well-layered units of the middle storey. (B) Example of conjugate set of subvertical silica veins (plan view of the cave roof); Veins are orthogonal to tectonic stylolites. (C) Example of closely-spaced, strata-bound tectonic stylolites developed in marly limestone. (D) Plumose structure developed on joint surface. (E) Stereographic projection (equal area projection, lower hemisphere of Schmidt net) of contoured pole to bedding in the TBV-TBR cave system; average bedding planes are indicated by the two cyclographics. (F) Contoured pole to veins and mean NNW-SSE-trending plane. (G) Contoured tectonic stylolites and related mean planes. (H) Rose diagram showing three main joint sets obtained by a Gaussian best fit of total joint data. C.i. = contouring interval. S_0 = bedding.

with scan lines due to limitations in cave outcrop exposures. Therefore, spacing of throughgoing fractures were not always directly measured by linear scan lines but estimated in map view after careful cave mapping (Klimchouk et al., 2016).

Furthermore, uniaxial compression strength (UCS) tests were performed with a portable Schmidt hammer in surfaces orthogonal to bedding to constrain the mechanical properties of the five units (e.g., Zoback, 2007; Yaşar and Erdoğan, 2004; Aydin and Basu, 2005; Aydin, 2009; Yurdakul et al., 2011; Alikarami et al., 2013). The values of UCS for the five units were obtained indirectly by empirical relations based on the Schmidt hammer rebound value (Kolaiti and Papadopoulos, 1993) and following pre-established standards by the American Society for Testing and Material (ASTM, 2001).

4. Results

4.1. Structural data

Deformational elements measured in the TBV-TBR cave system mostly consist of meter-scale gentle folds (Fig. 3A), bedding-parallel stylolites, mm-thick bed-perpendicular veins filled with silica of hydrothermal origin (Cazarin et al., 2019) and locally organized in conjugate sets (Fig. 3B), bedding-orthogonal tectonic stylolites (Fig. 3C), and opening-mode fractures including throughgoing joints and strata-bound joints with plumose structures (Fig. 3D). Subordinately, minor reverse and strike-slip faults were also measured.

Bedding-parallel stylolites in the units 1 and 5 (i.e., grainstones) are commonly characterized by rough-walled geometry with mm-to cm-long tooth. In units 2–4, bed-parallel stylolites are smooth and planar. Gentle folds are better developed in the middle storey, i.e. in the well-layered lithologies of units 2, 3 and 4, where master passages are localized. Collectively, fold limbs measured in 16 cave passages strike

N65°E and dip < 10–15° toward both NW and SE (Fig. 3E). Calculated mean fold hinge is sub-horizontal and oriented N65°E. Veins are sub-vertical and strike N25°W (Fig. 3F). Tectonic stylolites are orthogonal to bedding and particularly well developed in the marly limestone of unit 4; they strike ~ N65°E, i.e. sub-parallel to the fold hinge (Fig. 3G). Joints do not show a clustered trend but statistical analysis of total data indicates 3 main sets (Fig. 3H): set 1 strikes N27.2°W ± 12.8° (i.e., parallel to veins and orthogonal to inferred fold hinges), set 2 strikes N69.3°E ± 35.3° (i.e., parallel to tectonic stylolites and fold hinges), and set 3 strikes ~ E-W (N85.4°W ± 10.6°).

4.2. Stratigraphy and fracture pattern

The three speleo-stratigraphic storeys shown in Fig. 2B are characterized by fractures with different attributes (density, spacing, height or vertical persistence) which depend on the lithological properties of the stratigraphic units. In general, the lower and upper storeys are characterized by low fracture density imparted by vertically-persistent, non strata-bound (i.e., throughgoing) fractures in massive thick beds, whereas the middle storey is characterized by high fracture density associated with well-developed strata-bound fractures in thin beds.

In the lower storey, the cross-bedded oolitic grainstone (unit 1) consists of massive beds with thickness between ~3 and ~7 m (Fig. 4A and B). These m-thick beds are commonly amalgamated and characterized by well-developed bedding-parallel stylolites without clay-rich interlayers (inset in Fig. 4B). Such stylolites are rough-walled and generally not selectively dissolved. Subvertical joints, which commonly localize dissolution along feeders (Fig. 4A), are spaced 0.6–0.7 m in beds ~3 m thick (Fig. 4B) and ~3 m in beds 7 m thick (Table 1). In places, small NE-SW-trending strike-slip faults were observed (Fig. 4C). Such faults have left-lateral kinematics, and are characterized by m-thick damage zones with fractures spaced few centimetres up to decimetres.

In the middle storey, the well-stratified rocks (units 2–4) with distinct beds and interlayers are characterized by closely-spaced strata-bound fractures which collectively provide high fracture density (n° fractures per meter) (Fig. 5A). Fine-grained grainstones of unit 2 are 0.3–0.6 m thick and have fracture spacing between 0.25 and ~0.4 m (Fig. 5B, Table 1). Microbial limestones (stromatolites and laminites of unit 3) have beds 0.14–0.7 m thick, and spacing between 0.15 and 0.45 m (Fig. 5B, Table 1). Similarly, the fine siliciclastics and marls of unit 4 are 6–9 cm thick and characterized by fractures spaced between ~4 and ~7 cm (Fig. 5B and C, and Table 1).

In the upper storey, the Unit 5 is characterized by different fracture pattern (Fig. 6). The lower part of the cherty grainstone of unit 5A is characterized by beds 0.1–0.32 m thick and fracture spacing between 0.1 and 0.2 m (Fig. 6A, and Table 1). When visible, carbonate and marls between the lower and upper unit 5 (i.e., unit 5B) are characterized by beds 9 and 22 cm thick, and fracture spacing of ~5 and ~16 cm, respectively (Fig. 6B, Table 1). Finally, the upper micritic limestone of unit 5C, which is the only unit exposed in outcrops (Fig. 6C), is characterized by cm-to dm-thick beds and the absence of well-developed bed-to-bed interlayers (Fig. 6D and E); in this upper unit, throughgoing fractures are widely spaced up to tens of meters (i.e., fractures are developed in a mechanical unit of several meters thick which encompass many beds), showing localized dissolution features (Fig. 6C and D).

All fracture data described above are summarized in Fig. 7 where mean fracture spacing in each scan line is plotted in a log scale against corresponding position in the cave stratigraphy. Collectively, well-layered units (2, 3, 4, and 5B) with strata-bound fractures are characterized by high fracture density (n° fractures/m), whereas thick mechanical units 1 and 5C with broadly spaced throughgoing fractures have lower fracture density.

4.3. Fracture spacing versus bed thickness

Fracture spacing data are plotted against corresponding bed thickness (for strata-bound fractures) and mechanical unit thickness (for throughgoing fractures) in Fig. 8. Despite the large variability, it is evident that mechanical units with thickness < 1 m are characterized by closely-spaced strata-bound fractures (joints and stylolites), whereas mechanical units > 2–3 m thick, i.e. massive carbonates of lower Unit 1 and upper micritic mudstone of Unit 5C, have greater fracture spacing (mostly joints). Such direct relationship between fracture spacing and bed thickness is in general agreement with previous studies in layered carbonates (e.g., Narr and Suppe, 1991).

4.4. Throughgoing fractures

As mentioned in previous sections, lower unit 1 and upper units 5A-C contain also non strata-bound, throughgoing fractures. They are observed in the walls of passages and rooms of the lower and upper storeys and, where possible, were measured in scanline surveys

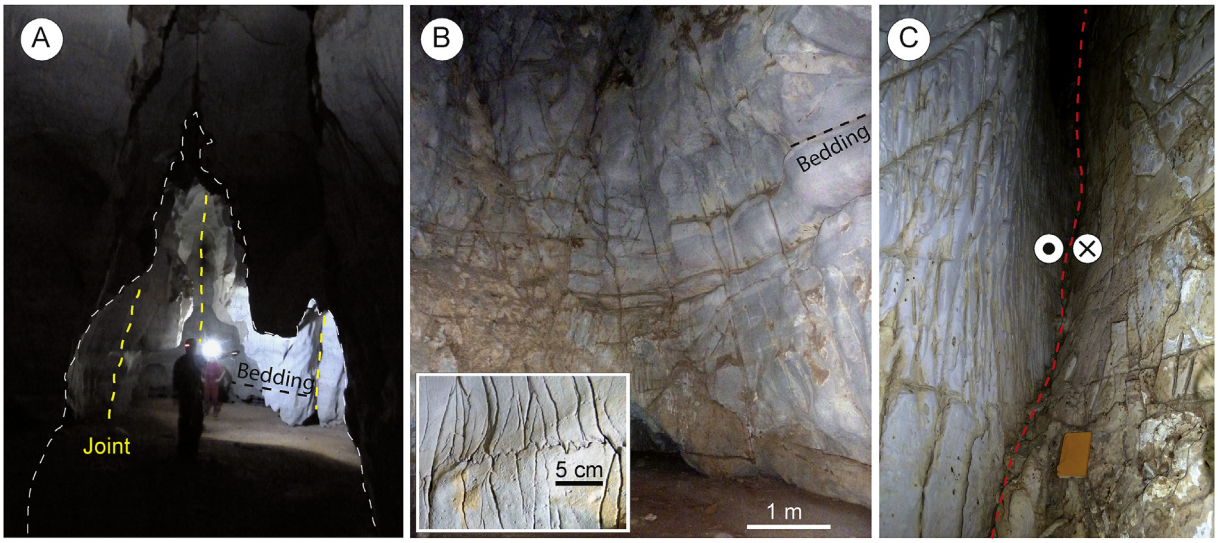

Fig. 4. Fracture pattern in the oolitic massive grainstone of the lower storey (Unit 1). (A) Example of dissolution controlled by fractures. (B) Fractures spaced 0.7–0.8 m in massive beds (insert shows tight and closed bedding-parallel stylolites). (C) Example of closely-spaced synthetic fractures developed in a left-lateral strike-slip fault zone oriented NE-SW. Note dissolution associated with this small scale fault zone. Field book for scale is 13 × 21 cm.

Table 1
Summary table showing the fracture statistics from all scan lines performed in the 5 units. (* = subsidiary fractures associated with major joint; ** = joint developed in a fault zone).

UNIT	LITHOLOGY	BED/MECH. UNIT THICKNESS (mm)	FRACTURE SPACING (mm)	ST. DEV.	FRACTURE HEIGHT (mm)	N° DATA	ELEMENT TYPE
5C	MICRITIC LIMESTONE	3400	2301.4	1414.1	> bed	6	N65°E Joint
5B	CARBONATE AND MARLS	92	46.9	30.5	strata-bound	47	N65°E Joint
5B	CARBONATE AND MARLS	220	158.7	88.2	strata-bound	26	N65°E Joint
5A	CHERTY GRAINSTONE	194	206.5	82.3	strata-bound	12	N26°W Joint
5A	CHERTY GRAINSTONE	160	171.7	55.2	strata-bound	12	N65°E Joint
5A	CHERTY GRAINSTONE	250	199.2	87.4	strata-bound	35	N26°W Joint
5A	CHERTY GRAINSTONE	110	123.1	68.1	strata-bound	25	N65°E Joint
5A	CHERTY GRAINSTONE	320	133.7	77.7	strata-bound	41	N26°W Joint
5A	CHERTY GRAINSTONE	140	138.5	58.6	strata-bound	20	N65°E Joint
4	SILTSTONES	60	67.7	54.8	strata-bound	44	N65°E Joint
4	SILTSTONES	60	54.6	99.0	strata-bound	64	N26°W Joint
4	SILTSTONES	90	44.2	27.1	strata-bound	37	N65°E Stylo
3	LAMINITES	200	149.6	114.2	strata-bound	27	N70°E Joint
3	LAMINITES	140	186.2	113.0	strata-bound	36	N26°W Joint
3	STROMATOLITE	230	255.5	115.2	strata-bound	23	N65°E Joint
3	STROMATOLITE	710	452.0	298.1	strata-bound	18	N26°W Joint
2	FINE GRAINSTONE	320	38.9	33.8	strata-bound	57	N65°E Joint
2	FINE GRAINSTONE	620	255.2	141.1	strata-bound	27	N65°E Joint
1	OOLITIC GRAINSTONES	7000	103	73.7	< bed	43	*N65E Joint
1	OOLITIC GRAINSTONES	2930	783.8	407.3	3739.2	13	N65°E Joint
1	OOLITIC GRAINSTONES	2870	583.6	253.5	1762.9	14	E-W Joint
1	OOLITIC GRAINSTONES	7000	3508.7	1970.0	5650.8	10	N26°W Joint
1	OOLITIC GRAINSTONES	3000	42.5	24.2	2000–3000	10	**E-W joints

(Table 1). However, these units are also characterized by the presence of major throughgoing fractures that are not represented, or barely represented, in scanlines, as they are completely or almost completely exploited by dissolution and consumed by the cave space (Fig. 9).

Traces of throughgoing fractures are sometimes observable in the ceilings of passages or in the walls in their lateral terminations (Fig. 9B and G), but in most cases they cannot be observed and measured as these surfaces are distant and not immediately accessible, or because these guiding fractures are often entirely consumed by the cave space. Some characteristics of throughgoing fractures consumed by speleogenesis can be inferred from the size, orientation, and spacing of linear cave elements formed along them.

In the lower storey (massive oolitic grainstone of unit 1), passages guided by vertical or steeply inclined throughgoing fractures occur in clusters which are largely isolated in the lateral directions from other similar clusters nearby (Fig. 9E and F). They have predominantly ~ NE-

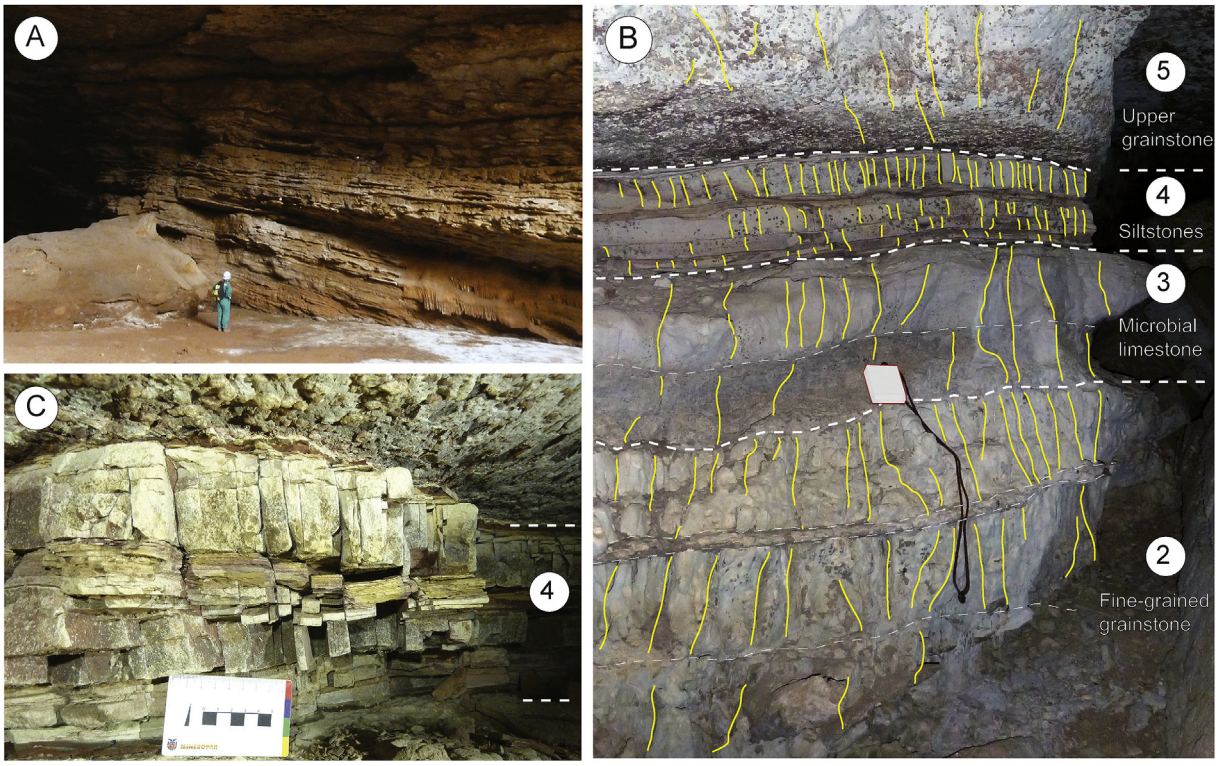

Fig. 5. Fracture pattern in the middle storey (Units 2, 3 and 4). (A) Meter-thick package of well-layered rocks of Unit 2, 3 and 4, characterized by intense fracturing. (B) Example of strata-bound fractures developed in Units 2, 3 and 4, visible in the wall of a NE-SW-trending master passage. Compass for scale. (C) High fracture density (n° elements per meter) in siliciclastics and marls of Unit 4. Note well developed bed-to-bed boundaries.

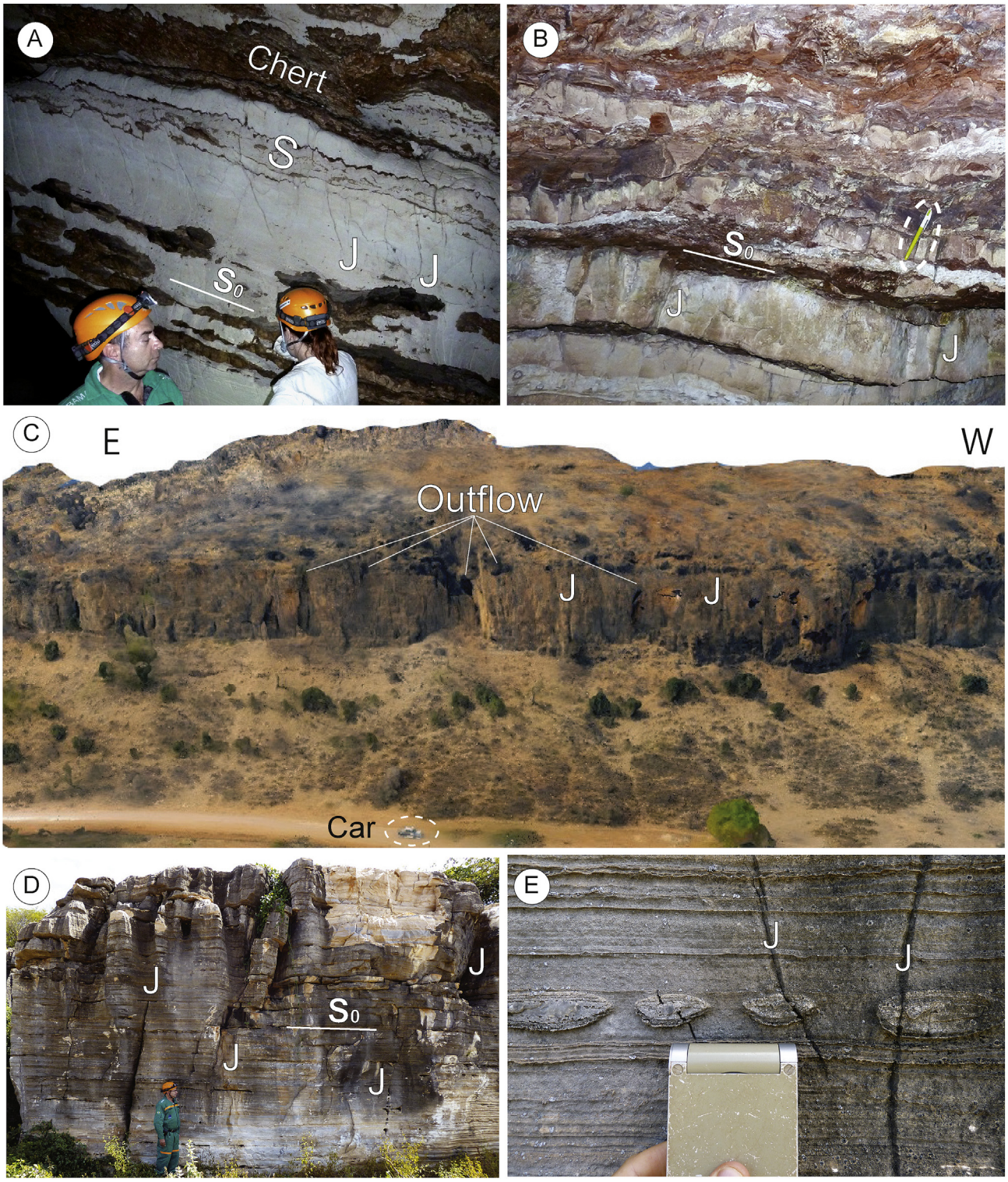

Fig. 6. Fracture pattern in the upper storey (Units 5A, B and C). (A) Fractures in the fine-grained, cherty grainstone in the lower part of unit 5A. Note bedding parallel stylolites. (B) Strata-bound fractures in the well-layered siliciclastics of unit 5B. Circle indicates pen for scale. (C) Outcropping micritic limestone of unit 5C, characterized by m-spaced fractures with local dissolution features. (D) Set of non strata-bound throughgoing fractures developed in the unit 5C, showing heights greater than bed thickness. (E) Detail of joints terminating at laminations and showing negative relief due to selective dissolution in unit 5C. S0 = bedding; S = stylolite; J = joint.

SW, and subordinately NW-SE, orientation and lengths ranging from 10 to 30–40 m. When such passages occur in systematic sets, as shown in Fig. 9E, their spacing can be estimated at 5–15 m. Vertical dimensions of throughgoing fractures cannot be determined as lower parts of passages formed along them are obscured by sediments (Fig. 9H and G). The minimal visible heights start at ~10 m but these fractures may extend down for many tens of meters. Some deep rift-like pits at the bottom of the lower-storey cavities further extend to depths of over 10 m, where they are blocked by boulders and sediments (Fig. 9H and J).

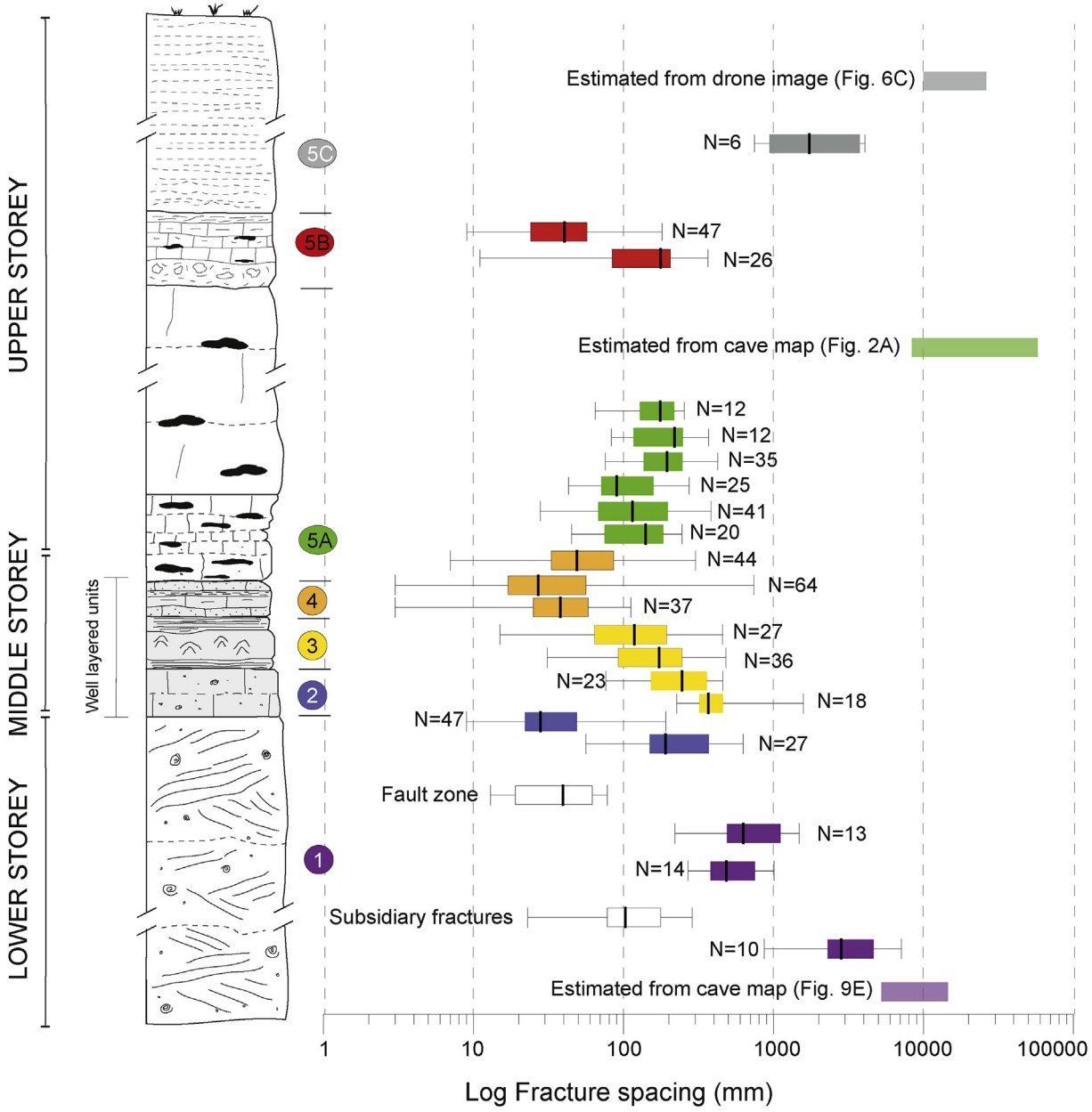

Fig. 7. Fracture spacing data versus cave stratigraphy (not to scale). Units 1, 5B, and 5C have throughgoing fractures spaced several meters up to tens of meters, whereas well-layered units 2, 3 and 4 have strata-bound fractures spaced from few mm up to 0.2 m. Stratigraphic units: 1) massive oolitic grainstone, 2) grainstone, 3) microbial carbonate and laminites, 4) silt, clay and marls, 5A) grainstone with chert lenses, 5B) breccia, carbonates and shale, 5C) micritic limestone.

Importantly, the most of throughgoing fractures in the lower storey terminate at the upper part of unit 1 and their top tips generally do not cross units 2–4. This is strongly evidenced by the fact that only tiny fracture traces (if any) can be observed at the ceiling of the lower-storey passages, and that such passages may go beneath the middle-story passages (units 2–4) being not connected to them (Fig. 9E). Only in rare occasions, the upper tips of throughgoing fractures in unit 1 reach units 2–4, which causes the formation of rising chimneys (outlets from the perspective of the lower story; Fig. 9G) connecting the lower storey with the passages in the middle storey (the connections are seen as feeders from the perspective of the middle story).

In the upper storey (units 5A-B), throughgoing fractures are represented by rift-like (rarely oval shaft-like) passages that infrequently occur throughout the cave system but form the most of central sector in TBV (Figs. 2 and 9A and B). In this sector, rift-like passages of heights up to over 10–15 m and lengths up to over 100 m are oriented predominantly E-W, with some passages trending NE-SW. Their spacing commonly varies between 20 and 60 m. These estimates give an idea of characteristics of guiding throughgoing fractures. Similar rift-like passages, partly unroofed, occur locally in unit 5C, observed in the quarry and in the cliff at the outskirts of the Laje dos Negros village (Figs. 6C and 9 C and D). Spacing values presented in this section are reported in the fracture log in Fig. 7.

4.5. Uniaxial compressive strength

The UCS data collected in the five lithostratigraphic units from TBV and TBR cave system are summarized in Fig. 10. Based on data distribution, the stratigraphic units can be grouped as three distinct geomechanical units, in which units 1 (massive grainstone with cross-bedding stratification), 2 (well layered fine grainstone with chert nodules), and 3 (well layered microbial carbonates) have similar

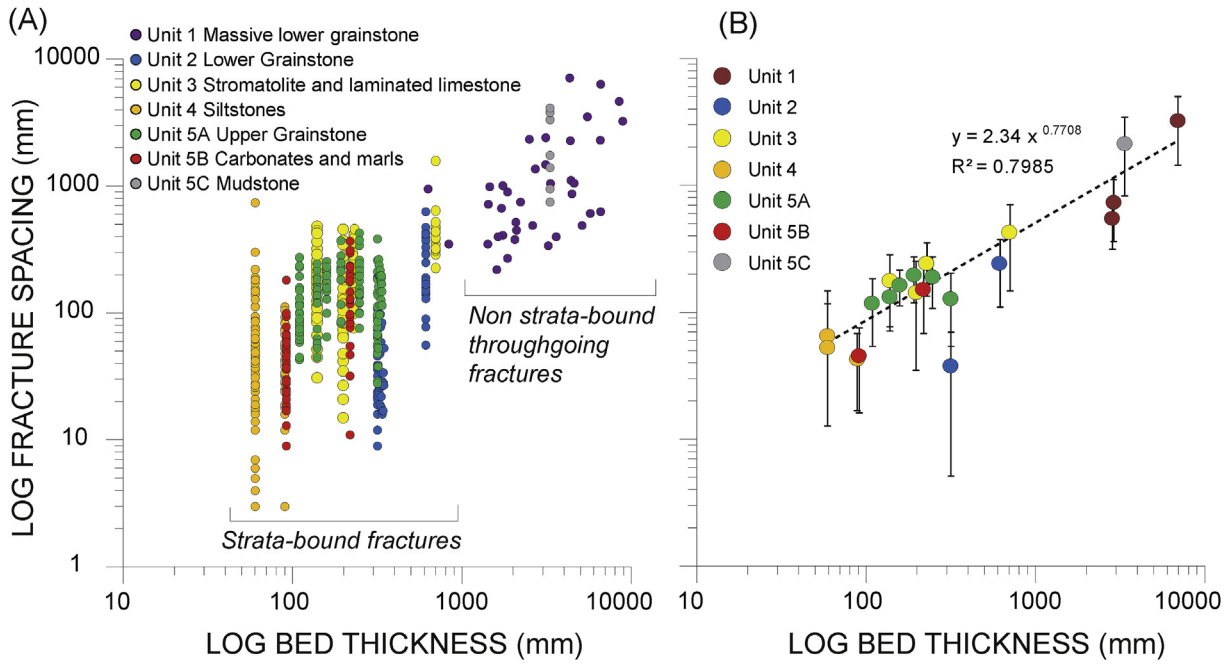

Fig. 8. Log-Log diagrams showing fracture spacing versus bed thickness. (A) Individual spacing data collected in each scan line. (B) Mean spacing values with standard deviations.

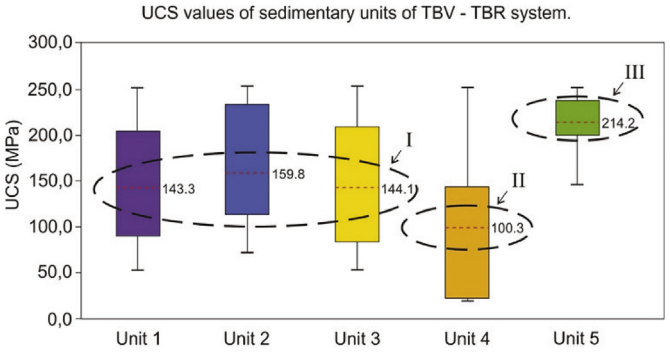

Fig. 9. Photographs showing passages at the upper (A through D) and the lower (G through J) stories of the TBV-TBR cave system, developed along throughgoing fractures. Panels E and F, modified from Klimchouk et al. (2016), show the plan and the section of a cluster of the lower-story passages (in orange) and their relationship with the middle-storey passages (in grey). Note that these stories are vertically connected only in one locality (through outlets-feeders). 1: feeders; 2: fractures. (For interpretation of the references to colour in this figure legend, the reader is referred to the Web version of this article.)

geomechanical behaviour with average UCS values ranging from 143.3 MPa to 159.8 MPa. Unit 4 (well layered fine siliciclastic layers and marls) and unit 5 (crystalline carbonate with chert layers) show the lower and higher values of 100.3 and 214.2 MPa, respectively.

5. Discussion

5.1. Structural evolution and cave pattern

It is well known that in contractional tectonic settings (i.e., folded carbonates) the fluid system structure is defined by the pathways along which fluids move (e.g., Evans and Fischer, 2012). Such permeability pathways mostly depend on the interaction between stratigraphy and fracture distribution, connectivity and hydrological properties (Odling et al., 1999). In the study area, the complex fracture network developed in the three different cave storeys, composed of strata-bound joints, throughgoing fractures (veins, joints and minor faults), strata-bound bed-normal stylolites, and bed-parallel stylolites, provided an effective pathway for dissolving rising fluids that led to the extensive development of hypogene TBV-TBR cave system. The NE-trending TBV-TBR caves are located in the proximity of a NE-trending regional thrust fault (Fig. 1), where fold-related deformation is greater than surrounding areas (Ennes-Silva et al., 2016). Klimchouk et al. (2016) pointed out that the TBV and TBR caves form a NE-SW-trending belt, sub-parallel the thrust fault, which localization is determined by specific structural conditions permitting an access of deep fluids to the bottom of the Salitre Formation and rising flow across it, most likely the presence of a corridor of throughgoing fractures disrupting both the Salitre carbonates and the underlying rocks.

Structural data presented in Fig. 3 support an interpretation of two main compressional events, consistent with Ennes-Silva et al. (2016). The first event (compression oriented NNW-SSE) was responsible for fracturing and gentle folding with hinges oriented N65°E, as indicated by bedding dip domains measured in the caves (Fig. 3A). Layer-parallel shortening during the early stage of this compressional event promoted both subvertical veins and joints oriented N25°W and tectonic stylolites oriented N65°E (Fig. 3F and G). With further compression, fold amplification passively rotated the previously-formed tectonic stylolites, as indicated by the constant orthogonal relationships between bedding planes and tectonic stylolites in the fold limbs (compare stereonets in Fig. 3E and G). Furthermore, also the N65°E joints (set 2 in Fig. 3H) probably developed during fold amplification by outer-arc extension.

A second, mild contractional event with and E-W horizontal compression is supported by the E-W-trending joints (set 3 in Fig. 3H) and by minor N-S-trending fold hinges (Ennes-Silva et al., 2016). The two deformational events provided the complex 3D network of fold hinges and fractures with multiple orientations that was used by deep dissolving fluids during the main speleogenetic phase. The link between tectonic evolution and cave development is indicated by the overall correspondence between fold hinges orientation, fractures orientations (Fig. 3E–H) and cave passages orientation in plan view (Fig. 2A; and compare Figs. 5 and 6 in Ennes-Silva et al., 2016). Furthermore, the complex deformation history documented in this study may have favoured the formation of large throughgoing fractures through linking strata-bound and non strata-bound fractures in different stratigraphic

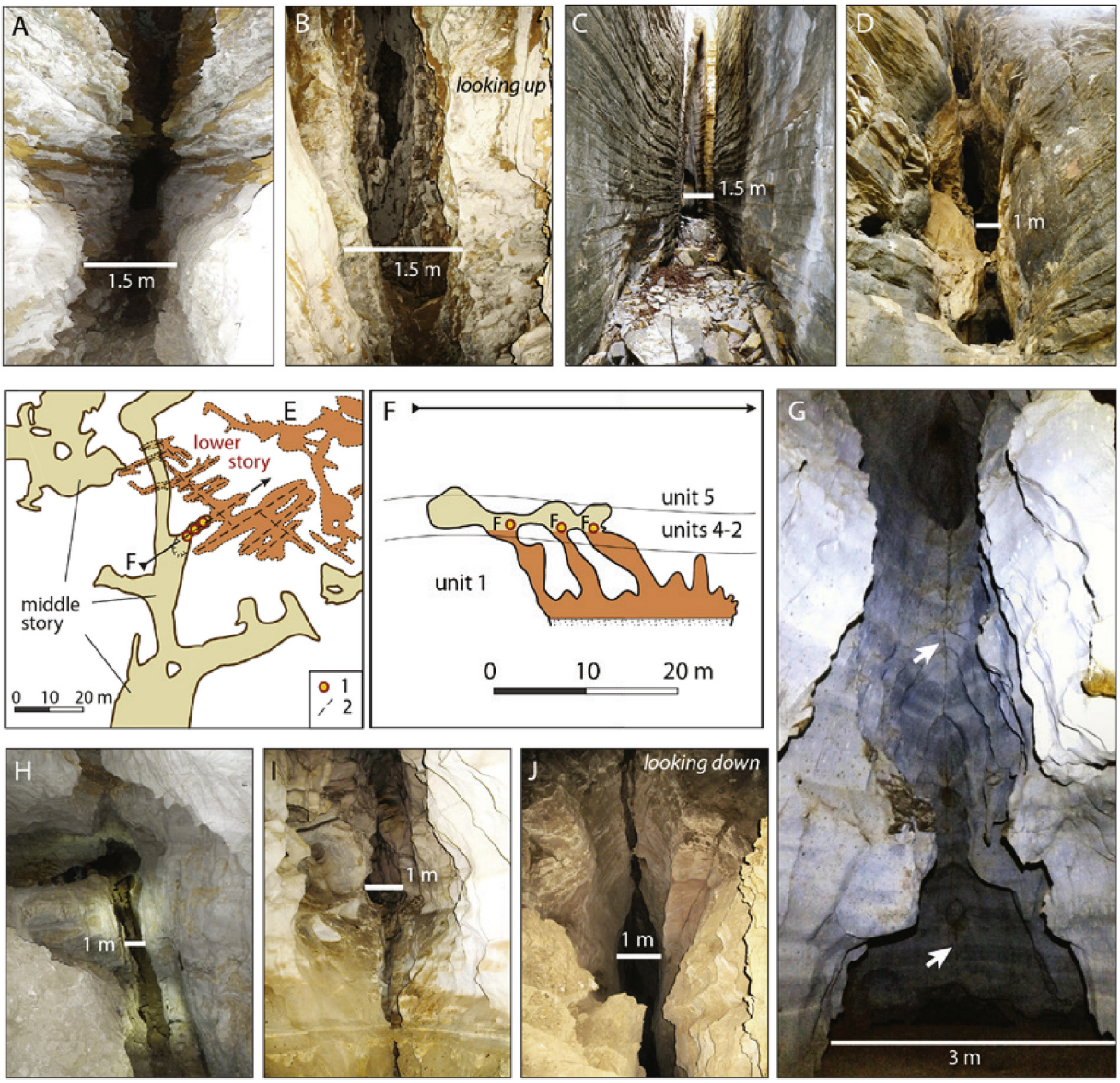

Fig. 10. Geomechanical data obtained from the five stratigraphic units in TBV – TBR cave system.

units, which locally increased fracture connectivity and determined the vertical, functional organization of TBV-TBR.

5.2. Fracture stratigraphy and functional organization of the cave system

Klimchouk (2005, 2007, 2019) stressed the importance of hydrostratigraphy (structure of a rock sequence from the perspective of the groundwater flow) in controlling patterns of hypogenic caves, and demonstrated that hydrostratigraphy and cave patterns can be determined not only by lithological differences but also by the vertical distribution of fractures, which does not necessarily coincide with lithostratigraphy.

The TBV-TBR cave system was formed under deep-seated, confined conditions by deep flow rising across the Salitre Formation within a ~NE-trending corridor (Klimchouk et al., 2016). Although the source of the cave-forming fluids is still uncertain, it is obvious that they came from below the bottom of the Salitre Formation. In layered carbonate sequences of low matrix porosity, the presence of throughgoing disruptions (throughgoing faults, fractures, and fracture zones; Gross and Eyal, 2007) is of primary importance for cross-formational flow and hypogene speleogenesis as they determine the vertical connectivity of different hydrostratigraphic units. The relationships between stratigraphy, fracture properties and the three speleo-stratigraphic storeys in the studied cave system are summarized in the conceptual model of Fig. 11 and discussed below.

This study shows that meter-thick dolomitic beds (unit 1) or very thick mechanical units made of thin marly limestone beds with high uniaxial compressive strength values (units 5A and 5C) are prone to develop widely spaced fractures (Fig. 7), including large throughgoing fractures, which determined vertical permeability anisotropy. Throughgoing fractures in TBV-TBR caves are characterized by large spacing and strong vertical persistence, and mostly consist of minor faults with fractured damage zone (Fig. 4C) and isolated opening-mode fractures such as veins and joints. The presence of large throughgoing fractures in unit 1 enabled inputs (recharge) to the cave system and controlled the formation of the lower cave-stratigraphy storey. Persistent fractures in units 5A-C enabled outputs (discharge) from the cave system, breaching the hydrostratigraphic seal formed by otherwise low-permeable unit 5A. Importantly, most of the lesser non strata-bound fractures (those documented in scanline surveys) do not demonstrate significant alteration by hypogene dissolution, whereas larger throughgoing fractures are almost invariably heavily used and largely consumed by dissolution. This clearly shows that the presence of large

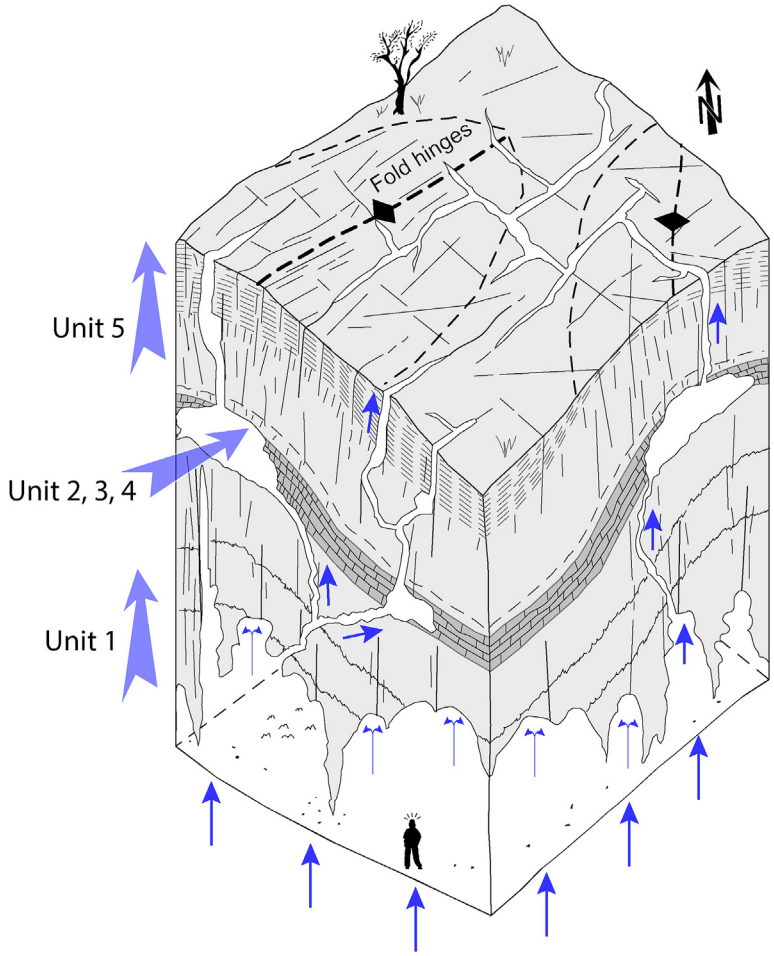

Functional organization	Fracture pattern	Permeability anisotropy
Unit 5 - Outflow discharge	Throughgoing and widely spaced joints	Vertical
Units 2, 3, 4 - Lateral redistribution	Strata-bound joints and stylolites spaced 0.1-0.3 m	Horizontal
Unit 1 - Recharge rising flow system	Throughgoing and widely spaced joints and faults	Vertical

Fig. 11. 3D block diagram showing a conceptual speleogenetic model with main structural, stratigraphic and morphological features of TBV-TBR caves in Brazil.

throughgoing fractures was critical in supporting cross-formational flow in units 1 and 5A-C. Also important is the fact that large throughgoing fractures in unit 1 and units 5A-C (and respective cavities formed along them) have different distributions through the area that mismatch each other in the plan view (Klimchouk et al., 2016). Individual sub-vertical feeders and their merged clusters at the lower cave-stratigraphy storey are more widely distributed across the cave area (although they tend to concentrate along the NW border of the cave), whereas rift-like and shaft-like components in the upper storey are generally much less in number and highly localized in a few locations. This mismatch forced generally upwelling flow to explore lateral pathways to integrate the input and output components.

On the contrary, gently folded thin beds with well-developed planar interlayers in units 2–4, despite the lower uniaxial compressive strength values, are prone to develop strata-bound fractures (both joints and stylolites, Fig. 3C and D), and resulting fracture density (n° fractures/m) is greater than thick mechanical units 1 and 5 (Figs. 5, Fig. 7, Fig. 8). This favors a greater horizontal permeability and fluid flow along these beds, also facilitated by erodible bed-to-bed planar interlayers. Thus, these units allowed for lateral redistribution of rising flow between the input and output components and eventual lateral integration of the cave system by the development of sub-horizontal passages along sub-vertical throughgoing fractures and ~NE-trending fold hinge zones. The larger and longer passages that form the backbone of the cave in the plan view developed along fold hinges, where the fracture density is greater. The fractured hinges in specific stratigraphic levels of units 2–4 served as along-strike major fluid conduits (cf. Fischer et al., 2009; Evans and Fischer, 2012, and references therein).

5.3. Role of bed-to-bed interlayers

Two other important factors may have controlled the permeability tensor anisotropy during TBV-TBR cave development, which are (1) the aperture of different types of fractures, and (2) the nature and characteristics of bed-to-bed interfaces (cf. Wang et al., 2017). It is well known that permeability structure of fractured rocks is sensitive to the magnitude of fracture aperture (both bed perpendicular and bed parallel). For example, Doolin and Mauldon (2001) showed that a reduction in bedding plane aperture reduces the bed normal permeability up to three orders of magnitude. The lower unit 1 has bedding-parallel stylolites with rough pattern imparted by cm-long tooth, and are not selectively dissolved (inset in Fig. 4B), indicating they were not used during speleogenesis and didn't provided significant horizontal flow pathways. Conversely, the dissolved bed-to-bed planar interfaces in well layered units 2–4 (Fig. 5A), also characterized by high fracture density (Fig. 7 and Table 1), indicate that horizontal flow was effectively enhanced in the middle storey. In the cherty limestone of lower unit 5, the absence of open bed-to-bed interfaces can contribute to the reduction of bed normal permeability. This unit served as a seal across most of the TBV cave (Cazarin et al., 2019), breached only by rare throughgoing fractures. This forced the fluid flow in lateral directions, mainly along fractured fold hinges characterized by well developed, open bed-to-bed interlayers. Our interpretation is also supported by numerical simulation in layered systems, devoted to investigate fluid flow in the bed-parallel versus bed-normal direction (Doolin and Mauldon, 1996; Wang et al., 2017, and references therein). Such works demonstrated that fluid flow direction depends mostly on the spacing and aperture of both joints and bedding planes, as well as by the

vertical persistence of bed-normal joints (Jourde et al., 2007), consistently with the model provided in Fig. 11. Furthermore, Jacquemyn et al. (2012) suggested that in layered carbonates containing stratabound joint networks, intensive karstification tends to occur selectively along bedding plane boundaries between mechanical units which show a contrast in fracture density (i.e., unit 1, units 2–4, and unit 5 in our case).

6. Conclusions

Our analyses confirm the functional organization of the TBV-TBR cave system, revealed in Klimchouk et al. (2016) and based mainly on the morphogenetic analysis, and demonstrate the major role of mechanical and fracture stratigraphy in controlling fluid flow and hypogene speleogenesis in layered carbonate sequences. Major results of our study can be summarized as follow:

1) Regional tectonic stress evolution imposes a complex fracture pattern derived from two compressional events that determined the position and the 3D geometry of the cave system.
2) Lower, m-thick dolomite beds show fractures greater than bed thickness (persistent throughgoing fractures) which acted as vertical feeders; intermediate, well-layered dm-thick silty carbonates are characterized by strata-bound fractures and host the main horizontal cave passages; upper mudstone and micritic limestone characterized by vertically extended fractures greater than bed thickness acted as vertical outflow for hypogenic fluid discharge. High density stratabound fractures in thin beds tend to form networks that are well connected, that serve as conduits of enhanced horizontal fluid flow connecting isolated vertical permeability structures from adjacent units.
3) Mechanical stratigraphy (unit 2, 3 and 4) and fracture stratigraphy (units 1 and 5) applied to speleogenetic studies represents a valuable tool to study karst systems in stratified carbonate rocks, allowing for the recognition of vertical patterns of conduit systems and horizons that favour vertical versus horizontal enhanced fluid flow.
5) The fracture stratigraphy presented in this study may serve as a first-order prediction of karst development and sealing properties in layered carbonate units from borehole data that can be expanded to the basin scale.

Author contribution section

Balsamo, F. – Structural data collection, data analysis, conceptualization, writing original draft. **Bezerra, F.H.R**– Structural data collection, conceptualization, funding acquisition, writing review and editing. **Klimchouk, A.B.** – Speleogenetic analysis, conceptualization, writing review and editing. **Cazarin, C.L.** – Funding acquisition, stratigraphic analysis, project administration. **Auler, A.S.** – Speleogenetic analysis, conceptualization, writing review and editing Nogueira, F.C. – Structural data collection. **Pontes C.** – *UCS data collection and analysis,* writing review and editing.

Acknowledgements

We kindly thank Joe De Waele and one anonymous reviewers for their constructive revision which significantly improved the manuscript. We thank the Brazilian Agency of Oil, Gas, and Biofuels (Agência Nacional do Petróleo, Gás e Biocombustíveis, ANP). This work was sponsored by two Petrobras/Federal University of Rio Grande do Norte projects, granted to F.H.R. Bezerra (1 - Faults, fractures, facies and fluidflow in karst carbonate system: implications for the architecture, prediction of secondary permeability–porosity in carbonate rocks; 2 - Advanced project of acquisition and interpretation of parameters for the characterization and modelling of karstified reservoirs).

Appendix A. Supplementary data

Supplementary data to this article can be found online at https://doi.org/10.1016/j.marpetgeo.2019.104207.

References

Alikarami, R., Torabi, A., Kolyukhin, D., Skurtveit, E., 2013. Geostatistical relationships between mechanical and petrophysical properties of deformed sandstone. Int. J. Rock Mech. Min. Sci. 63, 27–38. https://doi.org/10.1016/j.ijrmms.2013.06.002.

Antonellini, M., Nannoni, A., Vigna, B., De Waele, J., 2019. Structural control on karst water circulation and speleogenesis in a lithological contact zone: the Bossea cave system (Western Alps, Italy). Geomorphology 345, 106832. https://doi.org/10.1016/j.geomorph.2019.07.019.

ASTM, 2001. ASTM. Standard Test Method for Determination of Rock Hardness by Rebound Hammer Method. ASTM International, West Conshohocken.

Auler, A.S., 1999. Karst Evolution and Paleoclimate of Eastern Brazil. PhD thesis. University of Bristol.

Auler, A.S., 2017. Hypogene caves and karst of South America. In: In: Klimchouk, A., Palmer, A.N., De Waele, J., Auler, A.S., Audra, P. (Eds.), Hypogene Karst Regions and Caves of the World, Cave and Karst Systems of the World, vol. 2017 Springer International Publishing, Cham. https://doi.org/10.1007/978-3-319-53348-3.

Auler, A.S., Smart, P.L., 2003. The influence of bedrock-derived acidity in the development of surface and underground karst: evidence from the Precambrian carbonates of semi-arid northeastern Brazil. Earth Surf. Process. Landforms 28, 157–168. https://doi.org/10.1002/esp.443.

Aydin, A., 2009. ISRM Suggested method for determination of the Schmidt hammer rebound hardness: revised version. Int. J. Rock Mech. Min. Sci. 46, 627–634. https://doi.org/10.1016/j.ijrmms.2008.01.020.

Aydin, A., Basu, A., 2005. The Schmidt hammer in rock material characterization. Eng. Geol. 81, 1–14. https://doi.org/10.1016/j.enggeo.2005.06.006.

Balsamo, F., Clemenzi, L., Storti, F., Solum, J., Taberner, C., 2019. Tectonic control on vein attributes and deformation intensity in fault damage zones affecting Natih platform carbonates, Jabal Qusaybah, North Oman. J. Struct. Geol. 122, 38–57.

Barbier, M., Leprêtre, R., Callot, J.P., Gasparrini, M., Daniel, J.M., Hamon, Y., Lacombe, O., Floquet, M., 2012. Impact of fracture stratigraphy on the paleo-hydrogeology of the Madison Limestone in two basement-involved folds in the Bighorn basin, (Wyoming, USA). Tectonophysics 576–577, 116–132.

Bizzi, L.A., Schobbenhaus, C., Vidotti, R.M., Gonçalves, J.H., 2003. Geology, Tectonics and Mineral Resources of Brazil. Text, Maps and GIS. CPRM—Brazilian Geological Survey, Brasília (in Portuguese).

Bonfim, L.F.C., Rocha, A.J.D., Pedreira, A.J., Morais, J.C., Guimarães, J.T., Tesch, N.A., 1985. Projeto Bacia de Irecê. Salvador. CPRM (Relatório Final).

Brito Neves, B.B., Fuck, R.A., Pimentel, M.M., 2014. The Brasiliano collage in South America: a review. Braz. J. Genet. 44, 493–518.

Caxito, F.A., Ulhein, A., 2013. Arcabouço tectônico e estratigráfico da Faixa Riacho do Ponta, divisa Pernambuco-Piaui-Bahia. Geonomos 21, 19–37.

Cazarin, C.L., Bezerra, F.H.R., Borghi, L., Santos, R.V., Favoreto, J., Brod, J.A., Auler, A.S., Srivastava, N.K., 2019. The conduit-seal system of hypogene karst in Neoproterozoic carbonates in northeastern Brazil. Mar. Pet. Geol. 101, 90–107. https://doi.org/10.1016/j.marpetgeo.2018.11.046.

Dardenne, M., 1978. Síntese sobre a estratigrafia do Grupo Bambuí no Brasil Central. In: Congresso Bras. Geologia, vol. 31. SBG, Recife, pp. 597–610 Anais 2.

Doolin, D.M., Mauldon, M., 2001. Fracture permeability normal to bedding in layered rock masses. Int. J. Rock Mech. Min. Sci. 38, 199–210. https://doi.org/10.1016/S1365-1609(00)00056-3.

Doolin, D.M., Mauldon, M., 1996. Bed-normal permeability in fractured sedimentary rocks. In: 2nd North American Rock Mechanics Symposium. Montreal, Quebec, Canada, pp. 1793–1800.

D'Angeli, I.M., Parise, M., Vattano, M., Madonia, G., Galdenzi, S., De Waele, J., 2019. Sulfuric acid caves of Italy: a review. Geomorphology 333, 105–122.

Ennes-Silva, R.A., Bezerra, F.H.R., Nogueira, F.C.C., Balsamo, F., Klimchouk, A., Cazarin, C.L., Auler, A.S., 2016. Superposed folding and associated fracturing influence hypogene karst development in Neoproterozoic carbonates, São Francisco Craton, Brazil. Tectonophysics 666, 244–259. https://doi.org/10.1016/j.tecto.2015.11.006.

Evans, M.A., Fischer, M.P., 2012. On the distribution of fluids in folds: a review of controlling factors and processes. J. Struct. Geol. 44, 2–24. https://doi.org/10.1016/j.jsg.2012.08.003.

Fischer, M.P., Higuera-Díaz, I.C., Evans, M.A., Perry, E.C., Lefticariu, L., 2009. Fracture-controlled paleohydrology in a map-scale detachment fold: insights from the analysis of fluid inclusions in calcite and quartz veins. J. Struct. Geol. 31, 1490–1510. https://doi.org/10.1016/j.jsg.2009.09.004.

Ford, D.C., Williams, P.W., 1989. Karst Geomorphology and Hydrology. Unwin Human, London.

Ford, D., Williams, P.D., 2007. Karst Hydrogeology and Geomorphology. John Wiley & Sons.

Galdenzi, S., Menichetti, M., 1995. Occurrence of hypogenic caves in a karst region: examples from central Italy. Environ. Geol. 26, 39–47. https://doi.org/10.1007/BF00776030.

Gross, M.R., Eyal, Y., 2007. Throughgoing fractures in layered carbonate rocks. Bull. Geol. Soc. Am. 119, 1387–1404. https://doi.org/10.1130/0016-7606(2007)119[1387:TFILCR]2.0.CO;2.

Heward, A.P., Chuenbunchom, S., Mäkel, G., Marsland, D., Spring, L., 2000. Nang Nuan oil field, B6/27, Gulf of Thailand: karst reservoirs of meteoric or deep-burial origin?

Pet. Geosci. 6, 15–27. https://doi.org/10.1144/petgeo.6.1.15.
Jacquemyn, C., Swennen, R., Ronchi, P., 2012. Mechanical stratigraphy and (palaeo-) karstification of the Murge area (Apulia, southern Italy). Geol. Soc. Lond. Spec. Publ. 370, 169–186. https://doi.org/10.1144/SP370.4.
Japsen, P., Bonow, J.M., Grenn, P.F., Cobbold, P.R., Chiossi, D., Magnavita, L., Pedreira, A., 2012. Episodic burial and exhumation in NE Brazil after opening of the South Atlantic. Geol. Soc. Am. Bull. 124, 800–816.
Jourde, H., Fenart, P., Vinches, M., Pistre, S., Vayssade, B., 2007. Relationship between the geometrical and structural properties of layered fractured rocks and their effective permeability tensor. A simulation study. J. Hydrol. 337, 117–132. https://doi.org/10.1016/j.jhydrol.2007.01.027.
Klimchouk, A., 2005. Conceptualisation of speleogenesis in multi-storey artesian systems: a model of transverse speleogenesis. Int. J. Speleol. 34 (1), 45–64. https://doi.org/10.5038/1827-806X.34.1.4. ISSN 0392-6672.
Klimchouk, A., 2007. Hypogene Speleogenesis: Hydrogeological and Morphogenetic Perspective. Klimchouk, A.B., 2007. National Cave and Karst Research Institute, Carlsbad, NM.
Klimchouk, A., 2019. Speleogenesis – hypogene. In: White, W., Culver, D., Pipan, T. (Eds.), Encyclopedia of Caves, third ed. Elsevier.
Klimchouk, A.B., Ford, D.C., 2000. Lithologic and structural controls of dissolutional cave development. Speleogenes. Evol. Karst Aquifers 54–64.
Klimchouk, A., Auler, A.S., Bezerra, F.H.R., Cazarin, C.L., Balsamo, F., Dublyansky, Y., 2016. Hypogenic origin, geologic controls and functional organization of a giant cave system in Precambrian carbonates, Brazil. Geomorphology 253, 385–405. https://doi.org/10.1016/j.geomorph.2015.11.002.
Klimchouk, A., Palmer, A.N., De Waele, J., Auler, A.S., Audra, P., 2017a. Hypogene Karst Regions and Caves of the World, Cave and Karst Systems of the World. Springer International Publishing, Cham. https://doi.org/10.1007/978-3-319-53348-3.
Klimchouk, A., Ford, D.C., Palmer, A.N., Dreybrodt, W., 2000. Speleogenesis: Evolution of Karst Aquifers. National Speleological Society, Huntsville, Al.
Klimchouk, A., Palmer, A.N., De Waele, J., Auler, A.S., Audra, P., 2017b. Hypogene Karst Regions and Caves of the World, Cave and Karst Systems of the World Springer International Publishing, Cham. https://doi.org/10.1007/978-3-319-53348-3.
Kolaiti, E., Papadopoulos, Z., 1993. Évaluation de l'essai «schmidt rebound hammer»: Une approche critique. Bull. Int. Assoc. Eng. Geol. - Bull. l'Association Int. Géologie l'Ingénieur 48, 69–76. https://doi.org/10.1007/BF02594977.
Lagoeiro, L.E., 1990. Estudo da Deformação nas Sequências Carbonáticas do Grupo Uma na Região de Irecê. BA Tese Mestrado. Universidade Federal de Ouro Preto, Ouro Preto, MG, Brazil, pp. 102 1990.
Lamarch, J., Lavenu, A.P.C., Gauthier, B.D.M., Guglielmi, Y., Jayet, O., 2012. Relationships between fracture patterns, geodynamics and mechanical stratigraphy in Carbonates (South-East Basin, France). Tectonophysics 581, 231–245.
Laubach, S.E., Olson, J.E., Cross, M.R., 2009. Mechanical and fracture stratigraphy. Am. Assoc. Petrol. Geol. Bull. 93, 1413–1426. https://doi.org/10.1306/07270909094.
Lowe, D.J., 2000. Role of stratigraphic elements in speleogenesis: the speleoinception concept. Speleogenesis: Evolution of Karst Aquifers 65–76.
Narr, W., Suppe, J., 1991. Joint spacing in sedimentary rocks. J. Struct. Geol. 13, 1037–1048. https://doi.org/10.1016/0191-8141(91)90055-N.
Odling, N.E., Gillespie, P., Bourgine, B., Castaing, C., Chilés, J.P., Christensen, N.P., Fillion, E., Genter, A., Olsen, C., Thrane, L., Trice, R., Aarseth, E., Walsh, J.J., Watterson, J., 1999. Variations in fracture system geometry and their implications for fluid flow in fractured hydrocarbon reservoirs. Pet. Geosci. 5, 373–384. https://doi.org/10.1144/petgeo.5.4.373.
Ogata, K., Storti, F., Balsamo, F., Tinterri, R., Bedogni, E., Fetter, M., Gomes, L., 2017. Sedimentary facies control on mechanical and fracture stratigraphy in turbidites. Geol. Soc. Am. Bull. 129 (1–2), 76–92.
Palmer, A.N., 2000. Hydrogeologic control of cave patterns. 2000 In: In: Klimchouk, A., Ford, D.C., Palmer, A.N., Dreybrodt, W. (Eds.), Speleogenesis: Evolution of Karst Aquifers, vol. 240. pp. 145–146. https://doi.org/10.1016/s0022-1694(00)00341-3. J. Hydrol.
Palmer, A.N., 1991. Origin and morphology of limestone caves. Geol. Soc. Am. Bull. 103, 1–21. https://doi.org/10.1130/0016-7606(1991)103.
Palmer, A.N., 1989. Stratigraphic and structural control of cave development and groundwater flow in the Mammoth Cave region. In: Karst Hydrology: Concepts from the Mammoth Cave Area, pp. 293–316.
Palmer, A.N., 2007. Cave Geology. Cave books, Dayton.
Penha, A.E.P.P., 1994. MSc Dissertation. O calcário Caatinga de Ourolândia, Bahia: Feições diagnósticas, gênese e evolução de um perfil calcrete, vol. 1994 Universidade Federal da Bahia.
Pisani, L., Antonellini, M., De Waele, J., 2019. Structural control on epigenic gypsum caves: evidences from Messinian evaporites (Northern Apennines, Italy). Geomorphology 332, 170–186.
Rubbioli, E., Auler, A.S., Menin, D.S., Brandi, R., 2019. Cavernas. Atlas Do Brasil Subterrâneo. Editora IABS, Brasília, pp. 340.
Rustichelli, A., Torrieri, S., Tondi, E., Laurita, S., Strauss, C., Agosta, F., Balsamo, F., 2016. Fracture characteristics in Cretaceous platform and overlying ramp carbonates: an outcrop study from Maiella Mountain (central Italy). Mar. Pet. Geol. 76, 68–87.
Salvini, F., Billi, A., Wise, D.U., 1999. Strike-slip fault-propagation cleavage in carbonate rocks: the Mattinata Fault zone, southern Apennines, Italy. J. Struct. Geol. 21, 1731–1749. https://doi.org/10.1016/S0191-8141(99)00120-0.
Tectonic control on karst evolution (pp. 1-5). In: Shanov, S., Kostov, K. (Eds.), Dynamic Tectonics and Karst. Cave and Karst Systems of the World. Springer Berlin Heidelberg, Berlin, Heidelberg 123 pp.
Trompette, R., Uhlein, A., Egydio-Silva, M., Karmann, I., 1992. The Brasiliano São Francisco cráton revisited (Central Brazil). J. South Am. Earth Sci. 6 (1/2), 49–57.
van Golf-Racht, T.D., 1982. Fundamentals of Fractured Reservoir Engineering. Elsevier, Amsterdam.
Waltham, T., Waltham, A.C., Bell, F.G., Culshaw, M.G., 2005. Sinkholes and Subsidence: Karst and Cavernous Rocks in Engineering and Construction. Springer Science & Business Media.
Wang, X., Lei, Q., Lonergan, L., Jourde, H., Gosselin, O., Cosgrove, J., 2017. Heterogeneous fluid flow in fractured layered carbonates and its implication for generation of incipient karst. Adv. Water Resour. 107, 502–516. https://doi.org/10.1016/j.advwatres.2017.05.016.
Yaşar, E., Erdoğan, Y., 2004. Estimation of rock physicomechanical properties using hardness methods. Eng. Geol. 71, 281–288. https://doi.org/10.1016/S0013-7952(03)00141-8.
Yurdakul, M., Ceylan, H., Akdas, H., 2011. A Predictive Model for Uniaxial Compressive Strength of Carbonate Rocks from Schmidt Hardness. Am. Rock Mech. Assoc. 11–533. American Rock Mechanics Association (ARMA).
Zeeb, C., Gomez-Rivas, E., Bons, P.D., Blum, P., 2013. Evaluation of Sampling methods for fracture network characterization using Outcrops. Am. Assoc. Petrol. Geol. Bull. 97, 1545–1566. https://doi.org/10.1306/02131312042.
Zoback, M.D., 2007. Reservoir Geomechanics. Cambridge University Press, Cambridge. https://doi.org/10.1017/CBO9780511586477.

Marine and Petroleum Geology 128 (2021) 105046

Contents lists available at ScienceDirect

Marine and Petroleum Geology

journal homepage: www.elsevier.com/locate/marpetgeo

High-permeability zones in folded and faulted silicified carbonate rocks – Implications for karstified carbonate reservoirs

Vincenzo La Bruna [a,b,*], Francisco H.R. Bezerra [a,b], Victor H.P. Souza [c], Rubson P. Maia [d], Augusto S. Auler [e], Renata E.B. Araujo [b], Caroline L. Cazarin [c], Marcos A.F. Rodrigues [f], Lucieth C. Vieira [g], Maria O.L. Sousa [a]

[a] Departamento de Geologia, Universidade Federal do Rio Grande do Norte, Brazil
[b] Programa de Pós-Graduação em Geodinâmica e Geofísica, Universidade Federal do Rio Grande do Norte, Brazil
[c] Petrobras, Rio de Janeiro-RJ, Brazil
[d] Departamento de Geografia, Universidade Federal do Ceará, Brazil
[e] Instituto do Carste/Carste Ciência e Meio Ambiente, Brazil
[f] Departamento de Engenharia do Petróleo, Universidade Federal do Rio Grande do Norte, Brazil
[g] Instituto de Geociências, Universidade de Brasília, Brazil

ARTICLE INFO

Keywords:
Fracture corridors
Hypogene karst
Carbonate reservoir
Subseismic structural analog
Super-k
Fold hinges

ABSTRACT

Ascending hydrothermal fluid flow and subsequent hypogene karstification can control the formation of high-permeability zones in folded or faulted carbonate rocks. This study presents a multidisciplinary and multiscale approach to investigate the relationships between regional deformation and subseismic karst conduits along fracture corridors. We investigate the Cristal Cave Karst System, which is 6.7 km long and occurs in Mesoproterozoic carbonate-siliciclastic units affected by hydrothermal silicification in the São Francisco Craton, Brazil. Based on integrated techniques of ALOS PALSAR imagery, structural field surveys, stratigraphic and laboratory analyses in the caves and the surrounding surface outcrops, we highlight the following points: (1) the cave system occurs in a regional folded sector; (2) the internal architecture of the large regional folds is composed of subseismic folds; (3) fracture corridors occur along the subseismic fold hinges, forming high-permeability zones; and (4) the principal cave passages, which are oriented NNE-SSW, are concentrated along these fold hinges. We discuss the results in terms of a spatiotemporal conceptual model and unravel the deformation and karstification stages, which are characterized by the development of (i) precontractional and (ii) contractional structural networks followed by (iii) hydrothermal silicification and karstification processes. This cave system can be used as an analog for deformed, silicified, and karstified carbonate reservoirs, allowing for the in situ characterization of subseismic structural features. This study provides the key for first-order prediction and characterization of high-permeability zone internal structures, where both deformation and karstification processes occur.

1. Introduction

Carbonate rocks form the most important type of hydrocarbon reservoir and are of great importance for hydrocarbon exploitation, water resources, and gas sequestration (e.g., Ahr, 2011; Akbar et al., 2000; Aljuboori et al., 2019; Bourbiaux, 2010; Eliebid et al., 2018; Firoozabadi, 2000; Ford and Williams, 2013). In carbonate multilayered sequences, all subseismic structural elements, such as joints, stylolites, and fault zones can affect reservoir characteristics (e.g., Giuffrida et al., 2020; Panza et al., 2018; Roehl and Choquette, 2012). Fracture corridors, one of these subseismic elements, have attracted great interest over the past twenty years (Ogata et al., 2014; Watkins et al., 2015). They are one of the main structural discontinuities in fractured reservoirs in the subsurface and form high-permeability pathways or super-k zones (Bockel-Rebelle et al., 2004; Questiaux et al., 2010).

One additional issue in understanding carbonate reservoirs is the interconnectedness between regional tectonics, local geological and structural elements, and karst systems. Karstification (epigenic and

* Corresponding author. Programa de Pós-Graduação em Geodinâmica e Geofísica, Universidade Federal do Rio Grande do Norte, Brazil.
E-mail address: vincenzolabruna@gmail.com (V. La Bruna).

https://doi.org/10.1016/j.marpetgeo.2021.105046
Received 10 February 2021; Received in revised form 15 March 2021; Accepted 19 March 2021
Available online 24 March 2021

hypogenic) is a key factor influencing the quality of reservoirs (Fig. 1A) (e.g., Araújo et al., 2021; Cazarin et al., 2019; Ennes-Silva et al., 2015). Both karst and fractures contribute to high permeability zones and can play a fundamental role in geofluid storage and migration processes (e.g., Agar and Geiger, 2015; Giuffrida et al., 2019). These processes bypass the control exerted by the matrix or fractures, impacting both reservoir porosity and permeability (Fig. 1B). For example, Bagni et al. (2020) documented the control exerted by fracture corridors in the distribution and concentration of epigenic karstification within folded carbonate rocks. However, the control exerted by the regional tectonic framework (folds, faults, transfer structures, low-angle detachment surfaces, etc.) in karstified carbonate rocks is poorly investigated and documented (Antonellini et al., 2019). More case studies are needed to fully understand carbonate reservoirs, especially studies focusing on the role of karstification in fracture corridors.

Among karst systems, hypogenic karst deserves special attention. It is strictly connected to porous structures, which are subsequently widened by dissolution related to upwelling fluid flow (Klimchouk et al., 2012). Commonly, hypogene caves exert a structural control on the evolution of interconnected cave passages. Many studies highlight such a relationship between structural features and karst, such as in the giant gypsum cave systems in Western Ukraine (Klimchouk et al., 2009) and in Cathedral Cave (Osborne, 2007). Moreover, folds are described as a controlling factor for hypogene karst development (Ennes-Silva et al., 2015; Pisani et al., 2021). In some caves, a three-dimensional conduit system can form multistory levels connected by subvertical feeders, allowing upward fluids migration (Cazarin et al., 2019; Ennes-Silva et al., 2015; Klimchouk, 2009).

To bridge the gap between outcrop- and reservoir-scale analysis (Mäkel, 2007; Nelson, 2001), this work investigates the hypogenic Cristal Cave Karst System (CCKS), which can be considered a subsurface karstified/structural carbonate analog. The CCKS is located in the São Francisco Craton (northeastern Brazil) in the Mesoproterozoic Caboclo Formation, which is composed of an alternation between carbonate and terrigenous rocks (Berbert-Born and Horta, 1995; Rocha et al., 1992). Recently, Souza et al. (2021) documented a pervasive and intense hydrothermal silicification process associated with hypogenic geofluid migration and karst development. Nevertheless, little is known about

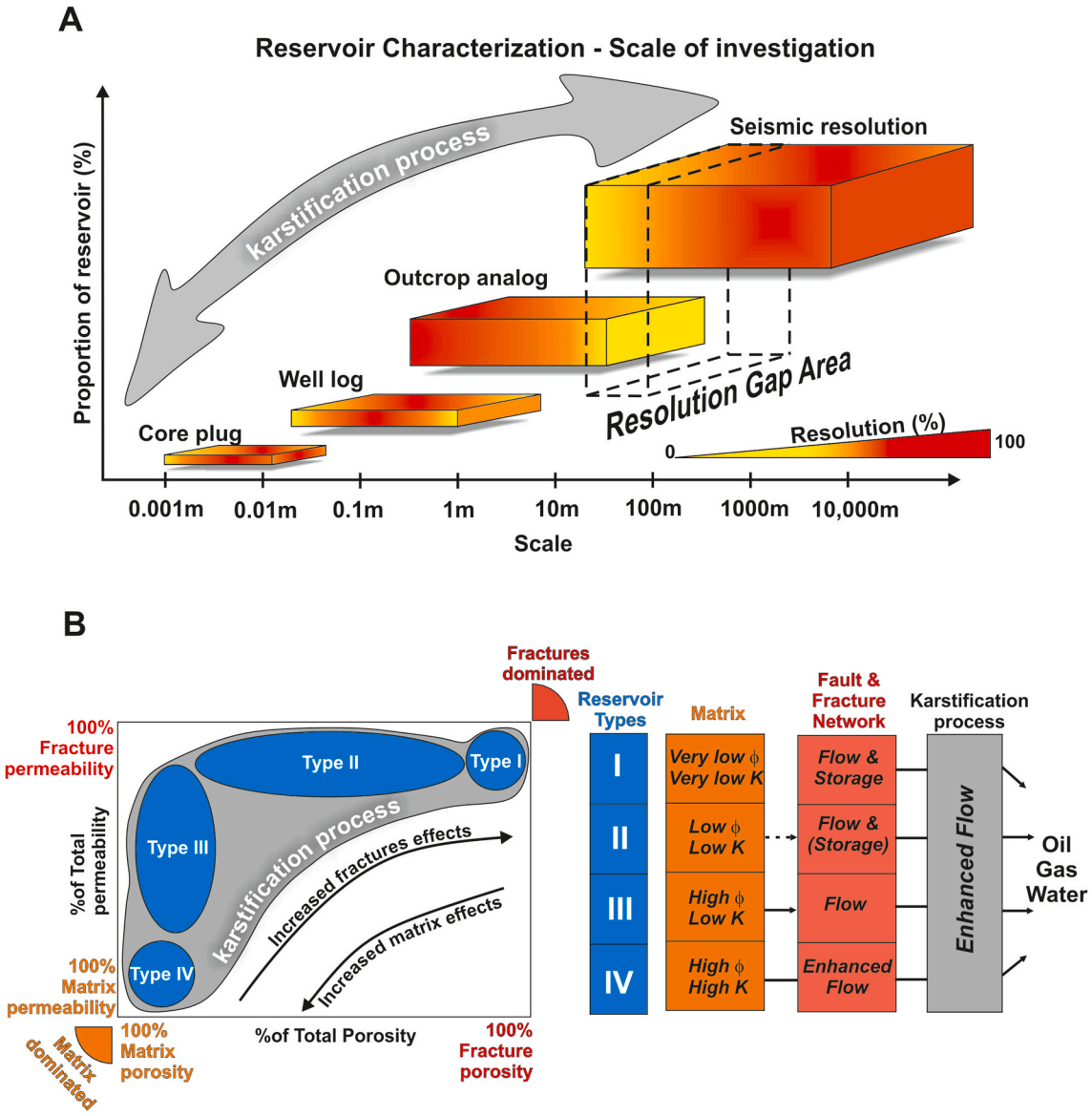

Fig. 1. (A) Graph showing the resolution of in situ and seismic-scale analyses with respect to the reservoir proportions and how karstification is not a scale-dependent process (modified after Giuffrida et al., 2020). (B) Graph displaying how karstification processes can affect all the different reservoir types, including altering the fractures or the contribution of the matrix (modified after Jolley et al., 2007; Nelson, 2001).

the control exerted by regional and local structural elements on geofluids migration and subsequent karst system development.

This study describes the internal architecture of these subseismic high-permeability zones in fold hinges. The data obtained after detailed field structural analysis were used, together with ALOS PALSAR imagery, to characterize and correlate the geometry and orientation of the fold-parallel subseismic cave passages with the largest regional structures. These structures determined the fracture corridors localization and subsequently guided the dissolution process. We also present petrographic and petrophysical properties of the stratigraphic sequence affected by hydrothermal silicification. Our study can provide a first-order prediction of the subseismic high-permeability zones in carbonate rocks controlled by regional-scale tectonic structures.

This work's results may be of great impact for improving knowledge related to the hydrocarbon and water reserves hosted in carbonate reservoirs affected by karstified and fractured discontinuities below seismic resolution. Hence, the use of carbonate outcrop analogs (Balsamo et al., 2020; Giuffrida et al., 2019; La Bruna et al, 2017, 2018, 2020) may provide insights into the genetic and evolutionary mechanisms that operate in these complex systems to minimize errors in development and production in carbonate reservoirs and allow for reliable reservoir reconstruction.

2. Geological setting

The study area is located in the São Francisco Craton (Fig. 2), which was preserved from the Brasiliano Orogeny (~740-560 Ma). This craton represents the western sector of a major cratonic area, which includes the Congo or Zaire Craton. They corresponded to a paleocontinental part of the Gondwanan supercontinent (Alkmim, 2004; Almeida et al., 2000; Heilbron et al., 2017). The São Francisco Craton recorded a rifting process that controlled and determined the development of sedimentary basins from the late Paleoproterozoic (Statherian) to the early Neoproterozoic (Tonian) ages (e.g., Alkmim and Martins-Neto, 2012; Costa and Danderfer Filho, 2017; Danderfer Filho et al., 2015; Danderfer Filho and Dardenne, 2002; Pedrosa-Soares and Alkmim, 2013).

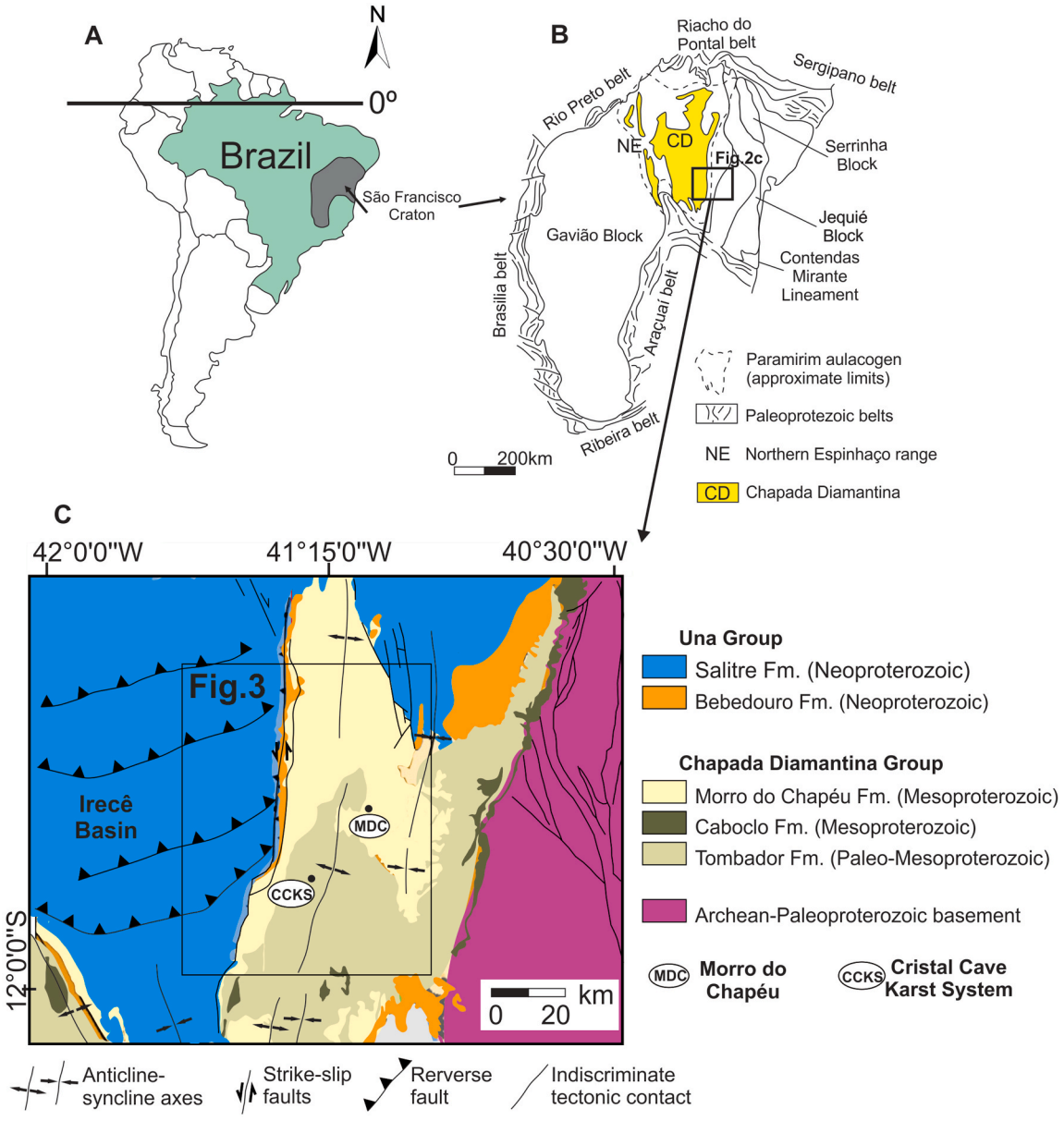

Fig. 2. (A) South America Continent. (B) São Francisco Craton showing the Archean blocks (modified after Cruz et al., 2007; D'Angelo et al., 2019). (C) Simplified geological map of Chapada Diamantina (modified after Danderfer et al., 2015; D'Angelo et al., 2019).

During the opening of the South Atlantic Ocean in the Late Jurassic-Early Cretaceous, the São Francisco-Congo Craton was fragmented (Trompette et al., 1992). In the time between its amalgamation and breakup, the Espinhaço Supergroup was formed within an intracontinental rift-sag basin (Alkmim and Martins-Neto, 2012). The Espinhaço Supergroup sequences and the São Francisco (Una Group) Supergroup were deposited on top of an Archean-Paleoproterozoic basement, which is exposed to the west in the Gavião block (Fig. 2B) (Barbosa and Barbosa, 2017). The Una Group, which is mainly composed of Neoproterozoic glacio-marine sedimentary rock, is capped by the Bebedouro and Salitre Formations. The Chapada Diamantina Group, which is predominantly composed of terrigenous sediments from the Mesoproterozoic era, is constituted from bottom to top by the Tombador, Caboclo, and Morro do Chapéu Formations.

The Caboclo Formation reaches a maximum thickness of 300 m (Pedreira et al., 1975; Rocha et al., 1992). These rocks are associated with shallow marine systems overlain by fluvial and shoreface sandstones with tidal influence from the Morro do Chapéu Formation (Souza et al., 2019) The most exposed and well-preserved portion of the carbonate sequence is located in the Cristal Cave area, where a 50 m thick succession crops out (Fig. 2C) (Souza et al., 2021). Several carbonate facies occur (Srivastava and Rocha, 1999), comprising the following lithologies: algal laminites, oncoliths, stromatolites, intraclastic calcarenites, calcilutites, and silexites deposited in a supra-to subtidal depositional system (Souza et al., 2021).

The structural framework of the study area is the result of several tectonic events (Fig. 2C). Archean to Paleoproterozoic deformations are recorded in the Gavião block with preferentially oriented NNW-SSE to N–S tectonic lineaments (Barbosa and Barbosa, 2017). Subsequently, several fold belts were formed in the São Francisco Craton during the Brazilian/Pan-African orogeny (Alkmim et al., 1993; Neves et al., 2014). Simultaneously, an E-W-oriented contraction affected the Paramirim aulacogen (Fig. 2B) in the Ediacaran (Cruz and Alkmim, 2007; Süssenberger et al., 2014).

The study area is located within the Morro do Chapéu structural domain, a few kilometers away from a major NNE-SSW- to N–S-striking fault that forms a tectonic boundary between the Chapada Diamantina Group and the Irecê Basin (Fig. 2C) (Danderfer Filho, 1990). A cylindrical regional-scale deformation was ascribed to this sector, generating parallel gentle and open folds formed by flexural slip (Danderfer Filho et al., 2015). Nearly symmetrical, ca. N–S-trending anticlines and synclines affect the Morro do Chapéu domain (Fig. 2C). These folds deform the rocks of the Chapada Diamantina Group and the glacial deposits of the Bebedouro Formation (D'Angelo et al., 2019). Furthermore, three sets of high-angle to bedding fractures are documented in the Morro do Chapéu domain. These fracture sets strike N–S, NW-SE, and NE-SW and are associated with the E-W-oriented compressional tectonic stress that affected the study area (Danderfer Filho, 1990).

Several studies have emphasized the hypogenic origin of caves in the region, mainly those in the Neoproterozoic Salitre Formation (Bertotti et al., 2020; Cazarin et al., 2019; Klimchouk et al., 2016). However, the start times of hypogene karstification cannot be determined with certainty, with late Proterozoic to Jurassic/Cretaceous ages being hypothesized by previous studies (Cazarin et al., 2019; Ennes-Silva et al., 2015; Heilbron et al., 2017; Klimchouk et al., 2016).

The CCKS occurs in the Mesoproterozoic Caboclo Formation (Fig. 2C), comprises an interconnected network of cave passages that extends for ca. 6.7 km and is located near the major left-lateral strike-slip NNE-SSW- to N–S-striking fault. This fault separates the Neoproterozoic carbonate units of the Irecê Basin from the Mesoproterozoic units of the Caboclo and Morro do Chapéu Formations (Berbert-Born and Horta, 1995) (Fig. 2). Souza et al. (2021) observed that the CCKS is hosted in a carbonate sequence affected by pervasive hydrothermal silicification. They concluded that hypogenic fluids were channelized through porous oolithic layers, allowing subsequent karst development. In fact, they state that a marl bed acted as a seal, allowing the concentration of silicification in the bottom stratigraphic interval to be mainly composed of porous well-sorted carbonate units favoring horizontal fluid migration. This finding showed that the stratigraphy played a key role in the subsequent hydrothermal silicification.

3. Methods

This study results from multidisciplinary analyses of the CCKS and its hosting carbonate sequence. It includes a compilation of previous geological maps associated with satellite imagery investigation, structural analysis of the cave and surrounding areas, and petrographic-petrophysics analysis of samples from the cave system.

3.1. ALOS PALSAR imagery analysis

The regional, seismic-scale study was based on several geological maps (e.g., Cruz et al., 2007; Danderfer Filho et al., 2015). We complemented the structural data with high-resolution ALOS PALSAR imagery (Advanced Land Observing Satellite Phased Array type L-band Synthetic Aperture Radar). The study covered a 100 × 40 km area using the digital elevation model extrapolated from ALOS PALSAR images, which were processed to enhance and visualize several parameters on a regional scale, such as faults, folds, and fracture trends. Topographic profiles were drawn in the N–S, E-W, NE-SW, and NW-SW directions to identify geomorphological and structural elements using a vertical color chart with an interval of 10 m.

3.2. Field analysis

This study performed a structural and stratigraphic analysis of the carbonate multilayer units inside and outside the CCKS. We used the cave map from the Brazilian Geological Survey and the Meandros Espeleo Club (Berbert-Born et al., 2012). The characterization of lithologies composing the sedimentary sequences in the CCKS was based on the study performed by Souza et al. (2021) and accompanied by a collection of 50 samples from different beds, which we used for petrographic and petrophysical analyses.

Mesoscale fracture analysis was carried out at 41 measurement sites. We completed the investigation with a qualitative structural analysis to decipher the nature, kinematics, relative timing, infilling material, and attitude of individual fractures crosscutting the sedimentary units at each study site. A total of 944 fractures, 41 veins, 588 bedding planes, and 27 fold hinges were measured, and their attitudes are presented in stereographic plots using Stereonet software (Allmendinger et al., 2011).

3.3. Laboratory analysis (petrographic and 3D porosity/permeability analyses)

Thirty standard-thickness thin sections cut perpendicular to bedding were analyzed using an Axioscope 5 polarizing optical microscope under parallel (//P) and crossed (XP) polarizers. The goal was to describe the allochems, sedimentary features, and structural elements. Rock textures were assessed according to the Dunham (1962) and Embry and Klovan (1971) classifications.

Petrophysical analyses included porosity, permeability, density, and volume pore measurements performed with a Coreval system by Vinci Technologies Company (unsteady-state gas permeameter and porosimeter at overburden pressure) on nine 1-inch (~2.5 cm) diameter and 4-cm long plugs. We obtained pore volume calculations using N_2 gas at a confining pressure of 600 psi, which simulated the pressures in analog reservoirs. Additionally, we computed the Klinkenberg permeabilities (mD) and used the Klinkenberg correction method (Jones, 1972; Klinkenberg, 1941; Li et al., 2016).

4. Results

4.1. ALOS PALSAR mapping analysis

The compiled structural map presents the primary morphostructural lineaments in an area of 100 × 40 km (Fig. 3). The tectonic structures were sorted into strike-slip faults, normal faults, reverse faults, and fold hinges based upon previous geological mapping (Cazarin et al., 2019; D'Angelo et al., 2019; Ennes-Silva et al., 2015; Souza et al., 2003). The lineaments were divided into the following three sets: NNE-SSW,

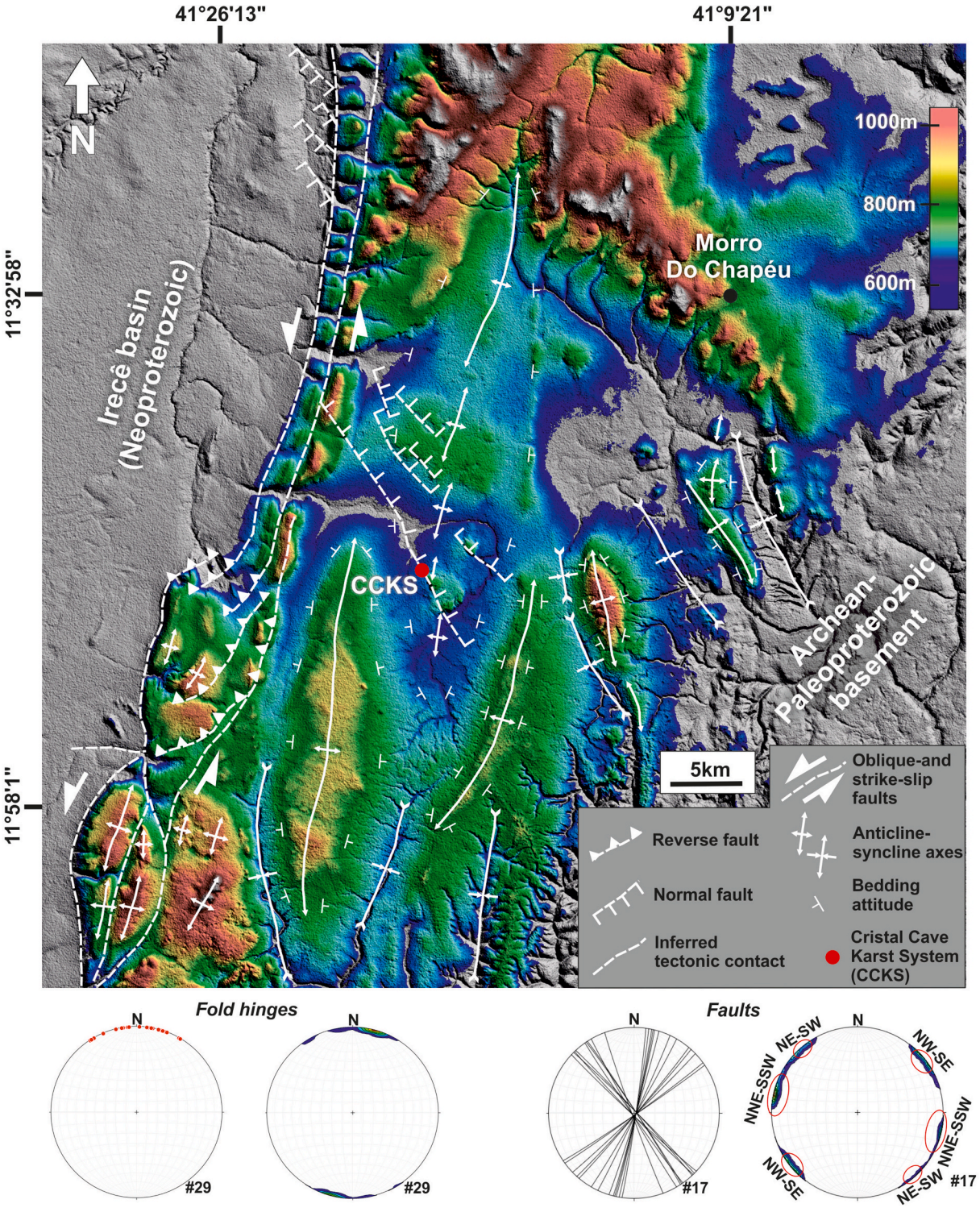

Fig. 3. Structural framework of the study area superposed on ALOS PALSAR imagery. The colored central part corresponds to the Mesoproterozoic sedimentary units, the Irecê Basin represents the Neoproterozoic sedimentary units, and the west block represents the Paleoproterozoic-Archean crystalline basement. Dashed lines represent the inferred faults. Continuous white lines represent both anticline and syncline axes. The inset shows lower hemisphere equal-area projections of fold hinges and relative density contour plots; the great circles represent the attitude of the documented faults and equal-area projection/density contour plots of the poles of the measured faults (the map location can be found in Fig. 2).

NE-SW, and NW-SE. The NNE-SSW set was interpreted as composed of strike-slip left-lateral faults, as already presented by D'Angelo et al. (2019) and Danderfer Filho et al. (2015), whereas the NE-SW set is composed of reverse faults, as shown by D'Angelo et al. (2019) and Reis et al. (2013). The NW-SE set was interpreted as composed of normal faults (D'Angelo et al., 2019).

Both the NE-SW- and NW-SE-striking fault sets terminate against the NNE-SSW- to N–S-striking fault set. Furthermore, a larger folded zone in the central portion of the study area was documented (Fig. 3). Previous works have described how this sector is affected by several anticlines and synclines (Cazarin et al., 2019; D'Angelo et al., 2019; Danderfer Filho et al., 2015; Ennes-Silva et al., 2015; Souza et al., 2003). The fold hinges mainly trend along the NNE-SSW to N–S directions (Fig. 3). In some cases, as observed near the Cristal cave, fold hinges are arranged following an en echelon left-stepping pattern (Fig. 3).

4.2. Stratigraphic and laboratory analyses

4.2.1. Stratigraphic and petrographical analyses

The sedimentary carbonate succession of the Caboclo Formation exposed in the Cristal Cave, according to Souza et al. (2021) (Fig. 4A), is composed of the following units: 1) ooidal grainstones (Figs. 4A), 2) intraclastic grainstones and rudstones (Figs. 4C), 3) heterolites (Fig. 4E) and 4) marls (Fig. 4G), fault-related hydraulic breccias and veins (Fig. 4I). The rocks in the CCKS are ca. 35 m thick continuous carbonate rock layers (Fig. 4).

The stratigraphic sequence is affected by moderate to pervasive silicification (Souza et al., 2021). Silica minerals and cements occur in different forms within the analyzed carbonate rocks of the CCKS: (i) microcrystalline quartz (Fig. 4B); (ii) cements with crystalline texture, ranging in size from fine to coarse crystals (Fig. 4D); (iii) chalcedony with crystals showing undulose extinction or spherulitic texture, both present as infill in pores and veins (Fig. 4F and H); and (iv) fine to coarse quartz crystals filling veins (Fig. 4J).

The silica mineral content varies significantly within the carbonate facies (Fig. 4). Ooidal grainstones (Unit 1) are intensely silicified (32.5%), whereas intraclastic grainstones and rudstones (Unit 2) have been subjected to moderate silicification (10.9%), and heterolites (Unit 3) have been subjected to weaker silicification (3.5%) (Souza et al., 2021). Compositional and textural variations are responsible for such lithologic differences.

4.2.2. Laboratory 3D porosity and permeability test

The results related to the ooidal grainstone plugs are reported in

Table 1
Porosity, permeability, bulk volume and bulk density.

Number	Study site	Porosity (%)	Permeability (mD)	Bulk Volume	Bulk Density
1	7	2.55	0.0013	13.79	2.78
2	3	2.22	22.0914	12.93	2.79
3	29	1.94	0.0021	13.47	2.80
4	37	2.04	0.0009	13.60	2.81
5	23	1.98	0.0008	15.30	2.75
6	20	2.00	0.0009	15.98	2.79
7	13	1.90	0.0020	13.71	2.79
8	25	3.10	0.0030	14.59	2.76
9	19	1.57	0.0012	17.49	2.81

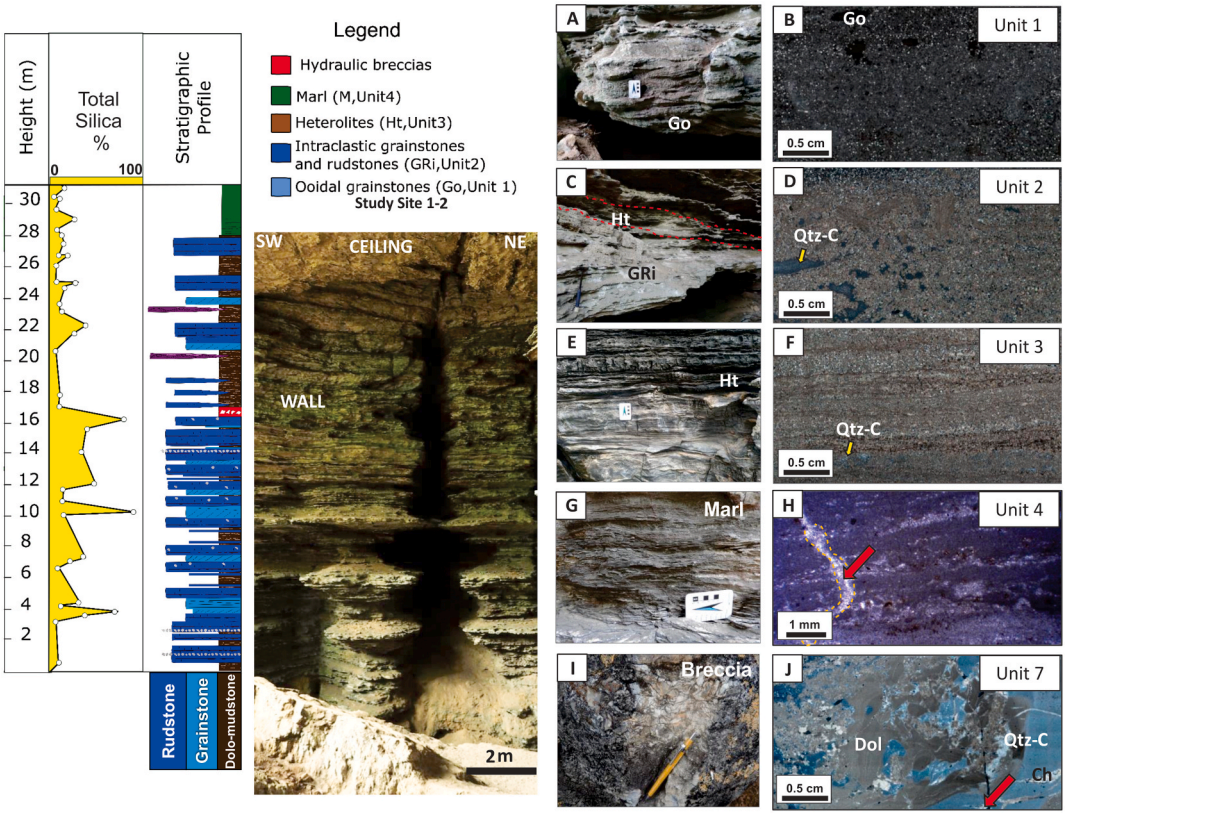

Fig. 4. Stratigraphic and silica content profile of the Caboclo Formation in Cristal Cave (modified after Souza et al., 2021). (A, C, E, G, I) Outcrop images of the Caboclo Formation exposed in Cristal Cave: (A) ooidal grainstones, (C) intraclastic grainstones and rudstones, (E) heterolites, (G) marls, and (I) breccias. (B, D, F, H, J) Thin section microphotographs associated with outcrop lithofacies presented above: (B) micro-ooidal silicified grainstones, (D) intraclastic grainstones, with the yellow arrow indicating silicified grains, (F) millimetric rhythmic layered heterolite, with the yellow arrow indicating microcrystalline quartz cement, (H) marl interval affected by quartz veins (red arrow), and (J) breccia showing dolomitic and quartz clasts. The red arrow indicates a quartz micro-vein. (For interpretation of the references to color in this figure legend, the reader is referred to the Web version of this article.)

Table 1, where both porosity and permeability values are displayed. Due to the high degree of alteration, it was not possible to collect plugs associated with the other units. The measured porosity values for the ooidal grainstones samples range between 1.57% and 3.10%, whereas permeability values range from 0.0008 mD to 22.0914 mD (Fig. 5A). Excluding the higher value, all the other plugs range between 0.0008 mD and 0.003 mD (Fig. 5B). The average density calculated for the samples is 2.79 g/cm^3; all the values range from 2.75 g/cm^3 to 2.81 g/cm^3. The average computed bulk volume is 14.54 cm^3, and it ranges between 12.93 cm^3 and 17.49 cm^3.

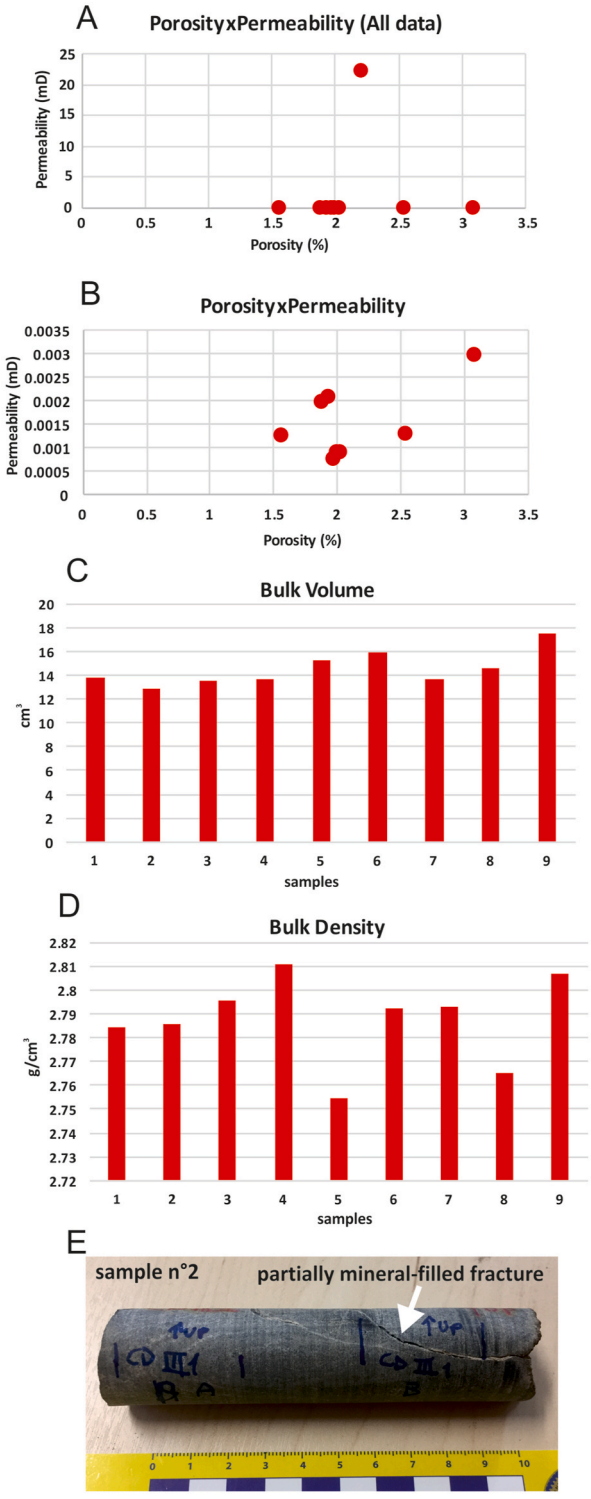

Fig. 5. Diagrams showing (A) the relationship between sample porosity and the Klinkenberg corrected permeability for all collected samples, (B) the relationship between sample porosity and the Klinkenberg corrected permeability, excluding sample n°2, (C) bulk volume and (D) density of the collected plug samples. (E) An ooidal grainstone plug affected by a partially cemented fracture.

4.3. General cave features and structural analysis

Cristal Cave is located at the eastern edge of a major N–S- to NNE-SSW-striking transpressional strike-slip fault system, which bounds the Irecê Basin and the Mesoproterozoic units (Figs. 2 and 3). In map view (Fig. 6), the cave is represented by a pattern with three main passage directions: NNE-SSW, NW-SE, and NE-SW to ENE-WSW. Cave passages have formed along large subvertical fractures and range from centimeter-scale dissolution features to passages that are accessible to humans (Fig. 7A and B). Moreover, subvertical feeders (outlets of upwelling fluids) have been documented at horizontal conduit terminations (Fig. 7C). Forty-one measurement stations were selected along the principal cave passages (Fig. 6), and structural analyses aimed at the characterization of different elements were performed. Their geometry, orientation, internal structure, infilling material (if present), possible offset, and crosscutting/abutting relationships were considered. Our dataset focused mainly on the master passages, which were usually subhorizontal or gently dipping toward the NNE.

4.3.1. Fold patterns in the cave

Sedimentary bedding measurements were performed along 30 study sites to analyze their relationship with the cave passages. All stereoplot diagrams show gentle folding of the sedimentary bedding and dipping ca. 5°–10° in opposite directions (Fig. 8). The main cave passages occur along the anticline hinges, which are highly fractured and karstified (Fig. 7A, B, C). Anticline fold limbs were measured, and the resulting cumulative sedimentary bedding data indicate the presence of a principal anticline set trending NNE-SSW to NE-SW and mainly plunging to the same directions (Figs. 6 and 8). These fold hinges display an en echelon left-stepping array (Fig. 8) similar to those observed in the regional map view (Fig. 3).

4.3.2. Joints, veins, and faults

High-resolution structural analysis was performed on faults, fractures, and veins. All structural elements were measured at many study sites in different cave locations (Figs. 6 and 9) to prevent or reduce bias in the data collection. The fractures were distinguished as opening mode fractures (joints and veins) (Figs. 9 and 10A, B, C, D, E, F), sheared joints, and faults (from incipient to well-developed faults) (Fig. 10A, B, 10E, 10F, 11, 12, 13). Three bed-perpendicular stratabound and non-stratabound joint sets striking NNE-SSW, NW-SE, and ENE-WSW were documented (Figs. 6, 9, 10 and 12). The NW-SE and ENE-WSW fracture sets showed mutual abutting relationships (Fig. 11) and systematically terminated against the NNE-SSW fracture set. In some cases, the NNE-SSW fracture set occurred as clustered non-stratabound/through-going fractures and veins in the fold hinges and at the cave conduit terminations (Figs. 7C, 12C and 12D). These features were documented and described as fracture corridors, which consist of sub-parallel trending fractures. The measured fracture corridors exhibit a horizontal width ranging from 0.5 m to 2 m, with vertical development spanning from few meters to the maximum cave height (c.a. 16 m). Two main stratabound and non-stratabound vein sets striking NW-SE and NE-SW, respectively, and a minor ca. N–S-oriented fracture set were identified (Figs. 1, 6 and 10A to F, 12C, 12D). Most of the faults documented in the cave were characterized by normal to strike-slip offsets (Fig. 13A, B, C); in some cases, feedersare located in fault extensional quadrants (Fig. 13C).

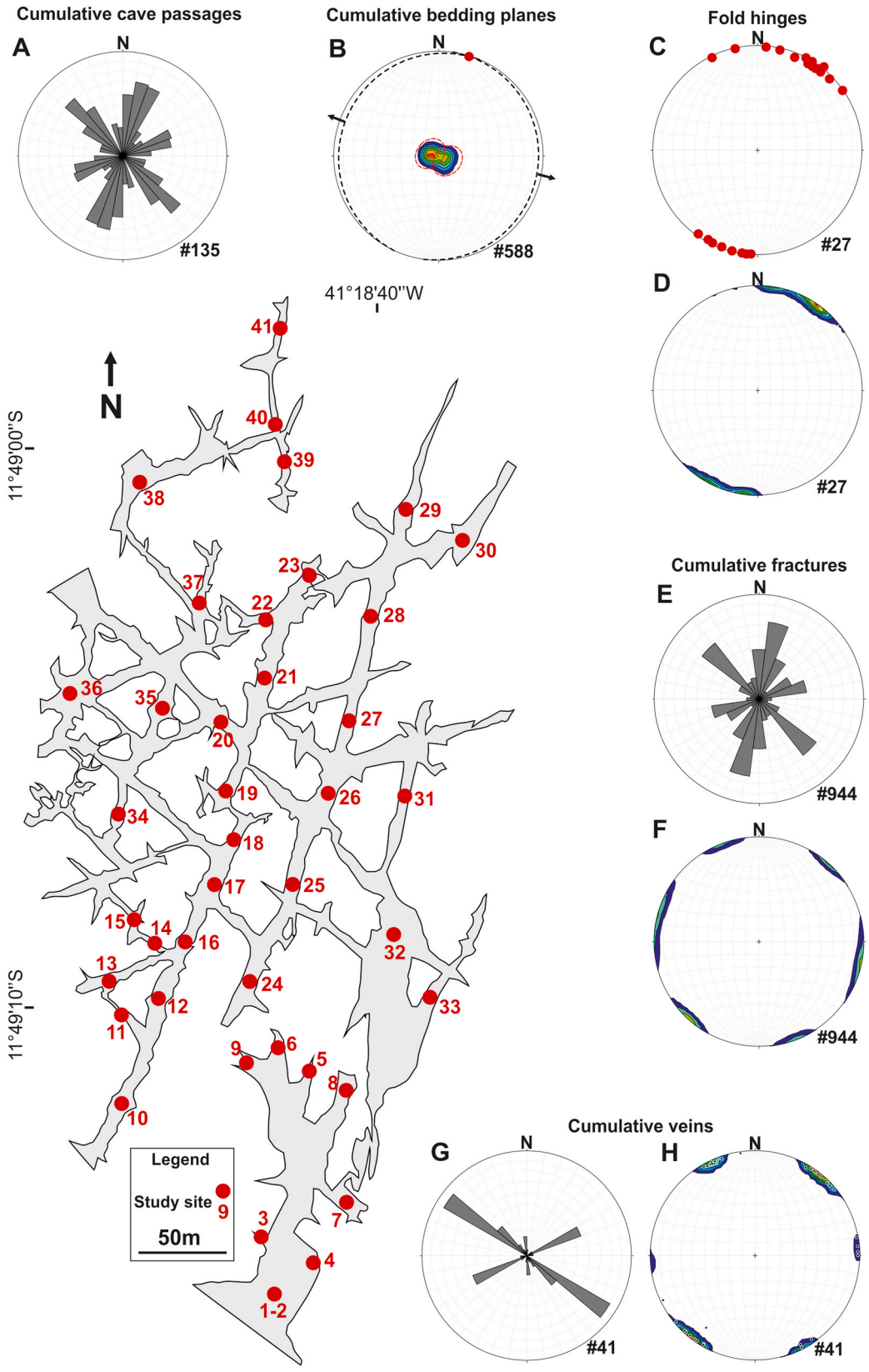

Fig. 6. Passage map of the CCKS reporting the location of the study site (map by the Brazilian Geological Survey and the Meandros Espeleo Clube). (A) Rose diagram of cave passages. (B) Lower hemisphere equal-area projection of the poles to bedding surfaces, mean beddings and mean fold hinge (red dot). (C) Lower hemisphere equal-area projection of fold hinges; the red dots represent the trend and plunge of each computed fold hinge. (D) Lower hemisphere equal-area projection of the contour density related to the computed fold hinges. (E) Rose diagram of fractures measured in the CCKS. (F) Lower hemisphere equal-area projections of the poles relative to the fracture planes presented in E. (G) Rose diagram of veins measured in the CCKS. (H) Lower hemisphere equal-area projections of the poles relative to the vein planes presented in G. (For interpretation of the references to color in this figure legend, the reader is referred to the Web version of this article.)

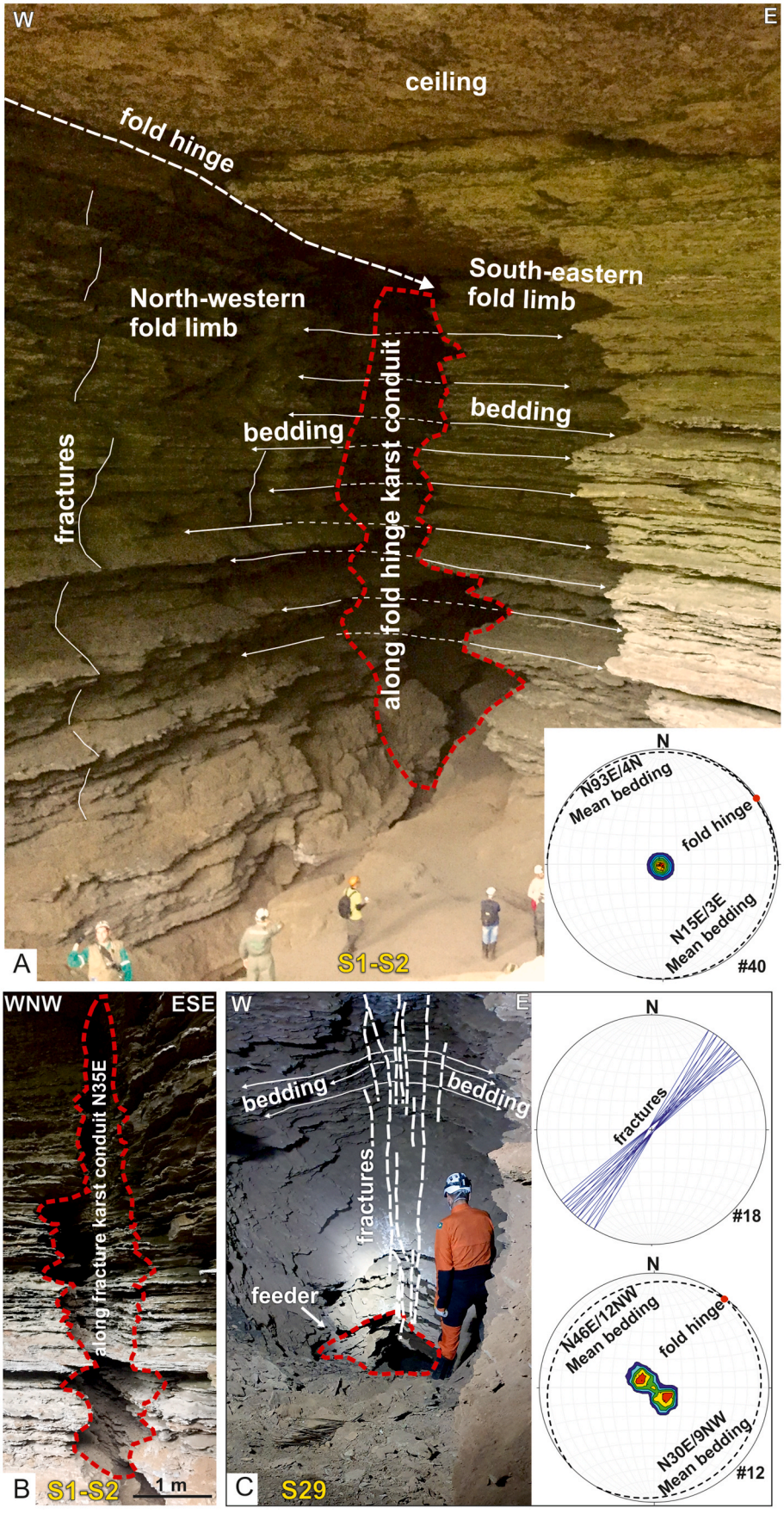

Fig. 7. (A) Cave passage formed along the anticline hinge, lower hemisphere equal-area projection of the mean bedding and relative poles density contour plot. The red dashed line highlights the major dissolved zone (study sites S1–S2). (B) Cave passage formed along a fracture zone. The red dashed line highlights the major dissolved zone (study sites S1–S2). (C) Outcrop view of a folded cave passage termination. High-angle fractures arranged in a fracture corridor configuration are documented along the maximum curvature of the folded sequence and are parallel to the fold hinge. Lower hemisphere equal-area projection of the great circles representing the attitude of the fractures (blue) and the mean bedding/relative poles density contour plot. The red dashed line highlights a feeder structure located on the cave floor (study site S29). (For interpretation of the references to color in this figure legend, the reader is referred to the Web version of this article.)

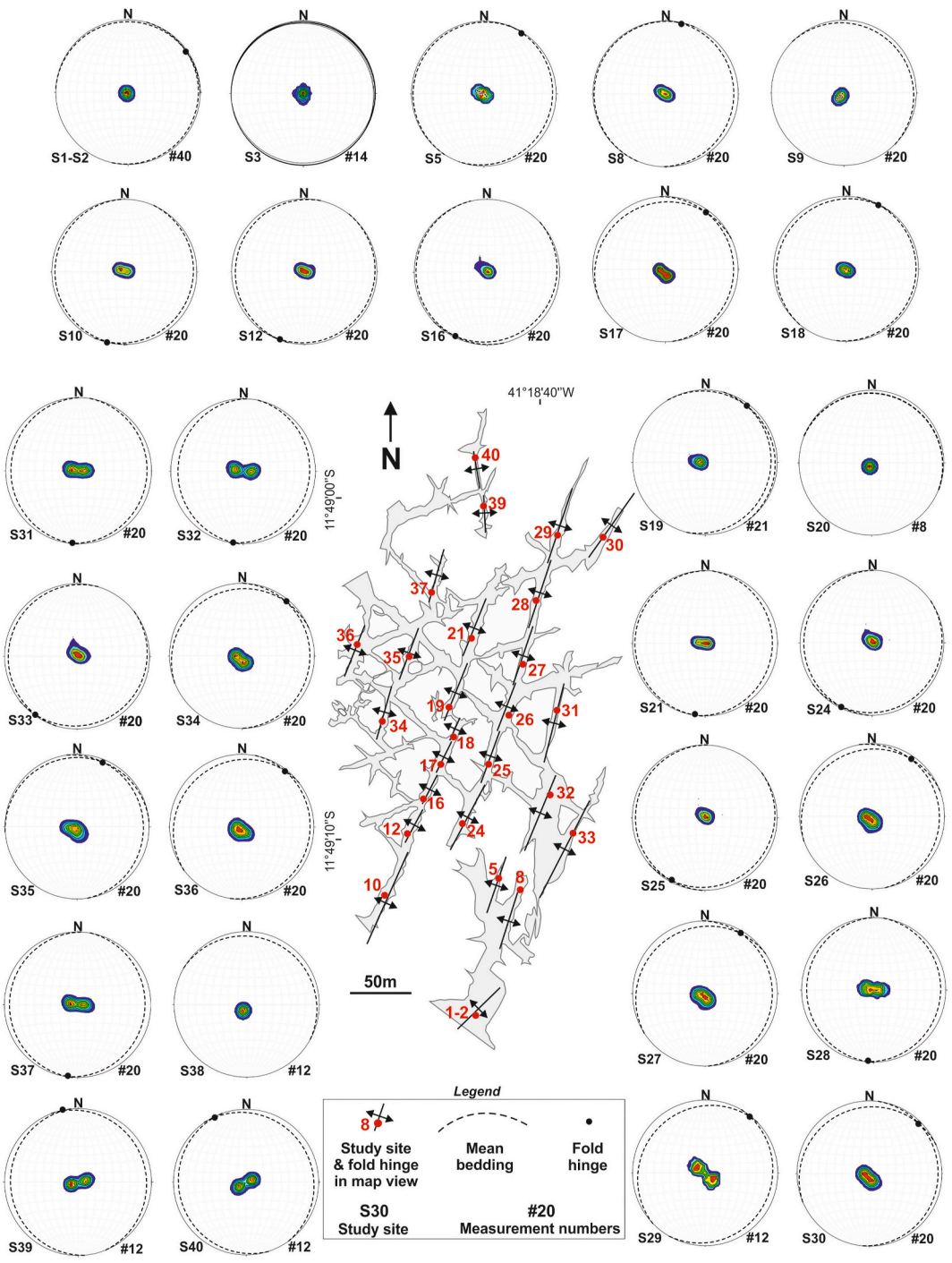

Fig. 8. Lower hemisphere equal-area projections of the poles to bedding surfaces, mean bedding (dashed black lines) and fold hinges (black dots). Black lines superimposed in map view are fold hinge locations.

5. Discussion

This discussion can shed light on the subseismic structural and karst elements ranging from cm to several m affecting the CCKS. Moreover, both the tectonic and cave evolution is summarized in an evolutionary conceptual model.

5.1. Tectonic evolution and karst development of the CCKS

The tectonic setting of the surrounding area is essential for the development of the CCKS. As documented in the previous results section, the CCKS is characterized by several deformation structures that mainly reflect the regional scale deformation style. Their relative time of formation at different stages was assessed, and an evolutionary model was proposed. The present conceptual model is characterized by three main stages (Fig. 14):

1. The first stage gave rise to the precontractional structural network, of pre-Ediacaran age, and corresponds to the background or diffuse deformation well documented within the whole Paramirim aulacogen (Barbosa and Barbosa, 2017). Such a network is composed of ca. N–S stratabound and non-stratabound joints and veins (Fig. 10A, B, C, D, E, F, 14B–I).

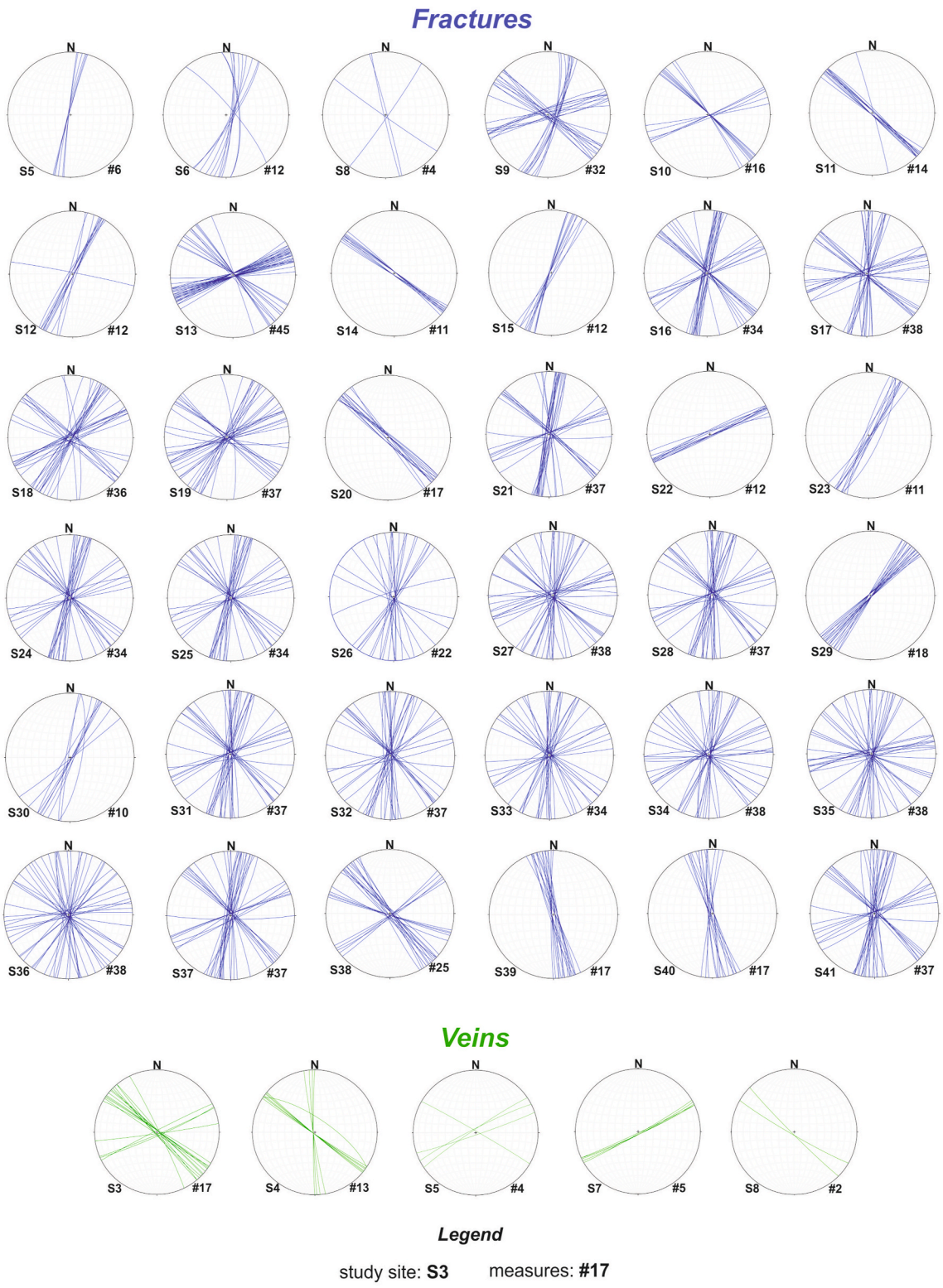

Fig. 9. Lower hemisphere equal-area projections of the great circles representing the attitude of the fractures (blue) and veins (green) measured along the CCKS study sites. (For interpretation of the references to color in this figure legend, the reader is referred to the Web version of this article.)

2. The second stage originated from the contractional structural network, is Ediacaran in age (Cruz and Alkmim, 2007; Süssenberger et al., 2014), and consists of a NNE-SSW-oriented gentle anticline (Figs. 6, 7A and 7C, 8, 14B-II). Non-stratabound fractures at a high angle to bedding formed parallel to the fold hinges; persistent fracture zones or fracture corridors were associated with this stage (Figs. 7 and 12C, D). Similar structures were previously documented by Ennes-Silva et al. (2015) in the São Francisco Craton and along the carbonate sequence of the Jandaíra Formation in the Potiguar Basin (Bagni et al., 2020). Furthermore, during this second stage, NW-SE- and ENE-WSW-striking high-angle fracture sets formed (Figs. 11 and 12A, B, 14B-II). These fracture sets were arranged as a conjugate fracture system, showing a

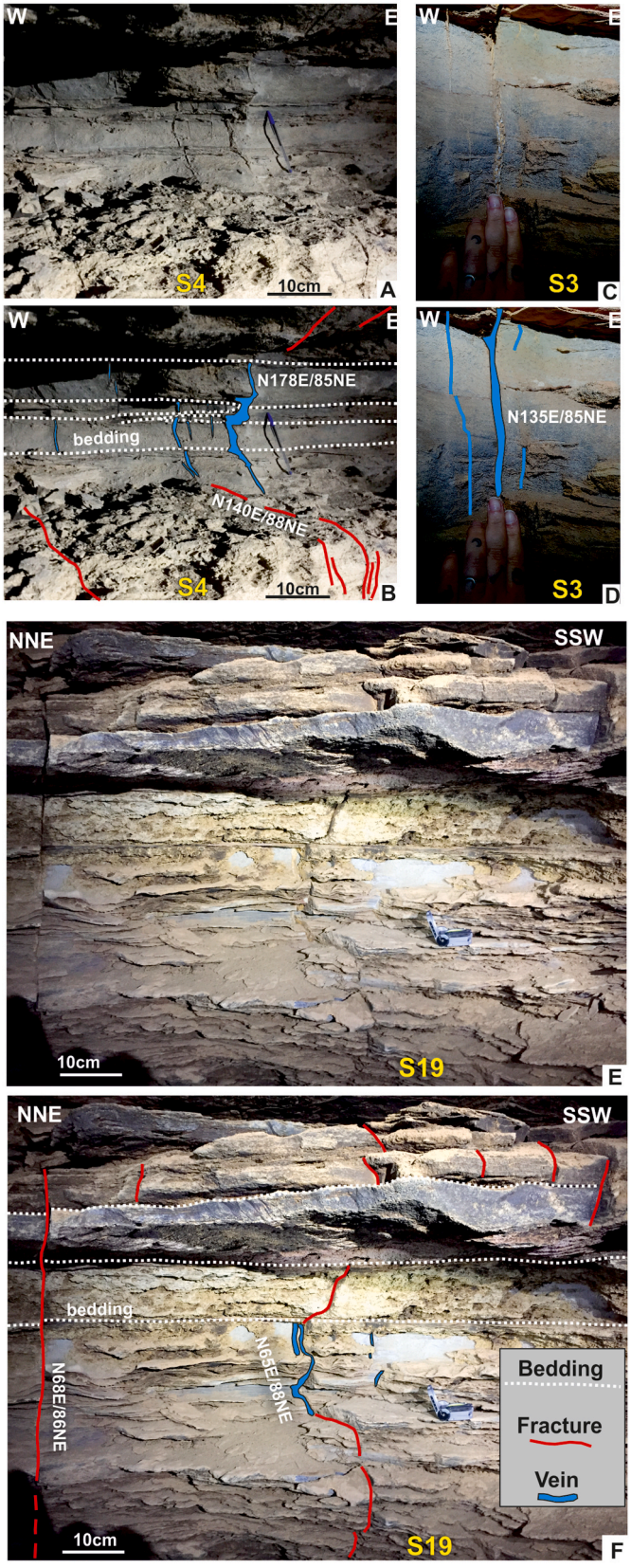

Fig. 10. (A, B, C, D, E, F) Outcrop view of strata-bound and non-stratabound fractures (red lines) and veins (blue segments) (study sites S3, S4, and S19). (For interpretation of the references to color in this figure legend, the reader is referred to the Web version of this article.)

mutual abutting relationship and suggesting an E-W-oriented contraction (Danderfer Filho, 1990).

3. The last stage is represented by the silicification and subsequent hypogenic karstification process affecting the carbonate sequence of the Caboclo Formation (Fig. 14B–III). The complex structural network, composed of folds, fractures, and faults, guided and localized geofluids migration, causing karst development along fold hinges and major fracture zones.

The computed structural maps and field analyses show how the superposed fold/fracture patterns concentrated fluid flow and the subsequent cave conduit development.

Previous studies conducted within the São Francisco Craton have already documented the hypogene origin of several karst systems in the Neoproterozoic Salitre Formation, which caps the host unit of the Cristal Cave (Auler and Smart, 2003; Bertotti et al., 2020; Cazarin et al., 2019; Ennes-Silva et al., 2015). The recent work presented by Souza et al. (2021) also suggests a hydrothermal genesis for the CCKS hosted in the Mesoproterozoic Caboclo Formation. These similarities suggest a common origin characterized by hydrothermal fluids from deep-seated sources for the CCKS and other karst systems located in the surrounding areas (e.g., Klimchouk et al., 2016). Therefore, considering the previous study conducted in the CCKS by Souza et al. (2021) and in the Irecê Basin within the Morro Vermelho Cave (Bertotti et al., 2020), a hypogenic origin of the CCKS is suggested.

The onset age of karstification can be connected to the hydrothermal silicification event, but further detailed geochronological and geochemical analyses must assess the mineralization process chronology. Other studies conducted in the São Francisco Craton ascribed the karstification to the late Proterozoic age during the Brasiliano orogeny (Bertotti et al., 2020; Heilbron et al., 2017; Misi et al., 2004; Neves et al., 2014) or to the breakup of Pangea in the Jurassic-Cretaceous period (Cazarin et al., 2019; Klimchouk et al., 2016).

The main karstification processes occurred along the folded portions of the Caboclo Formation (Figs. 4, 7 and 12), corresponding to highly deformed zones called fracture corridors (Ogata et al., 2014). These structures formed during regional ca. E-W-oriented subhorizontal contraction (Cruz and Alkmim, 2007; Ennes-Silva et al., 2015; Süssenberger et al., 2014). The fracture concentration along fold hinges has subsequently led to geofluid migration and karstification. A similar phenomenon was documented in an anticline, which affects a Cretaceous carbonate platform approximately 1200 km to the north of the study area in the Potiguar Basin (Bagni et al., 2020).

A key role was played by the structural control exerted from the deep-rooted high-angle NW-SE-striking normal faults localized along the SE extensional quadrant of the largest NNE-SSW left-lateral strike-slip fault (Figs. 3 and 14A) and by the dilatational features documented along the cave fold hinges (Figs. 7, 12C and 12D and 14B-II). Based on ascendent fluid origin, we suggest that fracture corridors and faults may have acted as preferential fluid pathways across the multilayers of the Caboclo Formation. This process has been observed elsewhere, where fault-controlled ascendent fluid migrated along high-angle extensional faults or fracture corridors (Pisani et al., 2021; Smeraglia et al., 2021).

Souza et al. (2021) documented the interplay between the stratigraphic features and the hydrothermal silicification process that allowed hypogenic karst development in the CCKS. However, persistent fracture corridors and fault zones allowed the interconnection between several stratigraphic intervals that show different degrees of dissolution (Figs. 4, 7, 12–14). Hence, fluid migration affecting the cave's stratigraphic sequence (Units 1, 2, and 3) moved along horizontal and vertical paths. The horizontal migration was mainly controlled by the rock texture/composition (Fig. 4) and bedding surfaces (Souza et al., 2021). On the other hand, vertical fluid migration was structurally driven and followed the main open discontinuities that affected the carbonate multilayer. A different behavior was observed in the marls of Unit 4 (Fig. 4), which acted as a seal for fluid migration (Souza et al., 2021) and corresponding

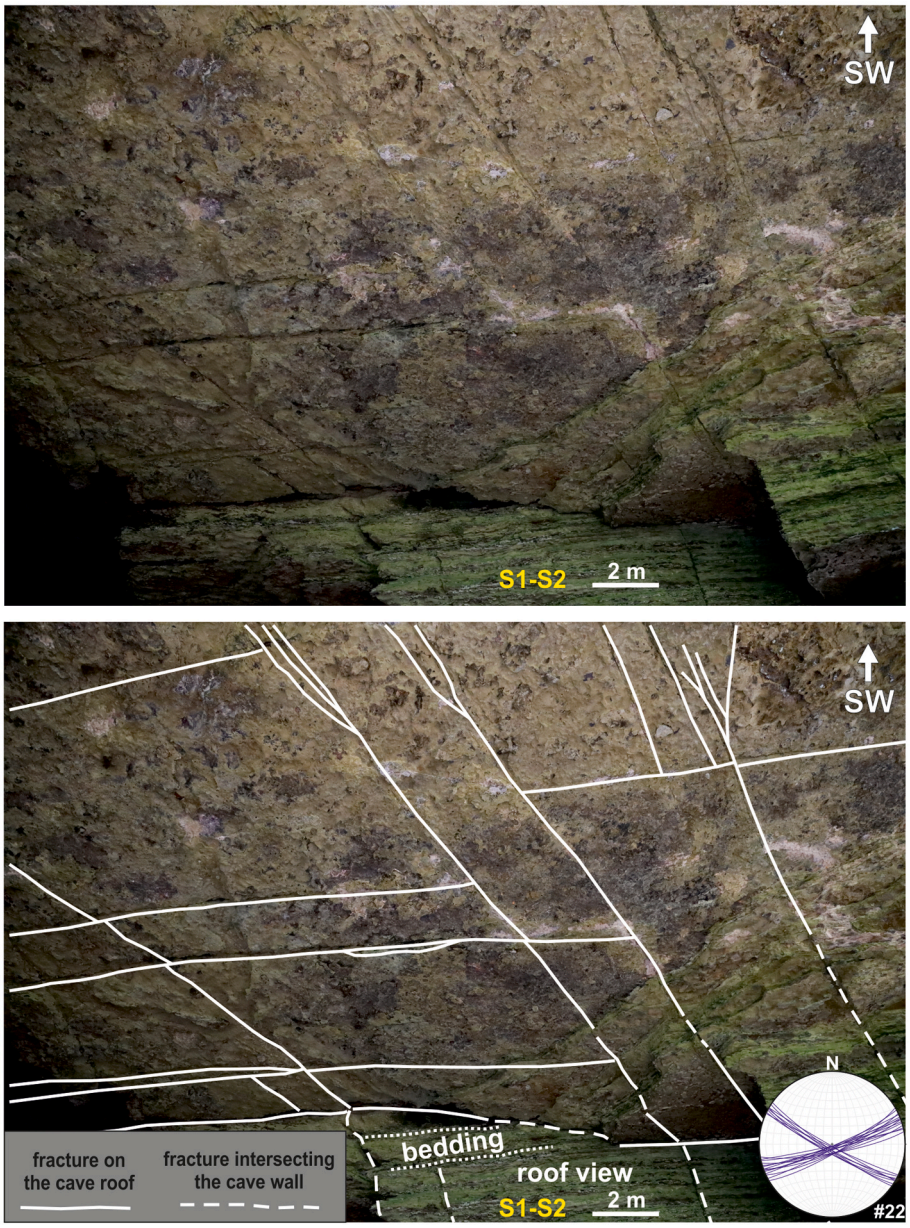

Fig. 11. Mutual abutting relationship among NW-SE and NE-SW fractures crosscutting the Caboclo Formation carbonates at study sites S1–S2 (cave ceiling view). Lower hemisphere equal-area projection of the great circles gives the attitude of the displayed fractures.

to a mechanical interface inhibiting faults and fractures upward propagation.

5.2. Implications for carbonate reservoirs

5.2 Implications for carbonate reservoirsThe presented ALOS-PALSAR imagery data highlighted several regional-scale folds (Figs. 3 and 14A); similar features were observed in seismic lines in the west sector of the São Francisco Craton within the buried portion of the Bambuí sequence (Reis et al., 2017). The resolution of the data above does not show karst evidence; in fact, only a high-resolution 3D seismic analysis could allow the epigenic karst features detection as documented by Zeng et al. (2010) within the Tarim basin (China).

However, all the documented karst features in the São Francisco Craton are at a subseismic scale and mostly associated with a hypogenic origin (Bertotti et al., 2020; Cazarin et al., 2019; Ennes-Silva et al., 2015; Klimchouk et al., 2016). To bridge the gap between the detection of hypogenic karst elements at the seismic scale, further analyses are needed. This will shed new light on dissolution processes in naturally fractured subsurface reservoirs.

A natural fracture surface reservoir is a double porosity medium characterized by the interconnection between the matrix and fractures, where a structural network is the best pathway for geofluids migration (Warren and Root, 1963). This model is widely used for reservoir studies and flow simulation but does not consider karst features. Due to their intrinsic heterogeneities, carbonate reservoirs are more challenging to characterize; this aspect is further complicated if the deformation and karstification processes are taken into consideration. The techniques commonly used in the oil and gas industry for a typical fractured reservoir are mainly well logs and seismic data. These same techniques are not fully suitable for karstified-silicified reservoir characterization. This study indicates that super-k (high-permeability) zones are associated with fracture corridors localized along fold hinges. In these zones, the fracture network connects several parts of the rock multilayer and allows flow (e.g., Agosta et al., 2010; Matthäi and Belayneh, 2004; Pollard and Aydin, 1988). Moreover, the subsequent karstification

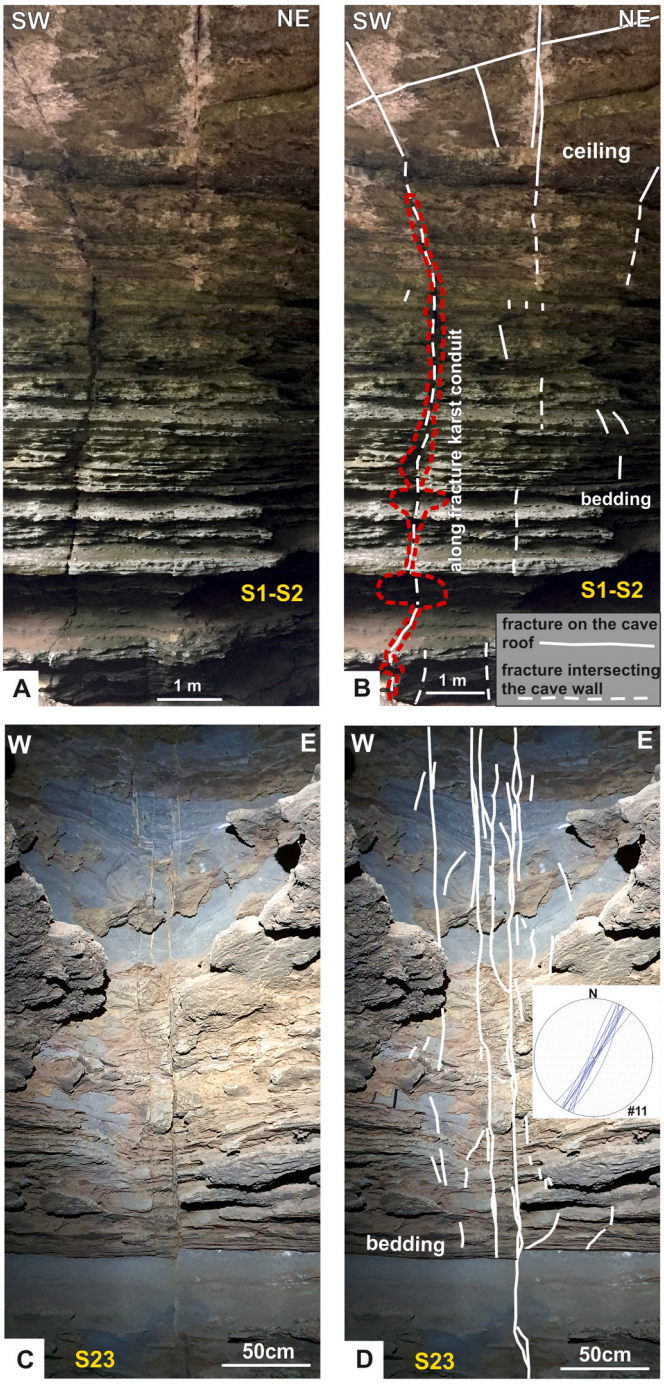

Fig. 12. (A, B) Cave wall affected by several non-stratabound fractures. A major non-stratabound persistent fracture crosscuts the carbonate sequence, acting as a connecting structure between the different carbonate layers and behaving as a preferential pathway for fluid migration. The red dashed line highlights the major dissolved zone (study sites S1–S2). (C, D) Outcrop view of a fracture corridor where high-angle partially mineralized fractures and sheared fractures crosscut the carbonate rocks. Lower hemisphere equal-area projection of great circles representing the attitude of the fractures measured along study site S23. (For interpretation of the references to color in this figure legend, the reader is referred to the Web version of this article.)

dramatically increases the permeability. All these aspects can improve hydrocarbon production, but at the same time, may connect the water table with overlying reservoirs and allow water breakthrough or cause large mud loss during drilling operations (Bagni et al., 2020).

A common approach regularly used for fracture frequency prediction is based on the assumption that greater curvature equals the strain increment (Roberts, 2001). This expectation is valid for folded structures but does not consider the karst process. Hence, the single use of the curvature attribute would incorrectly be interpreted for fracture permeability variability. Furthermore, the processes that occur during karst formation could produce extreme contrasts in porosity and permeability. In contrast, the hydrothermal silicification process could enhance or decrease the carbonate multilayer permeability properties (Menezes et al., 2019; Souza et al., 2021). According to Souza et al. (2021), hydrothermal silicification is stratigraphically and texturally controlled in the CCKS and is mainly localized within the coarse levels as grainstone intervals (Fig. 4). This mineralizing event allows pervasive cementation of the aforementioned layers, modifying the original porosity and permeability characteristics. The performed 3D permeability analyses display low values (0.003 mD) in the pristine rock portions (Fig. 5 and Table 1). In contrast, when the host rock is affected by the presence of structural discontinuities (Fig. 5 and Table 1), the permeability could reach as high as 23 mD. This evidence indicates that in mixed deformed, karstified and silicified reservoirs, the major permeable zones correspond to the most deformed zones. However, further detailed analysis could better define the interplay between the several processes affecting the studied sedimentary sequence.

Moreover, when subseismic karst features affect the reservoir, the uncertainty increases. It follows that drill holes and seismic surveys furnish only limited information (Gholipour, 1998; Gholipour et al., 2016). Subseismic analog studies could provide the best approach to solve the uncertainties for a realistic prediction of a karstified reservoir controlled by regional-scale tectonics. Previous works have already suggested studying deformed and karstified analogs (Cazarin et al., 2019; Ennes-Silva et al., 2015). In contrast, this study has documented that rock properties can drastically change due to combined deformation, karstification, and hydrothermal silicification processes. The previous relationship must be considered a keystone for characterizing the subseismic high-permeability zones in carbonate reservoirs.

This study has demonstrated that a karstified carbonate reservoir can drastically change its architecture and properties through spatiotemporal development. Therefore, karst processes integration and upscaling are needed in flow simulation and production to predict reservoir behavior and, consequently, optimize development decisions. Further analyses focused on mechanical/fracture stratigraphy, fluid geochemical investigation, and detailed petrophysical characterization of the whole units are required to assess the close connection between mechanical rock properties, flow pathways, and mineralizing processes. Moreover, an investigation of the neighboring sectors could allow understanding the extension of the proposed model and its applicability to any reservoir affected by similar processes. This will give a better understanding of super-k conduit development and distribution in fractured-karstified reservoirs.

6. Conclusions

This study aimed to characterize the architecture of high-permeability zones in subseismic-scale folded structures. These super-k zones are associated with the occurrence of fracture corridors in anticline hinges.

To better analyze these karstified fracture corridors, this study combined field and laboratory analyses to determine the tectonic evolution and karst development reconstruction of the Cristal Cave Karst System (CCKS) in the Mesoproterozoic carbonate units of the São Francisco Craton, Brazil. We deciphered the deformation events affecting the carbonate rocks and proposed a conceptual model related to the evolution of the structural assemblage and the subsequent karst formation.

At the boundary between the Irecê and Morro do Chapéu structural domains, the regional structural setting of the study area is dominated by transpression between a major left-lateral strike-slip fault system and

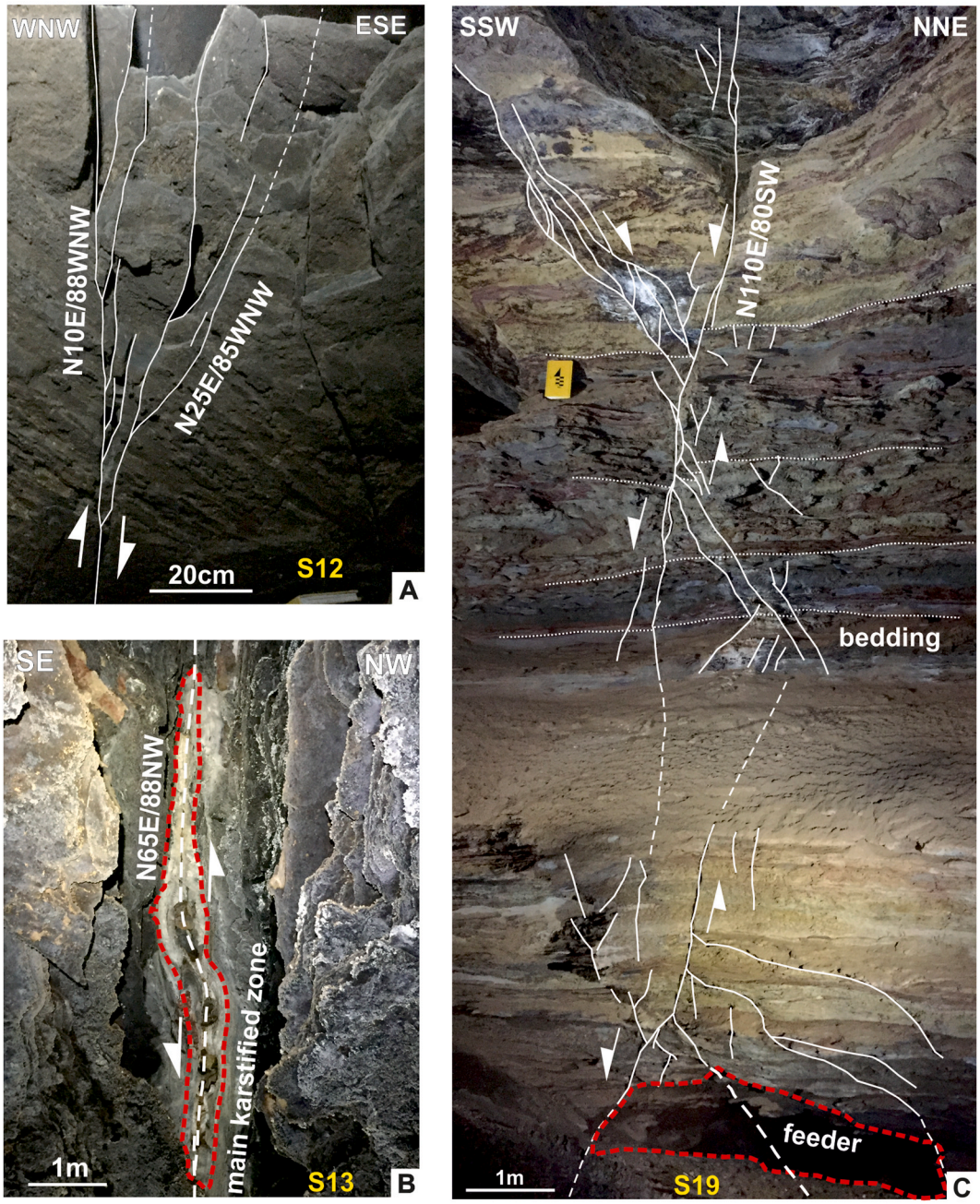

Fig. 13. (A) S12 study site. Cave ceiling view crosscut by a sheared fracture. Right-lateral slip along the N10E/88WNW sheared fracture, as shown by the structural architecture of the extensional quadrant. Traces of splay joints, mainly oriented N25E/85WNW, departing from the sheared structural element are also documented. (B) S13 study site. Cave ceiling view of a right-lateral sheared fracture linkage zone. The main dissolved zone is concentrated at the fracture linkage portion, acting as a conduit for fluid migration. (C) Outcrop view of a normal fault composed of through-going slip surfaces and tail joints, which are localized at their extensional quadrants and/or releasing jogs. A main karstified zone (red dashed line), recognized as a feeder, is located in the fault extensional quadrant (study site S19). (For interpretation of the references to color in this figure legend, the reader is referred to the Web version of this article.)

cylindrical-shaped regional scale deformation, generating parallel gentle/open folds. This study provides a detailed field geological analysis and interpretation of this structurally controlled karst system.

We proposed the following evolutionary stages

1. The first stage is associated with the precontractional structural network (pre-Ediacaran). It corresponds to the background deformation assemblage composed of ca. N–S strata-bound and non-stratabound joints and veins.

2. The second assemblage is related to the Ediacaran contractional event. It consists of several structural elements: NNE-SSW-oriented gentle anticlines, persistent fracture corridors distributed along NNE-oriented fold hinges, and a conjugate fracture system composed of NW-SE- and ENE-WSW-striking high-angle fractures.

3. The third stage is associated with the hypogenic karstification process. The karst development was controlled by the structural network generated during stages 1 and 2. The primary karstification process occurred along the fracture corridors parallel to the fold hinge zone; this highly deformed portion represents the preferential site for high karst porosity and permeability.

We proposed a correlation between the fold and fracture patterns documented in the CCKS with the major regional deformation structures and its relevance in understanding the relationships among regional and

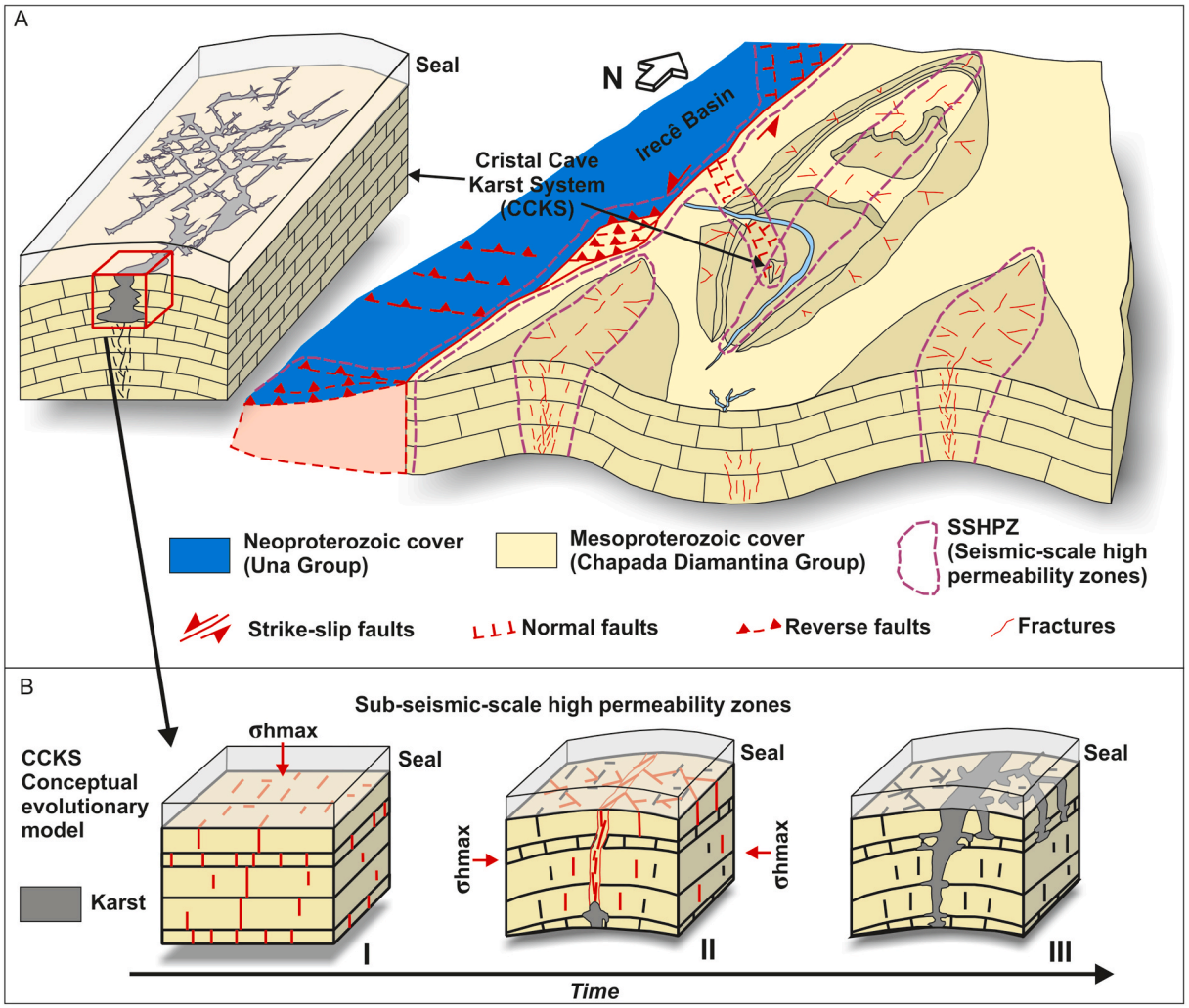

Fig. 14. Spatiotemporal evolution model proposed for the CCKS. (A) Cartoon displaying the current regional scale configuration. (B) Idealized block diagrams showing the overall structural assemblage evolution that favored geofluid migration and subsequent karstification.

local structural and karst processes. Moreover, this work provided a baseline to understand better and provide first-order predictions for subseismic fracture corridors, which are high permeability areas located in folded and faulted carbonate reservoir analogs. Their characterization is essential to improving the knowledge of karstification predictability in carbonate rocks affected by ascending hydrothermal fluids. We conclude that, in the studied sector, karst high-permeability zones in fold hinges mimic the geometry and orientation of structures recognized at the seismic scale; these pieces of evidence could be recognized elsewhere in rock sequences characterized by the same processes.

Credit author statement

Vincenzo La Bruna: Investigation, Data curation, Formal analysis, Visualization, Writing – original draft. Francisco H. R. Bezerra: Investigation, Data curation, Formal analysis, Visualization, Writing – review & editing. Victor H.P. Souza: Investigation, Data curation, Formal analysis, Writing – review & editing. Rubson P. Maia: Investigation, Data curation, Formal analysis, Writing – review & editing. Augusto S. Auler: Investigation, Data curation, Formal analysis, Writing – review & editing. Renata E.B. Araujo: Data curation, Formal analysis, Writing – review & editing. Caroline L. Cazarin: Investigation, Data curation, Writing – review & editing. Marcos A. F. Rodrigues: Data curation, Formal analysis, Writing – review & editing. Lucieth C. Vieira: Investigation, Data curation, Formal analysis, Writing – review & editing. Lucena M. O. Sousa: Data curation, Writing – review & editing.

Declaration of competing interest

The authors declare that they have no known competing financial interests or personal relationships that could have appeared to influence the work reported in this paper.

Acknowledgments

This work is part of a Petrobras/Federal University of Rio Grande do Norte – UFRN project (CristalDOM project, coordinated by FHB –UFRN and Caroline Cazarin – Petrobras). We thank the Brazilian Agency of Oil, Gas, and Biofuels (Agência Nacional do Petróleo, Gás e Biocombustíveis, ANP). The cave map of Cristal Cave was kindly provided by Mylene Berbert-Born from the CPRM (Geological Survey of Brazil) and the Meandros Espeleo Clube. The authors thank the Associate Editor Nicolas Beaudoin, and the reviewers Jo De Waele and Phillipe Audra for their advice and helpful correction on the manuscript.

References

Agar, S.M., Geiger, S., 2015. Fundamental controls on fluid flow in carbonates: current workflows to emerging technologies. Geol. Soc. London, Spec. Publ. 406, 1–59. https://doi.org/10.1144/SP406.18.

Agosta, F., Alessandroni, M., Antonellini, M., Tondi, E., Giorgioni, M., 2010. From fractures to flow: a field-based quantitative analysis of an outcropping carbonate reservoir. Tectonophysics 490, 197–213. https://doi.org/10.1016/j.tecto.2010.05.005.

Ahr, W.M., 2011. Geology of Carbonate Reservoirs: the Identification, Description and Characterization of Hydrocarbon Reservoirs in Carbonate Rocks, p. 296.

Akbar, M., Vissapragada, B., Alghamdi, A.H., Allen, D., Herron, M., Carnegie, A., Dutta, D., Olesen, J.-R., Chousasiya, R.D., Logan, D., Stief, D., Netherwood, R., Russell, S.D., Saxena, K., 2000. A snapshot of a carbonate reservoir evaluation. Oilfield Rev. 12, 20–21.

Aljuboori, F.A., Lee, J.H., Elraies, K.A., Stephen, K.D., 2019. Gravity drainage mechanism in naturally fractured carbonate reservoirs; review and application. Energies 12, 3699. https://doi.org/10.3390/en12193699.

Alkmim, F.D., 2004. O que faz de um cráton um cráton? O Cráton do São Francisco e as revelações almeidianas ao delimitá-lo. Geologia Do Continente Sul-Americano: Evolução Da Obra de Fernando Flávio Marques de Almeida, pp. 17–34.

Alkmim, F.F., Martins-Neto, M.A., 2012. Proterozoic first-order sedimentary sequences of the São Francisco craton, eastern Brazil. Mar. Petrol. Geol. 33, 127–139. https://doi.org/10.1016/j.marpetgeo.2011.08.011.

Alkmim, F.F., Neves, B.B.B., Alves, J.A.C., 1993. Arcabouço tectônico do cráton do São Francisco – Uma revisão. In: Dominguez, J.M.L., Barbosa, J.S.F. (Eds.), O Cráton Do São Francisco. SBG/NBA-SE, Salvador, pp. 45–62.

Allmendinger, R.W., Cardozo, N., Fisher, D.M., 2011. Structural Geology Algorithms: Vectors and Tensors, p. 304.

Almeida, F.F.M. de, Brito Neves, B.B. de, Dal Ré Carneiro, C., 2000. The origin and evolution of the South American Platform. Earth Sci. Rev. 50, 77–111. https://doi.org/10.1016/S0012-8252(99)00072-0.

Antonellini, M., Nannoni, A., Vigna, B., De Waele, J., 2019. Structural control on karst water circulation and speleogenesis in a lithological contact zone: the Bossea cave system (Western Alps, Italy). Geomorphology 345, 106832. https://doi.org/10.1016/j.geomorph.2019.07.019.

Araújo, R.E.B., La Bruna, V., Rustichelli, A., Bezerra, F.H.R., Xavier, M.M., Audra, P., Barbosa, J.A., Antonino, A.C.D., 2021. Structural and sedimentary discontinuities control the generation of karst dissolution cavities in a carbonate sequence, Potiguar Basin, Brazil. Mar. Petrol. Geol. 123 https://doi.org/10.1016/j.marpetgeo.2020.104753.

Auler, A.S., Smart, P.L., 2003. The influence of bedrock-derived acidity in the development of surface and underground karst: evidence from the Precambrian carbonates of semi-arid northeastern Brazil. Earth Surf. Process. Landforms 28, 157–168. https://doi.org/10.1002/esp.443.

Bagni, F.L., Bezerra, F.H., Balsamo, F., Maia, R.P., Dall'Aglio, M., 2020. Karst dissolution along fracture corridors in an anticline hinge, Jandaíra Formation, Brazil: implications for reservoir quality. Mar. Petrol. Geol. 115, 104249. https://doi.org/10.1016/j.marpetgeo.2020.104249.

Balsamo, F., Bezerra, F.H.R., Klimchouk, A.B., Cazarin, C.L., Auler, A.S., Nogueira, F.C., Pontes, C., 2020. Influence of fracture stratigraphy on hypogene cave development and fluid flow anisotropy in layered carbonates, NE Brazil. Mar. Petrol. Geol. 114, 104207. https://doi.org/10.1016/j.marpetgeo.2019.104207.

Barbosa, J.S.F., Barbosa, R.G., 2017. The paleoproterozoic eastern bahia orogenic domain. São Francisco Craton, Eastern Brazil, pp. 57–69. https://doi.org/10.1007/978-3-319-01715-0_4.

Berbert-Born, M., Horta, L.C.S., Costa, I.V.G., Zogbi, L., Born, R., Menin, D., Fakhouri, L., 2012. Gruta Do Cristal I - Ba - 206. CPRM - Serviço Geológico Do Bras. https://sites.google.com/site/meandrosespeleoclube/mapas?authuser=0.

Berbert-Born, M.L., Horta, L., 1995. Espeleologia. Salvador, CPRM Projeto Mapas Municipais-Informações Básicas Para o Planejamento e Administração Do Meio Físico. Município de Morro Do Chapéu (BA), pp. 158–202.

Bertotti, G., Audra, P., Auler, A., Bezerra, F.H., de Hoop, S., Pontes, C., Prabhakaran, R., Lima, R., 2020. The Morro Vermelho hypogenic karst system (Brazil): stratigraphy, fractures, and flow in a carbonate strike-slip fault zone with implications for carbonate reservoirs. Am. Assoc. Petrol. Geol. Bull. 104, 2029–2050. https://doi.org/10.1306/05212019150.

Bockel-Rebelle, M.-O., Hassall, J.K., Silva, F.P., Lozano, J.A., Al Deeb, M., Salem, S.E.A., Vesseron, M., Al Mehsin, K., 2004. Faults, fracture corridors and diffuse fracturing: ranking the main structural heterogeneities within onshore Abu Dhabi fields. In: Abu Dhabi International Conference and Exhibition. Society of Petroleum Engineers. https://doi.org/10.2118/88676-MS.

Bourbiaux, B., 2010. Fractured reservoir simulation: a challenging and rewarding issue. Oil Gas Sci. Technol. – Rev. l'Institut Français du Pétrole 65, 227–238. https://doi.org/10.2516/ogst/2009063.

Cazarin, C.L., Bezerra, F.H.R., Borghi, L., Santos, R.V., Favoreto, J., Brod, J.A., Auler, A. S., Srivastava, N.K., 2019. The conduit-seal system of hypogene karst in Neoproterozoic carbonates in northeastern Brazil. Mar. Petrol. Geol. 101, 90–107. https://doi.org/10.1016/j.marpetgeo.2018.11.046.

Costa, A.F., Danderfer Filho, A., 2017. Tectonics and sedimentation of the central sector of the Santo Onofre rift, north Minas Gerais, Brazil. Brazilian J. Geol. 47, 491–519. https://doi.org/10.1590/2317-488920172016012 8.

Cruz, S.C.P., Alkmim, F.F.D., 2007. A história de inversão do aulacógeno do Paramirim contada pela Sinclinal de Ituaçu, extremo sul da Chapada Diamantina. Rev. Bras. Geociencias 37, 92–110.

Cruz, S.C.P., Dias, V.M., Alkmim, F.F., 2007. A interação tectônica embasamento/cobertura em aulacógenos invertidos: um exemplo da Chapada Diamantina Ocidental. Rev. Bras. Geociencias 37, 11–127.

D'Angelo, T., Barbosa, M.S.C., Danderfer Filho, A., 2019. Basement controls on cover deformation in eastern Chapada Diamantina, northern São Francisco Craton, Brazil: insights from potential field data. Tectonophysics 772, 228231. https://doi.org/10.1016/j.tecto.2019.228231.

Danderfer Filho, A., 1990. Análise estrutural descritiva e cinemática do Supergrupo Espinhaço, na região da Chapada Diamantina – BA. Universidade Federal de Ouro Preto, Ouro Preto, p. 99.

Danderfer Filho, A., Dardenne, M.A., 2002. Tectonoestratigrafia da bacia espinhaço na porção centro-norte do cráton do São Francisco: registro de uma evolução policíclica, multitemporal e poliistórica. Rev. Bras. Geociencias 32, 449–460.

Danderfer Filho, A., Lana, C.C., Nalini Júnior, H.A., Costa, A.F.O., 2015. Constraints on the Statherian evolution of the intraplate rifting in a Paleo-Mesoproterozoic paleocontinent: new stratigraphic and geochronology record from the eastern São Francisco craton. Gondwana Res. 28, 668–688. https://doi.org/10.1016/j.gr.2014.06.012.

Dunham, R.J., 1962. Classification of carbonate rocks according to depositional textures. AAPG Spec 108–121, 108–121.

Eliebid, M., Mahmoud, M., Shawabkeh, R., Elkatatny, S., Hussein, I.A., 2018. Effect of CO2 adsorption on enhanced natural gas recovery and sequestration in carbonate reservoirs. J. Nat. Gas Sci. Eng. 55, 575–584. https://doi.org/10.1016/j.jngse.2017.04.019.

Embry, A.F., Klovan, J.E., 1971. A late Devonian reef tract on northeastern Banks Island. NWT. Bull. Can. Pet. Geol. 19, 730–781.

Ennes-Silva, R.A., Bezerra, F.H.R., Nogueira, F.C.C., Balsamo, F., Klimchouk, A., Cazarin, C.L., Auler, A.S., 2015. Superposed folding and associated fracturing influence hypogene karst development in Neoproterozoic carbonates, São Francisco Craton, Brazil. Tectonophysics 666, 244–259. https://doi.org/10.1016/j.tecto.2015.11.006.

Firoozabadi, A., 2000. Recovery mechanisms in fractured reservoirs and field performance. J. Can. Pet. Technol. 39 https://doi.org/10.2118/00-11-DAS.

Ford, D., Williams, P.D., 2013. Karst Hydrogeology and Geomorphology. John Wiley & Sons, p. 576.

Gholipour, A.M., 1998. Patterns and structural positions of productive fractures in the asmari reservoirs, southwest Iran. J. Can. Pet. Technol. 37 https://doi.org/10.2118/98-01-07.

Gholipour, A.M., Cosgrove, J.W., Ala, M., 2016. New theoretical model for predicting and modelling fractures in folded fractured reservoirs. Petrol. Geosci. 22, 257–280. https://doi.org/10.1144/petgeo2013-055.

Giuffrida, A., Agosta, F., Rustichelli, A., Panza, E., La Bruna, V., Eriksson, M., Torrieri, S., Giorgioni, M., 2020. Fracture stratigraphy and DFN modelling of tight carbonates, the case study of the Lower Cretaceous carbonates exposed at the Monte Alpi (Basilicata, Italy). Mar. Petrol. Geol. 112 https://doi.org/10.1016/j.marpetgeo.2019.104045.

Giuffrida, A., La Bruna, V., Castelluccio, P., Panza, E., Rustichelli, A., Tondi, E., Giorgioni, M., Agosta, F., 2019. Fracture simulation parameters of fractured reservoirs: analogy with outcropping carbonates of the Inner Apulian Platform. southern Italy. J. Struct. Geol. 123, 18–41. https://doi.org/10.1016/j.jsg.2019.02.007.

Heilbron, M., Cordani, U.G., Alkmim, F.F., 2017. The São Francisco craton and its margins. São Francisco Craton, Eastern Brazil, pp. 3–13. https://doi.org/10.1007/978-3-319-01715-0_1.

Jolley, S.J., Barr, D., Walsh, J.J., Knipe, R.J., 2007. Structurally complex reservoirs: an introduction. Geol. Soc. London, Spec. Publ. 292, 1–24. https://doi.org/10.1144/SP292.1.

Jones, S.C., 1972. A rapid accurate unsteady-state Klinkenberg permeameter. Soc. Petrol. Eng. J. 12, 383–397. https://doi.org/10.2118/3535-PA.

Klimchouk, A., 2009. Morphogenesis of hypogenic caves. Geomorphology 106, 100–117. https://doi.org/10.1016/j.geomorph.2008.09.013.

Klimchouk, A., Auler, A.S., Bezerra, F.H.R., Cazarin, C.L., Balsamo, F., Dublyansky, Y., 2016. Hypogenic origin, geologic controls and functional organization of a giant cave system in Precambrian carbonates, Brazil. Geomorphology 253, 385–405. https://doi.org/10.1016/j.geomorph.2015.11.002.

Klimchouk, A., Tymokhina, E., Amelichev, G., 2012. Speleogenetic effects of interaction between deeply derived fracture-conduit flow and intrastratal matrix flow in hypogene karst settings. Int. J. Speleol. 41, 161–179. https://doi.org/10.5038/1827-806X.41.2.4.

Klimchouk, A.B., Andreychouk, V.N., Turchinov, I.I., 2009. The Structural Prerequisites of Speleogenesis in Gypsum in the Western Ukraine, second ed. University of Silesia - Ukrainian Institute of Speleology and Karstology, Sosnowiec-Simferopol.

Klinkenberg, L.J., 1941. The permeability of porous media to liquids and gases. Am. Pet. Inst 200–213.

La Bruna, V., Agosta, F., Lamarche, J., Viseur, S., Prosser, G., 2018. Fault growth mechanisms and scaling properties in foreland basin system: the case study of Monte Alpi, Southern Apennines, Italy. J. Struct. Geol. 116, 94–113. https://doi.org/10.1016/j.jsg.2018.08.009.

La Bruna, V., Agosta, F., Prosser, G., 2017. New insights on the structural setting of the Monte Alpi area, Basilicata. Italy. Ital. J. Geosci. 136 https://doi.org/10.3301/IJG.2017.03.

La Bruna, V., Lamarche, J., Agosta, F., Rustichelli, A., Giuffrida, A., Salardon, R., Marié, L., 2020. Structural diagenesis of shallow platform carbonates: role of early embrittlement on fracture setting and distribution, case study of Monte Alpi (Southern Apennines, Italy). J. Struct. Geol. 131 https://doi.org/10.1016/j.jsg.2019.103940.

Li, C., Xu, P., Qiu, S., Zhou, Y., 2016. The gas effective permeability of porous media with Klinkenberg effect. J. Nat. Gas Sci. Eng. 34, 534–540. https://doi.org/10.1016/j.jngse.2016.07.017.

Mäkel, G.H., 2007. The modelling of fractured reservoirs: constraints and potential for fracture network geometry and hydraulics analysis. Geol. Soc. London, Spec. Publ. 292, 375–403. https://doi.org/10.1144/SP292.21.

Matthäi, S.K., Belayneh, M., 2004. Fluid flow partitioning between fractures and a permeable rock matrix. Geophys. Res. Lett. 31, 1–5. https://doi.org/10.1029/2003GL019027.

Menezes, C.P., Bezerra, F.H.R., Balsamo, F., Mozafari, M., Vieira, M.M., Srivastava, N.K., de Castro, D.L., 2019. Hydrothermal silicification along faults affecting carbonate-sandstone units and its impact on reservoir quality, Potiguar Basin, Brazil. Mar. Petrol. Geol. 110, 198–217. https://doi.org/10.1016/j.marpetgeo.2019.07.018.

Misi, A., Iyer, S.S.S., Tassinari, C.C.G., Franca-Rocha, W.J.S., Coelho, C.E.S., Cunha, I. de A., Gomes, A.S.R., 2004. Dados isotópicos de chumbo em sulfetos e a evolução metalogenética dos depósitos de zinco e chumbo das coberturas neoproterozóicas do Cráton do São Francisco. Rev. Bras. Geociencias 34, 263–274. https://doi.org/10.25249/0375-7536.2004342263274.

Nelson, R., 2001. Geologic Analysis of Naturally Fractured Reservoirs. Elsevier, p. 320.

Neves, B.B.de B., Fuck, R.A., Pimentel, M.M., 2014. The Brasiliano collage in South America: a review. Brazilian J. Geol. 44, 493–518. https://doi.org/10.5327/Z2317-4889201400030010.

Ogata, K., Senger, K., Braathen, A., Tveranger, J., 2014. Fracture corridors as seal-bypass systems in siliciclastic reservoir-cap rock successions: field-based insights from the Jurassic Entrada Formation (SE Utah, USA). J. Struct. Geol. 66, 162–187. https://doi.org/10.1016/j.jsg.2014.05.005.

Osborne, R.A.L., 2007. Cathedral cave, wellington caves, new South wales, Australia. A multiphase, non-fluvial cave. Earth Surf. Process. Landforms 32, 2075–2103. https://doi.org/10.1002/esp.1507.

Panza, E., Sessa, E., Agosta, F., Giorgioni, M., 2018. Discrete Fracture Network modelling of a hydrocarbon-bearing, oblique-slip fault zone: inferences on fault-controlled fluid storage and migration properties of carbonate fault damage zones. Mar. Petrol. Geol. 89, 263–279. https://doi.org/10.1016/j.marpetgeo.2017.09.009.

Pedreira, A.J.C.L., Arcanjo, J.B., Pedrosa, C.J., Oliveira, J.E., Silva, B.C.E., 1975. Projeto Bahia-Geologia da Chapada Diamantina. Relatório Final.

Pedrosa-Soares, A.C., Alkmim, F.F. de, 2013. How many rifting events preceded the development of the Araçuaí-West Congo orogen? Geonomos 19, 244–251. https://doi.org/10.18285/geonomos.v19i2.56.

Pisani, L., Antonellini, M., D'Angeli, I.M., De Waele, J., 2021. Structurally controlled development of a sulfuric hypogene karst system in a fold-and-thrust belt (Majella Massif, Italy). J. Struct. Geol. 145, 104305. https://doi.org/10.1016/j.jsg.2021.104305.

Pollard, D.D., Aydin, A., 1988. Progress in understanding jointing over the past century. Geol. Soc. Am. Bull. 100, 1181–1204. https://doi.org/10.1130/0016-7606(1988)100<1181:PIUJOT>2.3.CO;2.

Questiaux, J.-M., Couples, G.D., Ruby, N., 2010. Fractured reservoirs with fracture corridors. Geophys. Prospect. 58, 279–295. https://doi.org/10.1111/j.1365-2478.2009.00810.x.

Reis, H.L.S., Alkmim, F.F., Fonseca, R.C.S., Nascimento, T.C., Suss, J.F., Prevatti, L.D., 2017. The São Francisco basin. São Francisco Craton, Eastern Brazil. Springer, Cham, pp. 117–143. https://doi.org/10.1007/978-3-319-01715-0_7.

Reis, H.L.S., Gomes, C.J.S., Fragoso, D.G.C., Kuchenbecker, M., 2013. O cinturão epidérmico de antepaís da Bacia de Irecê, Cráton do São Francisco[/title]: [subtitle] principais elementos estruturais e modelagem física analógica. Geol. Usp. Série Científica 13, 125–139. https://doi.org/10.5327/Z1519-874X201300040007.

Roberts, A., 2001. Curvature attributes and their application to 3 D interpreted horizons. First Break 19, 85–100.

Rocha, A.J.D., Pereira, C.P., Srivastava, N.K., 1992. Carbonatos da Formação Caboclo (Proterozóico Médio) na região de Morro do Chapéu - estado da Bahia. Rev. Bras. Geociencias 22, 389–398.

Roehl, P.O., Choquette, P.W., 2012. Carbonate Petroleum Reservoirs. Springer Science & Business Media. Springer Science & Business Media, p. 622.

Smeraglia, L., Giuffrida, A., Grimaldi, S., Pullen, A., La Bruna, V., Billi, A., Agosta, F., 2021. Fault-controlled upwelling of low-T hydrothermal fluids tracked by travertines in a fold-and-thrust belt, Monte Alpi, southern apennines, Italy. J. Struct. Geol. 144, 104276. https://doi.org/10.1016/j.jsg.2020.104276.

Souza, E.G., Scherer, C.M.S., dos Reis, A.D., Bállico, M.B., Ferronatto, J.P.F., Bofill, L.M., Kifumbi, C., 2019. Sequence stratigraphy of the mixed wave-tidal-dominated Mesoproterozoic sedimentary succession in Chapada Diamantina Basin, Espinhaço supergroup– Ne/Brazil. Precambrian Res. 327, 103–120. https://doi.org/10.1016/j.precamres.2019.03.007.

Souza, J.D., Kosin, M., Melo, R.C., Santos, R.A., Teixeira, L.R., Sampaio, A.R., Guimarães, J.T., Vieira Bento, R., Borges, V.P., Martins, A.A.M., Arcanjo, J.B., Loureiro, H.S.C., Angelim, L.A.A., 2003. Mapa Geológico do Estado da Bahia - Escala 1:1.000.000, Salvador: CPRM. CBPM-CPRM.

Souza, V.H.P., Bezerra, F.H.R., Vieira, L.C., Cazarin, C.L., Brod, J.A., 2021. Hydrothermal silicification confined to stratigraphic layers: implications for carbonate reservoirs. Mar. Petrol. Geol. 124, 104818. https://doi.org/10.1016/j.marpetgeo.2020.104818.

Srivastava, N.K., Rocha, A.J.D., 1999. Fazenda Cristal, BA–Estromatólitos Mesoproterozóicos, Sítios Geológicos e Paleontológicos do Brasil. http://sigep.cprm.gov.br/sitio093/sitio093.pdf.

Süssenberger, A., Neves, B.B. de B., Wemmer, K., 2014. Dating low-grade metamorphism and deformation of the espinhaço supergroup in the Chapada Diamantina (bahia, NE Brazil): a K/Ar fine-fraction study. Brazilian J. Geol. 44, 207–220. https://doi.org/10.5327/Z2317-488920140002003.

Trompette, R., Uhlein, A., da Silva, M.E., Karmann, I., 1992. The Brasiliano São Francisco craton revisited (central Brazil). J. South Am. Earth Sci. 6, 49–57. https://doi.org/10.1016/0895-9811(92)90016-R.

Warren, J.E., Root, P.J., 1963. The behavior of naturally fractured reservoirs. Soc. Petrol. Eng. J. 3, 245–255. https://doi.org/10.2118/426-PA.

Watkins, H., Butler, R.W.H., Bond, C.E., Healy, D., 2015. Influence of structural position on fracture networks in the Torridon Group, Achnashellach fold and thrust belt, NW Scotland. J. Struct. Geol. 74, 64–80. https://doi.org/10.1016/j.jsg.2015.03.001.

Zeng, H., Loucks, B., Janson, X., Wang, Q., Xia, Y., Xu, L., 2010. An ultra-deep paleokarst system in the ordovician, north-central Tarim basin, China: high-resolution 3D seismic interpretation. In: SEG Technical Program Expanded Abstracts 2010. Society of Exploration Geophysicists, pp. 1526–1530. https://doi.org/10.1190/1.3513130.